

Development and Application of a Model Interface  
To couple Land Surface Models with Regional Climate Models  
For Climate Change Risk Assessment  
In the Upper Danube Watershed

Dissertation  
der Fakultät für Geowissenschaften  
der Ludwig-Maximilians-Universität München



vorgelegt von:  
Thomas Marke  
aus München

Eingereicht am: 04.08.2008

1. Gutachter: Prof. Dr. Wolfram Mauser  
2. Gutachter: Prof. Dr. Karsten Schulz

Tag der mündlichen Prüfung: 10.10.2008

„Alle reden vom Wetter, aber keiner unternimmt was dagegen.“  
*Karl Valentin (1882-1948)*



## PREFACE

In the last decades regional climate models (RCMs) have proven their ability to provide valuable information about potential future changes in the earth's climate system. Research projects like GLOWA-Danube (Global Change of the Water Cycle) are given the possibility to utilize RCM simulations as meteorological drivers for land surface model components. To adequately describe all sorts of water fluxes in the research area of the Upper Danube watershed the different components of the interdisciplinary DANUBIA model require data in high spatial and temporal resolution. While the latter can be satisfactorily provided by most RCMs, the spatial resolution at which atmospheric processes can be resolved is computationally limited to at best 10 x 10 km at present. A clear need has been identified to develop appropriate methods to bridge the gap between RCMs and high resolution land surface models. The application of such downscaling techniques is in particular necessary in highly complex terrain, where the limited spatial resolution of RCM simulations does not fully capture the natural climatic variability. In the present work a model interface has been developed that provides adequate scaling techniques to overcome the mismatch between the model scales permitting the investigation of climate change impacts at regional to local scales.

Besides the downscaling of meteorological simulations, the coupler scales up fluxes calculated at the land surface and provides the aggregated fluxes as inputs for the RCMs. As the latter allows to consider the nonlinearity and complexity of the interactions between the atmosphere and the land surface as well as the mutual dependency of the respective processes at the investigated scale the approach can be expected to contribute to a better understanding of the complex land-atmosphere-system. A comprehensive description of the implemented algorithms is given. Further first results of one-way coupled model runs using the regional climate model REMO to simulate the atmosphere and the hydrological model PROMET to describe all hydrological relevant processes at the land surface are presented. By comparing the results achieved for a potential future climate to those achieved for past climate conditions the climate change impact on the water resources is analyzed.

The model interface SCALMET has been developed in the framework of the GLOWA-Danube Project at the Ludwig-Maximilians-University in Munich. The financial funding of GLOWA-Danube by the German Ministry of Education and Research (BMB+F) is gratefully acknowledged.

At this point, I want to take the chance to thank all those people who have directly or indirectly contributed to the successful fulfillment of this work. First of all, I would like to express my deepest gratefulness to my supervisor and doctor father Prof. Dr. Wolfram Mauser. He not only gave me the opportunity to work in the fascinating field of coupled land-

atmosphere modeling after my graduation, but supported me for the whole duration of my work. His inspiring comments as well as the confidence he placed in me enabled me to develop and realize my own ideas. Beyond his support in the process of this thesis, I was given the opportunity to gain valuable experience by giving student courses and organizing field trips. Finally, I would like to thank him for the excellent working conditions as well as for the technical infrastructure I was provided. Both have been fundamental for the successful outcome of this work.

For taking on the second review of this work, I want to express my deepest gratefulness to Prof. Dr. Karsten Schulz.

As an interdisciplinary work can only be successfully realized with interdisciplinary support, my special thanks go to my project partners in the field of atmospheric science. I would like to thank Dr. Daniela Jacob for providing me the climate model simulations used in the framework of this work. I further thank her and the whole REMO developer team at the MPI-M (Dr. Sven Kotlarski, Holger Göttel, Swantje Preuschmann, Dr. Susanne Pfeifer and Dr. Stefan Hagemann) for the invaluable insights in the regional climate model REMO. Cordial thanks also go to Dr. Günther Zängl and Andreas Pfeiffer who kept supporting me with meteorological advice and expert knowledge concerning the regional climate model MM5. Further, I would like to thank all other project partners whose names are not mentioned here explicitly for the valuable insights into their disciplines and their willing cooperation.

Apart from the developers of the meteorological model components I would like to thank all colleagues who have contributed to the development of the PROMET model. Prof. Dr. Wolfram Mauser, Dr. Heike Bach, Tobias Hank, Markus Muerth, Monika Prasch and Daniel Waldmann should be explicitly mentioned here. Thank you for all your support and the valuable discussions concerning the different components of the PROMET model.

I greatly appreciate the friendly spirit at my working place and would like to thank all my colleagues at the institute for the excellent working atmosphere. Special thanks go to Dr. Alexander Löw, Dr. Ulrich Strasser and Dr. Florian Siebel, who have always helped me out with scientific advice even when they were very busy themselves. For the supply of meteorological data I want to thank Ruth Weidinger and Andrea Reiter, in particular.

I would also like to thank my office roommates Tobias Hank, Mathias Bernhardt and Florian Zabel for the very special atmosphere and all the valuable discussions in our office.

Finally, my thanks go to all my friends who encouraged me to take on and complete this thesis and, particularly, to my parents and my girlfriend Stefanie Mayer for their loyal and unlimited support, patience and understanding. Above all I want to thank my mum for all that she is and for all that she does. It is her I want to dedicate this work to.

## TABLE OF CONTENTS

LIST OF FIGURES .....	I
LIST OF TABLES .....	VII
LIST OF ACRONYMS .....	VIII
LIST OF SYMBOLS .....	X
SUMMARY .....	XVI
<b>1 INTRODUCTION.....</b>	<b>1</b>
1.1 THE ROLE OF NUMERICAL MODELS IN CLIMATE CHANGE RESEARCH .....	1
1.2 STATE OF THE ART.....	2
1.2.1 <i>General Characteristics Of Climate Models</i> .....	2
1.2.2 <i>Effects of a limited spatial resolution</i> .....	4
1.2.3 <i>Downscaling Techniques</i> .....	5
1.3 GLOWA-DANUBE.....	9
1.4 MOTIVATION OF THIS THESIS.....	11
<b>2 THE UPPER DANUBE WATERSHED.....</b>	<b>15</b>
2.1 CLIMATE .....	16
2.2 HYDROLOGY .....	18
2.3 GEOMORPHOLOGY AND GEOLOGY .....	20
2.4 SOILS .....	21
2.5 VEGETATION .....	22
2.6 SOCIO-ECONOMIC ASPECTS.....	23
<b>3 THE COUPLED MODEL SYSTEM .....</b>	<b>25</b>
3.1 THE HYDROLOGICAL MODEL PROMET.....	25
3.1.1 <i>The Meteorology Component</i> .....	26
3.1.2 <i>The Land Surface Energy and Mass Balance Component</i> .....	31
3.1.3 <i>The Vegetation Component</i> .....	31
3.1.4 <i>The Snow and Ice Component</i> .....	32
3.1.5 <i>The Soil Hydrological and Soil Temperature Component</i> .....	33
3.1.6 <i>The Groundwater Component</i> .....	33
3.1.7 <i>The Channel Flow Component</i> .....	34
3.1.8 <i>The Man-Made Hydraulic Structures Component</i> .....	34
3.2 THE REGIONAL CLIMATE MODEL REMO .....	35
3.3 THE MODEL COUPLING TOOL SCALMET .....	39

---

<b>4</b>	<b>THE SCALING OF METEOROLOGICAL VARIABLES IN SCALMET .....</b>	<b>42</b>
4.1	GENERAL DOWNSCALING PRINCIPLES IN SCALMET.....	42
4.1.1	<i>Direct Interpolation Methods .....</i>	<i>43</i>
4.1.2	<i>Regression Based Remapping.....</i>	<i>49</i>
4.1.3	<i>Submodel Approach.....</i>	<i>53</i>
4.1.4	<i>Conservation of Mass and Energy between the Model Scales .....</i>	<i>55</i>
4.2	DOWNSCALING THE INDIVIDUAL METEOROLOGICAL VARIABLES.....	56
4.2.1	<i>Solar Zenith Angle.....</i>	<i>57</i>
4.2.2	<i>Air Temperature.....</i>	<i>57</i>
4.2.3	<i>Air Humidity.....</i>	<i>61</i>
4.2.4	<i>Precipitation .....</i>	<i>65</i>
4.2.5	<i>Incoming Shortwave Radiation.....</i>	<i>69</i>
4.2.6	<i>Incoming Longwave Radiation .....</i>	<i>72</i>
4.2.7	<i>Wind Speed.....</i>	<i>75</i>
4.2.8	<i>Surface Pressure .....</i>	<i>79</i>
4.2.9	<i>Method Discussion.....</i>	<i>80</i>
4.3	UPSCALING OF LAND SURFACE MODEL OUTPUTS.....	81
<b>5</b>	<b>APPLICATION TO PAST CLIMATE CONDITIONS .....</b>	<b>83</b>
5.1	VALIDATION OF THE LAND SURFACE MODEL PROMET .....	83
5.2	EVALUATION OF THE SCALING METHODS IN SCALMET .....	85
5.2.1	<i>Meteorological Method Comparison.....</i>	<i>86</i>
5.2.2	<i>Hydrological Method Comparison.....</i>	<i>102</i>
5.3	COUPLED MODEL RUNS FOR PAST CLIMATE CONDITIONS .....	109
5.3.1	<i>Choice of Remapping Methods.....</i>	<i>110</i>
5.3.2	<i>Model Results .....</i>	<i>111</i>
<b>6</b>	<b>APPLICATION TO CLIMATE PROJECTIONS .....</b>	<b>127</b>
6.1	THE IPCC SCENARIOS .....	127
6.2	THE A1B SCENARIO – METEOROLOGICAL CONDITIONS IN THE UPPER DANUBE WATERSHED.....	129
6.2.1	<i>Temperature .....</i>	<i>130</i>
6.2.2	<i>Precipitation .....</i>	<i>133</i>
6.3	THE A1B SCENARIO – HYDROLOGICAL IMPACT IN THE UPPER DANUBE WATERSHED.....	137
6.3.1	<i>Evapotranspiration .....</i>	<i>138</i>
6.3.2	<i>Snow Hydrology.....</i>	<i>141</i>
6.3.3	<i>Area Runoff and River Discharge.....</i>	<i>143</i>
<b>7</b>	<b>CONCLUSION AND OUTLOOK .....</b>	<b>149</b>
<b>8</b>	<b>REFERENCES.....</b>	<b>157</b>

---

<b>9</b>	<b>APPENDIX .....</b>	<b>172</b>
A-1:	EQUATIONS USED TO CONVERT BETWEEN DIFFERENT FORMS OF AIR HUMIDITY .....	172
A-2:	TEMPERATURE-ELEVATION DEPENDENCE AS REFLECTED IN THE STATION OBSERVATIONS USED FOR THE DETERMINATION OF MONTHLY LAPSE RATES FOR THE UD .....	174
A-3:	DEWPOINT TEMPERATURE-ELEVATION DEPENDENCE AS REFLECTED IN THE STATION OBSERVATIONS USED FOR THE DETERMINATION OF MONTHLY LAPSE RATES FOR THE UD .....	176
A-4:	SCALMET INPUT FILE CONTAINING THE REQUIRED REMAPPING PARAMETERS .....	178
A-5:	INCOMING LONGWAVE RADIATION FOR THE REFERENCE RUN AND THE SCENARIO RUN .....	179
A-6:	INCOMING SHORTWAVE RADIATION FOR THE REFERENCE RUN AND THE SCENARIO RUN .....	180
A-7:	THE METEOROLOGICAL STATIONS USED FOR THE EVALUATION OF THE REMAPPING TECHNIQUES IN SCALMET .....	181
A-8:	MAE STATISTIC FOR ALL STATIONS USED WITHIN THE EVALUATION OF TEMPERATURE REMAPPINGS .....	182
A-9:	MAE STATISTIC FOR ALL STATIONS USED WITHIN THE EVALUATION OF PRECIPITATION REMAPPINGS .....	184
A-10:	MAE STATISTIC FOR ALL STATIONS USED WITHIN THE EVALUATION OF WIND SPEED REMAPPINGS .....	186
<b>10</b>	<b>CURRICULUM VITAE .....</b>	<b>188</b>

## LIST OF FIGURES

<b>Fig. 1.1:</b> Schematic representation of the structure and the basic characteristics of a climate model	3
<b>Fig. 1.2:</b> Representation of land surface heterogeneities following the tile approach	4
<b>Fig. 1.3:</b> Schematic diagram of the time-slice technique	6
<b>Fig. 1.4:</b> Schematic diagram of the statistical downscaling approach	7
<b>Fig. 1.5:</b> Schematic overview of the decision support system DANUBIA	9
<b>Fig. 1.6:</b> The integrative model approach in GLOWA-Danube	10
<b>Fig. 1.7:</b> Schematic diagram of the coupled model system	12
<b>Fig. 1.8:</b> Representation of different land cover types in different spatial resolutions	13
<b>Fig. 2.1:</b> The Danube watershed and the Upper Danube watershed together with the main tributaries of the Danube river	15
<b>Fig. 2.2:</b> Average summer and winter precipitation in the Upper Danube watershed for the hydrological years 1971-2000	16
<b>Fig. 2.3:</b> Annual mean temperature and average number of days with snow cover in the Upper Danube watershed for the hydrological years 1971-2000	17
<b>Fig. 2.4:</b> River network and major water bodies in the Upper Danube watershed	19
<b>Fig. 2.5:</b> Hydrogeologic profile of the Upper Danube watershed	20
<b>Fig. 2.6:</b> Topography and simplified hydrogeology of the Upper Danube watershed	21
<b>Fig. 2.7:</b> The Upper Danube watershed and its major cities, its traffic network and water ways and the countries sharing and surrounding the catchment	23
<b>Fig. 3.1:</b> Schematic diagram of the different components and interfaces in PROMET	25
<b>Fig. 3.2:</b> The network of meteorological stations used for the generation of meteorological distributions in PROMET	27
<b>Fig. 3.3:</b> Temporal interpolation of rainfall over the time past between the observations for the two categories of long and short rain events	28
<b>Fig. 3.4:</b> The origins of the regional climate model REMO and schematic illustration of a hybrid vertical coordinate system	35
<b>Fig. 3.5:</b> The one-way double nesting model setup used for the REMO simulations	36
<b>Fig. 3.6:</b> The model domain of the regional climate model REMO together with the Upper Danube watershed representing the model domain of the land surface model PROMET	38
<b>Fig. 3.7:</b> Schematic diagram of the coupled model system together with the inputs needed for the remapping in SCALMET and the outputs optionally given out by the coupler	41
<b>Fig. 4.1:</b> Representation of topography in the Upper Danube watershed at different spatial resolutions	42
<b>Fig. 4.2:</b> The general quadrilateral grid structure of the bilinear interpolation process	44
<b>Fig. 4.3:</b> Example of two overlapping quadrilateral grids	47

<b>Fig. 4.4:</b> Directly interpolated REMO control run temperature using the conservative, bilinear and inverse distance weighted interpolation scheme _____	49
<b>Fig. 4.5:</b> The different steps in the process chain of the regression based scaling approach shown by the example of temperature remappings _____	53
<b>Fig. 4.6:</b> The different steps in the process chain of the submodel approach shown by the example of shortwave radiation _____	54
<b>Fig. 4.7:</b> The temperature-elevation dependence in REMO control run simulations for two model time steps in the year 1982 _____	58
<b>Fig. 4.8:</b> The two-layer atmosphere in SCALMET _____	59
<b>Fig. 4.9:</b> The elevation dependence of monthly mean air temperature for December and June _____	60
<b>Fig. 4.10:</b> The dewpoint temperature-elevation dependence for a model time step in the year 1982 _____	62
<b>Fig. 4.11:</b> The elevation dependence of monthly mean dewpoint temperature for December and June _____	63
<b>Fig. 4.12:</b> REMO air humidity, remapped air humidity achieved using the constant lapse rate approach and remapping result using the regression based remapping for a model time step in the year 1982 _____	65
<b>Fig. 4.13:</b> Precipitation-elevation dependence in REMO control run simulations and frequency distribution of simulated precipitation for a model time step in the year 1982 _____	66
<b>Fig. 4.14:</b> Process chain in the determination of monthly precipitation adjustment factors for the model domain shown for the month of June _____	68
<b>Fig. 4.15:</b> Monthly precipitation adjustment factors derived for the Upper Danube watershed together with those used by LISTON AND ELDER (2006) (left) and the dependence of the precipitation adjustment function on elevation difference for a summer month (right) _____	69
<b>Fig. 4.16:</b> Bilinearly interpolated REMO cloud cover and the amount of diffuse and direct radiation calculated by the shortwave radiation submodel in SCALMET for a model time step in the year 1982 _____	72
<b>Fig. 4.17:</b> REMO shortwave simulations, remapped shortwave radiation and conservatively aggregated remapped shortwave radiation for a model time step in the year 1982 _____	72
<b>Fig. 4.18:</b> The dependence of incoming longwave radiation on terrain elevation in REMO control run simulations for a model time step in the year 1982 and REMO incoming longwave radiation vs. simulated cloud cover for the same model time step _____	73
<b>Fig. 4.19:</b> Conservatively remapped incoming longwave radiation together with the results of the submodel calculations for a model time step in the year 1982 _____	74
<b>Fig. 4.20:</b> The elevation dependence of simulated wind speed for a model time step in the year 1982 _____	76
<b>Fig. 4.21:</b> Terrain curvature calculated for the Upper Danube watershed and schematic illustration of the parameters involved in the remapping of wind speed simulations by the wind submodel in SCALMET _____	77
<b>Fig. 4.22:</b> The CI remapped REMO wind speed simulations, the regression based wind speed remapping and the results of the wind model calculations by the example of a model time step in the year 1982 _____	79

<b>Fig. 4.23:</b> Illustration of the upscaling process _____	81
<b>Fig. 5.1:</b> PROMET discharge simulations for the proxel representing the gauge in Achleiten _____	84
<b>Fig. 5.2:</b> Simulated vs. measured daily discharge at the gauge of the Upper Danube watershed in Achleiten _____	84
<b>Fig. 5.3:</b> Schematic illustration of the processing of observation based meteorological distributions for the later evaluation of the different remapping approaches (SCALMET) _____	87
<b>Fig. 5.4:</b> The climate stations used within the meteorological evaluation process _____	88
<b>Fig. 5.5:</b> Comparison of remapped and observed daily temperatures at the three climate stations in St. Leonhard-Neurur, Rauris and Jenbach for the period 1994-1996 _____	90
<b>Fig. 5.6:</b> Elevation difference (DEM 1 x 1 km - DEM 10 x 10 km) for the Alpine part of the Upper Danube watershed _____	91
<b>Fig. 5.7:</b> Frequency distribution of the mean absolute error (MAE) in temperature remappings for the conservative interpolation, the bilinear interpolation, the constant lapse rate remapping (CLR) and the regression based remapping (RBR) for the period 1994-1996 _____	92
<b>Fig. 5.8:</b> Results of the temperature remappings carried out within the synthetic evaluation approach _____	93
<b>Fig. 5.9:</b> Results of the precipitation remappings carried out within the synthetic evaluation approach _____	94
<b>Fig. 5.10:</b> Comparison of remapped and observed daily precipitation at the three climate stations in St. Leonhard-Neurur, Rauris and Jenbach for the period 1994-1996 _____	96
<b>Fig. 5.11:</b> Frequency distribution of the mean absolute error (MAE) in precipitation remappings for the different remapping methods over the period 1994-1996 _____	97
<b>Fig. 5.12:</b> Comparison of remapped and observed daily wind speeds at climate stations in St. Leonhard-Neurur, Rauris and Jenbach for the period 1994-1996 _____	98
<b>Fig. 5.13:</b> Frequency distribution of the mean absolute error (MAE) in wind speed remappings for the conservative interpolation, the bilinear interpolation and the regression based remapping (RBR) for the period 1994-1996 _____	99
<b>Fig. 5.14:</b> Comparison of remapped and observed daily global radiation at climate station Weihenstephan _____	100
<b>Fig. 5.15:</b> Observed and remapped course of daily global radiation throughout the year 1994 at climate station Weihenstephan _____	101
<b>Fig. 5.16:</b> The different steps within the hydrological evaluation of the remapping methods implemented in SCALMET _____	103
<b>Fig. 5.17:</b> Correlation between modeled and measured discharge at the gauge of the Upper Danube watershed in Achleiten and temporal course of simulated and observed discharge at the gauge for the period 1994-1996 _____	104
<b>Fig. 5.18:</b> Correlation between modeled (QPB I) and measured discharge at the gauge of the Upper Danube watershed in Achleiten and temporal course of the reference run discharge and the QPB I run discharge at the pixel representing the gauge of the Upper Danube watershed in Achleiten for the period 1994-1996 _____	105

<b>Fig. 5.19:</b> Correlation between modeled (QPB II) and measured discharge at the gauge of the Upper Danube watershed in Achleiten and temporal course of the reference run discharge and the QPB I run discharge at the pixel representing the gauge of the Upper Danube watershed in Achleiten for the period 1994-1996	105
<b>Fig. 5.20:</b> Correlation between modeled (BI) and measured discharge at the gauge of the Upper Danube watershed in Achleiten and temporal course of the reference run discharge and the BI run discharge at the pixel representing the gauge of the Upper Danube watershed in Achleiten for the period 1994-1996	106
<b>Fig. 5.21:</b> Correlation between modeled (CI) and measured discharge at the gauge of the Upper Danube watershed in Achleiten and temporal course of the reference run discharge and the CI run discharge at the pixel representing the gauge of the Upper Danube watershed in Achleiten for the period 1994-1996	107
<b>Fig. 5.22:</b> Difference between simulated and observed discharge at the gauge in Achleiten for two SCALMET-PROMET model runs over the period 1994-1996	107
<b>Fig. 5.23:</b> Difference in simulated snow water equivalent between two SCALMET-PROMET model runs	108
<b>Fig. 5.24:</b> Remapped average annual mean temperature and difference between the remapped distributions and those provided by the meteorological preprocessor in PROMET for the period 1971-2000	112
<b>Fig. 5.25:</b> Observation based and remapped monthly mean temperatures in the Upper Danube watershed for the period 1971-2000 and difference in monthly mean temperature between remapped REMO control run data and spatially distributed observations	113
<b>Fig. 5.26:</b> Remapped average annual precipitation and difference between the remapped simulations and the spatially distributed observations for the hydrological years 1971-2000	114
<b>Fig. 5.27:</b> The average annual precipitation for the Austrian subcatchments within the domain of the Upper Danube watershed (1961-1990)	115
<b>Fig. 5.28:</b> Remapped REMO precipitation as used in the coupled reference run REMO-SCALMET-PROMET (CRR) for the hydrological years 1971-2000 and observation based area mean annual precipitation in the Upper Danube watershed as used within the uncoupled reference run (URR) for the hydrological years 1971-2000	117
<b>Fig. 5.29:</b> Observation based and remapped average monthly precipitation in the Upper Danube watershed for the period 1971-2000 and difference in monthly precipitation between the remapped REMO data and spatially distributed observations	118
<b>Fig. 5.30:</b> The average modeled water balance in the Upper Danube watershed for the hydrological years 1971-2000	119
<b>Fig. 5.31:</b> Mean monthly discharge (1971-2000) simulated in the coupled reference run (CRR) together with discharge observation and mean monthly discharge simulated in the uncoupled reference run (URR) together with discharge observations at the gauge in Achleiten	120

<b>Fig. 5.32:</b> Monthly peak-flow discharge (1971-2000) simulated in the coupled reference run (CRR) together with discharge observations and monthly peak-flow discharge simulated in the uncoupled reference run (URR) together with discharge observations at the gauge in Achleiten _____	121
<b>Fig. 5.33:</b> Monthly low-flow discharge (1971-2000) simulated in the coupled reference run (CRR) together with discharge observations and monthly low-flow discharge simulated in the uncoupled reference run (URR) together with discharge observations at the gauge in Achleiten _____	121
<b>Fig. 5.34:</b> Low-flow and flood return periods based on PROMET simulations for the coupled reference run (CRR) and observations (OBS) (left) and sorted peak-flow simulations (CRR and URR) together with sorted peak-flow observations (OBS) for the gauge at Achleiten (right) _____	123
<b>Fig. 5.35:</b> Average monthly evapotranspiration (1971-2000) as reflected by the results of the coupled reference run (CRR) and the uncoupled reference run (URR) (left) and difference in monthly evapotranspiration (CRR-URR) (right) _____	125
<b>Fig. 5.36:</b> Annual mean evapotranspiration in the Upper Danube watershed and areal standard deviation for the coupled reference run and the uncoupled reference run _____	125
<b>Fig. 6.1:</b> The CO <sub>2</sub> -emissions and changes in temperature for the different IPCC scenarios _____	129
<b>Fig. 6.2:</b> Change in annual mean temperature in the Upper Danube watershed _____	131
<b>Fig. 6.3:</b> Annual area mean temperature in the Upper Danube watershed as reflected in remapped REMO control run and A1B scenario run data _____	131
<b>Fig. 6.4:</b> Seasonal change in area mean temperature in the Upper Danube watershed _____	132
<b>Fig. 6.5:</b> Monthly mean temperatures of the coupled reference run and the scenario run (left) and absolute change in monthly mean temperatures for the Upper Danube watershed (right) _____	133
<b>Fig. 6.6:</b> Relative change in average annual precipitation in the Upper Danube watershed _____	134
<b>Fig. 6.7:</b> Change in annual area mean precipitation for the area of the Upper Danube watershed _____	134
<b>Fig. 6.8:</b> Seasonal change in area mean precipitation for the area of the Upper Danube watershed _____	135
<b>Fig. 6.9:</b> Average monthly precipitation for the reference run and scenario run meteorology (left) and change in average monthly precipitation in the Upper Danube watershed (right) _____	136
<b>Fig. 6.10:</b> Relative change in average seasonal precipitation for the Upper Danube watershed _____	137
<b>Fig. 6.11:</b> The average modeled water balance in the Upper Danube watershed for the hydrological years 2011-2060 _____	138
<b>Fig. 6.12:</b> Modeled annual evapotranspiration for the coupled reference run and the scenario run _____	138
<b>Fig. 6.13:</b> Change in area mean evapotranspiration for the area of the Upper Danube watershed _____	139
<b>Fig. 6.14:</b> Simulated mean monthly evapotranspiration for the coupled reference run (CRR) and the coupled scenario run (CSR) (left) and difference in evapotranspiration between both runs (right) _____	140
<b>Fig. 6.15:</b> Change in average plant available soil water (upper 20 cm of the soil) in July for the area of the Upper Danube watershed _____	140
<b>Fig. 6.16:</b> Change in annual snowfall for the area of the Upper Danube watershed _____	141

---

<b>Fig. 6.17:</b> <i>Change in the number of days characterized by the presence of a snow cover (SWE &gt; 1 mm) and change in annual snowfall in the Upper Danube watershed</i>	142
<b>Fig. 6.18:</b> <i>Decadal change in the number of days characterized by the presence of a snow cover (SWE &gt; 1 mm) relative to the reference period</i>	143
<b>Fig. 6.19:</b> <i>Modeled annual mean discharge at the gauge in Achleiten for the reference period and the scenario period</i>	144
<b>Fig. 6.20:</b> <i>Mean monthly discharge volumes at the gauge in Achleiten modeled within the reference run and the scenario run</i>	145
<b>Fig. 6.21:</b> <i>Mean monthly peak-flow discharge and low-flow discharge volumes at the gauge in Achleiten modeled for the reference run and the scenario run</i>	145
<b>Fig. 6.22:</b> <i>NM7Q and NM7Q<sub>50</sub> discharge volumes at the gauge in Achleiten for the reference run and the scenario run (left) and frequency distribution of the NM7Q occurrence according to discharge simulations (reference run and scenario run) and discharge recordings (right)</i>	146
<b>Fig. 6.23:</b> <i>HQ and HQ<sub>50</sub> discharge volumes at the gauge in Achleiten for the reference run and the scenario run (left) and frequency distribution of the HQ occurrence according to discharge simulations (reference run and scenario run) and discharge recordings (right)</i>	147
<b>Fig. 6.24:</b> <i>Low-flow and flood return periods based on PROMET simulations for the coupled reference run (CRR) and the scenario run (CSR)</i>	148

## LIST OF TABLES

<b>Tab. 2.1:</b> <i>Hydrological characteristics of the Danube and its main tributaries</i>	19
<b>Tab. 3.1:</b> <i>Seasonal factors for the calculation of the atmospheric transmissivity for direct solar radiation in the midlatitudes (HOTTEL 1976)</i>	29
<b>Tab. 4.1:</b> <i>Monthly temperature lapse rates derived for the Upper Danube watershed in comparison to those presented by KUNKEL (1989) for the Western United States</i>	61
<b>Tab. 4.2:</b> <i>Monthly dewpoint temperature lapse rates derived for the Upper Danube watershed in comparison to those presented by KUNKEL (1989) for the Western United States</i>	64
<b>Tab. 4.3:</b> <i>Monthly precipitation adjustment factors presented by LISTON AND ELDER (2006) and those derived for the Upper Danube watershed</i>	68
<b>Tab. 4.4:</b> <i>Coefficients for the calculation of the atmospheric emissivity (LISTON AND ELDER 2006)</i>	74
<b>Tab. 5.1:</b> <i>Elevation and geographical coordinates of the stations St. Leonhard-Neurur, Jenbach, Rauris and Weihenstephan</i>	89
<b>Tab. 5.2:</b> <i>The constellation of the remapping methods used in the four PROMET runs over the period 1994-1996</i>	102
<b>Tab. 5.3:</b> <i>The main characteristics of the different model runs used for the simulation of past and future hydrological conditions in the Upper Danube watershed</i>	109
<b>Tab. 5.4:</b> <i>The combination of remapping approaches used for the downscaling of REMO simulations within the reference run and the scenario run</i>	110
<b>Tab. 5.5:</b> <i>Statistical characteristics for the average annual precipitation in the Austrian subcatchments of the Upper Danube watershed</i>	116
<b>Tab. 5.6:</b> <i>Statistical characteristics for annual precipitation for the hydrological years 1971-2000 for the uncoupled reference run and the coupled reference run</i>	117

## LIST OF ACRONYMS

ACRONYM	DESCRIPTION
AOGCM	<b>A</b> tmosphere- <b>O</b> cean <b>G</b> eneral <b>C</b> irculation <b>M</b> odel
AOI	<b>A</b> rea <b>O</b> f <b>I</b> nterest
BI	<b>B</b> ilinear <b>I</b> nterpolation
BMB+F	German Ministry of Research and Education
CI	1st Order <b>C</b> onservative <b>I</b> nterpolation
CLR	<b>C</b> onstant <b>L</b> apse Rate <b>R</b> emapping
CNTRL	REMO <b>C</b> ontrol <b>R</b> un
CRR	<b>C</b> oupled <b>R</b> eference <b>R</b> un
CSR	<b>C</b> oupled <b>S</b> cenario <b>R</b> un
DEM	<b>D</b> igital <b>E</b> levation <b>M</b> odel
DJF	<b>D</b> ecember, <b>J</b> anuary and <b>F</b> ebruary
UD	<b>U</b> pper <b>D</b> anube Watershed
DWD	<b>D</b> eutscher <b>W</b> etter <b>D</b> ienst
ECMWF	<b>E</b> uropean <b>C</b> entre for <b>M</b> edium-Range <b>W</b> eather <b>F</b> orecasts
GCM	<b>G</b> eneral <b>C</b> irculation <b>M</b> odel
GLOWA	<b>G</b> lobal Change of the <b>W</b> ater Cycle
HAA	<b>H</b> ydrological <b>A</b> tlas of <b>A</b> ustria
HQ	Annual peak-flow discharge
IDW	<b>I</b> nverse <b>D</b> istance <b>W</b> eighted <b>I</b> nterpolation
IPCC	<b>I</b> ntergovernmental <b>P</b> annel on <b>C</b> limate <b>C</b> hange
JJA	<b>J</b> une, <b>J</b> uly and <b>A</b> ugust
LAM	<b>L</b> imited <b>A</b> rea <b>M</b> odel
LSM	<b>L</b> and <b>S</b> urface <b>M</b> odel
MAE	<b>M</b> ean <b>A</b> bsolute <b>E</b> rror
MAM	<b>M</b> arch, <b>A</b> pril and <b>M</b> ay
MPI-M	<b>M</b> ax- <b>P</b> lanck- <b>I</b> nstitute for <b>M</b> eteorology
NM7Q	Annual 7-days average low-flow discharge
PIXEL	Picture Element
PROMET	<b>P</b> rocess of <b>R</b> adiation, <b>M</b> ass and <b>E</b> nergy <b>T</b> ransfer <b>M</b> odel
PROXEL	<b>P</b> rocess <b>P</b> ixel
RBR	<b>R</b> egression <b>B</b> ased <b>R</b> emapping
RCM	<b>R</b> egional <b>C</b> limate <b>M</b> odel

RMSE	<b>R</b> oot <b>M</b> ean <b>S</b> quare <b>E</b> rror
SCALMET	Model to <b>S</b> cale <b>M</b> eteorological Variables
SON	<b>S</b> eptember, <b>O</b> ctober and <b>N</b> ovember
SRES	<b>S</b> pecial <b>R</b> eport on <b>E</b> mission <b>S</b> cenarios
SWE	<b>S</b> now <b>W</b> ater <b>E</b> quivalent
UBA	German Federal Environment Agency
UML	<b>U</b> nified <b>M</b> odelling <b>L</b> anguage
URR	<b>U</b> ncoupled <b>R</b> eference <b>R</b> un
ZAMG	<b>Z</b> entralanstalt für <b>M</b> eteorology und <b>G</b> eodynamik

## LIST OF SYMBOLS

SYMBOL	DESCRIPTION	UNIT
$a$	Parameter of the linear model	[none]
$a_h$	Coefficient for the calculation of vapor pressure	[none]
$a_{est}$	Estimate of $a$	[none]
$a_0$	Coefficient for the calculation of the atmospheric transmissivity	[none]
$a_1$	Coefficient for the calculation of the atmospheric transmissivity	[none]
$a_2$	Coefficient for the calculation of the atmospheric transmissivity	[none]
$b$	Parameter of the linear model	[none]
$b_h$	Coefficient for the calculation of vapor pressure	[none]
$b_{est}$	Estimate of $b$	[none]
$c_h$	Coefficient for the calculation of vapor pressure	[none]
$c_p$	Specific heat of the air at constant pressure	[J/kg °C]
$d$	Angular distance	[rad]
$day$	Current model day	[DOY]
$d_e$	Extreme flow discharge	[m <sup>3</sup> /s]
$d_s$	Day of the summer solstice	[DOY]
$d_y$	Average number of days in a year	[d/a]
$e_a$	Actual vapour pressure	[hPa]
$e_s$	Saturation vapour pressure	[hPa]
$f$	Flux at a given source grid cell	[depends]
$f_{AOI}$	Fractional contribution to the mass/energy budget of an AOI	[fraction]
$f(d_e)$	Probability density function of discharge $d_e$	[none]
$f_l$	Flux at source grid cell $l$	[depends]
$f_P$	Function at point $P_x$	[depends]
$f_{sw\_dif}$	Fraction of diffuse shortwave radiation	[fraction]
$f_{sw\_dir}$	Fraction of direct shortwave radiation	[fraction]
$f_1$	Factor for the calculation of the atmospheric transmissivity	[none]
$f_2$	Factor for the calculation of the atmospheric transmissivity	[none]
$f_3$	Factor for the calculation of the atmospheric transmissivity	[none]
$g$	Gravity	[m/s <sup>2</sup> ]
$h$	Hour of the day	[h]
$i$	Logically-rectangular grid index	[none]
$i_s$	Angle between the solar radiation beam and a sloping surface	[rad]

$j$	Logically-rectangular grid index	[none]
$k$	Destination grid cell	[none]
$l$	Source grid cell	[none]
$n$	Total number of data pairs	[none]
$n_{clim}$	Regional climate model pixel	[none]
$p_{ls}$	Adjusted precipitation at land surface grid resolution	[mm]
$p_{ref\_int}$	Spatially interpolated precipitation	[mm]
$q$	Specific humidity	[kg/kg]
$q_s$	Specific humidity at saturation	[kg/kg]
$r_a$	Aerodynamic resistance	[s/m]
$r_{clim}$	Residual at regional climate model resolution	[depends]
$r_{ls}$	Interpolated residuals at land surface model resolution	[depends]
$r_s$	Canopy resistance	[s/m]
$\Delta_s$	Slope of the saturation vapour pressure curve	[hPa /°C]
$std\_dev$	Standard deviation	[depends]
$sp_{clim\_int}$	Spatially interpolated pressure simulations	[pa]
$sp_{ls}$	Surface pressure at land surface model resolution	[pa]
$sp_0$	Reference sea level pressure	[pa]
$t_{clim}$	Simulated temperature	[°C]
$t_{clim\_int}$	Spatially interpolated regional climate model temperature	[°C]
$td_{clim}$	Simulated dewpoint temperature	[°C]
$td_{ref\_int}$	Spatially interpolated reference level dewpoint temperature	[°C]
$t_{ls}$	Remapped air temperature	[°C]
$t_{ref}$	Temperature at reference level elevation	[°C]
$t_{ref\_int}$	Spatially interpolated reference level temperature	[°C]
$ws_{ls}$	Topographically adjusted wind speed	[m/s]
$ws_{ls\_int}$	Spatially Interpolated wind speed	[m/s]
$ws_{u\_int}$	Spatially interpolated u wind component	[m/s]
$ws_{v\_int}$	Spatially interpolated v wind component	[m/s]
$x$	Independent variable of the linear model	[depends]
$x_{coord}$	X-grid coordinate	[m]
$y$	Dependent variable of the linear model	[depends]
$y_{coord}$	Y-grid coordinate	[m]
$\hat{y}$	Predicted value of the dependent variable $y$	[depends]
$y_b$	Ratio of actual and potential evapotranspiration	[fraction]

$y_{clim}$	Flux simulated by the regional climate model	[depends]
$\hat{y}_{clim}$	Flux predicted at regional climate model resolution	[depends]
$\Delta y_{clim}$	Mass/energy overrun/deficit at climate model resolution	[depends]
$y_{ls}$	Corrected flux at land surface model resolution	[depends]
$y_{ls\_AOIcor}$	Flux corrected for the AOI mass/energy budget at land surface	[depends]
$\hat{y}_{ls}$	Flux predicted at land surface model resolution	[depends]
$\bar{y}_{ls}$	Mean conditions over all pixels covered by grid cell n	[depends]
$\Delta y_{ls}$	Interpolated mass/energy overrun/deficit	[depends]
$y_s$	Ratio of actual and potential evapotranspiration (snow months)	[fraction]
$z$	Terrain elevation	[m.a.s.l.]
$\Delta z$	Difference in elevation	[m]
$z_{clim}$	Terrain elevation of the regional climate model	[m.a.s.l.]
$z_E$	Grid cell elevation in eastern direction	[m.a.s.l.]
$z_{ls}$	Terrain elevation of the land surface model	[m.a.s.l.]
$z_{ref}$	Reference level elevation	[m.a.s.l.]
$z_N$	Grid cell elevation in northern direction	[m.a.s.l.]
$z_S$	Grid cell elevation in southern direction	[m.a.s.l.]
$z_W$	Grid cell elevation in western direction	[m.a.s.l.]
$A_k$	Angular area of the destination grid cell k	[rad <sup>2</sup> ]
$A_{lk}$	Angular area of cell l covered by cell k	[rad <sup>2</sup> ]
$B$	Ground heat flux	[W/m <sup>2</sup> ]
$C_f$	Cloud fraction	[fraction]
$C_{f\_int}$	Spatially interpolated climate model cloud cover	[fraction]
$D_e$	Considered extreme flow discharge	[m <sup>3</sup> /s]
$ET$	Latent heat flux	[W/m <sup>2</sup> ]
$ET_{pot}$	Potential annual evapotranspiration	[mm]
$ET_{pot\_s}$	Sum of potential evapotranspiration (snow months)	[mm]
$F(d_e)$	Probability distribution function of discharge $d_e$	[none]
$\bar{F}_k$	Area averaged flux at destination cell k	[depends]
$H$	Sensible heat flux	[W/m <sup>2</sup> ]
$H_s$	Scale height of the atmosphere	[m]
$H_0$	Null hypothesis	[none]
$I_0$	Solar irradiance at the top of the atmosphere	[W/m <sup>2</sup> ]
$L$	Number of source grid cells	[none]

$MAE$	Mean absolute error	[depends]
$N_c$	Number of concordances found within the data	[none]
$N_d$	Number of discordances found within the data	[none]
$N_{neighbors}$	Number of neighbors	[none]
$P$	Annual precipitation	[mm]
$P_{cor}$	Water balance corrected annual precipitation	[mm]
$P_x$	Destination grid point	[grid unit]
$P_e$	Probability for the occurrence of discharge $D_e$	[%/100]
$Q$	Annual discharge	[mm]
$R$	Radiation balance	[W/m <sup>2</sup> ]
$R^2$	Coefficient of determination	[none]
$R_g$	Gas constant	[J/kg K]
$RH$	Relative humidity	[%]
$R_k$	Kendall coefficient of correlation	[none]
$R_{lw}$	Longwave radiation at the land surface	[W/m <sup>2</sup> ]
$R_{lw\_in}$	Longwave radiation emitted by the atmosphere	[W/m <sup>2</sup> ]
$R_{lw\_out}$	Longwave radiation emitted by the land surface	[W/m <sup>2</sup> ]
$R_p$	Pearson coefficient of correlation	[none]
$RP$	Return period	[a]
$R_{sw\_dif}$	Diffuse component of the incoming solar radiation	[W/m <sup>2</sup> ]
$R_{sw\_dif\_cor}$	Diffuse component of the corrected incoming solar radiation	[W/m <sup>2</sup> ]
$R_{sw\_dir}$	Direct component of the incoming solar radiation	[W/m <sup>2</sup> ]
$R_{sw\_dir\_cor}$	Direct component of the corrected incoming solar radiation	[W/m <sup>2</sup> ]
$R_{sw\_in}$	Incoming shortwave radiation	[W/m <sup>2</sup> ]
$R_{sw\_in\_cor}$	Corrected incoming shortwave radiation	[W/m <sup>2</sup> ]
$R_{sw\_net}$	Net shortwave radiation at the land surface	[W/m <sup>2</sup> ]
$R_{sw\_out}$	Reflected shortwave radiation	[W/m <sup>2</sup> ]
$R_{sw\_pot}$	Potential incoming shortwave radiation	[W/m <sup>2</sup> ]
$\Delta S$	Change in water storage	[mm]
$SWE$	Snow water equivalent	[mm]
$SZA$	Solar zenith angle	[rad]
$T_c$	Temperature	[°C]
$T_d$	Dewpoint temperature	[°C]
$T_k$	Temperature	[K]
$T_{dif}$	Atmospheric transmissivity for diffuse radiation	[fraction]

$T_{dir}$	Atmospheric transmissivity for direct radiation	[fraction]
$T_{mean}$	Mean temperature	[K]
$VF$	View factor for the calculation of the diffuse radiation	[none]
$X$	Coefficient for the calculation of incoming longwave radiation	[none]
$Y$	Coefficient for the calculation of incoming longwave radiation	[K/Pa]
$Y_{AOI\_cons}$	Mass/energy budget for an AOI resulting from conservative	[depends]
$Y_{AOI\_adj}$	Mass/energy budget for an AOI resulting from subgrid	[depends]
$\Delta Y_{AOI}$	Difference in mass/energy budgets for an AOI	[depends]
$Z$	Coefficient for the calculation of incoming longwave radiation	[none]
$\alpha$	Significance level	[%]
$\alpha_P$	Local y-coordinate of $P_x$	[grid unit]
$\beta$	Terrain slope	[rad]
$\beta_P$	Local x-coordinate of $P_x$	[grid unit]
$\gamma_s$	Slope weight	[none]
$\varepsilon_{ls}$	Emissivity of the land surface	[fraction]
$\varepsilon_a$	Emissivity of the atmosphere	[fraction]
$\epsilon$	Random error variate	[depends]
$\eta$	Curvature length scale	[m]
$\theta$	Solar declination angle	[rad]
$\vartheta$	Wind direction	[rad]
$\vartheta_f$	Wind direction diverting factor	[none]
$\vartheta_{ls}$	Terrain adjusted wind direction	[rad]
$\kappa$	Small number to prevent zero divisions	[none]
$\lambda$	Geographical longitude	[rad]
$\lambda_d$	Geographical longitude of the destination grid cells	[rad]
$\lambda_P$	Geographical longitude of point $P_x$	[rad]
$\lambda_s$	Geographical longitude of the source grid cells	[rad]
$\lambda_{1...4}$	Geographical longitude of the surrounding grid cell centers	[rad]
$\mu$	Solar azimuth	[rad]
$\mu_{d_e}$	Mean of the logarithmized extreme flow $d_e$	[m <sup>3</sup> /s]
$\xi_n$	Terrain slope azimuth (north is zero azimuth)	[rad]
$\xi_s$	Terrain slope azimuth (south is zero azimuth)	[rad]
$\rho$	Density of the air	[kg/m <sup>3</sup> ]
$\sigma$	Stefan-Boltzmann constant ( $5.6704 \times 10^{-8}$ )	[W /m <sup>2</sup> K]

---

$\sigma_{d_e}$	Standard deviation of the logarithmized extreme flow $d_e$	[m <sup>3</sup> /s]
$\tau$	Hour angle measured from local solar noon	[rad]
$\varphi$	Geographical latitude	[rad]
$\varphi_d$	Geographical latitude of the destination grid cells	[rad]
$\varphi_P$	Geographical latitude of point P	[rad]
$\varphi_s$	Geographical latitude of the source grid cells	[rad]
$\varphi_{TC}$	Geographical latitude of the Tropic of Cancer	[rad]
$\varphi_{1...4}$	Geographical latitude of the surrounding grid cell centers	[rad]
$\kappa$	Empiric constant	[none]
$\omega$	Weight for a considered neighboring source grid cell	[none]
$\omega_{ws}$	Weight used to modify the interpolated wind speed	[none]
$\omega_{1lk}$	Second order weight 1 for remapping cell l to grid cell k	[none]
$\omega_{2lk}$	Second order weight 2 for remapping cell l to grid cell k	[none]
$\omega_{3lk}$	Second order weight 3 for remapping cell l to grid cell k	[none]
$\Gamma_t$	Temperature lapse rate	[°C/km]
$\Gamma_{td}$	Dewpoint temperature lapse rate	[°C/km]
$\Omega_c$	Grid cell curvature	[none]
$\Omega_s$	Slope in wind direction	[rad]
$\lambda$	Precipitation adjustment factor	[1/km]

## SUMMARY

Climate change continues to alter weather patterns around the globe, affecting our environment in ways that we are only beginning to understand. In order to quantify possible future developments in the earth's climate system, global circulation models (GCMs) are utilized to describe climate relevant processes over decades to centuries at a global scale. However, there is evidence that many consequences of climatic change occur at far finer spatial scales than those currently resolved by GCMs. This applies to changes in the climate system as well as to the response to these changed meteorological conditions at the land surface. Provided appropriate meteorological drivers, the latter can be investigated by means of physically based high resolution land surface models (LSMs).

As GCMs are not capable to deliver these meteorological drivers with sufficient spatial resolution at present, different downscaling techniques are currently applied to provide the climate research community with climatic information at higher spatial detail than presently achievable with GCMs. An approach that is commonly pursued is to nest regional climate models (RCMs) in the model domain of GCMs. Driven by the global simulations, the RCMs allow to describe atmospheric processes at higher spatial resolutions within a spatially limited geographic area. Still, the spatial resolution at which atmospheric processes can be resolved by RCMs is computationally limited to at best 10 x 10 km and does not fully meet the high demands on meteorological drivers made by high resolution LSMs (1 x 1 km). A clear need has been identified to develop appropriate methods to overcome the scale mismatch between the models for the atmosphere and those operating at the land surface in order to permit the investigation of climate change impacts at a regional to local scale.

In the framework of the present thesis the software interface SCALMET has been developed. The coupler provides different scaling techniques to adequately span the gap between the spatial resolution of RCMs and that of high resolution LSMs. By transferring RCM simulations to a finer scale, SCALMET addresses the needs for high resolution meteorological drivers within the GLOWA-Danube project (Global Change of the Water Cycle). The GLOWA-Danube project, by which the present study was initiated and funded, aims to investigate the climate change impact on the water cycle of the Upper Danube watershed. To enable the research, the integrated decision support system DANUBIA has been developed combining the profound knowledge of experts in various disciplines with water related concerns. The DANUBIA model is composed out of different interacting numerical models simulating all relevant natural and socio-economic processes involved in the hydrological cycle of the catchment. To adequately describe the water fluxes at the land surface the models depend on meteorological drivers in a spatial resolution of 1 x 1 km.

The meteorological fields (temperature, precipitation, air humidity, shortwave radiation, longwave radiation, wind speed and surface pressure) which are provided by different RCMs and which are scaled down by SCALMET therefore belong to the key quantities required to investigate future changes in the hydrological cycle. The study area of the Upper Danube watershed is characterized by steep relief and climate gradients. The complex terrain on the one hand emphasizes the need to correct coarse grid meteorological simulations with respect to subgrid topography, but on the other hand makes the downscaling of the RCM simulations a scientific challenge.

Beyond the downscaling of RCM output in one-way coupled model runs, SCALMET gives the option to aggregate the water, energy and momentum fluxes calculated at the land surface. Using these spatially aggregated fluxes as inputs for RCMs in the framework of two-way coupled model runs is expected to considerably contribute to an improved understanding of the complex interactions between the land surface and the atmosphere.

While two-way coupled model runs represent a top priority for future applications of SCALMET, the present work focuses on the description of the coupler and the implemented scaling methods as well as the presentation of results achieved in first one-way coupled model runs. The latter includes coupled model runs for past and possible future climate conditions. Comparing the results achieved for past climate conditions to those achieved within the scenario run (SRES A1B) allows to analyze the change signal contained in the model results of the coupled model system. To provide a computationally efficient test environment, the land surface in these one-way coupled model runs is reduced to the hydrological model PROMET representing the FORTRAN version of the hydrological model component in DANUBIA. The meteorological drivers for PROMET in the present study are supplied by the regional climate model REMO and are scaled down from 10 x 10 km to 1 x 1 km in advance of the application in the hydrological model using the methods implemented in SCALMET. To transfer the meteorological simulations from the coarse grid mesh of the RCM to the finer grid mesh of the hydrological model a roundup of direct interpolation methods such as bilinear or inverse distance weighted interpolators have been implemented in the coupler. Additionally, an interpolation scheme is introduced that ensures a conservative treatment of fluxes within the remapping between the grid scales. However, direct interpolators introduce a considerable smoothing and do not compensate the loss of climatic variability resulting from a coarse representation of the land surface in RCMs. To overcome these drawbacks, more sophisticated scaling approaches have been implemented into the software interface. Much care has been taken to guarantee a full transferability of the developed downscaling techniques to other RCMs as well as to other geographic regions. The whole range of computations performed within the remapping of the different meteorological variables is carried out during the run-time of the coupled model system.

While the latter noticeably reduces the required data storage capacities, it on the other hand limits the complexity of the implemented algorithms for the sake of computational efficiency. As many meteorological variables strongly vary with terrain elevation, high resolution elevation information is used to adjust meteorological simulations with respect to subgrid topography. A regression based remapping approach is presented that analyzes the elevation dependence of a considered variable (e.g. temperature, dewpoint temperature or precipitation) during the run-time of the coupled model run. Additionally, methods have been implemented that apply monthly constant elevation corrections to adjust the comparatively coarse RCM outputs beyond the capabilities of direct interpolation methods. As these elevation adjustment parameters vary over space and time, meteorological observations have been used to derive area specific adjustment parameters for the Upper Danube watershed for each month of the year. Naturally not all of the variables required by the land surface components of DANUBIA are characterized by a significant elevation dependence. Hence, several submodels have been implemented in SCALMET that use additional topographic information (slope, aspect, exposure) to adequately span the gap between the model scales (e.g. a shortwave radiation model, a longwave radiation model, wind model). Irrespective of the applied remapping method, the adjusted high resolution meteorology is realigned to the mass/energy budget predetermined by the RCM simulations. Combining mass and energy conservation with subgrid adjustments, the techniques implemented in SCALMET represent a novel approach.

The conservation of mass and energy is essential, in particular in two-way coupled model runs. However, conserving mass and energy between the model scales implies taking over all biases that are included in the meteorological simulations. As biases are known to exist in RCM simulations spatially distributed observations are used to quantify the uncertainties related to the different remapping methods. These aggregated observations (10 x 10 km) are redistributed to the finer grid in SCALMET by means of different remapping algorithms, treating the data exactly the same way as the REMO simulations in one-way coupled model runs. A comparison of the remapped fields with station observations reveals that the more sophisticated scaling techniques in SCALMET notably enhance the quality of the remapped fields. Further, using the remapped meteorological data to force PROMET shows that the application of remapping methods that account for subgrid variability of topography leads to a more realistic simulation of water fluxes and therefore allows the hydrological model to more accurately reproduce observed discharge volumes.

To investigate the overall performance of the coupled model system a one-way coupled model run (REMO-SCALMET-PROMET) is set up covering the years 1961 to 2000. For the simulation of the meteorological forcings the regional climate model REMO is set up in a one-way double nesting technique. The RCM in this setup is driven by the coupled ocean-

atmosphere model ECHAM5/MPI-OM at the boundaries of the model domain. The regression based approach in SCALMET is used to remap temperature, air humidity and precipitation simulations from the coarse grid of the regional climate model to the finer grid of the hydrological model. Wind speed, shortwave and longwave radiation are remapped using the respective submodels. The applied algorithms are chosen as they do not include calibrations conducted at present-day climate conditions and can therefore be expected to be valid under future climate conditions. Further an uncoupled PROMET run is set up for the period 1971 to 2000. The spatially distributed meteorological observations used to force PROMET in this run are compared to the remapped REMO simulations to get an impression of the quality related to the meteorological drivers used within the coupled model run.

The comparison of the remapped REMO data to distributed observations shows an average overestimation of annual mean temperature of 0.8 °C by the remapped REMO simulations for the Upper Danube watershed (1971-2000). Further, an overestimation of annual mean precipitation of approximately 11 % is observed in the remapped REMO data. To include another source of reference, data originating from the Hydrological Atlas of Austria (1961-1990) is consulted. The comparison of REMO precipitation simulations to both observation based precipitation datasets (1961-1990) shows that the highest overestimation of annual precipitation can be found in the alpine part of the catchment. However, it is pointed out that all precipitation distributions involved in the comparison are based on model results and therefore include considerable uncertainties. The hydrological simulations carried out within the coupled model run (REMO-SCALMET-PROMET) show a slightly increased evapotranspiration relative to the results of the uncoupled PROMET run considering the period 1971 to 2000. The comparison of the annual mean runoff in the watershed simulated within the coupled model run to discharge recordings at the gauge in Achleiten further reveals an overestimation of measured discharge of 29 %. Comparing discharge simulations to discharge recordings on a monthly time basis unfolds that the highest degree of overestimation occurs in the months of June and November. The latter applies to the simulated mean monthly discharge, as well as to mean monthly peak-flow discharge. In the case of low-flow discharge, the highest degree of overestimation is found in the months of June and December. This general tendency to an overestimation of actual discharge conditions in the Upper Danube watershed is shown to limit the ability of the coupled model system to reproduce low-flow and flood return periods.

After the uncertainties related to the reproduction of past and present-day conditions have been clarified, a second one-way coupled model run is set up for the period 2011 to 2060. The radiative forcings of the ECHAM5/MPI-OM model in the scenario run reflect the greenhouse gas concentrations as defined for the SRES A1B scenario. All biases quantified for the one-way coupled reference run (REMO-SCALMET-PROMET) are assumed to affect

the model results of the scenario run to a similar extent. Based on this assumption a relative comparison of the meteorological and hydrological simulations resulting from the reference run to those achieved for the scenario run can be carried out. Comparing the average annual mean temperature of the remapped REMO simulations for the reference period (1961-2000) to that of the scenario period (2011-2060) a considerable rise in annual mean temperatures can be observed for the Upper Danube watershed ( $\approx 1.2$  °C). In particular the higher elevations of the Alps are concerned with an increase in annual mean temperature of up to 1.9 °C compared to the reference period. Besides the enhanced warming in higher elevated regions of the Alps compared to the Alpine Foreland, which is reflected by the 10 x 10 km REMO simulations as well, a subgrid elevation dependence is found in the change signal when comparing the remapped temperature simulations for both runs. The latter can be explained by the fact that the mean temperature lapse rate reflected by the REMO reference run simulations is higher than that of the scenario run. The regression based remapping therefore differently corrects the simulated temperatures with respect to subgrid elevation. These circumstances emphasize the outstanding importance of applying remapping techniques that are not calibrated and allow the adaption to future meteorological conditions. The temperature increase rate in the Upper Danube watershed with approximately 5.2 °C/100 years unfolds to be about 1.8 times higher than the global average temperature increase rate associated with the A1B scenario family ( $\approx 2.9$  °C/100 years).

Considering the seasonal trends in simulated precipitation a significant decrease in summer and autumn can be observed within the scenario period (2011-2060), whereas spring and winter are not characterized by significant trends. However extending the analysis upon the whole time period of available REMO scenario simulations (2000-2100) clearly shows that the change signal in simulated precipitation severely depends on the time period considered within the REMO scenario run. Both, changes in summer precipitation (-) and changes in winter precipitation (+) are stronger when considering the end of the century (2070-2100) than the period analyzed in the present study (2011-2060). Relative to the reference period 1961 to 2000 the years 2011 to 2060 show a general increase in annual precipitation of approximately 5 %.

The hydrological response to the climate change signal is analyzed by comparing the hydrological simulations of the reference period to those achieved for the scenario run (delta change approach). As a result of the considerable enhancements in the water and energy budget of the Upper Danube watershed a significant increase in annual evapotranspiration is found with highest increase rates for the seasons of winter, spring and autumn. In contrast, modeled evapotranspiration for the summer months shows much lower increase rates. July is even characterized by lower evapotranspiration rates in the scenario run compared to the reference run. As evapotranspiration is already very high for these months in the reference

run the potential for an increase here is comparatively small. Moreover, water availability is limited as a result of the decrease in summer precipitation and the strong increase in evapotranspirative water consumption observed for the preceding months. This assumption is confirmed by the analysis of the available soil water content, which shows a significant decrease in the month of July up to the end of the scenario period in the year 2060. The total increase in average annual evapotranspiration amounts to 3.5 % relative to the reference period (1961-2000).

As a consequence of the increase in winter temperatures the annual amount of precipitation in the solid state of snow as well as the number of days characterized by the presence of a snow cover severely decrease compared to the reference period. The latter two criteria serve as a particularly suitable climate change indicator as the temporal storage of water in the solid form of snow is very sensitive to climate change. Not only because snowfall and snow cover directly react upon temperature and precipitation changes. These quantities further represent important water reservoirs in which different aspects of climate change add up and interact. Both analyzed criteria show largest decreases in the northern part of the watershed. The low temperatures in the higher elevated parts of the Alps as well as of the Bavarian Forest result in lowest decreases in snowfall amounts as well as in annual snow cover in these regions.

To analyze the impact of the scenario meteorology upon the runoff conditions in the Upper Danube watershed the simulated annual area mean runoff of the scenario run is compared to that of the reference run. Since only a small fraction of the additionally available precipitation is consumed by the process of evapotranspiration at the land surface, mean annual runoff increases by 5.7 %. The simulated mean annual discharge at the gauge in Achleiten does not show a significant trend within the scenario period. Monthly mean discharge as well as monthly peak-flow and low-flow discharge volumes at the gauge in Achleiten are characterized by a notable increase in particular in the hydrological winter half year (November-April). In contrast the decrease in summer precipitation in the case of all three monthly discharge criteria for some summer months (e.g. August) results in lower discharge volumes in summer for the scenario run.

The lowest annual mean 7-days discharge (NM7Q), which represents a reasonable criterion for low-flow conditions, does not show a significant trend within the scenario period. An explanation for the fact that the NM7Q is not subject to a decrease can be found in its temporal occurrence. As could be shown, the NM7Q is mostly found in the hydrological winter half year. This time of the year is characterized by an increase in runoff available water due to an increase in (liquid) precipitation together with a rise in near surface temperatures. However, the lowest NM7Q volumes simulated within the scenario period notably fall below the lowest NM7Q discharges found in the simulations for the reference period. Further, a

slight shift of the NM7Q towards the hydrological summer half year can be observed in the scenario run. The latter indicates an increased potential for the occurrence of extreme low-flow events in the hydrological summer half year in the future.

Parallel to the NM7Q, the highest daily discharge in the course of one year (HQ) does not show a significant trend within the scenario period. However, comparing the flood return periods between the one-way coupled reference run and the scenario run, the discharge volumes related to a certain return period are significantly lower in the scenario run. This tendency to lower flood-flow discharge volumes in the scenario run is well explicable, as highest discharge volumes according to observations and simulations are primarily found in the summer half year, which is characterized by a decrease in precipitation and lower melt water discharge in the scenario run. Compared to the changes in flood return periods, the low-flow return periods are rather unaffected by the climatic changes in the Upper Danube watershed.

The present work has successfully shown the general applicability of the one-way coupled model system. The presented methods allow a more realistic reproduction of the climate conditions in the research area of the Upper Danube watershed. It was further shown that the methods described permit a more accurate simulation of all hydrological determinant processes in the catchment. Supplying physically based land surface models with high resolution meteorological drivers, SCALMET offers manifold opportunities for future climate change investigations. Representing the land surface component in the coupled model system, PROMET has proven to be capable to fully utilize the potential of RCM simulations.

The regional climate change aspects analyzed in the framework of the present thesis will be completed by further investigations carried out within the GLOWA-Danube project. The inclusion of other disciplines cooperating in the framework of GLOWA-Danube (plant physiology, glaciology, tourism, water resources management, economy) within future one-way coupled model runs opens a variety of climate change research possibilities. Using different RCMs (REMO, MM5 and CLM) as well as different climate change scenarios (SRES A1B, A2 and B1) within future model runs further will allow to reflect a wider range of uncertainties and potential future climatic changes as well as hydrological reactions. In a medium-term view, the biases that are presently encountered within the coupled model system can be expected to diminish as a result of further improvements in the RCMs.

Further challenges consist in the application of the coupled model system in different geographic regions. In the framework of the BRAHMATWINN project, the coupled model system (CLM-SCALMET-PROMET) will be utilized to analyze climate change impacts on the water resources in the river basin of the Brahmaputra. The top-priority for future applications however is the application of SCALMET in two-way coupled model runs in which SCALMET aggregates the energy, mass and momentum fluxes calculated by the land surface model

PROMET and provides these fluxes as inputs for the RCMs (MM5 and REMO). As coupling high resolution land surface models with mesoscale climate models belongs to the greatest challenges in interdisciplinary research, practical difficulties can be expected to arise. However, the technical prerequisites for two-way coupled model runs could be successfully completed within the present work.

# 1 INTRODUCTION

## 1.1 THE ROLE OF NUMERICAL MODELS IN CLIMATE CHANGE RESEARCH

The atmosphere and the related processes of weather and climate are of highest importance for human existence on earth. Without the presence of greenhouse gases in the atmosphere, the global mean earth surface temperature would rather take values of  $-18\text{ }^{\circ}\text{C}$  than  $+15\text{ }^{\circ}\text{C}$  as currently the case. While there has been a physical understanding of the greenhouse effect for about hundred years, the risk of an anthropogenic climate change did not become commonly recognized until the 1970's (LOZAN ET AL. 2001). The anthropogenic buildup of atmospheric greenhouse gas concentrations together with the observed increase in the average near surface temperature have stimulated international research activities designed to analyze and understand to what extent and in which way possible impacts will affect the social and natural system at different spatial scales.

Parallel to the increasing need for adequate tools to investigate future climate changes and their impacts, climate science has shown an increasing rate of advancement in recent decades. This implies research in the field as well as notable evolution of scientific methodology, including the models that enable and support the research. An important example for this progress is the additional physics and physiology incorporated in climate models over the last decades.

Numerical models represent the primary tools for investigating future impacts of global change (HEWITSON AND CRANE 1996). Furthermore, models are capable of explaining what happened in the past. As published in the latest IPCC report, climate model simulations confirm the great anthropogenic influence on global warming by pointing out that the observed patterns of warming and their changes over time could only be simulated by climate models that include anthropogenic forcing (IPCC 2007). The model requirements to project future climate conditions are clearly formulated. Running the climate models over a period of several years with parameters and forcings appropriate to the present climate, the models should be able to reproduce the observed climate. If parameters reflecting an increasing amount of atmospheric  $\text{CO}_2$ -concentrations are introduced, these models should also be able to predict the resulting climate change.

The increase in supercomputer speeds by roughly a factor of a million in the three decades from the 1970's to the present has offered the possibility to include more and more processes and components in the numerical models. At the same time spatial resolution and the length of simulations could be drastically increased.

As a consequence of all these improvements, current climate models are more realistic than those a decade ago. They are able to reproduce the observed large scale changes in temperature throughout the 20th century and project the response of many climate variables to various scenarios of greenhouse gas and other human-related emissions. The resulting climate simulations provide the meteorological drivers for physically based land surface models allowing the analysis of climate change impacts at the land surface. However, there are still deficiencies in the climate models that limit their application in climate change research. The spatial resolution at which atmospheric processes can presently be described still suffers computational limitations. Moreover, there are deficiencies in the climate models (e.g. uncertainties in the representation of clouds and their interaction with radiation and aerosols) resulting in the fact that confidence in the climate estimates is higher for some variables (e.g. temperature) than for others (e.g. precipitation) (RANDALL ET AL. 2007).

## 1.2 STATE OF THE ART

The following chapters give a deeper insight in the field of climate modeling. The general characteristics of climate models as well as currently encountered limitations are briefly described.

### 1.2.1 GENERAL CHARACTERISTICS OF CLIMATE MODELS

Climate models have developed from early generations of weather prediction models. While both types of models still share many characteristics, models used for numerical weather prediction are typically run at higher spatial resolution than is possible for climate simulations. Although the first generation of general circulation models (GCMs) extremely oversimplified the complex climate system, MANABE AND WETHERALD (1967) were already able to simulate the effect of global warming as a reaction to doubled CO<sub>2</sub>-concentrations in the atmosphere using a GCM in 1967.

Current climate projections make use of complex coupled atmosphere-ocean models, sometimes even including interactive chemical or biochemical components. These atmosphere-ocean general circulation models (AOGCMs) provide the best representation of the climate system and its dynamics, unfortunately at high computational costs (RANDALL ET AL. 2007). Physical processes are separately described for different spheres of the natural system (atmosphere, ocean, land surface, cryosphere and biosphere), including the complex interactions between the spheres. The process description is based on fundamental physical

laws (e.g. Newton's laws of motion) represented by mathematical equations that are solved using a three-dimensional grid laid over the globe (see Fig. 1.1).

The different spheres are typically characterized by a different mesh size and number of vertical layers. As an example the coupled ocean-atmosphere model ECHAM5/MPI-OM, which plays a major role in the later course of this thesis, simulates the atmosphere at a spatial resolution of approximately  $1.9 \times 1.9^\circ$  including 31 vertical layers (ROECKNER ET AL. 2003). In this coupled model system, the ocean is represented in a horizontal resolution of  $1.5 \times 1.5^\circ$  and a vertical resolution of 40 layers (MARSLAND ET AL. 2003). Like most current AOGCMs, the ECHAM5/MPI-OM no longer needs flux adjustments between the coupled components, which were previously required to maintain a stable climate (JUNGCLAUS ET AL. 2003).

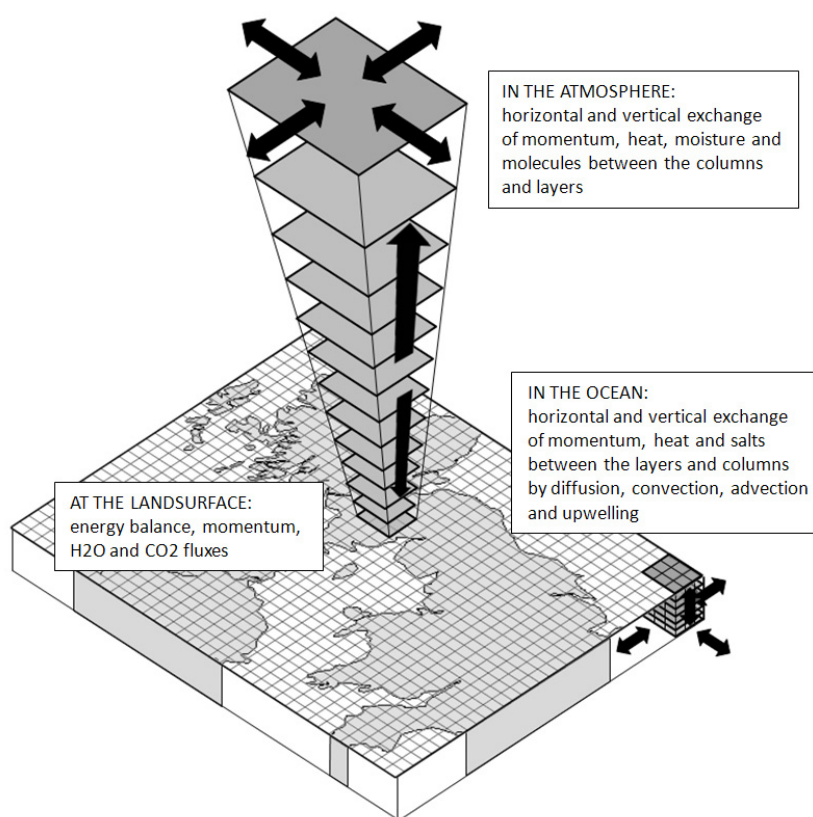


Fig. 1.1: Schematic representation of the structure and the basic characteristics of a climate model. Ocean and atmosphere are represented by a set of interacting columns often with different spatial resolutions (based on THOMPSON AND PERRY (1997)).

Besides the huge improvements in climate modeling, there is a continuing awareness that these models do not provide a perfect simulation of reality, because resolving all important spatial or time scales remains far beyond current capabilities. Although computing resources have extremely advanced over the last years, the obligation to high spatial coverage and temporal resolution, which are required to adequately simulate the global climate conditions over time periods from decades to centuries, still limits spatial resolution.

### 1.2.2 EFFECTS OF A LIMITED SPATIAL RESOLUTION

The presently encountered limitations in the spatial resolution at which all climate relevant processes can be described in climate models lead to uncertainties in the model results. One reason for this is that meteorological phenomena can only be resolved if their spatial extent exceeds the mathematical grid size by a factor of four (VON STORCH ET AL. 1993). As a consequence many physical processes that occur at smaller scales, such as those related to clouds, cannot be properly modeled and their known properties must be averaged over the larger scale in a technique known as parameterization. These parameterizations often contain empirically determined parameters, trying to describe each process as accurately as possible. Occasionally, incorrect descriptions of the underlying processes lead to errors in parameterizations which have a negative influence on the quality of the climate model output (COSGROVE ET AL. 2003). As only some of these parameters can be measured, it is a common approach to adjust parameter values in order to optimize model results. These parameter adjustments are also known as ‘tuning’ and are only permitted under certain conditions (RANDALL ET AL. 2007):

- Constraints of parameter ranges based on observations are not to be exceeded
- The number of degrees of freedom in the tuneable parameters has to be less than the number of degrees of freedom in the observational constraints used in model evaluation

A further effect of a rather coarse spatial resolution is that land surface heterogeneities cannot be properly represented in climate models. At present, the land surface in climate models is often represented by the most common land surface type in the area covered by the grid box or by using the so called ‘tile approach’ (see Fig. 1.2).

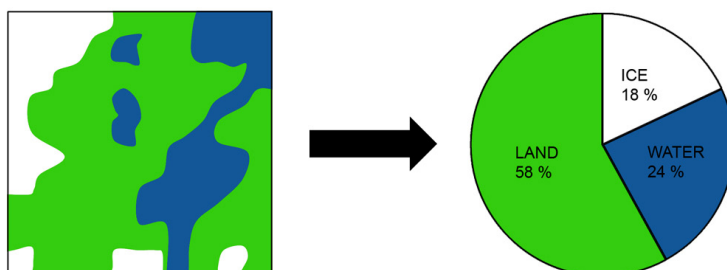


Fig. 1.2: Representation of land surface heterogeneities within a climate model grid cell following the tile approach.

The latter partitions each climate model grid cell among the underlying land surface types so that each type represents a percental fraction of the total cell area (PITMAN 2003). A cell

averaged response is calculated by averaging the surface fluxes according to the area fractions covered by the different surface types (KLINK 1995). The averaged flux is then delivered to the lowest atmospheric level of the respective grid cell. However, this representation of subgrid heterogeneities neither allows the atmosphere to respond differently to heterogeneous surface forcings, nor does it allow taking into account the geographic distribution of the different land surface types as well as their interaction.

Another problem is that a low climate model resolution implies a coarse representation of topography. The result is a local height discrepancy between the orography of the simulation and the real orography (FRÜH ET AL. 2006). As a consequence the climate simulations (e.g. precipitation) differ from observations (DALY ET AL. 1994). The overall effect of a coarse spatial model resolution is, that local consequences of future climate changes, which are the ones posing a direct effect on human beings and the environment, can hardly be investigated under the given limitations (GERSTENGARBE 2001). While global models explicitly resolving e.g. the dynamics of convective clouds may become computationally feasible in a medium-term view, so called ‘downscaling’ techniques are presently used to derive higher resolution climate data on the basis of available coarse resolution global climate.

### 1.2.3 DOWNSCALING TECHNIQUES

Although the conceptual application of downscaling methods in form of techniques used to translate across spatial scales, e.g. from the synoptic to the regional and local scales, has existed for many years, the explicit use of the term in climatological applications has only recently become widespread. Basically, there are two different approaches to compensate the insufficiency in the spatial resolution of the climate models. While the dynamical approach scales the meteorological simulations in a physically based manner, statistical downscaling techniques use empiric relations to bridge the scales.

Besides these two techniques and the different combinations between them, there are further scaling approaches mainly used for the distribution of meteorological observations. A brief overview of existing downscaling techniques is given in the following.

#### 1.2.3.1 DYNAMICAL DOWNSCALING OF CLIMATE SIMULATIONS

The dynamical downscaling approach constitutes a process based technique unfortunately connected to high computational costs. A typical dynamical technique is the nesting of limited area models (LAMs) in the domain of a GCM as done for the simulation of the meteorological fields used in this work by utilizing the coupled ocean-atmosphere model ECHAM5/MPI-OM

(ROECKNER ET AL. 2003) to supply the meteorological boundary conditions for the embedded regional climate model REMO (JACOB 2001). The reduction in the grid mesh size achieved by dynamical downscaling methods allows taking into account small scale climate processes and enables a higher spatial resolution over a given area (GERSTENGARBE 2001). The integration of regional climate models (RCMs) shows that distributions of temperature and precipitation contain a significant signal on scales not resolved by the GCMs, whereas the large scale circulation follows that of the driving GCM (MURPHY 1999). As a consequence, orographically induced precipitation and cyclonic activity at midlatitudes can be better reproduced (MACHENHAUER ET AL. 1996). While the method was limited to the simulation of short time periods some years ago, computer capacities allow long term applications by now. Another dynamical downscaling technique is the time-slice technique (see Fig. 1.3).

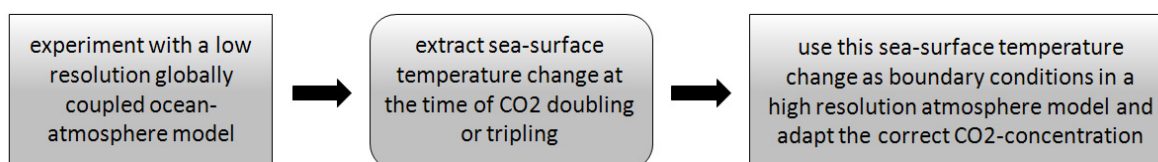


Fig. 1.3: Schematic diagram of the time-slice technique (based on (CUBASCH 2001)).

In this approach a higher resolution uncoupled atmosphere model is driven by the change of the sea temperature as well as the change of the sea ice distribution, both simulated with a coarse resolution model (CUBASCH 2001). In other words, the atmospheric high resolution model is forced by the mean boundary conditions simulated by a low-resolution AOGCM (ZORITA AND VON STORCH 1999).

### 1.2.3.2 STATISTICAL DOWNSCALING OF CLIMATE SIMULATIONS

The alternative method of statistical downscaling represents a practical approach for addressing current needs in the climate change research community and is computationally efficient compared to dynamical downscaling techniques (HEWITSON AND CRANE 1996). The approach makes use of quantitative relations between observed large scale circulation and small scale local climate (see Fig. 1.4). Empirical techniques can be divided in the following subcategories:

- weather generators
- classification methods
- transfer functions

A stochastic weather generator is a numerical model that produces synthetic daily time series of a suite of climate variables, such as precipitation, temperature and solar radiation, with certain statistical properties (SEMENOV ET AL. 1998). The big advantage of this approach is that weather generators can simulate many ‘realisations’ of the climate and thus provide a wide range of feasible situations. They represent a computationally inexpensive tool to produce site-specific climate change scenarios at the daily time step (SEMENOV ET AL. 1998). Although the general principle underlying the classification methods is simple, the practical implementation can become quite complicated. After the development of an atmospheric circulation classification scheme for an area of interest, a pool of meteorological observations is distributed into the defined classes. The circulations simulated by the GCM can then be directly linked to one of the defined classes, including the underlying observations of the local variable (ZORITA AND VON STORCH 1999).

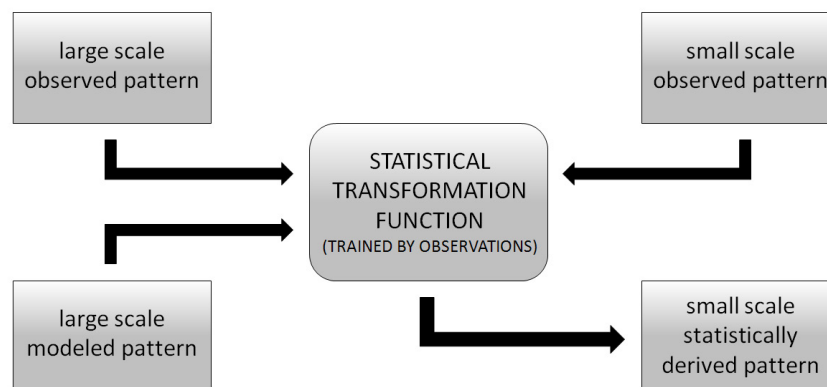


Fig. 1.4: Schematic diagram of the statistical downscaling approach (based on (CUBASCH 2001)).

The transfer function approach is one of the earliest downscaling methods and is considered to be of practical importance in the context of climate change (KIM ET AL. 1984). The technique is based on linear or nonlinear relationships between a large scale predictor variable and a local variable denoted as the predictand. The transfer function in some form of  $y = f(x)$  is used to derive the small scale local climate from large scale climate simulations, assuming that the relationship is valid for the simulation and that it remains stable even in the case of climate change. The method does not necessarily imply using the same variable as predictor and predictand. As an example, VON STORCH ET AL. (1993) related winter rainfall in the Iberian Peninsula to sea level pressure patterns in the North Atlantic using a canonical correlation technique.

In practice, most downscaling techniques are not restricted to just one of the described downscaling categories but are a combination of them. Although all of these downscaling methods help to increase detail in climate simulations, they strongly depend on the quality of the meteorological data provided by the coarse grid model.

### 1.2.3.3 TECHNIQUES TO SPATIALLY DISTRIBUTE CLIMATE OBSERVATIONS

Beside the statistical and dynamical methods used to scale climate model simulations, there are further approaches, which are often used to derive meteorological distributions from observational climate data. All of these methods make use of available subgrid information (e.g. elevation) within scale adjustments.

The statistical regression model PRISM (parameter-elevation regressions on independent slopes model) for example is a regression-based approach that uses point data, a digital elevation model, other spatial data sets, a knowledge base and human-expert parameterization to generate high resolution distributions of climatic elements (DALY ET AL. 1992, DALY ET AL. 2001, JOHNSON ET AL. 2000). The resulting meteorological fields can be found in various atlases, e.g. the first official update of the manually drawn Climate Atlas of the United States (USDOC 1968) or the Hydrological Atlas of Switzerland (SCHWARB ET AL. 2001a) (SCHWARB ET AL. 2001b). HIJMANS ET AL. (2005) use the ANUSPLIN package to derive monthly distributions of temperature and precipitation aggregated over the years 1950-2000 for global land areas in a spatial resolution in 1 x 1 km. ANUSPLIN fits thin plate smoothing spline functions of longitude, latitude and elevation to climate observations (HUTCHINSON 1991, HUTCHINSON 2004). WALTER ET AL. (2006) generated a high resolution reference data set of German wind velocity for the years 1951-2001 using a so called 'relative altitude' scheme. Relative altitude is computed by positioning each station at the center of a 10 x 10 km grid box and subtracting the mean altitude inside the grid box from the real station altitude (WALTER ET AL. 2006). A simple linear regression is used to derive a wind-altitude dependency that is later applied for elevation corrections of spatially interpolated wind speed observations. The resulting high resolution wind data is used for the evaluation of RCM simulations.

While most of the methods described above focus on the development of annual or monthly climate maps, other authors have presented techniques to generate high resolution meteorological forcings for the application in land surface models on an hourly time basis (LISTON AND ELDER 2006, LISTON AND STURM 1998, COSGROVE ET AL. 2003, MAUSER AND BACH 2008). The meteorological distribution system MICROMET developed by LISTON AND ELDER (2006) corrects spatially and temporally interpolated meteorological observations using known temperature-elevation, wind-topography, humidity-cloudiness, and radiation-cloud-topography relationships. Although some of the implemented methods originate from earlier works focusing on the distribution of daily meteorological fields (THORNTON ET AL. 1997), the algorithms have been intensively validated for an application on hourly observations. COSGROVE ET AL. (2003) generate real-time and retrospective atmospheric forcings (0.125 x 0.125 °) on the basis of coarse grid meteorological data (40 x 40 km),

derived from merging observations with model fields. After a temporal and spatial interpolation hourly values of temperature, specific humidity, incoming longwave radiation and surface pressure are corrected for subgrid topography on the basis of differences in the terrain elevation of the involved grids. The approach has been followed by various other authors in the recent past (KATO ET AL. 2007, SHEFFIELD ET AL. 2006).

After this short survey of existing downscaling techniques, the GLOWA-DANUBE project will be presented in the next paragraphs, followed by a description of the project's demands concerning meteorological data.

### 1.3 GLOWA-DANUBE

The GLOWA-initiative (Global Change of the Water Cycle), which this thesis emerges from, is funded by the German Ministry of Research and Education (BMB+F) and has been established to address the manifold consequences of Global Change on regional water resources in a variety of medium sized catchment areas with different natural and cultural characteristics (LUDWIG ET AL. 2003). The GLOWA-Danube project focuses on the Upper Danube watershed, hereinafter referred to as the UD. The watershed states a representative mesoscale test site for mountain-foreland regions in the temperate midlatitudes. The project's main objective is to develop and utilize simulation tools and instruments, allowing the formulation and realization of strategies for sustainable and future oriented water management, while taking into account global environmental changes and socio-economic framework conditions (MAUSER AND LUDWIG 2002). To investigate the sustainability of future water use inside the UD, the integrated decision support system DANUBIA has been developed (see Fig. 1.5).

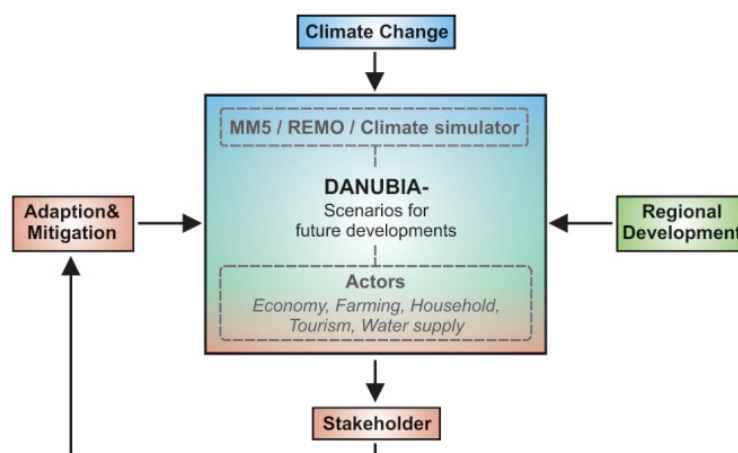


Fig. 1.5: Schematic overview of the decision support system DANUBIA (GLOWA-DANUBE 2008).

The object-oriented, spatially distributed and raster-based DANUBIA model system comprises the profound knowledge of experts with water related competence in the fields of engineering, social and natural sciences to address all facets of possible climate change impacts on the water cycle (LUDWIG ET AL. 2003).

The project core groups represent the scientific disciplines Hydrology, Remote Sensing/GIS, Meteorology, Water Resources Management (groundwater and surface waters), Plant Ecology, Environmental Psychology, Environmental Economy, Agricultural Economics and Computer Science. All these disciplines have developed separate submodels containing the essential physical and socio-economic processes required to quantitatively describe the interactions of the different disciplines concerned with water fluxes (see Fig. 1.6). Besides these core groups there are several bridge groups representing the scientific disciplines Glaciology, Remote Sensing in Meteorology and Tourism Research, which operate specific interfaces in the model framework (MAUSER AND LUDWIG 2002).

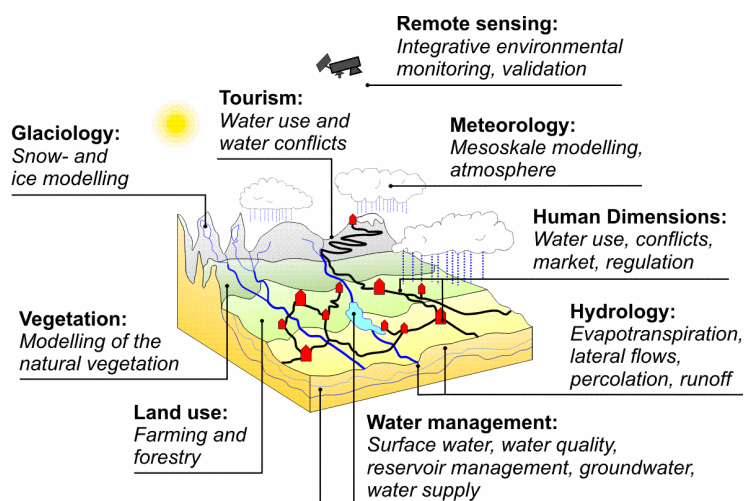


Fig. 1.6: The integrative model approach in GLOWA-Danube (GLOWA-DANUBE 2008).

To guarantee the practical relevance of the investigated future water related problems, a strong cooperation with stakeholders in water resources management of the UD has been established. For the generation of a common understanding between the project partners, a standardized notation of parameters and functions has been established, employing the unified modeling language (UML). UML represents an industry standard for the structuring and coordination of large projects in software development and allows a platform-independent structure of computational methods and interfaces (BOOCH ET AL. 2005).

The basic object for the process description in the DANUBIA model is the 'proxel' (process pixel). In these three-dimensional grid elements, the processes simulated in different modules (e.g. plant growth, evapotranspiration, snowfall) interact using strictly defined interfaces. The proxel itself is connected to the surrounding environment through fluxes.

Although the size of the proxels is conceptually adjustable depending on the scale of the application, for the mesoscale modeling of surface fluxes, as well as for the simulation of key socio-economic processes inside the UD, each proxel is commonly defined to cover 1 x 1 km.

## 1.4 MOTIVATION OF THIS THESIS

In spite of all the undeniable progress in climate modeling and the subsequent processing of climate model simulations, the currently available climate data do not fully meet the requirements of climate research projects like GLOWA-Danube. The demands of land surface models applied to investigate climate change impacts as well as the primary needs of a society attempting to plan for or respond to climate change, lie at far finer spatial resolutions than those resolved by global or RCMs (HEWITSON AND CRANE 1996, LISTON AND ELDER 2006, WILBY ET AL. 2004, GACHON AND DIBIKE 2007). Although setting up RCMs at high spatial resolutions is in principle practicable, it is computationally prohibitive (LISTON AND ELDER 2006). The described existing statistical downscaling techniques are currently used to derive climatological distributions at high spatial resolutions but in most cases only in form of daily or monthly values (MURPHY 1999) (MURPHY 2000) (KILSBY ET AL. 1998) (BECKMANN AND BUIHAND 2002) (WOOD ET AL. 2004) (DALY ET AL. 2002). While such low temporal resolutions might satisfy the needs of some climate change investigations, other applications, in particular the utilization of climate simulations as meteorological forcings for land surface models, require higher temporal resolutions (HEWITSON AND CRANE 1996).

The objective of this thesis is to develop an instrument that is capable of **SCALing MET**eological variables (SCALMET) provided by different RCMs (REMO (JACOB 2001), MM5 (GRELL ET AL. 1995) and CLM (BÖHM ET AL. 2006)) for a later application in the transdisciplinary catchment scale model DANUBIA (MAUSER AND LUDWIG 2002). The DANUBIA model requires hourly values of meteorological variables with a spatial resolution of 1 x 1 km. While the temporal resolution is satisfied by most current RCMs, adequate scaling techniques need to be applied to bridge the gap between coarse climate model outputs and the fine grid resolution of the terrestrial model components. The scaling techniques implemented in SCALMET could most adequately be described as quasi-physically based approaches as they include statistical methods as well as the description of small scale processes in different submodels (e.g. a longwave radiation submodel).

Unlike other downscaling studies, which produce high resolution meteorological fields for long time periods a priori to the application in climate change analysis, SCALMET processes

the climate simulations during run-time of the coupled land-atmosphere model and thus minimizes data storage requirements. To enable this real-time data processing during the coupled model run, the software is required to be as computationally efficient as possible. For the downscaling of the meteorological variables from the coarse climate model resolution to the finer land surface grid, this limits the complexity of the implemented scaling techniques. The scaling methods, as presented in the framework of this work, therefore represent an approach to treat every variable individually and as physically based as possible, thus minimizing the computational costs to allow long term coupled model runs over decades to centuries. Although some of the implemented scaling techniques have been used in other studies before (LISTON AND ELDER 2006, LISTON AND STURM 1998, COSGROVE ET AL. 2003) they have mostly been applied to observational data and have at present never been used in connection with the central aim to conserve fluxes over the scales. The latter in particular states an inevitable requirement for bilateral coupled model runs. Combining existing techniques for mass and energy conservation with methods accounting for subgrid heterogeneities within the distribution of meteorological variables, SCALMET states a novel approach in the field of coupled land-atmosphere modeling.

Another top priority in SCALMET is the transferability of the implemented methods to an arbitrary RCM and area of interest. Therefore, besides methods that have been parameterized for the model domain of the UD, several downscaling methods are included, that allow an unrestrained technical and spatial transferability.

Besides the downscaling of climate model output, SCALMET provides aggregated land surface fluxes as inputs for the meteorological models (see Fig. 1.7).

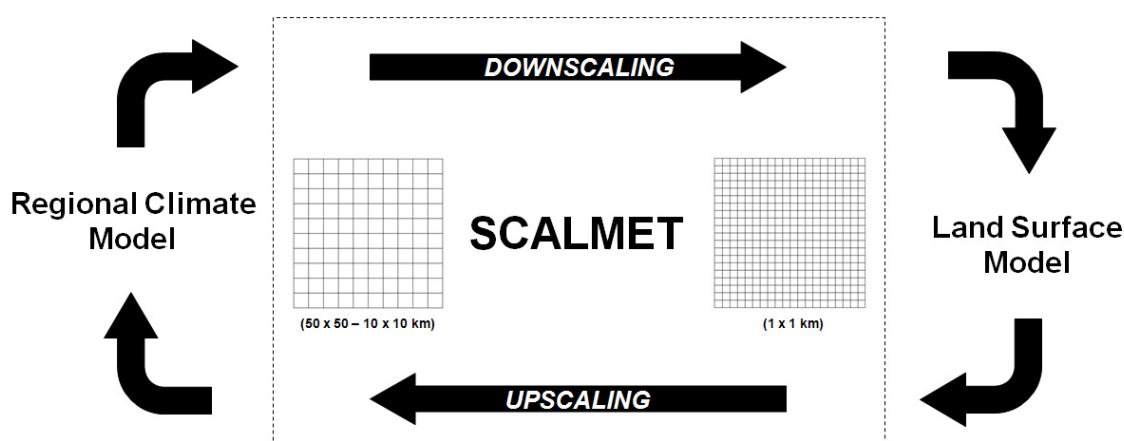


Fig. 1.7: Schematic diagram of the coupled model system.

The latter addresses recently expressed needs to support the climate modeling community with expertise in the simulation of various land surface processes (PITMAN 2003).

The feedback effect between atmospheric and hydrological variables (e.g. soil moisture) has been shown by SCHÄR ET AL. (1999), who demonstrated that the potential for convective activity increased if soil moisture was increased. Moreover, SCHÄR ET AL. (2004) suggested that an active soil moisture precipitation feedback was linked to the anomalously hot European summer in 2003. Further, other authors showed that relatively small improvements to the land surface models lead to significant improvements in climate modeling (MILLY AND SHMAKIN 2002). Providing RCMs with high resolution surface fluxes represents the best approach presently available to account for heterogeneities at the land surface as it allows the RCM to fully benefit from the high resolution process description carried out by physically based land surface models (KLINK 1995, PITMAN 2003). In consequence, many negative effects resulting from a coarse representation of the land surface (see chapter 1.2.2) can be resolved. Unlike the physical parameterizations found in climate models, a more realistic representation of the land surface (see Fig. 1.8) in combination with an explicit simulation of the processes at the land surface at high spatial resolutions accounts for the nonlinearity of many climate-related processes.

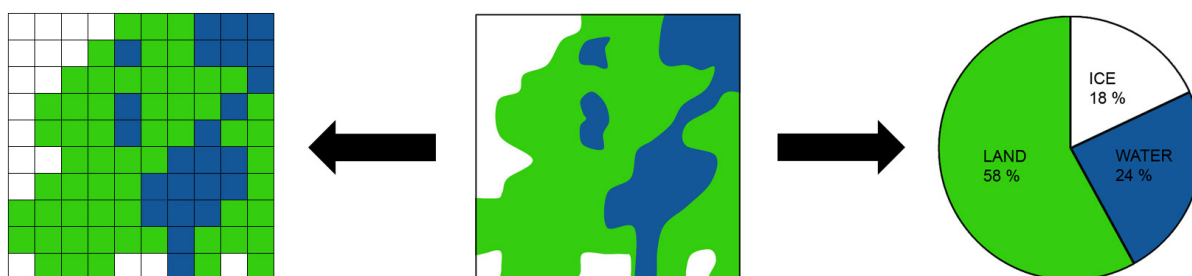


Fig. 1.8: Representation of different land cover types in an area of 10 x 10 km in a land surface model (spatial resolution 1 x 1 km) (left), in the spatial resolution of the land cover classification (middle) and in a RCM using the 'tile approach' (spatial resolution 10 x 10 km).

The high resolution process description moreover reduces the risk of errors in parameterizations, which often negatively affect the quality of the climate model simulations (COSGROVE ET AL. 2003), and thus offers an immense contribution to climate model improvements (RANDALL ET AL. 2007, LISTON 2004, BETTS ET AL. 1997, KOSTER AND SUAREZ 1992). But two-way coupled model runs not only promise to enhance the understanding of the land-atmosphere-system and to bring along advances in climate modeling. Moreover, the two-way coupled model approach enables the atmosphere to react on vegetation changes taking place in the framework of global change. The latter becomes increasingly important when considering the fact that changes in vegetation that follow a local change in climate are likely to cause a modification in the climate vice versa (HENDERSON-SELLERS AND MCGUFFIE 1994). The considerable effect of land cover changes on regional scale precipitation and evapotranspiration has recently been shown by LI AND MÖLDERS (2008). Moreover, these

authors found that due to the significant interactions between CO<sub>2</sub>-concentrations and vegetation, local land cover changes can have a substantial regional impact under climate change conditions, even if they have little impact under present time temperature conditions. Due to the atmospheric transport of water an impact of changes in vegetation and in consequence changes in the water cycle can even be expected for regions characterized by unchanged land cover conditions (LI AND MÖLDERS 2008). A more comprehensive summary of the land surface representation in climate models as well as of presently known aspects of land surface influence on long and short-term climate conditions has recently been given by PITMAN (2003).

While the land surface feedback to the atmosphere is of major interest for the GLOWA-Danube project, the present work only sets the technical prerequisites and does not include the analysis of two-way coupled model runs. Instead, it focuses on the description of the implemented scaling methods, their evaluation for past climate conditions and the analysis of one-way coupled runs using both, meteorological simulations for current and future climate conditions as input for the process description at the land surface. The meteorological data applied is provided by the regional climate model REMO (JACOB AND PODZUN 1997, JACOB 2001). In a cooperative study designed to analyze future climate change in Germany, Austria and Switzerland, which has been carried out by the Max-Planck-Institute for Meteorology (MPI-M) and the German Federal Environment Agency (UBA) in the year 2006, REMO has successfully been setup over the years from 2000 to 2100 to deliver climate change scenarios at a regional scale. For the first time the public could be provided with meteorological simulations at an extraordinary high spatial resolution of 10 x 10 km, setting the perfect basis for an application of this data in the framework of the present thesis.

The land surface model driven by the remapped REMO meteorology within the one-way coupled model runs presented in this work is the hydrological model PROMET (MAUSER AND BACH 2008). The model has been developed within the GLOWA-Danube project and represents the land surface component in the DANUBIA model. A more detailed description of the coupled model system is given in chapter 3.



## 2.1 CLIMATE

According to the effective KÖPPEN-GEIGER Climate Classification (KÖPPEN 1936), the climate in the UD is denoted as a Cfb-climate. While characterized by a warm temperate main climate (C), the region belongs to the fully humid areas with warm summers (KOTTEK ET AL. 2006). The genetic FLOHN Classification classifies the area of the UD as a transition climate belonging to the extra tropical zone of Westerlies (FLOHN 1971). Geographically located in the northern midlatitudes, the climate in the UD is dominated by the prevailing Westerlies and is strongly influenced by the Atlantic climate and its high precipitation amounts. Westerly and northwesterly winds dominate in the summer, changing to southwestern wind directions in the winter. The heterogeneity of the relief, in particular the differences in the extent of exposure to the prevailing winds, as well as the differences in altitude diversify the general climate pattern inside the catchment. Northerly winds often carry along humid Atlantic air masses causing large advective rainfall. Southerly wind conditions on the other hand can result in a regional climatologic phenomenon called foehn. For areas located north of the Alps down to the Danube Valley, the foehn is accompanied by dry warm air masses and dissolving clouds. Temperature and precipitation show distinct gradients that are closely related to topographic features in the UD. Annual mean precipitation increases from north to south with values of approximately 700 mm in the Danube Valley to far above 2000 mm at higher elevations in the Alps (see Fig. 2.2).

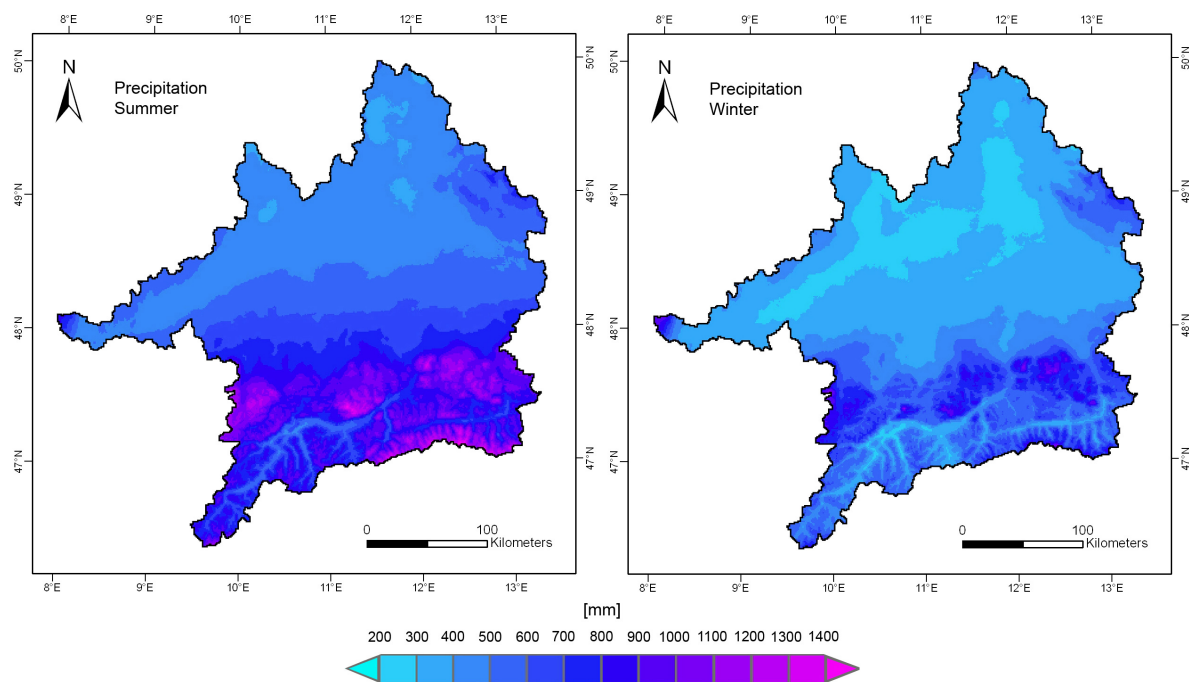


Fig. 2.2: Average summer and winter precipitation in the Upper Danube watershed for the hydrological years 1971-2000. The maps are based on spatially distributed observations provided by the meteorological preprocessor in PROMET (MAUSER AND BACH 2008).

The northern rim of the Alps shows an annual mean precipitation of around 1500 mm, largely traced back to the holdup of humid air at the Alpine barrier (LUDWIG 2000) (RZD 1986). Similar amounts of precipitation can be found in higher elevations of the Bavarian and Black Forest. Precipitation minima ( $\approx 650$  mm) occur in the lower elevations of the Naab and Altmühl basins as well as in the Nördlinger Ries (BMU 2000). Some Alpine valleys like the Inn Valley in Austria also show comparatively low precipitation amounts. Precipitation maxima occur in summer, often in connection with convective rain events. In the Alpine Foreland and in the Alps, these events frequently cause serious floods. In the lowland areas, summer precipitation represents more than 60 % of annual precipitation (RANK ET AL. 2005). Only in the higher elevations of low mountain ranges, a secondary maximum is found in the winter months of December and January. Compared to the long-term average precipitation, extreme years can show variations of up to 150 % in Alpine areas. Extreme daily precipitation amounts take values of 150 to 200 mm/d. In most cases these extreme events are related to 5b weather situations (RZD 1986). The mean annual area precipitation in the German part covering about 73 % of the UD is about 950 mm (RZD 1986).

Temperature inside the UD is also closely connected to the prevailing relief gradients (see Fig. 2.3, left). Temperature lapse rates decrease from 0.5-0.7 K/100 m in summer to 0.2-0.4 K/100 m in winter, resulting from an increasing occurrence of atmospheric inversions in winter (RZD 1986).

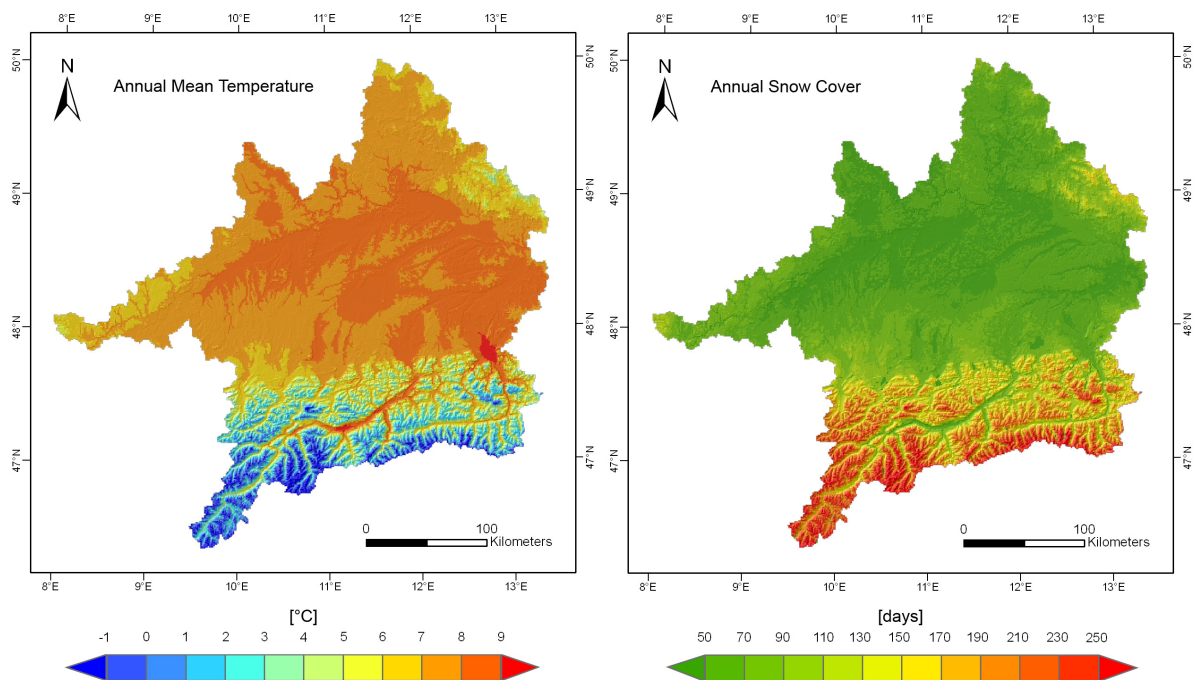


Fig. 2.3: Annual mean temperature (left) and average number of days with snow cover (right) in the Upper Danube watershed for the hydrological years 1971-2000. The temperature map represents spatially distributed observations provided by the meteorological preprocessor in PROMET, the snow cover map is based on PROMET model results (PRASCH ET AL 2008a).

Compared to the large variability of temperature in the Alpine regions, the long-term mean annual temperature in large parts of the Alpine Foreland is rather homogeneously around 7 to 8 °C (see Fig. 2.3, left). With mean temperatures of about 10 °C, the domain of the Danube Valley as well as the lower Isar and Naab Valley, represent comparatively warm parts of the catchment. In contrast, at higher elevated regions of the low mountain ranges and large parts of the Allgäu, mean temperatures are only around 5 to 7 °C. January with approximately -3 to -2 °C in the Alpine Foreland and -6 to -13 °C in higher elevations, states the coldest month, whereas maximum monthly temperatures of around 16 to 18 °C, representative for large parts of the area, are situated in July. However, temperatures reaching less than -20 °C casually occur (BMU 2000, RZD 1986).

Besides its influence on temperature and precipitation, orographic variability is also reflected by the local radiation balance, wind regimes and cloud and snow cover resulting in a very specific local climate in the Alpine parts of the catchment. Unlike large parts of the catchment that are characterized by less than 100 days of snow cover over the time of one year (see Fig. 2.3, right), annual snow cover in the Alps can last up to 8 months in altitudes above 2000 m.a.s.l., changing into a perennial coverage in heights between 2900-3200 m.a.s.l. (RZD 1986). The temporary storage of water in form of snow is of high importance considering the increasing flood risk due to snowmelt contributions to the catchment's runoff.

## 2.2 HYDROLOGY

The hydrological regime of the Danube is distinctly influenced by the regional precipitation patterns and the different tributaries of the Danube. The size and heterogeneity of the catchment leads to a strong temporal and spatial differentiation of runoff behaviour. Consequently the regime changes several times as a result of the different flow regimes of its affluents, covering all discharge regimes from straight nival to pluvial (LUDWIG ET AL. 2003). In particular the rivers Iller, Lech, Isar and Inn contribute to the Alpine character of the Upper Danube. Due to an increasing portion of solid precipitation with increasing altitude, the concentrated melting in spring can contribute up to 80-90 % to the total runoff in high-mountainous regions (DOMOKOS AND SASS 1990). Even if in most cases floods inside the UD are induced by convective summer rains, water amounts related to snow melt and glacier runoff in combination with characteristic large scale weather patterns (e.g. 5b situations) also pose a serious flood risk inside the catchment (LUDWIG ET AL. 2003).

The river Inn contributes the largest amounts of water inside the Upper Danube watershed and is the third largest tributary in the entire Danube basin (see Tab. 2.1). At its mouth in

Passau (see Fig. 2.4), the Inn adds as much water to the Danube as the Danube itself contains at the point of confluence, although the Inn's catchment area with 26 000 km<sup>2</sup> is only half as large as the one of the Danube at this point (ICPD 2005).

Tab. 2.1: Hydrological characteristics of the Danube and its main tributaries (1st order tributaries with catchments > 4000 km<sup>2</sup>) (based on ICPD 2005).

River	Mouth at Danube [river km]	Length [km]	Catchment size [km <sup>2</sup> ]	Average discharge [m <sup>3</sup> /s]	Discharge time series
Danube	0	2780	801463	6460	1914-2003
Lech	2497	254	4125	115	1982-2000
Naab	2385	191	5530	49	1921-1998
Isar	2282	283	8964	174	1926-1998
Inn	2225	515	26130	735	1921-1998

In the course of time, the Danube has lost a number of tributaries to the more erosive Rhine river system. Even at present, it loses about half its discharge to the Rhine Basin through underground passages in its upper course near Immendingen (ICPD 2005).

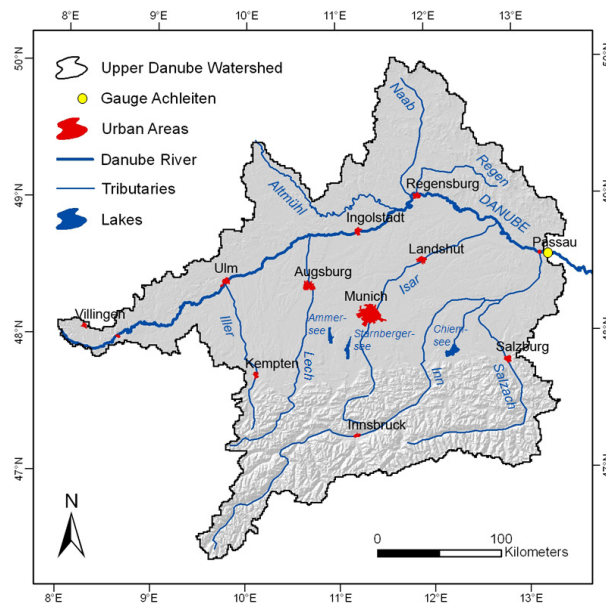


Fig. 2.4: River network and major water bodies in the Upper Danube watershed.

In contrast to the Alpine rivers, tributaries coming from the north are characterized by a pluvial regime type with maxima in the winter.

The anthropogenic regulation of some of the rivers in the watershed has led to unnatural discharge and sediment characteristics, providing man the possibility to influence the storage and release of large water amounts and thus reduce the dangers related to floods to a

certain extent. Besides their value in flood protection, these artificial reservoirs provide the option to increase river discharge in winter, where particularly the Alpine tributaries are characterized by low discharge volumes. Unlike these artificial water storages, the various lakes inside the catchment pose natural retention basins also largely influencing the water flow dynamics within the UD.

## 2.3 GEOMORPHOLOGY AND GEOLOGY

The Upper Danube watershed includes a variety of different landscapes and geological media. Giving a brief geographical overview, the area can be divided into an area of low mountain ranges, the Alpine Foreland and the Alpine region. While the central part of the Alpine Massif is dominated by metamorphous crystalline material, the northern part mostly consists of calcareous material, showing the typical karst formations (PAWELLEK ET AL. 2001). Along the foot of the limestone part of the Alps the tertiary deposits flysch and molasse were caught up in the later stages of the Alpine folding, forming a belt of hills and low mountains (see Fig. 2.5 and Fig. 2.6, right).

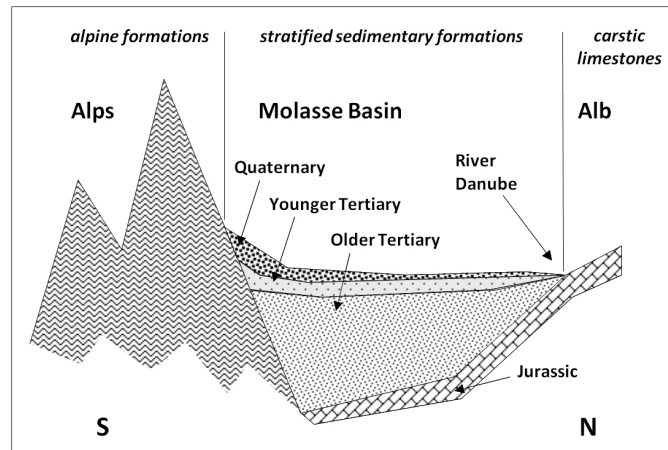


Fig. 2.5: Hydrogeologic profile of the Upper Danube watershed (BARTHEL ET AL. 2005, modified).

The southern Alpine Foreland with its quaternary sedimentations, largely shaped by the ice ages, is showing the typical glacial and glaciofluvial forms. Within the terminal moraines, which mark the points where the glacier lobes once came to rest, many lakes such as the Starnberger See and the Ammersee still testify the former presence of the ice masses. Both tertiary hills and moraines are partly covered by thick loess layers. Outside the moraines, floodwaters have deposited sheets of gravel, which extend as gravel plains and river terraces along the courses of tributaries flowing north to the Danube. Leaving the tertiary hills to the

north, the Danube Valley is bounded by the mesozoic carbonate sediments of the Swabian and Franconian Alb in the north and the crystalline mountains of the Bavarian Forest in the northeast (JERZ 1993).

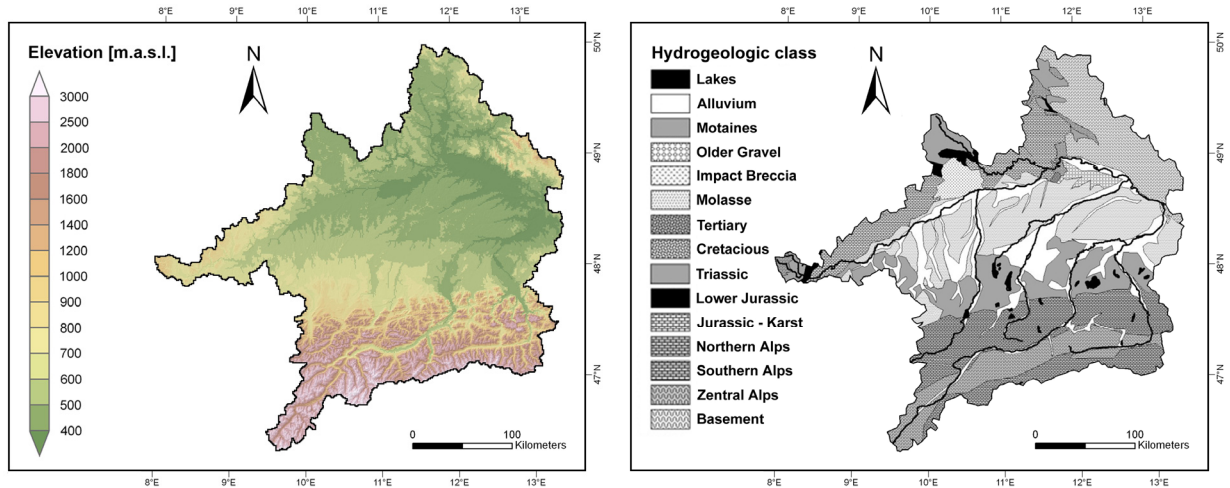


Fig. 2.6: Topography and simplified hydrogeology of the Upper Danube watershed (NGDC 1998, BARTHEL ET AL. 2005, modified).

The Upper Danube watershed is characterized by step relief gradients. An overview of the topographic conditions in the UD is given in Fig. 2.6 (left). The point of maximal elevation is located at Piz Bernina with a height of 4049 m.a.s.l., which, taking into account the height of the gauge at Achleiten (287 m.a.s.l.), gives a total difference in altitude of 3762 m within the catchment.

## 2.4 SOILS

Pedogenesis is influenced by many factors and processes. The manifold environmental boundary conditions inside the UD lead to a variety of different soils. In particular the presence of large ice masses during the ice ages and the processes related to these climatic boundaries are largely reflected by the present soil conditions.

Regional distinctions in vegetation, climate, relief, bedrock and the time available for the development of the soils lead to soil types ranging from very fertile luvisols, situated on loess sediments, to barely developed leptosols in mountainous areas (ESBN 2004). Soil texture is manifold as well, ranging from coarse sands to loamy clays. The sloped mountain regions are often connected to umbric and rendzinic leptosols. Umbric leptosols as well as albic luvisols have developed on the crystalline material of the Central Alps, whereas the well wooded altitudinal belts show regosols and chromic cambisols developed on calcareous

rocks. Inside the Alpine valleys hydromorphic soils like gleyic luvisols and gleysols can be found (KUNTZE ET AL. 1994). In the floodplains, the Danube and its tributaries have deposited alluvial sediments of varying depth resulting in frequent occurrence of fluvisols in the Upper Danube area (ESBN 2004). The highly permeable gravel bedrock of the plains and moraines established the basis for the development of luvisols in large areas of the Alpine Foreland (ESBN 2004). Together with cambisols, the luvisols pose the dominant soils situated on the loess sediments of the tertiary hills. In regions with high groundwater levels, they are accompanied by gleysols and gleyic luvisols. Fens characterized by the typical peat soils can be found in the catchment as well, in particular at the northern rim of the Alps.

Fertile cambisols and umbric leptosols are the predominant soil types situated on the crystalline material of the Bohemian, Bavarian and Black Forest in the north of the Danube Valley. The jurassic parent material of the Franconian and Swabian Alps sets the basis for gleyic luvisols and vertisols on the lower jurassic and rendzic leptosols as well as chromic cambisols on the upper Jurassic (KUNTZE ET AL. 1994).

## 2.5 VEGETATION

Vegetation in the UD represents the product of the prevailing climatic, geomorphologic, geologic and anthropogenic boundary conditions and thus shows a high spatial variability. Free from human influence, the area would mostly be covered by forest, except of the high Alpine regions, where climate conditions are limiting the botanic habitat (RZD 1986). Among the deciduous forest species, oak (*quercus robur* and *quercus petraea*) and beech (*fagus sylvatica*) would cover the largest areas. In reality, man has limited forested areas to sites that are inapplicable for agricultural cultivation. Substituting the natural vegetation by large plantations of spruce (*picea abies*), forestry has left over only few pure deciduous forests. There are still few places along the river banks of the Danube and its tributaries, where the absence of human attention allows a natural development for a variety of species. Besides these unique biomes some of the once widespread moorlands have been preserved in their natural state in the south of Bavaria.

Mixed forest, composed by spruce (*picea abies*), white fir (*abies alba*) and beech (*fagus sylvatica*) together with pure coniferous forests make up the forested areas in the higher elevated montane and subalpine regions. Human influence has made spruce the dominating forest species in these areas as well. Moreover, spruce is found at the timberline of around 1900 m.a.s.l. Mixed forests are replaced by spruce in the lower regions of the climatologically dryer central part of the Alps. In higher regions larch (*larix decidua*) and sometimes swiss

stone pine (*pinus cembra*) as well as mountain pine (*pinus mugo*) reach up to the local timberline of 2400 m.a.s.l.. The unfavourable climate conditions above the timberline are tolerated only by very few plant species such as grass species (*carex curvula*) and ericaceae (*calluna vulgaris*) that have adapted to the extreme environmental conditions (ELLENBERG 1996).

## 2.6 SOCIO-ECONOMIC ASPECTS

The UD is largely influenced by human activity. Five different countries share the total catchment area. With a percental coverage of 72.7 % the German federal states of Bavaria and Baden-Württemberg make up the largest part of the total area (62 % Bavaria, 11 % Baden-Württemberg), followed by Austria and Switzerland with fractional contributions of approximately 24.1 % and 2.2 % respectively (see Fig. 2.7). With 0.7 % and 0.3 % the Czech Republic and Italy only cover small fractions of the river catchment (BLFW 1999).

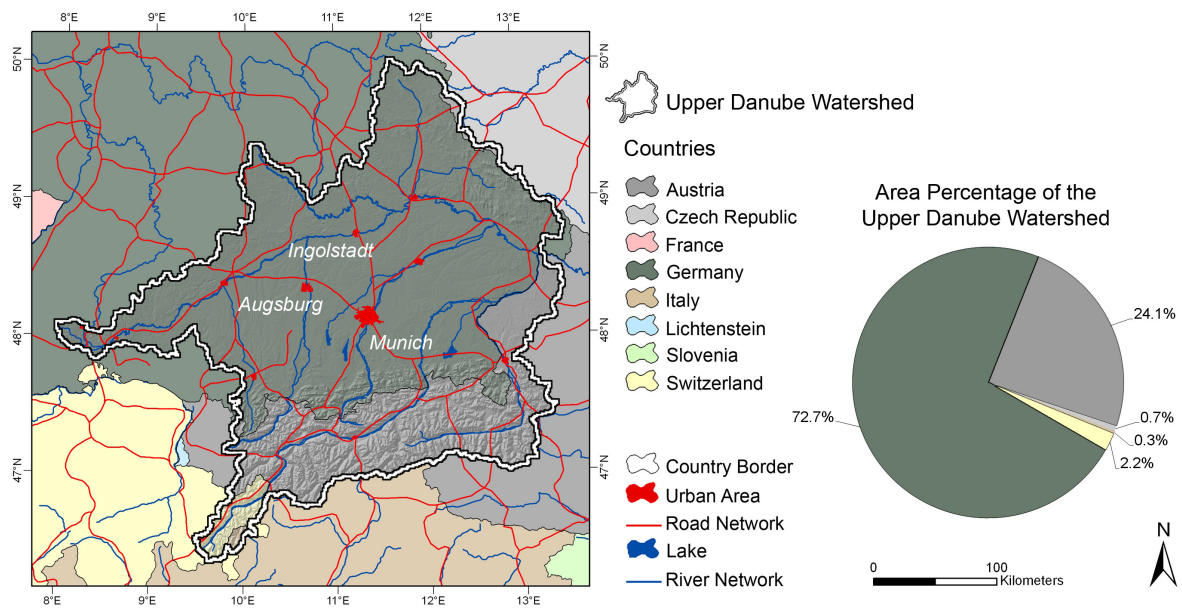


Fig. 2.7: The Upper Danube watershed and its major cities, its traffic network and water ways and the countries sharing and surrounding the catchment (based on the ESRI World Database (ESRI 2008)).

Its role as a unique international waterway, flowing 2857 km across Europe, as well as the agricultural suitability of the environment has encouraged civilisations and cultures to develop on the banks of the Danube since early times (DOMOKOS AND SASS 1990). At present, more than 10 million people are hosted in the catchment of the Upper Danube with a high density of population (> 100 inhabitants/km<sup>2</sup>). The cities Munich (1.2 Mio. inhabitants), Augsburg (260 000 inhabitants) and Ingolstadt (115 000 inhabitants) state the most important

industrial agglomerations. Outside these densely populated areas land use is dominated by forestry and agricultural use of different intensity (LUDWIG ET AL. 2003).

Most commonly cultivated crops range from sugar-beet (*beta vulgaris*), potatoes (*solanum tuberosum* L.) and canola (*brassica napus* L.) to winter and summer grains (mostly *triticum* L., *hordeum vulgare* L., *secale cereale* L.) and maize (*zea mays* L.). Some regions have specialized on the cultivation of asparagus (*asparagus* L.) or hops (*humulus* L.) as well. While the areas favouring an agricultural production are located in the climatically privileged basins along the Danube, high precipitation and low temperatures limit the agricultural production in higher elevations of the catchment area. As a consequence, these areas are extensively used as pastures and grasslands. Besides agriculture and industry, tourism has developed into an economic branch of substantial size. In particular the mountainous landscapes of the Alps and the Bavarian Forest are attracting tourists throughout the year.

Water use and management is complex in the UD and includes drinking and industrial water supply, hydropower and navigation. Apart from its role in water supply and energy production, water management is concerned with flood protection and low-flow management. The need to protect land and people against floods as well as the extended water usage for energy production are reflected by the large number of river regulations, dams and storage reservoirs inside the Upper Danube watershed. Unfortunately the benefit of controlling the regional water resources is largely affecting the natural system, as can be seen in the substantial shortening of river courses and the destruction of natural retention basins. The Danube is navigable below the mouth of the Altmühl near Kelheim and is connected to the Rhine-Main River System via the Rhine-Main-Danube-Channel. While it is already used to export water from the UD into other regions at present, the export of water using this waterway might intensify in the future, due to changes in water availability in Europe (LUDWIG ET AL. 2003).

### 3 THE COUPLED MODEL SYSTEM

#### 3.1 THE HYDROLOGICAL MODEL PROMET

The distributed hydrological model PROMET (Process of Radiation, Mass and Energy Transfer) has been developed within the GLOWA-DANUBE project as part of the decision support system DANUBIA. Within the interdisciplinary DANUBIA model, PROMET represents the land surface component. Besides the JAVA version implemented in DANUBIA, a FORTRAN version of PROMET is available, which is used within the coupled model setup in the present work. The computational efficiency of the FORTRAN language, together with the option to exclude some of the disciplines that are not necessarily required for the development of the coupled model system (e.g. tourism or traffic) make the model an ideal test environment that can be setup on an ordinary desktop PC. The model's origins go back to studies by MAUSER AND SCHÄDLICH (1998), where the SVAT-type model PROMET was used for the simulation of evapotranspiration on the basis of remote sensing data. The current version of the model allows a physically based simulation of various land surface processes and can be applied to different spatial scales and arbitrary regions of interest. Fig. 3.1 presents a diagram of the model and its major components.

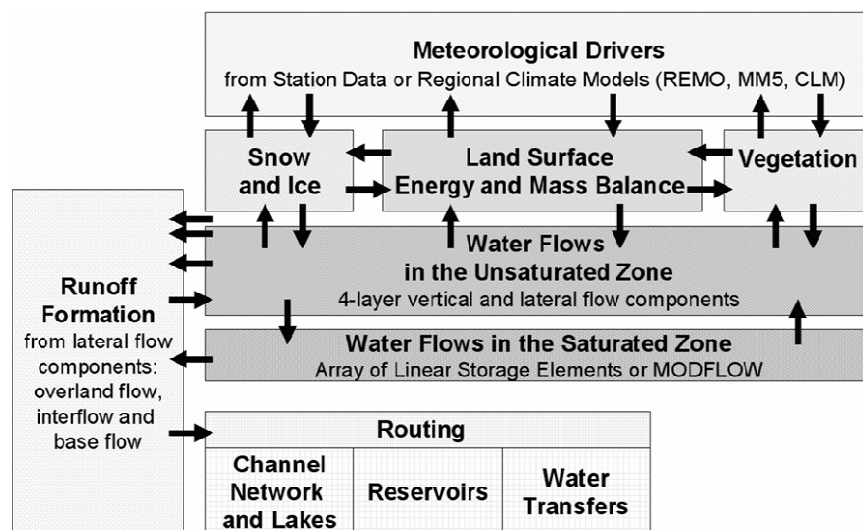


Fig. 3.1: Schematic diagram of the different components of PROMET (boxes) and the interfaces between them (arrows). The arrows indicate the direction of data flow. (MAUSER AND BACH 2008).

As the diagram shows the model is composed of eight interacting subcomponents, which will be briefly described in the following. For more detailed information on the model and its parameterization it is referred to MAUSER AND BACH (2008).

### 3.1.1 THE METEOROLOGY COMPONENT

The meteorological forcings are supplied by a meteorological preprocessor in the models standard configuration. This preprocessor can optionally be substituted by SCALMET, providing the technical prerequisite to couple the land surface model with RCMs. The meteorological drivers are of great importance for the overall model performance as they determine both, the water and the energy budget at the land surface. PROMET requires spatial distributions of the following meteorological variables:

- Precipitation [mm]
- Temperature [°C]
- Humidity [%]
- Incoming shortwave radiation (direct) [W/m<sup>2</sup>]
- Incoming shortwave radiation (diffuse) [W/m<sup>2</sup>]
- Incoming longwave radiation [W/m<sup>2</sup>]
- Wind speed [m/s]
- Surface pressure [Pa]

While the generation of meteorological distributions in SCALMET will be described in a later chapter (see chapter 4), the following paragraphs will give a survey of the processing of station observations in PROMET. The latter is necessary as the meteorological distributions provided by the meteorological preprocessor in PROMET will serve as reference in various aspects in the later course of this work.

To assure a high degree of quality, homogeneity and continuity, meteorological observations at a total number of 377 meteorological stations in Germany (DWD) and Austria (ZAMG) are used for the generation of the meteorological fields needed for the simulation of land surface processes in PROMET (see Fig. 3.2). Temporal resolution and time of measurement vary within the meteorological stations. Up to April 2001, measurements at the DWD weather stations were taken three times a day at the so called 'Mannheimer Stunden' (7:30 a.m., 2:30 p.m. and 9:30 p.m.). From that time on, the data acquisition system has been partly automated and the times of readings have been shifted to 7:00 a.m., 2:00 p.m. and 9:00 p.m. In addition to these measurements, hourly synoptic DWD observations have been integrated in the climate database. Measurements in the Austrian part of the area are taken twice a day for precipitation and 3 times a day for the rest of the required variables. To supply hourly values of the meteorological variables for each raster element, temporal and spatial interpolation methods need to be applied.

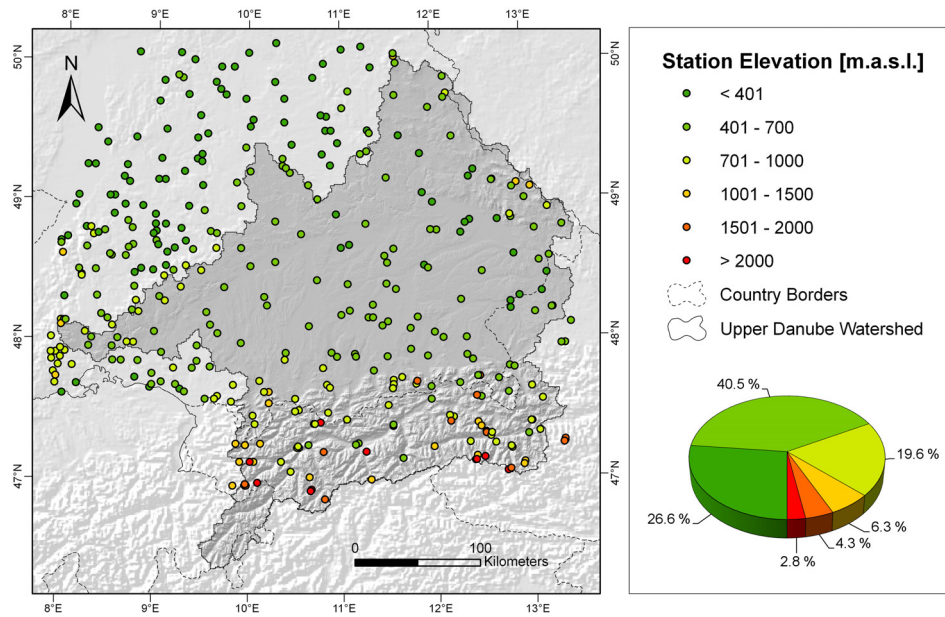


Fig. 3.2: The network of meteorological stations used for the generation of meteorological distributions in PROMET.

### 3.1.1.1 TEMPORAL INTERPOLATION OF METEOROLOGICAL OBSERVATIONS

Continuous meteorological variables like temperature, air humidity and wind speed are interpolated, fitting a cubic function through four successive measurements (MAUSER AND BACH 2008). In contrast to these meteorological variables, precipitation is connected to single events and therefore highly variable over space and time. To adequately distribute precipitation observations over the time past between the measurements, several assumptions have been made in order to account for regional precipitation characteristics. The approach makes a distinction between long events (steady rain) with rather low intensities and short events (showers) characterized by high intensities. While short events are related to just one singular recording, long term events are associated with at least two consecutive precipitation recordings (MAUSER AND BACH 2008).

The temporal distribution of long rainfall events is carried out in several steps. The beginning of the rain event is simulated by slowly increasing rainfall up to the point of time affiliated to the measurement. This is done by dividing the first observation into 55.5 equal parts that are subsequently multiplied with increasing weights (1.5, 3, 5, 7, 9, 14, 16). The same procedure is used to 'fade out' a precipitation event using the last observed rainfall amount (LUDWIG 2000). Rainfall intensities between two consecutive recordings are calculated by equally distributing the recorded precipitation over the time between the two measurements (see Fig. 3.3). For the temporal distribution of precipitation over the time steps before an event a Gaussian distribution is applied in case of short events (MAUSER AND BACH. 2008).

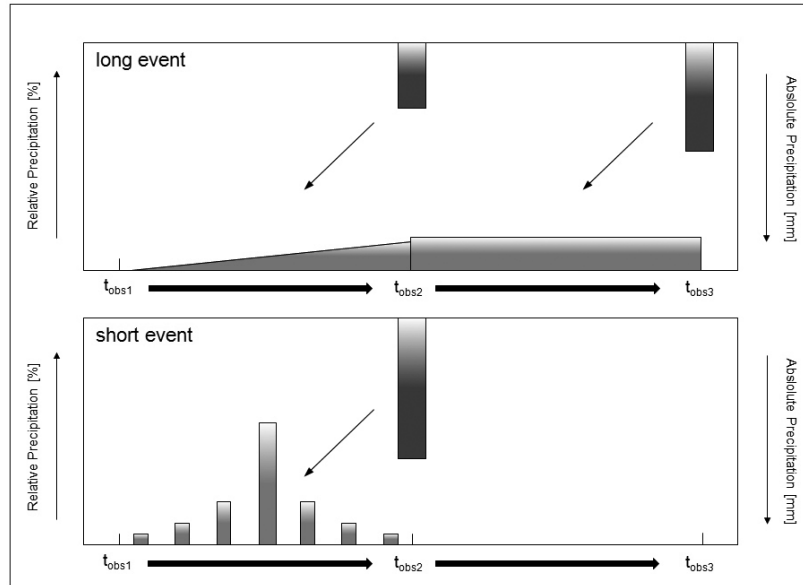


Fig. 3.3: Temporal interpolation of rainfall over the time past between the observations for the two categories of long and short rain events (LUDWIG 2000, modified).

### 3.1.1.2 SPATIAL DISTRIBUTION OF METEOROLOGICAL OBSERVATIONS

After the meteorological observations have been temporally interpolated, the resulting hourly values need to be spatially distributed. The method applied in PROMET makes use of parameter-elevation dependencies, which are known to exist for many meteorological variables. In a first step, the method determines the prevailing parameter-elevation dependency for the current model time step by means of statistic data analysis. The result is a regression function that is used in combination with distributed elevation information, supplied by a digital elevation model (DEM), to compute a value for the considered meteorological variable for each raster element.

In a next step, the same meteorological observations used to derive the altitudinal lapse rates are utilized to account for local deviations from the functional relation. This is done by subtracting the observations from the normal field. The residuals, expressed as the difference between the predicted values and the observations, are spatially interpolated using an Inverse Distance Interpolation approach (IDW). Finally, the interpolated residuals are used to correct the predictions made on the basis of the regression function. The method allows the consideration of the elevation dependence of the remapped parameters, forcing the remapped field through the observations at the station locations.

Relative humidity, which shows a nonlinear height dependency, is transformed into an absolute humidity before the regression analysis and is retransformed to a relative humidity subsequent to the remapping process.

### 3.1.1.3 THE RADIATION SUBMODEL IN PROMET

While precipitation, temperature, humidity, surface pressure and wind speed are directly measured at the weather stations, short- and longwave radiative fluxes are computed within a radiation submodel using spatially and temporally interpolated cloud cover observations (MAUSER AND BACH 2008). The potential incoming shortwave radiation ( $R_{sw\_pot}$ ) is calculated as a function of topographic (elevation, slope, aspect) and astronomic parameters (local time, time of sunrise and sunset, sun zenith and azimuth, solar constant and eccentricity of the earth orbit) (BRUDSAERT 1982). It is composed of direct and diffuse radiation components. For the computation of the atmospheric transmissivity for direct solar radiation an approach presented by HOTTEL (1976) is applied. The method provides different parameterizations for summer and winter conditions in the midlatitudes and accounts for differences in local altitude (HOTTEL 1976). Following this approach for the standard atmosphere with clear 23-km visibility the atmospheric transmissivity for direct radiation ( $T_{dir}$ ) can be written as:

$$T_{dir} = a_0 + a_1 * e^{\frac{-a_2}{\cos(SZA)}} \quad \text{Eq. 3.1}$$

$$a_0 = \left[ 0.4237 - 0.00821 \cdot (6 - (0.001 \cdot z))^2 \right] \cdot f_1$$

$$a_1 = \left[ 0.5055 + 0.00595 \cdot (6.5 - (0.001 \cdot z))^2 \right] \cdot f_2$$

$$a_2 = \left[ 0.2711 + 0.01858 \cdot (2.5 - (0.001 \cdot z))^2 \right] \cdot f_3$$

- with:
- $SZA$  = Solar zenith angle
  - $f_1$  = Factor depending on season and geographic latitude
  - $f_2$  = Factor depending on season and geographic latitude
  - $f_3$  = Factor depending on season and geographic latitude
  - $z$  = Terrain Elevation

The factors  $f_1 - f_3$  are listed for the midlatitudes in Tab. 3.1.

Tab. 3.1: Seasonal factors for the calculation of the atmospheric transmissivity for direct solar radiation in the midlatitudes (HOTTEL 1976).

Season	$f_1$	$f_2$	$f_3$
Summer	0.97	0.99	1.02
Winter	1.03	1.01	1.00

Diffuse transmissivity ( $T_{dif}$ ) is deducted using the relation between direct and diffuse atmospheric transmissivity presented by LIU AND JORDAN (1960):

$$T_{dif} = 0.271 - 0.2939 * T_{dir} \quad \text{Eq. 3.2}$$

The transmissivity for direct solar radiation allows to calculate the direct solar radiation component ( $R_{sw\_dir}$ ) in form of:

$$R_{sw\_dir} = T_{dir} * R_{sw\_pot} \quad \text{Eq. 3.3}$$

For the calculation of the diffuse radiation a view factor ( $VF$ ) is introduced. The factor is calculated according to the local slope ( $\beta$ ) as:

$$VF = (1 + \cos(\beta))/2 \quad \text{Eq. 3.4}$$

The diffuse solar radiation component ( $R_{sw\_dif}$ ) can be calculated using the atmospheric transmissivity for diffuse solar radiation and the view factor as:

$$R_{sw\_dif} = T_{dif} * R_{sw\_pot} * VF \quad \text{Eq. 3.5}$$

Finally, the calculated values of direct and diffuse solar radiation are corrected for cloud cover on the basis of studies by MÖSER AND RASCHKE (1983).

The available longwave radiation on the land surface ( $R_{lw}$ ) depends on the thermal emission of the land surface ( $R_{lw\_out}$ ) and the longwave radiation emitted towards the land surface by the atmosphere ( $R_{lw\_in}$ ):

$$R_{lw} = R_{lw\_in} - R_{lw\_out} \quad \text{Eq. 3.6}$$

The emitted radiation of the land surface and the atmosphere are determined with respect to their temperature and emissivity as:

$$R_{lw\_out} = \varepsilon_{ls} * \sigma * T_k^4 \quad \text{Eq. 3.7}$$

$$R_{lw\_in} = \varepsilon_a * \sigma * T_k^4 \quad \text{Eq. 3.8}$$

with:

- $\varepsilon_{ls}$  = Emissivity of the land surface
- $\varepsilon_a$  = Emissivity of the atmosphere
- $\sigma$  = Stefan-Boltzmann constant
- $T_k$  = Temperature [K]

For the case that the cloud fraction ( $C_f$ ) is greater than zero, the radiation emitted by the atmosphere is corrected according to BOLZ (1949) as follows:

$$R_{lw\_in} = 0.99 * (\epsilon_a * \sigma * T_k^4) * (1 + 0.243 * C_f^{2.5}) \quad \text{Eq. 3.9}$$

As the result of all calculations within the radiation submodel in PROMET the incoming shortwave radiation, separated into to direct and diffuse components, as well as the longwave radiation balance on the earth surface can be provided for every raster cell and every time step. After this short introduction to the meteorological component of the PROMET model, the following will give an overview of the different subcomponents describing water fluxes at the land surface. While the meteorological input data are spatially distributed in advance of all model calculations for a given time step, the land surface processes are subsequently described for each of the grid cells in different subcomponents.

### 3.1.2 THE LAND SURFACE ENERGY AND MASS BALANCE COMPONENT

The land surface energy and mass balance component iteratively closes the energy balance on the land surface which is given as

$$R_{sw\_in} + R_{lw\_in} - ET - H - B - R_{sw\_out} - R_{lw\_out} = 0 \quad \text{Eq. 3.10}$$

where  $R_{sw\_in}$  and  $R_{lw\_in}$  represent the incoming radiative fluxes of shortwave and longwave radiation respectively,  $ET$  is the latent heat flux given by the actual evapotranspiration,  $H$  is the sensible heat flux,  $B$  is the ground heat flux, and  $R_{sw\_out}$  and  $R_{lw\_out}$  represent the outgoing components of shortwave and longwave radiation (MAUSER AND BACH 2008). Depending on the aerodynamic resistance of the land surface the component describes the transportation of water vapour through the boundary layer into the atmosphere based on CAMPBELL AND NORMAN (1998) and MONTEITH (1973). Moreover, the momentum flux is calculated as a function of the friction velocity. As it includes the determination of all quantities that can optionally be aggregated by SCALMET and can be provided as inputs for RCMs in two-way coupled model runs, the land surface energy and mass balance component is of particular importance for the coupled model system.

### 3.1.3 THE VEGETATION COMPONENT

The vegetation component simulates the water transport and carbon allocations in the canopy (MAUSER AND BACH 2008). Carbon and water fluxes are described as a function of a plant species specific canopy resistance, which is calculated according to the plants LAI and

stomatal conductance as well as the predominant radiation, temperature, air humidity and soil water conditions.

While the current model version also offers a dynamic simulation of plant growth and all other plant related processes within a biophysical canopy model (HANK 2008), the present work is based on the conventional approach as described in detail by MAUSER AND BACH (2008). The method calculates the actual evapotranspiration following the PENMAN-MONTEITH equation (PENMAN 1956, MONTEITH 1965) in form of:

$$ET = \frac{\Delta_s * (R - B) + \rho * c_p * \frac{(e_s - e_a)}{r_a}}{\Delta_s + \gamma * \frac{1 + r_s}{r_a}} \quad \text{Eq. 3.11}$$

- with:
- $ET$  = evapotranspiration
  - $\Delta_s$  = slope of the saturation vapour pressure curve
  - $R$  = radiation balance
  - $B$  = ground heat flux
  - $\rho$  = density of the air
  - $c_p$  = specific heat of the air at constant pressure
  - $e_s$  = saturation vapour pressure
  - $e_a$  = actual vapour pressure
  - $r_a$  = aerodynamic resistance
  - $r_s$  = canopy resistance
  - $\gamma$  = psychrometric constant

Evapotranspiration is controlled by various plant specific parameters, determining the decrease of stomatal conductance due to unfavourable boundary conditions (BALDOCCHI ET AL. 1987). Based on the assumption that vegetation is inactive during the time of snow coverage, the vegetation model is substituted by a snow model whenever the land surface is covered by a snow layer.

### 3.1.4 THE SNOW AND ICE COMPONENT

The physically based snow submodel inside PROMET was developed by STRASSER (1998) and is further developed by PRASCH ET AL. (2008) and STRASSER ET AL. (2008). Resolving the energy balance in the snow layer, the model calculates the accumulation or ablation of snow water equivalent for each pixel and model time step. The algorithm used for energy balance

closure distinguishes between 'no melt conditions' (air temperature < 273.16 K) and possible 'melt conditions' (air temperature  $\geq$  273.16 K) (MAUSER AND BACH 2008). While for the latter case a snow surface temperature of 273.16 K is assumed within the solution of the energy balance, the balance is iteratively solved for temperatures below 273.16 K. This is done by considering all relevant sources of energy, including long and shortwave radiation, the energy stored in liquid or solid precipitation and the energy related to condensation and sublimation processes. The snow albedo needed for the solution of the radiation balance is calculated as a function of snow age. Snow melt is simulated according to the available energy budget if temperatures meet the above mentioned requirements. Still snow water only leaves the snow package if the liquid water storage inside the package is saturated. For a detailed description of the implemented algorithms it is referred to STRASSER ET AL. (2008). With its ability to account for water storage and release due to snow accumulation or ablation, the snow model is of great importance for a realistic description of many hydrological processes in the land surface model PROMET (e.g. river discharge).

### 3.1.5 THE SOIL HYDROLOGICAL AND SOIL TEMPERATURE COMPONENT

Including the simulation of water fluxes related to infiltration, percolation, capillar rise and exfiltration, the soil model in PROMET calculates the volumetric soil water content, the soil matrix potential and the soil temperature in the unsaturated soil layers. Besides vertical water flow components, the soil model also describes the lateral flows of water in and on the unsaturated soil (MAUSER AND BACH 2008). Therefore an approach presented by EAGLESON (1978) has been extended to 4 soil layers with different thickness characteristics.

The calculated matrix potential defines whether the water stored in the soil is available for evapotranspiration or not. Excluding the deepest soil layer, all layers can drain vertically and horizontally. Percolation of the bottom soil layer directly adds to the groundwater body. Besides its influence on local evapotranspiration, the soil conditions largely affect the process of runoff formation.

### 3.1.6 THE GROUNDWATER COMPONENT

The groundwater component simulates water flow in the saturated parts of the catchment and represents the linking element between the unsaturated soil layers and the channel network (MAUSER AND BACH 2008). Two subcomponents are available for the simulation of groundwater fluxes. The first component, which represents the one used in the present work, consists of a linear storage element that is filled by the percolation of the deepest soil layer of

every pixel and that is depleted by the process of capillar rise or the discharge into the proxels channel (MAUSER AND BACH 2008). A time constant is assigned to each linear storage element, depending on the distance between the respective proxel and the next main channel. The time constant defines the time that passes until the water storage is assigned to the river discharge and takes values ranging from one year (remote proxels) to one hour (proxels situated on a main channel).

Alternatively to the linear storage model, the bottom soil layer can be coupled to the MODFLOW ground water model. A detailed description of this subcomponent is given by BARTHEL ET AL. (2007) and HARBAUGH ET AL. (2000).

### 3.1.7 THE CHANNEL FLOW COMPONENT

The channel flow component directs the lateral water flow concentrations of the soil component into the river runoff and further routes the river runoff through the channel network and natural reservoirs (MAUSER AND BACH 2008). It is based on the assumption that each proxel is part of the channel network and that all proxels are hydraulically interconnected by topography. Within the process of transporting the runoff from one proxel to its hydraulic neighbor, the lateral flow types overland flow, interflow and groundwater flow are treated differently (MAUSER AND BACH 2008). Once the water has entered the channel network, it is routed using the Muskingum-Cunge scheme (CUNGE 1969) with modifications proposed by TODINI (2007). In order to avoid instabilities within the routing process, the time interval of the channel flow component is increased towards a routing pulse of 30 times per hour leading to a time step of 2 minutes (MAUSER AND BACH 2008).

Besides the description of water flow in the channel network, the component accounts for runoff retention in natural reservoirs where the inflow of water adds to the water volume and changes the lake water level. Further information about the channel flow component and the exact parameterization is given by MAUSER AND BACH (2008).

### 3.1.8 THE MAN-MADE HYDRAULIC STRUCTURES COMPONENT

The man-made hydraulic structure component is organized analogously to the natural water reservoirs concerning the uptake of water. It includes the 15 largest reservoirs in the catchment, storing a maximum of 1 125 000 000 m<sup>3</sup>, which corresponds to 2.2 % of the total river discharge volume at the gauge of the UD in Achleiten (MAUSER AND BACH 2008). Furthermore it includes 30 water transfer diversions regulating the transfer of water inside the catchment as well as between the catchment and the surrounding watersheds using artificial

hydraulic connections between the proxels. The outflow of water from the reservoirs as well as the transfer of water is determined by look up tables opening a flexible way to supply the model with water management strategies.

For the internal process description, PROMET requires a set of non distributed vegetation and soil parameters as well as different spatially distributed information in a user specified spatial resolution (soil data, digital elevation model, land use maps). Temporal resolution is user defined although the temporal dynamics of the meteorological boundary conditions suggest a temporal resolution of at least one hour. Some internal processes (e.g. percolation) require an overclocking to adequately simulate the related fluxes though.

### 3.2 THE REGIONAL CLIMATE MODEL REMO

The climate simulations used in the framework of the present work have been generated by the regional climate model REMO (JACOB 2001, JACOB ET AL. 2001, JACOB AND PODZUN 1997). The model is based on the Europa-Modell (EM) (MAJEWSKI 1991), which represents the former weather prediction model of the German Weather Service. REMO has been further developed by the Max-Planck-Institute for Meteorology (JACOB 2001) including the implementation of additional physical parameterizations adopted from the ECHAM4 climate model (ROECKNER ET AL. 1996). An illustration of the origins of the REMO model is given in Fig. 3.4 (left). REMO is a hydrostatic atmospheric circulation model. It is based on the primitive equations of atmospheric motion which are solved on a terrain-following hybrid vertical coordinate system (JACOB AND PODZUN 1997) (see Fig. 3.4, right).

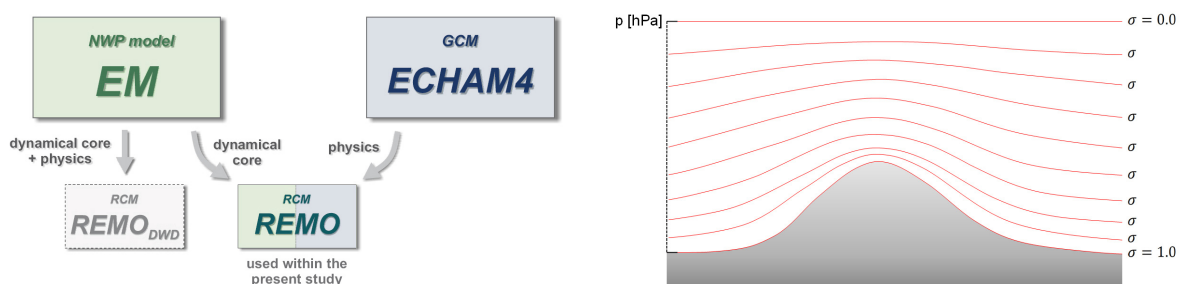


Fig. 3.4: The origins of the regional climate model REMO (left) (KOTLARSKI 2007) and schematic illustration of a hybrid vertical coordinate system (right).

In a sigma coordinate system the vertical position of a point in the atmosphere is described as the ratio of the pressure difference between the point and the top of the domain to the pressure difference between the land surface and the top of the domain. Since the sigma

coordinate system is pressure based and normalized the governing equations of the atmosphere can be casted into a relatively simple form. Atmospheric processes in REMO are described for 20 vertical layers with level intervals increasing from the lower atmospheric levels to the higher atmosphere (PFEIFER 2006).

Temporal integration is approached using a leap frog scheme with semi implicit correction in combination with an Asselin-Filter (ASSELIN 1972). Horizontally, the finite difference forms of the governing atmospheric equations are written on an Arakawa C-grid where all meteorological variables but the wind components are defined by the centers of the individual grid boxes (KOTLARSKI 2007). The grid center positions are defined by the coordinates of a rotated spherical grid (KOTLARSKI 2007). Rotated coordinate systems are often used in the framework of meteorological simulations to minimize latitudinal distortions by forcing the equator through the model domain. In case of the current model setup, the grid is rotated in such a way that the rotated grid north-pole holds the real geographic coordinates of 162 ° western longitude and 39.25 ° northern latitude.

Following a dynamical downscaling approach (see chapter 1.2.3.1), the RCM is set up in a double nesting technique to successively bridge the gap between the global and the regional scale in a physically based manner (see Fig. 3.5).

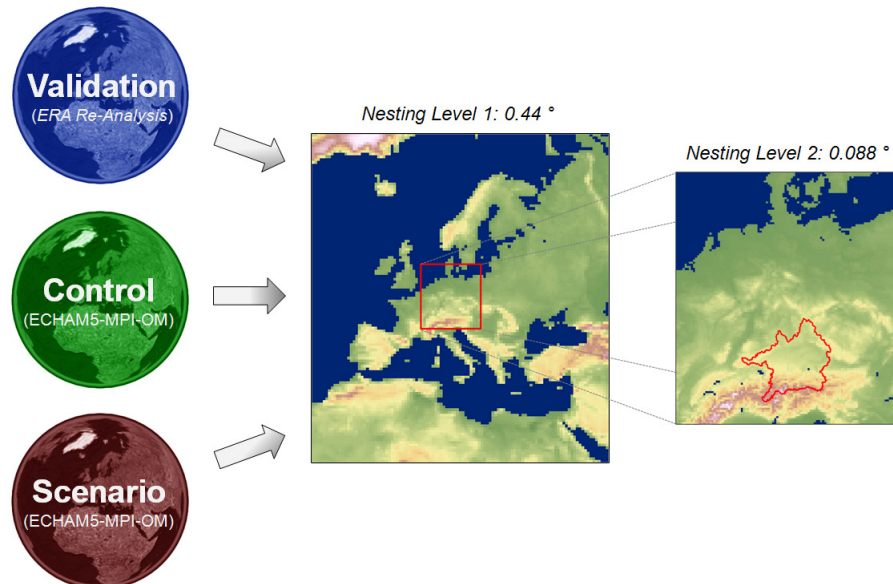


Fig. 3.5: The one-way double nesting model setup used for the REMO simulations. Large scale boundaries are supplied by different data sources.

While also two-way nesting simulations have been set up recently (LORENZ AND JACOB 2005), REMO in the present one-way nesting mode merely updates its meteorological boundaries from large scale simulations every 6 hours without giving any feedback to the global model (JACOB 2001). The process of updating the RCM with the large scale meteorological

boundaries takes place in a relaxation region of 8 grid boxes. In this lateral sponge zone, the prognostic large scale variables (surface pressure, horizontal wind components, specific humidity, temperature and cloud liquid water) are smoothly transmitted into the limited-area model domain following a relaxation scheme proposed by DAVIES (1976). The relaxation zone should not be considered when analyzing the meteorological simulations.

Boundary conditions for the REMO model can be supplied by different data sources (see Fig. 3.5). For the model validation the boundaries have been provided by the ECMWF ERA-15 re-analysis data (GIBSON ET AL. 1999). These so called 'perfect boundaries' allow the best possible model performance, but are naturally constrained to time periods with presence of meteorological observations.

To simulate future climate conditions, the model is forced by global boundaries, provided by the coupled ocean-atmosphere model ECHAM5/MPI-OM (ROECKNER ET AL. 2003). Different emission scenarios (A1B, B1 and A2), defined by the Intergovernmental Panel on Climate Change (IPCC), have been used in scenario runs (2001-2100) to simulate possible future climate conditions (JACOB AND PODZUN 1997, JACOB ET AL. 2001). Still, a reasonable analysis of the climate change signal included in the scenario runs is only possible if a common basis of comparison is ensured.

To clarify the model's capability to statistically reproduce the current climate conditions using GCM boundaries, REMO has been set up for a control run covering the years 1950-2000 with the ECHAM5/MPI-OM forcing the model at the boundaries of the model domain ('REMO Climate of the 20<sup>th</sup> Century Run') (JACOB AND PODZUN 1997, JACOB ET AL. 2001). A comparative analysis between the REMO simulations driven by ECHAM5/MPI-OM in combination with current greenhouse gas concentrations to REMO simulations driven by ECHAM5/MPI-OM in combination with assumed future greenhouse gas concentrations allows the isolation of the climate change signal within the model results. A detailed description of the scenario families together with detailed information about the scenario run used in the present work is given in chapter 6.1 of this work.

Alternatively to the climate mode in which the model is run for the generation of all datasets used in the present work, the model can be set up in a forecast mode. Unlike the forecast mode, the climate mode will not realistically produce a single weather event. As suggested by its denotation, the climate mode only realistically simulates the long term climate (JACOB 2001). Thus, the nesting approach in combination with the climate mode has some important advantages over the forecast mode. The comparatively high spatial resolution of the RCM together with the long run-time of the model in the climate mode allows the development of mesoscale meteorological phenomena that are not resolved by the global model and that are

partly suppressed by the frequent model restarts that are affiliated to the forecast mode (JACOB 2001).

For the utilization within in the GLOWA-Danube project the rotated REMO grid is transformed to a common Lambert Conformal Conic projection, which represents the standard projection used in the project. Fig. 3.6 shows the REMO model domain in the Lambert projection. The REMO model domain is overlapping the Upper Danube watershed without invading the relaxation zone of the 8 boundary REMO grid boxes.

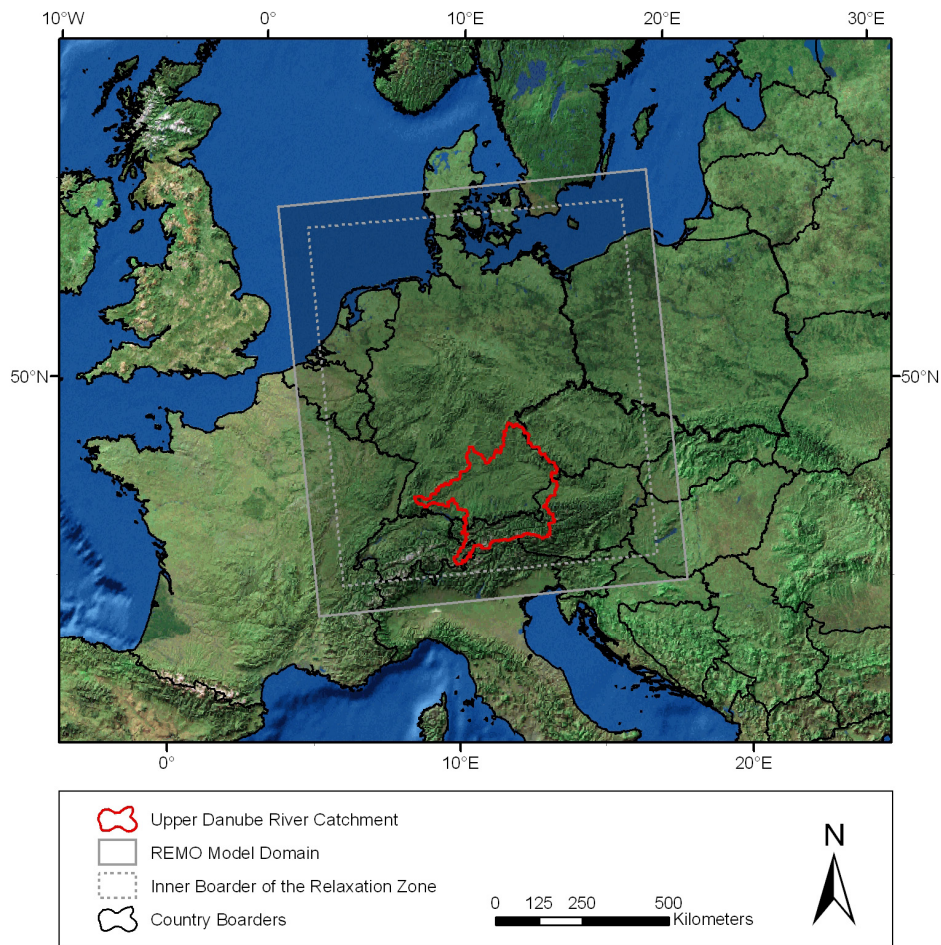


Fig. 3.6: The model domain of the regional climate model REMO together with the Upper Danube watershed representing the model domain of the land surface model PROMET.

While the model was run with a horizontal standard resolution of about 18 x 18 km and 55 x 55 km in the past years, the data used in the present work originate from model runs carried out at an extraordinarily high spatial resolution of approximately 10 x 10 km, which is about the highest spatial resolution that can be achieved using hydrostatic climate models. The applied runs have been conducted in the framework of a cooperative study carried out by the Max-Planck-Institute for Meteorology (MPI-M) and the German Federal Environment Agency (UBA) to analyze future climate change in Germany, Austria and Switzerland.

### 3.3 THE MODEL COUPLING TOOL SCALMET

The coupling tool SCALMET has been developed to perform a synchronized exchange of energy and water fluxes between the models for the land surface and the atmosphere. While the land surface model PROMET describes all processes at a spatial resolution of 1 x 1 km, the simulation of the atmospheric processes in climate models at present is limited to a coarser spatial resolution of at best 10 x 10 km in case of the regional climate model REMO. To bridge the gap between the model scales, adequate scaling techniques have been implemented in the software interface. The scaling methods applied combine direct interpolation methods, also found in conventional couplers, with more sophisticated scaling techniques allowing the consideration of subgrid-scale heterogeneities. As also two-way coupled model runs are to be realized, special techniques have been implemented that conserve mass and energy between the model scales. As reflected in the aim to conserve water and energy fluxes within the remapping process, SCALMET is not pursuing the correction of biases in climate model outputs as it is proposed by various authors (KIDSON AND THOMPSON 1998, MURPHY 1999, WILBY ET AL. 2000). The research carried out in this work, intends to analyze the potential of using present RCM simulations as inputs for the terrestrial models without applying any bias corrections.

The meteorological preprocessor embedded in PROMET is substituted by an interface allowing the import of RCM simulations in the coupled model setup. Additionally an export interface has been established in PROMET, allowing an export of climate relevant land surface simulations to SCALMET, where fluxes are aggregated and exported to the RCM. The temporal exchange rate (coupling frequency) depends on the configuration of the participating model components. While bilateral coupled model runs will probably require higher exchange rates to resolve climate relevant processes in both model components, one-way coupled model runs are set up at a temporal resolution of one hour at present.

For an application inside the GLOWA-Danube project, the technical implementation of SCALMET has to meet the following requirements:

- Transferability to an arbitrary region of interest
- Transferability to an arbitrary regional climate model
- Assurance of validity for future climate conditions
- Optional conservation of mass & energy between the model scales
- Low computational costs

Although all simulation tools emerging from the GLOWA-Danube project are developed, validated and firstly utilized inside the UD, regional transferability should be given as a matter of principle. The rapid development of climate models as well as the scientific request for climate model intercomparison further requires the flexibility of the coupler concerning an application on different RCMs. As the algorithms are to be applied on both, past and future climate conditions, no assumptions should be made that are not valid for future conditions. The conservation of mass and energy states another important requirement for a coupler. Although many authors propose to apply bias corrections in the framework of the downscaling process, which are systematically excluded as soon as fluxes follow conservation laws, the option to conserve fluxes from one grid to the other must be given to prevent model drifts in two-way coupled model runs. Furthermore, the technical implementation of mass and energy conservation within the remapping plays an important role in the process chain of the downscaling techniques (see chapter 4.1.3).

One of the main technical principles in SCALMET is that the meteorological simulations affiliated to a given model time step are spatially distributed at run-time of the coupled model system, which requires a minimization of computational costs. For one-way coupled model runs the fact that data are stored in RCM resolution and are mapped to the LSM resolution for every time step merely reduces storage requirements. For two-way coupled model setups, the interdependence of model results makes the real-time processing of model output an inevitable prerequisite. To minimize computational costs at run-time of the coupled model run, SCALMET precomputes the interpolation weights according to the interpolation algorithm that is chosen by the user in advance of the model run. The methods used for the weight computation originate from the SCRIP interpolation package (JONES 1998a) that can be found in many couplers like for example the OASIS coupler (VALCKE AND REDLER 2006) connecting the MPI-OM and the ECHAM5 model. Once computed, SCALMET writes the weights to file. If a run with the same grid constellation and interpolation configuration is started, the stored weights can be read into memory further reducing computation time.

For the remapping of fluxes between the models, SCALMET needs additional sources of information. The user has to provide several remapping parameters in form of an ASCII input file (see Fig. 3.7). An example parameter input file is given in the appendix (see A-4). Beside these inputs, SCALMET needs spatially distributed information on the underlying topography in both, RCM and LSM grid resolution. Further, a mask in LSM resolution needs to be supplied defining the grid area for which total mass and energy conservation between the involved grids should be guaranteed (see chapter 4.1.4). Optionally, a mask in RCM resolution can be provided to limit the regression analysis on a certain RCM grid area (see chapter 4.1.2).

The computation of the interpolation weights as well as some of the methods applied in the framework of the implemented scaling techniques further require the exact coordinates for the pixel centers and pixel corners for both grids involved. While the land surface model PROMET operates on the Lambert Conformal Conic Coordinates System, atmospheric grids vary depending on the RCM used. The regional climate model REMO for example uses a rotated coordinate system which implies coordinate transformations between the models for the land surface and the atmosphere (see chapter 3.2). Fig. 3.7 gives an overview of the different inputs and outputs of the coupling tool.

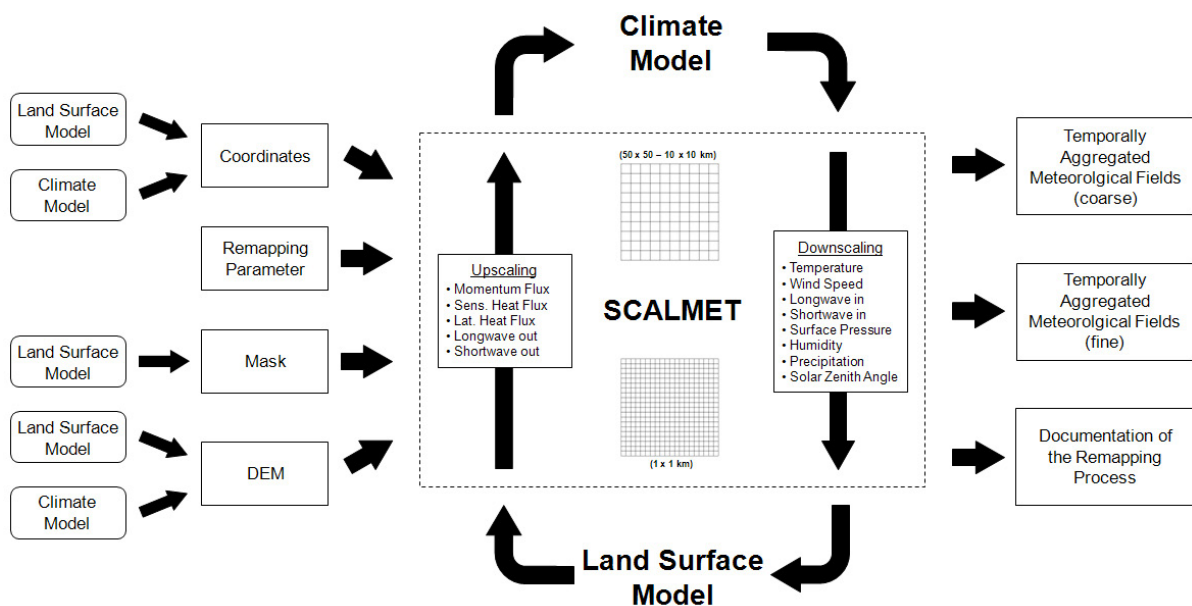


Fig. 3.7: Schematic diagram of the coupled model system together with the inputs needed for the remapping in SCALMET (left) and the outputs optionally given out by the coupler (right).

Apart from the exchange of meteorological data with the atmospheric model and the land surface model, SCALMET provides the option to store the remapping results as well as the climate model meteorology in a user defined temporal aggregation (daily, monthly or yearly mean/sum).

## 4 THE SCALING OF METEOROLOGICAL VARIABLES IN SCALMET

### 4.1 GENERAL DOWNSCALING PRINCIPLES IN SCALMET

SCALMET includes different approaches to bridge the gap between the model scales. Direct interpolation techniques (see chapter 4.1.1) in combination with more sophisticated downscaling techniques (see chapter 4.2) have been implemented in the software interface to adequately scale RCM simulations. Allowing the consideration of subgrid-scale heterogeneities, the latter try to compensate the loss of climatic variability, that is systematically caused by the coarse representation of topography in climate models (FRÜH ET AL. 2006). As can be seen in Fig. 4.1, especially in mountainous regions with steep climate gradients, a coarse spatial resolution does not allow to fully capture environmental variability.

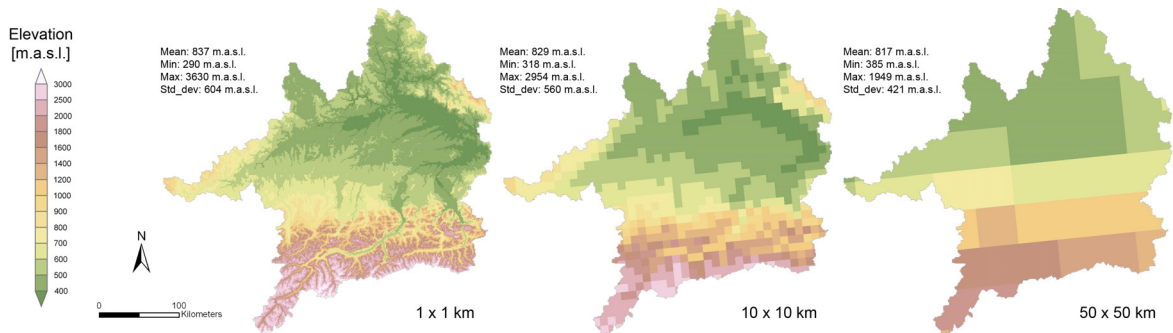


Fig. 4.1: Representation of topography in the Upper Danube watershed at different spatial resolutions (1 x 1 km (left) 10 x 10 km (middle) and 50 x 50 km (right)).

The decrease in spatial resolution pictured in Fig. 4.1 moreover goes together with an increasingly flattened topography. The result is a local height discrepancy between the real orography and that used within the RCM, leading to a discrepancy between the observed and modeled meteorology (DALY ET AL. 1994, FRÜH ET AL. 2006).

To compensate the loss of climatic variability in RCM outputs, different quasi-physically based methods have been implemented in SCALMET. Although the different techniques can be arbitrarily combined, they are divided into the following categories for a detailed description in the framework of this work:

- Direct interpolation methods
- Regression based remapping
- Submodel approach (e.g. shortwave radiation submodel)

Although the regression based remapping could generally be denoted as a submodel as well, the approaches are treated separately as the processing chains slightly differ. Technical details are given in chapter 4.1.2 and 4.1.3. The following paragraphs describe the direct interpolation techniques in SCALMET.

#### 4.1.1 DIRECT INTERPOLATION METHODS

The coupling tool SCALMET includes a roundup of direct interpolation algorithms such as inverse distance or bilinear interpolation methods. Beyond these techniques, a conservative remapping method is implemented. The method assures conservation of mass and energy when meteorological fields are directly interpolated between different model scales (JONES 1998b). Since direct interpolation methods do not compensate the loss of climatic variability caused by a coarse RCM topography, these algorithms only produce satisfying results in combination with high resolution climate data or in flat terrain. However direct interpolation algorithms constitute essential parts in the remapping processes described in the later course of this work. Unless otherwise indicated, the interpolation methods described below are based on JONES (1998a).

##### 4.1.1.1 INVERSE DISTANCE WEIGHTED INTERPOLATION

The inverse distance weighted (IDW) method is a rather simple but computationally efficient interpolator. An arbitrary destination grid value is determined as a function of the distance between the considered cell itself and a given number of surrounding source grid cells. The distance between two cells is determined by the differences in the geographical coordinates of the pixel centers. The angular distance  $d$  is calculated as

$$d = \cos^{-1}(\cos\varphi_d \cos\varphi_s (\cos\lambda_d \cos\lambda_s + \sin\lambda_d \sin\lambda_s) \sin\varphi_d \sin\varphi_s) \quad \text{Eq. 4.1}$$

where  $\varphi_d$  and  $\varphi_s$  are the latitudes and  $\lambda_d$  and  $\lambda_s$  are the longitudes of the destination grid cells and source grid cells respectively. The larger the angular distance, the smaller is the influence a source grid cell has on the output value. The number of neighboring source grid cells to be considered is user defined. Studies by WEBER AND ENGLUND (1994) showed that inverse distance estimators are very sensitive to the type of data, to the number of neighbors considered and to the power of distance chosen for the weighting. The approach presented by JONES (1998a) therefore has been enhanced allowing a linear, quadratic and cubic weighting of the angular distance.

Applying a linear distance function the weights for all considered source grid cells can be calculated as:

$$\omega = \frac{1/(d + \kappa)}{\sum_n^{N_{neighbors}} (1/d_n + \kappa)} \quad \text{Eq. 4.2}$$

- with:
- $\omega$  = Weight for a given neighboring source grid cell
  - $N_{neighbors}$  = Number of neighbors considered
  - $d$  = Angular distance
  - $\kappa$  = Small number to prevent zero divisions

To minimize computational costs, distance is not computed between every destination grid cell and every source grid cell. Instead, the search for the nearest neighbors is narrowed by dividing the participating grids into latitude bins. Only those source grid cells located in the same latitude bin (e.g. between 40 and 41 °) are considered in the process of finding the nearest neighbors.

#### 4.1.1.2 BILINEAR INTERPOLATION

The bilinear interpolation scheme implemented in SCALMET uses a local bilinear approximation to determine interpolated values for a point in a quadrilateral grid. Just like the IDW interpolator, the bilinear interpolation method (BI) calculates the value for a given destination grid cell as a weighted average of the surrounding source grid cells. Before the value for a given destination grid point  $P_x$  can be computed, the algorithm has to check which four source grid centers are located next to point  $P_x$  (see Fig. 4.2).

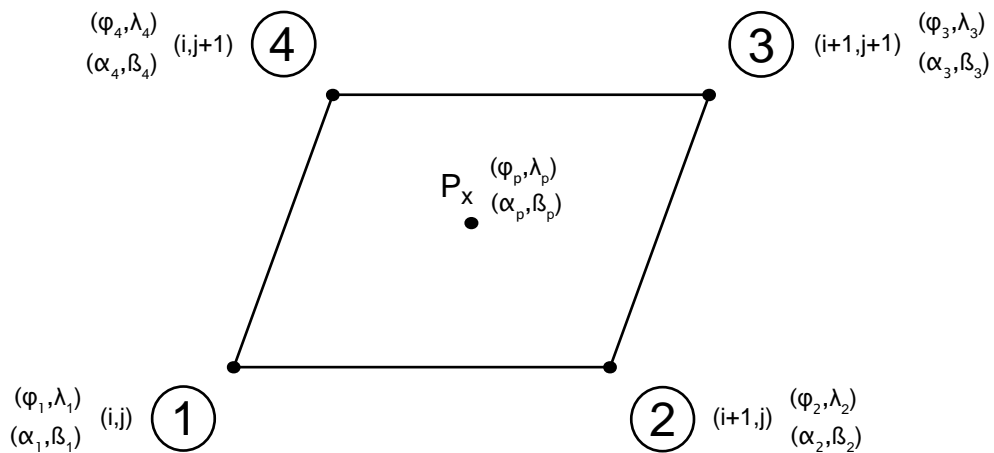


Fig. 4.2: The general quadrilateral grid structure of the bilinear interpolation process.

The point  $P_x$  in Fig. 4.2 is surrounded by four source grid centers, each characterized by their geographical coordinates  $(\varphi, \lambda)$  as well as their continuous local coordinates  $(\alpha, \beta)$ . Assigning point 1 the logical coordinates (0,0), the logically-rectangular i-j-grid structure shown in Fig. 4.2 returns a logical grid coordinate for all points in form of (1,0) at point 2, (1,1) at point 3 and (0,1) at point 4.

If the logical coordinates  $(\alpha_p, \beta_p)$  of point  $P_x$  were known, the function  $(f_p)$  at point  $P_x$  could be approximated as:

$$f_p = (1 - \alpha_p)(1 - \beta_p)f(i, j) + \alpha_p(1 - \beta_p)f(i + 1, j) + \alpha_p\beta_p f(i + 1, j + 1) + (1 - \alpha_p)\beta_p f(i, j + 1) \quad \text{Eq. 4.3}$$

$$= \omega_1 f(i, j) + \omega_2 f(i + 1, j) + \omega_3 f(i + 1, j + 1) + \omega_4 f(i, j + 1)$$

The geographical coordinates  $(\varphi_p, \lambda_p)$  of point  $P_x$  are known and can be expressed as:

$$\varphi_p = (1 - \alpha_p)(1 - \beta_p)\varphi_1 + \alpha_p(1 - \beta_p)\varphi_2 + \alpha_p\beta_p\varphi_3 + (1 - \alpha_p)\beta_p\varphi_4 \quad \text{Eq. 4.4}$$

$$\lambda_p = (1 - \alpha_p)(1 - \beta_p)\lambda_1 + \alpha_p(1 - \beta_p)\lambda_2 + \alpha_p\beta_p\lambda_3 + (1 - \alpha_p)\beta_p\lambda_4 \quad \text{Eq. 4.5}$$

The nonlinear character of Eq. 4.4 and Eq. 4.5 requires an iteration process to determine the logical coordinates needed to calculate the weights. The equations can be differentiated to:

$$\begin{pmatrix} \delta\varphi_p \\ \delta\lambda_p \end{pmatrix} = A \begin{pmatrix} \delta\alpha_p \\ \delta\beta_p \end{pmatrix} \quad \text{Eq. 4.6}$$

with:

$$A = \begin{pmatrix} (\varphi_2 - \varphi_1) + (\varphi_1 - \varphi_4 + \varphi_3 - \varphi_2)\beta_p & (\varphi_4 - \varphi_1) + (\varphi_1 - \varphi_4 + \varphi_3 - \varphi_2)\alpha_p \\ (\lambda_2 - \lambda_1) + (\lambda_1 - \lambda_4 + \lambda_3 - \lambda_2)\beta_p & (\lambda_4 - \lambda_1) + (\lambda_1 - \lambda_4 + \lambda_3 - \lambda_2)\alpha_p \end{pmatrix} \quad \text{Eq. 4.7}$$

The inversion of this equation system returns the two equations needed for the iteration of the local coordinates  $(\alpha_p, \beta_p)$ :

$$\delta\alpha_p = \begin{vmatrix} \delta\varphi_p & (\varphi_4 - \varphi_1) + (\varphi_1 - \varphi_4 + \varphi_3 - \varphi_2)\alpha_p \\ \delta\lambda_p & (\lambda_4 - \lambda_1) + (\lambda_1 - \lambda_4 + \lambda_3 - \lambda_2)\alpha_p \end{vmatrix} \div \det(A) \quad \text{Eq. 4.8}$$

$$\delta\beta_p = \begin{vmatrix} (\varphi_2 - \varphi_1) + (\varphi_1 - \varphi_4 + \varphi_3 - \varphi_2)\beta_p & \delta\varphi_p \\ (\lambda_2 - \lambda_1) + (\lambda_1 - \lambda_4 + \lambda_3 - \lambda_2)\beta_p & \delta\lambda_p \end{vmatrix} \div \det(A) \quad \text{Eq. 4.9}$$

Initializing  $\alpha_p$  and  $\beta_p$  with values of zero, Eq. 4.8 and Eq. 4.9 can be repeatedly resolved until  $\delta\alpha_p$  and  $\delta\beta_p$  are appropriately small. For simple latitude-longitude grids, the iteration converges in the first iteration. Iterated values for  $\alpha_p$  and  $\beta_p$  can finally be utilized to calculate the interpolation weights following Eq. 4.3.

#### 4.1.1.3 CONSERVATIVE INTERPOLATION

The conservation of energy, mass and momentum is a fundamental concept of physics. In coupled model systems it is indispensable to transfer heat and water fluxes between the model components in an accurate and conservative manner in order to maintain the energy and water budgets of the coupled climate system. The conservative interpolation method used in SCALMET, hereinafter referred to as the CI, is based on JONES (1998b). It is accurate up to second-order and conservative to machine accuracy. Unlike other conservative remapping methods, the approach is completely general and allows an application on any type of grid on a sphere. While for the spatial interpolation within both, the bilinear and the IDW approach the distance between the cell centers is used within the remapping process, the conservative interpolation method described below determines the pixel values according to the overlapping area of source and destination grid cells. Hence, the coordinates of the pixel corners, which mark out the pixel area, rather than the pixel's centers are the determinant interpolation criteria within the conservative approach.

To meet the requirements of conservation, a flux computed for an arbitrary destination grid cell (k) must satisfy:

$$\bar{F}_k = \frac{1}{A_k} \int_{A_k} f dA \quad \text{Eq. 4.10}$$

with:  $\bar{F}_k$  = Area averaged flux at destination cell k  
 $f$  = Flux at a source grid cell  
 $A_k$  = Area of the destination grid cell k

As the integral in Eq. 4.10 is over the area of the destination grid cell, only those source grid cells that are at least partly covered by the destination grid cell (k) contribute to the destination grid value. For the destination grid cell overlapping L source grid cells the equation can be written as

$$\bar{F}_k = \frac{1}{A_k} \sum_{l=1}^L \int_{A_{lk}} f_l dA \quad \text{Eq. 4.11}$$

- with:
- $\bar{F}_k$  = Area averaged flux at destination cell k
  - $f_l$  = Flux at source grid cell l
  - $A_k$  = Area of the destination grid cell k
  - $A_{lk}$  = Area of the source grid cell l covered by the destination cell k
  - $L$  = Number of source grid cells overlapped by k

To compute the overlapping cell areas, the algorithm searches the exact location of the end point of a segment and then the next intersection with the other grid. Dependent on the grid cells that are associated with the considered subsegment, the integrals can be computed and summed.

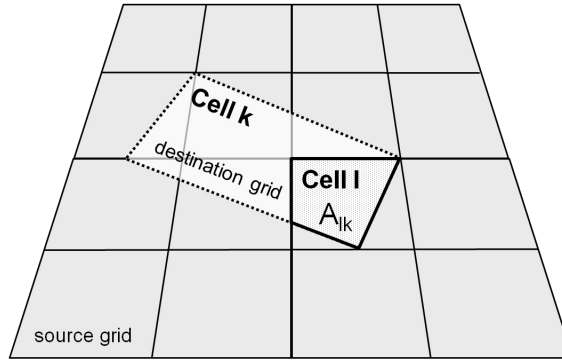


Fig. 4.3: Example of two overlapping quadrilateral grids. Destination grid cell k overlaps source grid cell l over the area of  $A_{lk}$ .

Assuming a constant source grid value  $f_l$  over the whole grid cell, this first order conservative remapping scheme equals an area-weighted interpolation. Unfortunately this assumption is a very poor approximation for fields with high spatial frequency making the first order conservative interpolation less accurate than bilinear methods. Note that accuracy here relates to the ability to interpolate between two data points. Yet, the conservative character as well as the low computational costs, make the first order conservative Interpolation the standard interpolation scheme used in coupled model systems whenever energy and mass have to be conserved (JONES 1998b). The introduction of a constant gradient in x- and y-direction for each source grid cell extends the method to a second order conservative Interpolation scheme. The remapping equation then takes the form of

$$\bar{F}_k = \sum_{l=1}^L \left[ \bar{f}_l \omega_{1lk} + \left( \frac{\partial f}{\partial \varphi} \right)_l \omega_{2lk} + \left( \frac{1}{\cos(\varphi)} \frac{\partial f}{\partial \lambda} \right)_l \omega_{3lk} \right] \quad \text{Eq. 4.12}$$

where  $\varphi$  and  $\lambda$  represent geographical latitude and longitude respectively and the weights  $\omega_{1lk}$ ,  $\omega_{2lk}$  and  $\omega_{3lk}$  are calculated as:

$$\omega_{1lk} = \frac{1}{A_k} \int_{A_{lk}} dA \quad \text{Eq. 4.13}$$

$$\omega_{2lk} = \frac{1}{A_k} \int_{A_{lk}} (\varphi - \varphi_l) dA = \frac{1}{A_k} \int_{A_{lk}} \varphi dA - \frac{\omega_{1lk}}{A_l} \int_{A_l} \varphi dA \quad \text{Eq. 4.14}$$

$$\omega_{3lk} = \frac{1}{A_k} \int_{A_{lk}} \cos(\varphi)(\lambda - \lambda_l) dA = \frac{1}{A_k} \int_{A_{lk}} \lambda \cos(\varphi) dA - \frac{\omega_{1lk}}{A_l} \int_{A_l} \lambda \cos(\varphi) dA \quad \text{Eq. 4.15}$$

The second order weights calculated above are an area-weighted distance from the source cell centroid. As the remapping from fine grids to coarse grids represents an averaging process, the calculation of gradients is not advantageous in case of this remapping direction. The gradient components average to zero, when an averaging over the entire source grid cell is performed. The disadvantage of the second order conservative remapping is that the additional computation of gradients increases computational costs by a factor of 3 (JONES 1998b). Gradients for meteorological fields have to be calculated using the neighboring source grid cells. For fields showing strong gradients, numerical approximations to the gradient may be too steep, so that the expected value might even be overshoot. This can be prevented by limiting the gradients. For the remapping of fields with high spatial frequency using constant gradients for each source grid cell however poorly enhances the remapping accuracy. As a consequence of the increased computational costs in combination with the questionable benefit, the second order conservative scheme is not applied within the presented study, although it has been implemented in SCALMET. Instead, the first order conservative remapping scheme, which for the further course of this work will be referred to as the CI technique, will be used to conservatively transfer fluxes between the model scales.

#### 4.1.1.4 METHOD DISCUSSION

Three different interpolation methods that are used in SCALMET have been described above. Since these methods only consider the spatial relationships among the grid cells, they do not compensate the loss of climatic variability caused by a coarse RCM topography (see Fig. 4.4). Moreover, the values at a certain destination grid cell are never smaller than the minimum or greater than the maximum of the surrounding source grid cells, resulting in a smoothed representation of the source grid values. While all of these methods perform similar in the flat terrain of the Alpine Foreland, the high-frequent temperature changes in the complex terrain of the Alps is considerable smoothed, in particular in case of the IDW

method. The direct interpolation algorithms presented above, therefore only produce satisfying results in combination with high resolution climate data or in flat terrain (LISTON AND ELDER 2006, MARQUÍNEZ ET AL. 2003, MARKE AND MAUSER 2008).

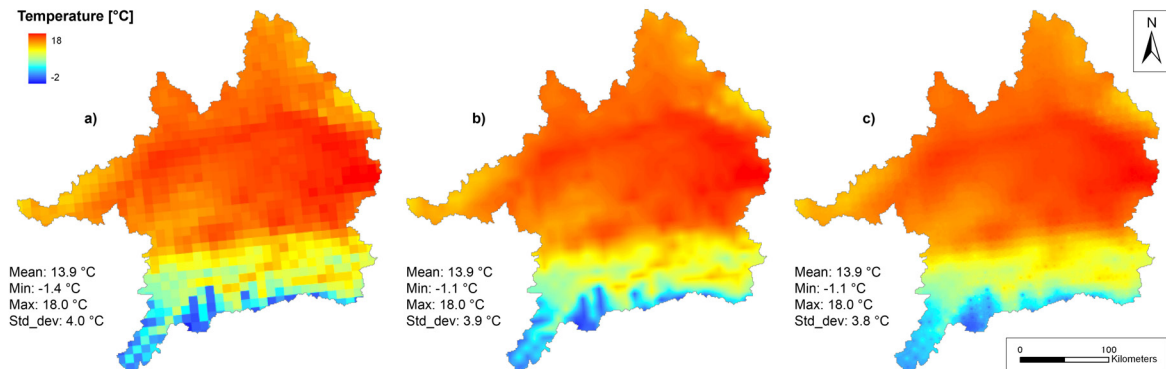


Fig. 4.4: Directly interpolated REMO control run temperature using the conservative (a), bilinear (b) and inverse distance weighted interpolation scheme (c). In case of the c) 4 neighboring grid cells have been regarded linearly weighting the distance between the grid cell centers (based on REMO simulations for May 17<sup>th</sup>, 1982 (6 p.m.)).

In SCALMET, direct interpolation techniques rather represent important components of the remapping process, than solely applied techniques for the spatial distribution of meteorological simulations. The methods described are accompanied by more sophisticated approaches to adjust the different meteorological variables beyond the possibilities of direct interpolation methods.

#### 4.1.2 REGRESSION BASED REMAPPING

Many meteorological variables strongly vary with elevation (OKE 1987, BARRY AND CHORLEY 1987). This climate-elevation dependence can be found in both, meteorological measurements and simulations. The fact that elevation data are globally available at much higher spatial resolutions than climate data makes elevation an excellent statistical predictor variable for the generation of meteorological distributions (DALY ET AL. 2002).

Similar to an approach proposed by MAUSER AND BACH (2008) to spatially distribute meteorological observations, SCALMET gives the option to analyze the elevation dependence of a meteorological parameter during the run-time of the coupled model system for each single time step. Within this process, the mathematical function is determined that most closely describes the relationship between the simulated meteorological variable and the associated elevation. It should be noted, that due to the fact that RCMs simulate mean conditions for the area covered by a model pixel, this functional relationship is based on mean meteorological conditions and mean terrain elevation in the spatial resolution of the

RCM as well. Although SCALMET is technically capable of performing nonlinear regressions, the regression function is, following recommendations of DALY ET AL. (2002), constrained to a linear functional description of the parameter-elevation dependence for the following reasons:

- Climate-elevation dependence is often linear or can be converted to proximate linearity (HIBBERT 1977, HANSON 1982, OSBORN 1984, VUGLINSKI 1972)
- a linear function allows a stable extrapolation far beyond the elevations of the database (DALY ET AL. 2002)
- a similar (linear) treatment of all meteorological variables decreases the risk of inconsistencies arising from the interaction of meteorological variables (e.g. temperature-humidity)

The linear model may be written as

$$y = a + bx + \epsilon \quad \text{Eq. 4.16}$$

where  $y$  is the dependent variable,  $x$  is the independent variable,  $a$  and  $b$  are parameters and  $\epsilon$  is a random error variate (residual). Only in case of a perfect relationship  $\epsilon$  will be zero and all  $y$  can be perfectly well estimated using values of  $x$ . Of course this will rarely occur as we are dealing with a statistical and not a precise mathematical relationship between the analyzed variables.

A common approach to estimate the parameters  $a$  and  $b$  is the least squares technique. After these parameters are determined, the regression function can be expressed as

$$\hat{y} = a_{est} + b_{est}x \quad \text{Eq. 4.17}$$

where  $\hat{y}$  is the predicted value of the dependent variable  $y$ ,  $x$  is the independent (predictor) variable and  $a_{est}$  and  $b_{est}$  are the estimates of  $a$  and  $b$  respectively. For linearly related, normally distributed data, the least square method assures the determination of the best-fitting curve.

Unlike many continuous variables, hourly and daily rainfall show a frequency distribution function that is often positively skewed and leptokurtic due to its lower boundary of zero and the strong presence of precipitation values near that natural boundary (LETTENMAIER 1995, VON STORCH AND ZWIERS 1995). Also a transformation to a Gaussian distribution in advance of the regression process is technically feasible, the frequent occurrence of near zero rainfall amounts make a transformation very problematic in case of precipitation (ZORITA AND VON

STORCH 1999, COHN ET AL. 1989). To widen the applicability of the regressive approach on not normally distributed data, the ordinary least square approach in SCALMET is accompanied by a distribution free regression approach. The method draws back on THEIL (1950) and was reviewed by SEN (1968) and PEGORARO (1991). It is median based and thus insensitive to outliers. While the Theils-method is slightly less powerful compared to the least squares approach when the data meet all assumptions of normality, it allows a much better estimate of slope and intercept of the regression line when the distribution is not Gaussian or data are auto-correlated (HELSELAND HIRSCH 1992, HUSSIAN AND SPRENT 1983, DIETZ 1987). The choice of the regression method (parametric-nonparametric) depends on the frequency distribution of the data, which is tested using a Kolmogorov-Smirnov test (KOLMOGOROV 1933, SMIRNOV 1933). Since the pixel values simulated by the meteorological models are samples originating from a larger statistic population, the significance of the relationship between  $x$  and  $y$  needs to be further investigated. Following recommendations of various authors, two statistic significance tests are conducted within the regression analysis (BAHRENBERG ET AL. 1999, SCHÖNWIESE 2000, KING 1969).

One test investigates the significance of the regression function by checking if the regression coefficient  $b_{est}$  is significantly different from 0. According to conventional definitions, a significance level  $\alpha = 5\%$  is used for the rejection of the null hypothesis ( $H_0: b_{est} = 0$ ). The significance level  $\alpha$  represents the probability of making the decision to reject the null hypothesis although it is actually true.

A second test analyzes the significance of the correlation between the meteorological variable and elevation by testing whether the coefficient of correlation is significantly different from 0 or not. While the traditional Pearson product-moment coefficient  $R_p$  is used for normally distributed data, the Kendall rank order coefficient  $R_k$  is used in case of significant deviations from the Gaussian distribution function. Unlike  $R_p$ , the Kendall coefficient is a distribution-free statistical measure of correlation (SCHÖNWIESE 2000). Correlation is determined by computing the number of concordant and discordant changes within the two data sets. The Kendall coefficient  $R_k$  is calculated as

$$R_k = \frac{[2(N_c - N_d)]}{n(n - 1)} \quad \text{Eq. 4.18}$$

where  $N_c$  and  $N_d$  are the number of concordances and discordances found in the data and  $n$  is the total sample size (SCHÖNWIESE 2000). The coefficient takes values of -1 for only discordant changes, of +1 for only concordant changes in the data and a value of 0 if concordances and discordances are equally presented in the data.

The significance is tested again using a significance level of  $\alpha = 5\%$  for the rejection of the null hypothesis ( $H_0: R_k = 0$ ). For a more detailed description of the significance tests performed refer to SCHÖNWIESE (2000).

As proposed by DALY (2002), the data are spatially interpolated whenever no significant relation between a meteorological variable and terrain elevation can be determined for a given time step.

If the significance tests confirm a significant relationship between a climate model simulation  $y_{clim}$  and climate model elevation  $z_{clim}$ , the regression function allows the computation of a value  $\hat{y}_{clim}$  in the spatial resolution of the RCM as a function of climate model elevation  $z_{clim}$  in form of:

$$\hat{y}_{clim} = a_{est} + b_{est}z_{clim} \quad \text{Eq. 4.19}$$

The same coefficients  $a_{est}$  and  $b_{est}$  can be used to calculate a value ( $\hat{y}_{ls}$ ) for the considered meteorological variable for every grid cell at the spatial resolution of the LSM using land surface model elevation ( $z_{ls}$ ):

$$\hat{y}_{ls} = a_{est} + b_{est}z_{ls} \quad \text{Eq. 4.20}$$

As the derived function will not be able to reproduce the exact value the RCM simulated for each grid box, the algorithm produces a residual ( $r_{clim}$ ) for every climate model grid box in form of:

$$r_{clim} = y_{clim} - \hat{y}_{clim} \quad \text{Eq. 4.21}$$

To account for these local differences between the climate model simulations ( $y_{clim}$ ) and the calculated values ( $\hat{y}_{clim}$ ), the residuals ( $r_{clim}$ ) are horizontally interpolated to the land surface grid. The interpolated residuals ( $r_{ls}$ ) can be used to correct the calculated subgrid-values ( $\hat{y}_{ls}$ ). A subgrid value ( $y_{ls}$ ) can finally be computed as:

$$y_{ls} = \hat{y}_{ls} + r_{ls} \quad \text{Eq. 4.22}$$

The single steps in the process chain of the regression based remapping are illustrated in Fig. 4.5. As can be seen, the regression based remapping produces high resolution meteorological fields that largely preserve the conditions predetermined by the coarse grid meteorological input data. The latter is well explicable considering the fact that correcting the calculated values  $\hat{y}_{ls}$  by the interpolated residuals  $r_{ls}$  forces the remapped fields through the simulations at the grid cell centers.

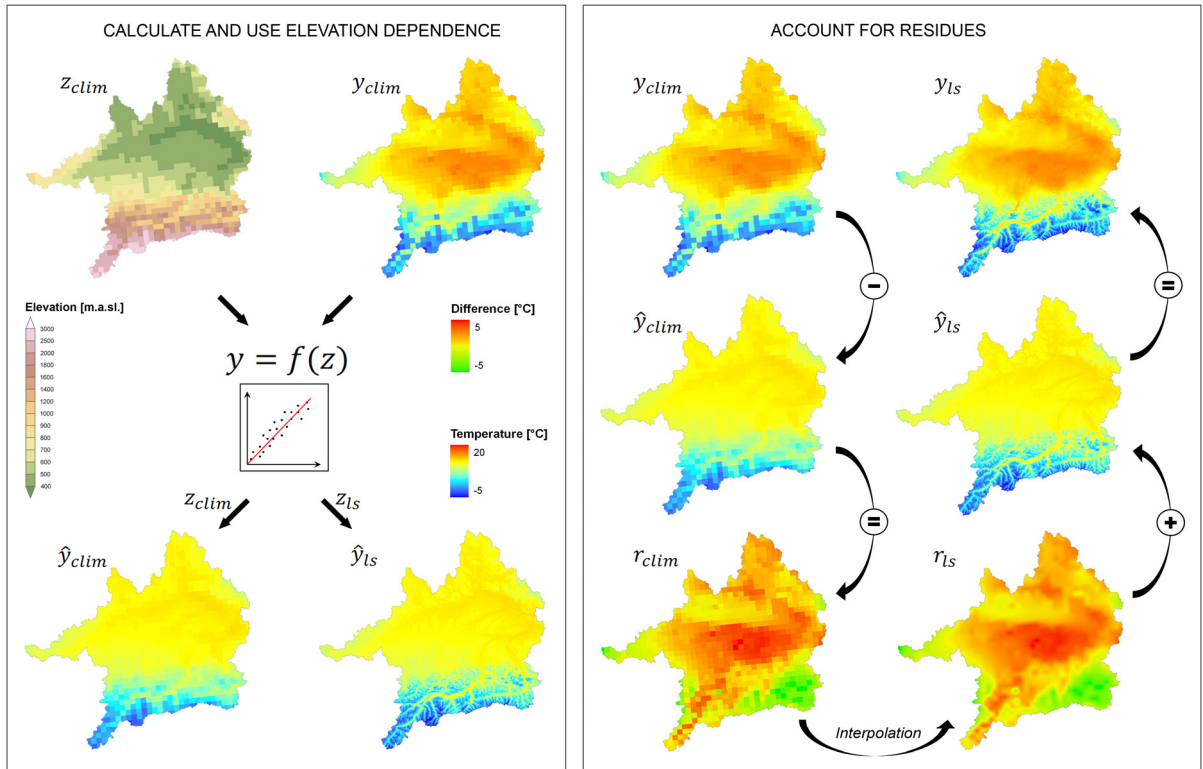


Fig. 4.5: The different steps in the process chain of the regression based scaling approach shown by the example of temperature remappings.

#### 4.1.3 SUBMODEL APPROACH

The different submodels in SCALMET include further approaches based on elevation corrections but also techniques that allow subscale adjustments for those meteorological variables that are poorly predictable on the basis of elevation information only. Shortwave radiation for example is known to increase with altitude due to a decreasing thickness of the atmosphere above but its temporal and spatial distribution is largely determined by other topographic features than elevation (e.g. slope, aspect).

To distribute these parameters in physically realistic ways, several submodels have been implemented in SCALMET that will be described in detail in chapter 4.2 (e.g. wind model, longwave and shortwave radiation model). Similar to the dynamical downscaling methods described in chapter 1.2.3.1, the submodels compute meteorological distributions within the domain of the RCM. In this process, subscale information as well as the meteorological boundaries provided by the RCM are taken into account to compute a value  $\hat{y}_{ls}$  for a considered meteorological variable and all cells within the model domain.

As the mean meteorological conditions are predetermined by the RCM simulations, the destination grid values underlying a given climate model pixel  $n_{clim}$  need to be corrected by the associated climate model pixel value  $y_{clim}$ .

To calculate the correction term, all destination grid values that are fully or partly overlapped by pixel  $n_{clim}$  are conservatively remapped to the coarse resolution of the climate model. The mass/energy overrun or deficit  $\Delta y_{clim}$  in climate model resolution can be expressed as

$$\Delta y_{clim} = y_{clim} - \bar{y}_{ls} \quad \text{Eq. 4.23}$$

with  $\bar{y}_{ls}$  representing the mean conditions over the underlying land surface pixel calculated within the conservative remapping process.

Analogously to the residuals in the regression approach,  $\Delta y_{clim}$  is spatially interpolated from the coarse resolution of the atmosphere to the finer spatial resolution of the land surface grid. The interpolated mass/energy overrun or deficit  $\Delta y_{ls}$  is then used to correct the submodel calculations  $\hat{y}_{ls}$  in form of

$$y_{ls} = \hat{y}_{ls} + \Delta y_{ls} \quad \text{Eq. 4.24}$$

where  $y_{ls}$  is the corrected land surface pixel value. Fig. 4.6 shows the different steps of the submodel remapping process.

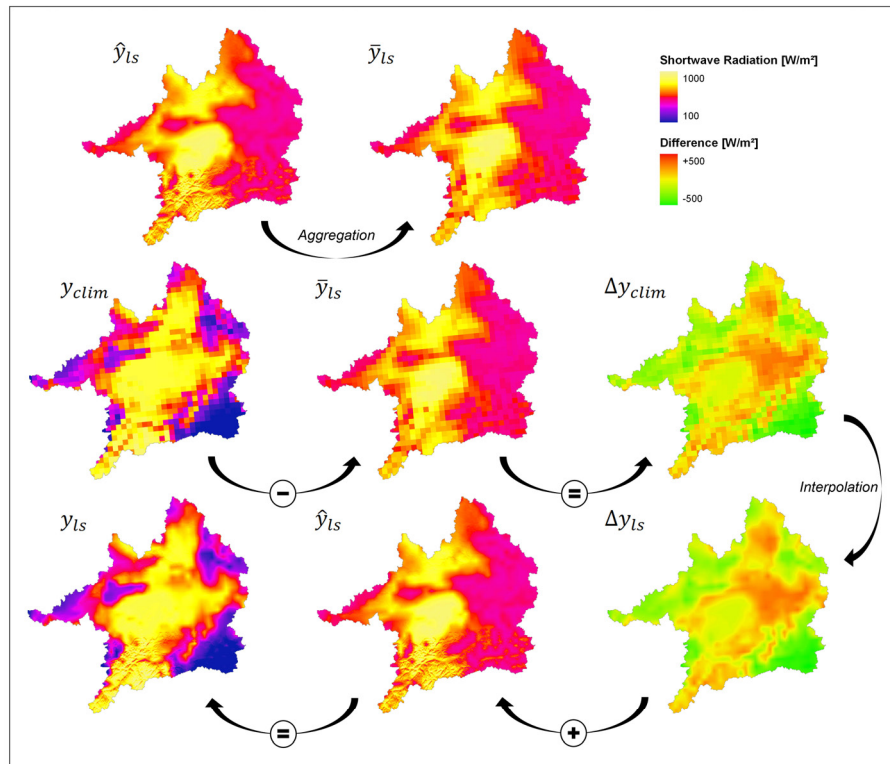


Fig. 4.6: The different steps in the process chain of the submodel approach shown by the example of shortwave radiation.

#### 4.1.4 CONSERVATION OF MASS AND ENERGY BETWEEN THE MODEL SCALES

The conservative interpolation method described in chapter 4.1.1.3 systematically assures the conservation of mass and energy between the model scales. Yet, as soon as subgrid scale adjustments are carried out, the conservation of mass and energy is not necessarily given. Even in the case of the submodel approach, where the subgrid adjusted land surface grid values are realigned to the RCM simulations, conservation of mass and energy between the climate model grid and the underlying land surface grid is not given for those cases where non-conservative spatial interpolators (IDW or BI) have been applied for the interpolation of the energy/mass deficit or overrun  $\Delta y_{ls}$  (see chapter 4.1.3). While using the CI for the interpolation of  $\Delta y_{ls}$  would result in a conservative treatment of fluxes, it is unfortunately connected to optical flaws (see chapter 4.1.1.3). To combine the optical advantages of non-conservative remapping methods with the conservative treatment of fluxes given by the CI, the non-conservative interpolations performed in the regression model or the quasi-physically based submodels are accompanied by further processing steps.

In a first step, the remaining minor differences between the mean conditions of the remapped fields and the associated RCM pixels are calculated according to Eq. 4.23. The flux difference  $\Delta y_{clim}$  in a next step is conservatively interpolated from the RCM resolution to the spatial resolution of the LSM using the CI. The interpolated difference  $\Delta y_{ls}$  is then used to correct the land surface grid values following Eq. 4.24.

Processing the remapped data as described above works satisfactorily well for most meteorological variables but reaches its limits whenever a meteorological variable is characterized by a natural boundary of zero (e.g. precipitation). Whenever these variables are corrected in such a way that this natural boundary is under-run, the respective value needs to be set to zero and mass and energy conservation are consequently not fully given. Although this mass or energy overrun/deficit is extremely small in most cases, further data processing is required to fully conserve fluxes between the model scales. In these final processing steps, the whole destination grid area or a masked out area of interest (AOI) (e.g. watershed) is used as the basis for conservation. The total mass/energy to be distributed on the considered AOI is determined by using the CI to conservatively remap the meteorological simulations to the destination grid and by computing the sum  $Y_{AOI\_cons}$  of all conservatively remapped destination grid values included in the considered AOI. Comparing the computed mass/energy budget to the sum of all subgrid adjusted destination grid values  $Y_{AOI\_adj}$  within the same AOI returns the mass/energy overrun or deficit  $\Delta Y_{AOI}$  given by:

$$\Delta Y_{AOI} = Y_{AOI\_cons} - Y_{AOI\_adj} \quad \text{Eq. 4.25}$$

A final correction is carried out for each destination grid cell in form of

$$y_{ls\_AOIcor} = y_{ls} + f_{AOI} \Delta Y_{AOI} \quad \text{Eq. 4.26}$$

where  $y_{ls\_AOIcor}$  is the mass/energy budget corrected destination grid value and  $f_{AOI}$  is the fractional contribution of a considered destination grid cell to the mass/energy budget  $Y_{AOI\_adj}$  given by:

$$f_{AOI} = \frac{y_{ls}}{Y_{AOI\_adj}} \quad \text{Eq. 4.27}$$

Besides the approach described above, SCALMET gives the option to conceptually pursue mass and energy conservation rather for a predefined area of interest than for every individual RCM pixel. This implies that mass and energy could generally be transferred between neighboring grid cells, while at the same time the conservation of mass and energy for a the AOI inside the model domain is not violated. Practically, this option could be of interest in the distribution of precipitation across the land surface grid. In its current version, REMO does not include an advection of falling rain. Hence, the regional climate model does not allow water leaving the upper atmosphere in form of precipitation to be drifted by wind. The water reaches the surface in the same atmospheric model column it originated from. On top of that, the coarse representation of topography in RCMs leads to a systematic displacement of orographic rain which could be compensated by disregarding the conservation of mass and energy on a pixel basis. However it is not quite clear at present in how far shifting mass or energy is applicable in two-way coupled model runs. Hence, the option to conceptually conserve mass and energy rather on the basis of a user defined area than for each climate model pixel is not further pursued in the framework of this work.

## 4.2 DOWNSCALING THE INDIVIDUAL METEOROLOGICAL VARIABLES

The general downscaling principles in SCALMET have been described in the preceding chapters. The following covers the specific scaling options that are available for the remapping of each meteorological variable and give detailed information on the procedures involved. Although the presented methods are transferable to an arbitrary climate model, this work considers the application on REMO simulations only. The data used for the illustrations originate from REMO control run simulations (JACOB AND PODZUN 1997, JACOB ET AL. 2001), which are described in chapter 3.2. For the control run, the RCM is forced by ECHAM5/MPI-OM simulations at the boundary of the model domain. As climate is only statistically

reproduced in this model setup, the data used for the visualization must not be directly compared to observations.

#### 4.2.1 SOLAR ZENITH ANGLE

The solar zenith angle plays an important role for many processes at the land surface (e.g. distribution of photosynthetic active radiation in the canopy). As it is not affected by the underlying earth surface, no subscale adjustments need to be carried out. The coarse grid values can directly be remapped from the coarse atmospheric grid to the finer grid representing the land surface. For those climate models that do not provide solar zenith angle information by default, SCALMET calculates the solar zenith angle *SZA* as a function of time and geographical position of the considered pixel in form of

$$\cos SZA = \sin \theta \sin \varphi + \cos \theta \cos \varphi \cos \tau \quad \text{Eq. 4.28}$$

where  $\theta$  is the solar declination angle,  $\varphi$  is the geographical latitude and  $\tau$  is the hour angle measured from local solar noon (LISTON AND ELDER 2006). The solar declination angle can be approximated as

$$\theta = \varphi_{TC} \cos \left[ 2\pi \left( \frac{day - d_s}{d_y} \right) \right] \quad \text{Eq. 4.29}$$

where  $\varphi_{TC}$  is the latitude of the tropic of Cancer, *day* is the day of the year,  $d_s$  is the day of the summer solstice and  $d_y$  is the average number of days in a year. The hour angle  $\tau$  is calculated according to the hour of the day *h* as:

$$\tau = \pi \left( \frac{h}{12} - 1 \right) \quad \text{Eq. 4.30}$$

Besides the relevance within the land surface model calculations the solar zenith angle is of great importance in the shortwave radiation submodel in SCALMET that will be described in detail in chapter 4.2.5.

#### 4.2.2 AIR TEMPERATURE

Simple interpolation algorithms have often been applied in the past to generate high resolution temperature distributions on the basis of available temperature observations (BURROUGH AND McDONNELL 2000). These interpolation techniques did not include any topographic adjustments and therefore tended to misrepresent the natural temperature

distributions in areas characterized by a significant topographic variability (LISTON AND ELDER 2006). Since temperature typically decreases with increasing elevation (OKE 1987), recent studies try to optimize the quality of temperature remappings by taking advantage of this strong temperature elevation dependence (LISTON AND ELDER 2006, DODSON AND MARKS 1997, COSGROVE ET AL. 2003, HIJMANS ET AL. 2005). In SCALMET there are basically two options for the correction of temperature simulations on the basis of available subgrid elevation. The two methods of the regression based and the constant lapse rate remapping of temperature simulations are introduced in the following. The denotation temperature, as it is used hereinafter, refers to the near surface temperature associated to a height of 2 m above ground.

#### 4.2.2.1 REGRESSION BASED REMAPPING

The regression based remapping (RBR) analyzes the temperature-elevation dependence for every model time step separately. Apart from the conventional approach described in chapter 4.1.2, SCALMET for the remapping of air temperature offers the option to divide the atmosphere into two vertical layers. Using a two-layer atmosphere allows a realistic treatment of temperature inversions, which are a common meteorological phenomenon in the Alpine Foreland. Examples showing the temperature-elevation dependence found in REMO simulations are illustrated in Fig. 4.7. As can be seen in the temperature simulations, there is an accumulation of simulated values around 0 °C covering an altitudinal range from 1300 to 3000 m.a.s.l. (see Fig. 4.7, right).

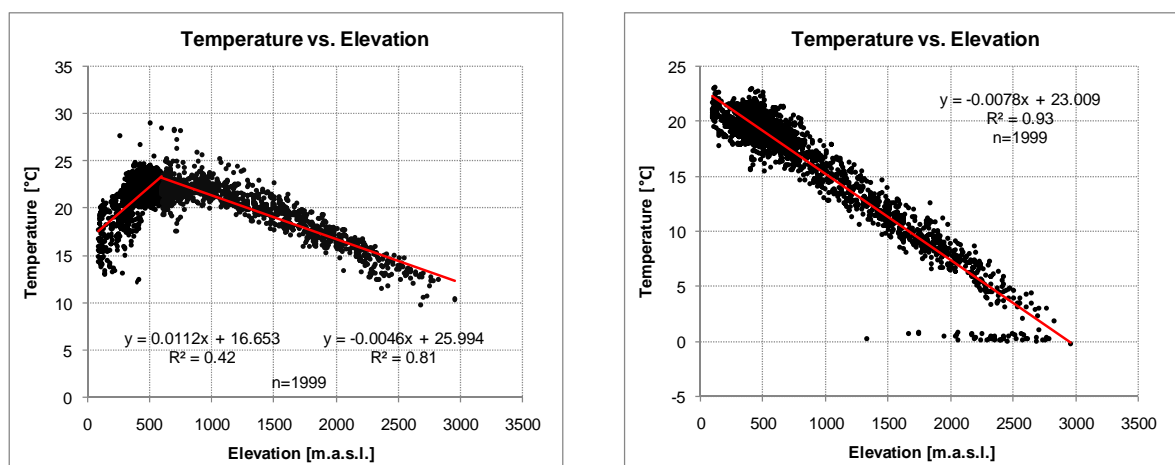


Fig. 4.7: The temperature-elevation dependence in REMO control run simulations for two model time steps in the year 1982 (left: November 5<sup>th</sup> (11 a.m.), right: May 17<sup>th</sup> (6 p.m.)). The left diagram displays a temperature inversion which is described by two separate regression functions.

The explanation for this behavior is found in the underlying land surface. The near zero air temperatures are located at grid cells that are covered by melting snow, which is

characterized by a surface temperature of 0 °C. The turbulent exchange of fluxes (momentum, sensible and latent heat) between the land surface and the lowest atmospheric level in REMO is based on the Monin-Obukhov theory (MONIN AND OBUKHOV 1954). For a surface temperature of 0 °C it results in a near surface temperature close to zero. While the right diagram pictures the normal decrease in temperatures up to higher elevations, the diagram on the left of Fig. 4.7 gives an example for a temperature inversion reflected by the RCM simulations. To determine the approximate height of inversion, the boundary between the two atmospheric layers is iteratively shifted from the lowest elevation found in the climate model DEM towards higher elevations (see Fig. 4.8). While the increment in this process can be arbitrarily set, the current configuration uses a step size of 100 m as a compromise of accuracy and computational costs. For each iteration step, separate regression functions are determined for both atmospheric layers, describing the temperature-elevation dependence in the respective layer.

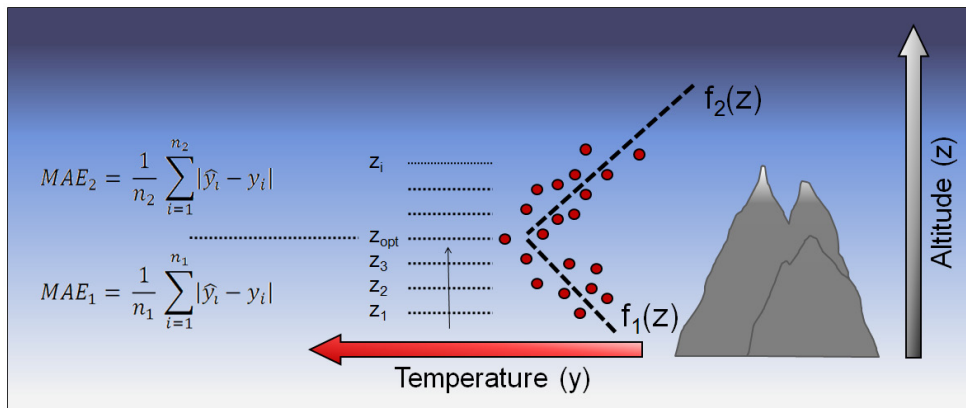


Fig. 4.8: The two-layer atmosphere in SCALMET. Altitudinal temperature variations in case of temperature inversions are described by two separate regression functions

The boundary elevation that produces the lowest mean absolute error (MAE) between the predictions as a product of the layer's regression functions, and the simulations found inside the different atmospheric layers is finally representing the inversion height. The mean absolute error is given by

$$MAE = \frac{1}{n} \sum_{i=1}^n |\hat{y}_i - y_i| \quad \text{Eq. 4.31}$$

where  $\hat{y}$  are the values predicted by the regression function,  $y$  are the observations (here RCM simulations) and  $n$  is the total number of data pairs.

The total MAE is computed as the mean error of both atmospheric layers. The process of determining the actual inversion layer is illustrated in Fig. 4.8. For the case that the smallest

overall MAE for both atmospheric layers is not smaller than the MAE resulting from an application of just one linear function, the atmosphere is treated as one layer.

#### 4.2.2.2 CONSTANT LAPSE RATE REMAPPING

Alternative to the RBR, a scaling approach based on earlier studies by LISTON AND ELDER (2006), COSGROVE ET AL. (2003) and DODSON AND MARKS (1997) has been implemented in SCALMET. These authors propose the utilization of constant temperature lapse rates to adjust interpolated temperature data for subgrid topography. As noted by DODSON AND MARKS (1997), lapse rates are expected to vary largely over space and time. Therefore LISTON AND ELDER (2006) choose monthly varying temperature lapse rates published by KUNKEL (1989) over an application of constant values throughout the year as done by COSGROVE ET AL. (2003). In analogy to LISTON AND ELDER (2006), monthly lapse rates are used for temperature elevation corrections in SCALMET. To account for the local climate conditions inside the Upper Danube watershed, temperature observations at a total number of 221 meteorological stations located in Germany and Austria have been analyzed to derive monthly temperature lapse rates for the model domain. These stations represent a subset of the stations used for the generation of the meteorological forcings in uncoupled PROMET runs (see chapter 3.1.1). Fig. 4.9 displays the temperature-elevation dependence reflected by the station observations over the period 1971-2000 exemplarily for winter and summer situations.

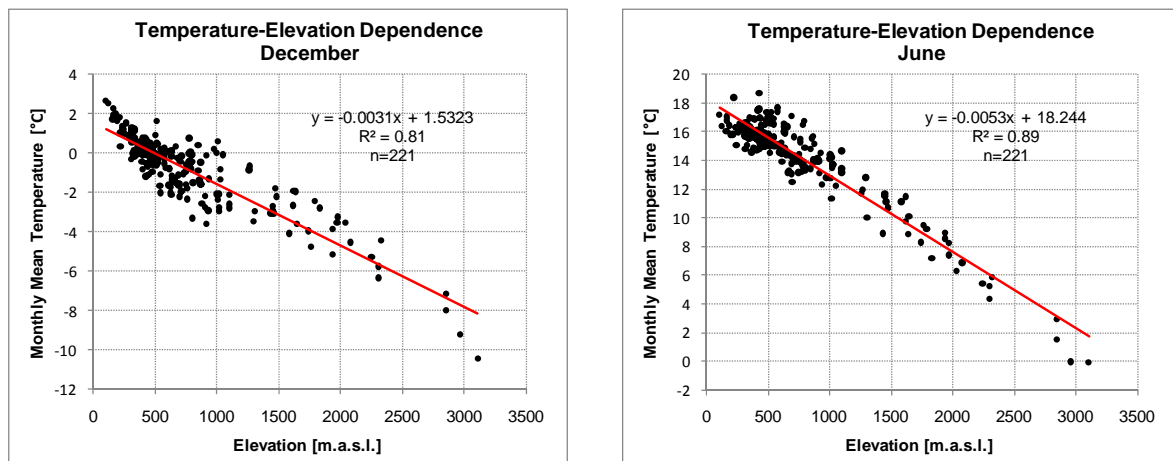


Fig. 4.9: The elevation dependence of monthly mean air temperature for December and June. The data have been recorded at 221 stations in Germany (DWD) and Austria (ZAMG) over the years 1971-2000.

For the months not displayed in Fig. 4.9 similar diagrams can be found in the appendix (see A-2). As displayed, temperature gradients are much steeper in summer than in winter, which can be explained by the frequent presence of temperature inversions in the winter months.

Even though the number of available observations decreases with altitude, the close linear relationship between altitude and temperature allows a stable extrapolation. The exact values of the lapse rates derived for the UD together with the lapse rates published by KUNKEL (1989) are given in Tab. 4.1. As shown the lapse rates by KUNKEL (1989) severely overvalue the temperature decrease with increasing elevation in the Upper Danube watershed.

Tab. 4.1: Monthly temperature lapse rates  $\Gamma_t$  derived for the Upper Danube watershed (UD) in comparison to those presented by KUNKEL (1989) for the Western United States.

Month	Jan	Feb	Mar	Apr	May	Jun	Jul	Aug	Sep	Oct	Nov	Dec
$\Gamma_t$ [°C/km] Kunkel (1989)	4.4	5.9	7.1	7.8	8.1	8.2	8.1	8.1	7.7	6.8	5.5	4.7
$\Gamma_t$ [°C/km] UD	2.6	3.5	4.7	5.3	5.2	5.3	4.9	4.7	4.2	3.3	3.5	3.1

Following LISTON AND ELDER (2006) temperature simulations  $t_{clim}$  are adjusted to a reference level  $z_{ref}$ , which was chosen to be sea level, in a first step. This is done by using the terrain elevation of the climate model  $z_{clim}$  and the monthly varying temperature lapse rate  $\Gamma_t$  in form of:

$$t_{ref} = t_{clim} - \Gamma_t (z_{clim} - z_{ref}) \quad \text{Eq. 4.32}$$

Adjusted to the reference level, temperatures are directly interpolated from the RCM resolution to the finer resolution of the land surface grid. The spatially interpolated reference temperatures  $t_{ref\_int}$  in a next step are adjusted to the topographic height of the land surface grid  $z_{ls}$ , using the same temperature lapse rate  $\Gamma_t$  in form of

$$t_{ls} = t_{ref\_int} + \Gamma_t (z_{ls} - z_{ref}) \quad \text{Eq. 4.33}$$

where  $t_{ls}$  is the temperature obtained for every grid cell within the land surface grid. Subsequent to the topographic adjustment of the interpolated temperature fields, the mean temperature over all pixels covered by a certain climate model pixel is realigned to the associated RCM pixel value. The exact procedure is described in detail in chapter 4.1.3. A comparison of the different remapping methods implemented for the remapping of temperature is carried out in 5.2.1.1.

### 4.2.3 AIR HUMIDITY

Air humidity is provided in form of different humidity variables depending on the RCM used (absolute humidity, specific humidity or dewpoint temperature). The land surface model

PROMET requires spatial information on the actual air moisture content in form of the relative air humidity. Relative humidity reflects the air's potential to incorporate and transport moisture and thus plays an important role for many hydrological processes. As humidity is a nonlinear function of terrain elevation, SCALMET uses the dewpoint temperature, which is almost linearly related to elevation, for the humidity-elevation adjustments. In case of the regional climate model REMO, dewpoint temperature is directly provided and does not need to be calculated on the basis of other humidity variables. Using the dewpoint temperature-elevation dependence within the remapping process, the remapping options for the distribution of air humidity are quite similar to those available for the remapping of temperature.

#### 4.2.3.1 REGRESSION BASED REMAPPING

The regression based remapping determines the dewpoint temperature lapse rate for a given time step on the basis of the RCM simulations during the run-time of the coupled model run. The determined lapse rate allows to correct the simulated dewpoint temperatures for subgrid topography as described in detail in chapter 4.1.2. An example for the dewpoint temperature-elevation dependence found in REMO simulations is given in Fig. 4.10.

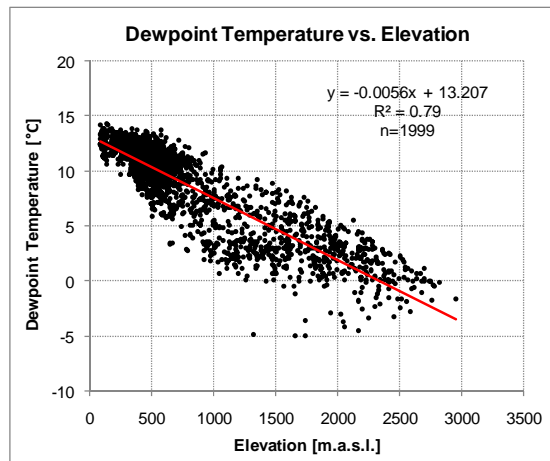


Fig. 4.10: The dewpoint temperature-elevation dependence for a model time step in the year 1982 (May 17<sup>th</sup>, 6 p.m.).

As can be seen, the scattering of simulations around the regression line is slightly larger compared to that of temperature simulations for the same time step (see chapter 4.2.2.1, Fig. 4.7). Thus the coefficient of determination with a value of 0.79 proves the significant elevation dependence for the considered model time step.

#### 4.2.3.2 CONSTANT LAPSE RATE REMAPPING

Alternatively to the statistic data analysis, an approach based on the application of constant monthly dewpoint temperature lapse rates, hereinafter referred to as the constant lapse rate remapping (CLR), has been implemented in SCALMET. The method is based on studies by KUNKEL (1989) and has been successfully applied for the generation of humidity distributions by LISTON AND ELDER (2006).

Again lapse rates need to be adjusted to the climate conditions within the UD. The required dewpoint temperature data were derived on the basis of relative humidity and temperature observations (1970-2000), measured at the same stations used for the determination of the temperature lapse rates (see chapter 4.2.2.2). The equations used for the humidity conversions are given in the appendix (see A-1).

As done for the determination of temperature lapse rates, observations have been aggregated to monthly means before the analysis. The dewpoint temperature-elevation dependence is shown exemplarily for December and June in Fig. 4.11. Similar diagrams can be found for all other months of the year in the appendix (see A-3).

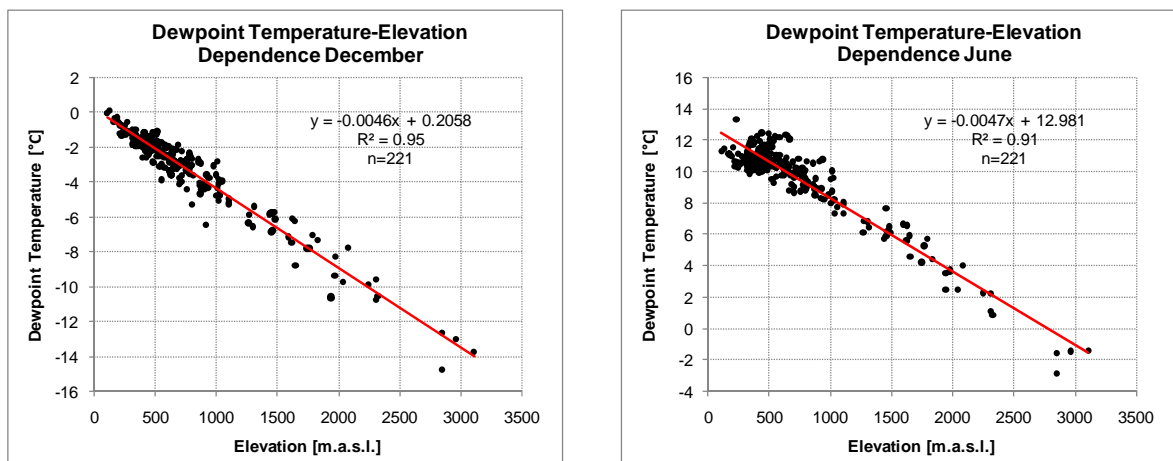


Fig. 4.11: The elevation dependence of monthly mean dewpoint temperature for December and June. The data have been recorded at 221 stations in Germany (DWD) and Austria (ZAMG) over the years 1971-2000.

Both graphs show that the strong elevation dependence of the monthly dewpoint temperature is well reflected in the station observations. The variation within mean lapse rates throughout the year is shown in Tab. 4.2 for the lapse rates derived for the UD in combination with those presented by KUNKEL (1989). While similar values occur in the summer months from June to September, deviations of more than 1 °C/km can be found in the winter months. The results underline the importance of adjusting lapse rates to the local climate conditions in the model domain of the Upper Danube watershed.

Tab. 4.2: Monthly dewpoint temperature lapse rates  $\Gamma_{td}$  derived for the Upper Danube watershed (UD) in comparison to those presented by KUNKEL (1989) for the Western United States.

Month	Jan	Feb	Mar	Apr	May	Jun	Jul	Aug	Sep	Oct	Nov	Dec
$\Gamma_{td}$ [°C/km] Kunkel (1989)	5.6	5.8	5.5	5.4	5.2	5.0	4.5	4.5	5.0	5.1	5.5	5.5
$\Gamma_{td}$ [°C/km] UD	4.4	4.6	4.9	4.8	4.6	4.7	4.3	4.2	4.5	4.4	4.7	4.6

In analogy to the lapse rate remapping of temperature simulations, the derived monthly lapse rates are used to adjust the simulated dewpoint temperatures  $td_{clim}$  to a reference level  $z_{ref}$  in a first step

$$td_{ref} = td_{clim} - \Gamma_{td} (z_{clim} - z_{ref}) \quad \text{Eq. 4.34}$$

where  $z_{clim}$  is the terrain elevation of the climate model and  $\Gamma_{td}$  is the dewpoint temperature lapse rate of the current month. Again the reference level is defined as 0 m.a.s.l. Reference level dewpoint temperatures are directly interpolated from the RCM resolution to the finer resolution of the land surface grid.

Finally, the spatially interpolated reference temperatures  $td_{ref\_int}$  are adjusted to the topographic height of the land surface grid  $z_{ls}$  using the monthly lapse rate  $\Gamma_{td}$  in form of

$$td_{ls} = td_{ref\_int} + \Gamma_{td} (z_{ls} - z_{ref}) \quad \text{Eq. 4.35}$$

where  $t_{ls}$  is the dewpoint temperature at a given land surface grid cell. As the dewpoint temperature does not scale linearly, the adjusted dewpoint temperatures  $td_{ls}$  as well as the simulated dewpoint temperatures  $td_{clim}$  are converted to a specific humidity subsequent to the elevation adjustments. On the basis of specific humidity, the land surface humidity is aligned to the climate model humidity following the general adjustment approach described in chapter 4.1.3.

Fig. 4.12 shows the results of the two remapping approaches presented in the preceding paragraphs together with the REMO humidity simulations exemplarily for a model time step in the year 1982. Note that the relative humidity shown in Fig. 4.12 a) does not represent a direct output of the REMO model. It is calculated on the basis of dewpoint temperature, temperature and near surface pressure simulations. This accounts for the remapped humidity as well, with the difference that the temperature and surface pressure used to calculate the relative humidity represent remapping results here as well. Surface pressure is consequently remapped using an approach presented by COSGROVE ET AL. (2003) (chapter 4.2.8) for both remapping approaches, whereas temperature is remapped using the constant lapse rate approach in case of b) and the regression based remapping in case of c).

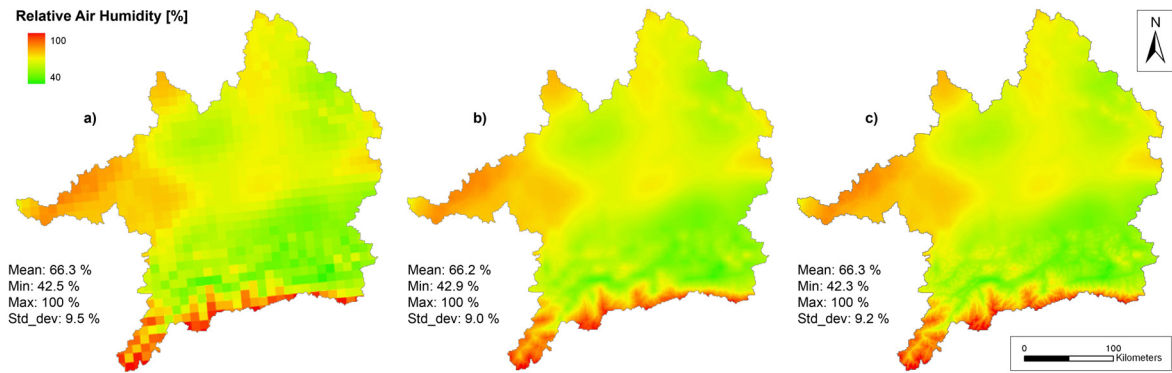


Fig. 4.12: REMO air humidity (a), remapped air humidity achieved using the constant lapse rate approach (b) and remapped air humidity achieved using the regression based remapping (c). Air humidity is calculated on the basis of dewpoint temperature, temperature and surface pressure (based on REMO simulations for a model time step in the year 1982 (May 17<sup>th</sup>, 6 p.m.)).

As displayed, in the case of the regression based remapping subgrid topography seems little more pronounced. However, differences between the remapping approaches for the current model time step are rather small. An explanation is given by the fact that the temperature lapse rate as well as the dewpoint temperature lapse rate calculated within the regression analysis (see Fig. 4.7 (right) and Fig. 4.10) are quite similar to the constant lapse rates used for the month of May (see Tab. 4.1 and Tab. 4.2). The exact equations used for all humidity conversions in SCALMET are given in the appendix (see A-1).

#### 4.2.4 PRECIPITATION

Since precipitation typically displays complex spatial patterns, the downscaling of precipitation is one of the biggest challenges in the field of atmosphere-land surface interactions (FRÜH ET AL. 2006). The manifold interactions between topography and local rainfall contribute to the large spatial variability of rainfall amounts particularly in mountainous regions. Besides the approach of dynamically scaling precipitation simulations (SCHMIDLI ET AL. 2007), there are several statistical techniques for the downscaling of simulated rainfall using various large scale predictors in different atmospheric pressure levels (e.g. 700 hPa) like geopotential height (KIDSON AND THOMPSON 1998, ZORITA AND VON STORCH 1999), geostrophic vorticity (WILBY ET AL. 1998), wind speed (MURPHY 1999), atmospheric moisture (BECKMANN AND BUIHAND 2002), sea level pressure (CAVAZOS 1999) or precipitation itself (WIDMANN ET AL. 2003). Unfortunately these methods sometimes require extensive, climate model dependent calibrations (HUTCHINSON 1998) and make use of parameters that are often not accessible to the user of the climate simulations. Efforts using terrestrial information for the generation of rainfall distributions include the application of various topographic predictors like altitude, latitude, continentality, slope, exposure (BASIST ET AL. 1994, WEISSE

AND BOIS 2001, WOTLING ET AL. 2000, NINYEROLA ET AL. 2000) as well as climatological relationships between simulated and observed precipitation (FRÜH ET AL. 2006).

SCALMET takes advantage of the fact that precipitation generally increases with elevation (SPREEN 1947, SMITH 1979). Using this precipitation-elevation relationship, the scaling methods applied to distribute precipitation simulations follow a rather pragmatic approach that has been pursued in many studies in the recent past (MAUSER AND BACH 2008, GOOVAERTS 2000, PRUDHOMME AND DUNCAN 1999, MARTÍNEZ-COB 1996, HIJMANS ET AL. 2005). In analogy to the options given for temperature remappings, precipitation can either be distributed by using the regression based approach or by applying elevation corrections in a separate precipitation submodel.

#### 4.2.4.1 REGRESSION BASED REMAPPING

SCALMET gives the option to analyze the precipitation-elevation dependence for each model time step individually. However the elevation dependence of hourly rainfall simulations is rather moderate to that found in case of other meteorological variables. Fig. 4.13 (left) shows an example for the precipitation-elevation dependence in REMO simulations. As can be seen, the scattering of points around the regression line is relatively high. The coefficient of determination ( $R^2$ ) with a value of 0.53 confirms the rather moderate correlation between hourly rainfall and elevation for the considered model time step.

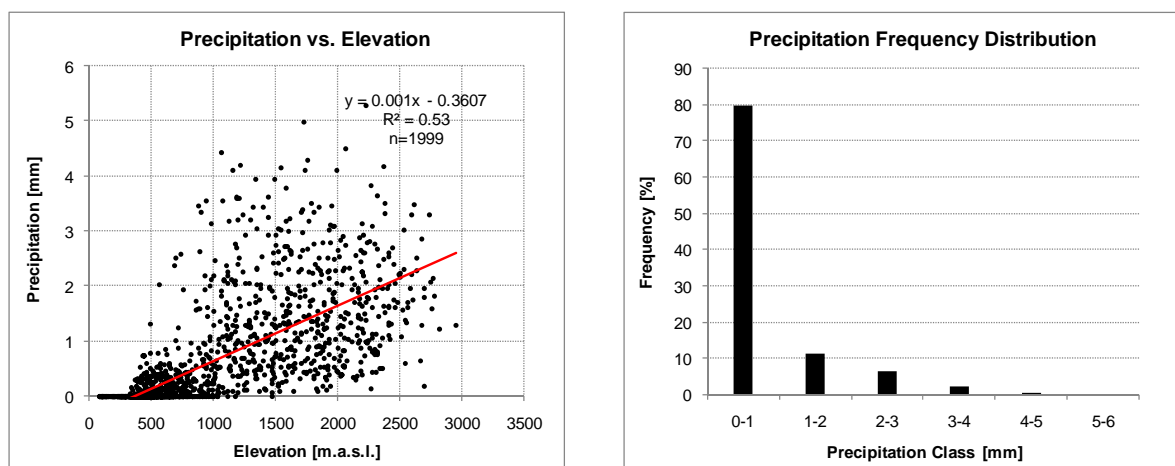


Fig. 4.13: Precipitation-elevation dependence in REMO control run simulations (left) and frequency distribution of simulated precipitation (right) (based on REMO simulations for October 17<sup>th</sup>, 1982 (4 p.m.)).

As precipitation simulations often show strong deviations from the Gaussian distribution (see Fig. 4.13, right), the Kendall coefficient ( $R_k$ ) is consulted as an additional statistic criterion for the analysis of the altitudinal trend in simulated precipitation. Unlike the coefficient of determination, the Kendall coefficient does not require the data to be normally distributed.

With a  $R_k$  of 0.47 the Kendall coefficient proves the rather moderate correlation between elevation and precipitation for the current time step. Though the correlation is highly significant at a significance level of  $\alpha = 0.1\%$  and is thus regarded to improve the remapping of simulated precipitation compared to a simple interpolation. In general, the precipitation-elevation dependence found in REMO simulations is often not significant resulting in rather moderate elevation corrections (see 5.3.2.1.2).

#### 4.2.4.2 ADJUSTMENT FACTOR REMAPPING

Alternatively to the regression based approach, subgrid adjustments can be carried out using an approach presented by THORNTON ET AL. (1997) which is used for the generation of hourly precipitation distributions in the meteorological distribution model (MICROMET) developed by LISTON AND ELDER (2006). In a first step, simulated precipitation is bilinearly interpolated from the spatial resolution of the RCM to the land surface grid resolution. The reference level in case of precipitation adjustments is chosen to be the interpolated terrain elevation of the RCM to account for the nonlinear character of the elevation adjustment function (see Fig. 4.15, right). The interpolated rainfall  $p_{ref\_int}$  can be adjusted to the land surface topography  $z_{ls}$  using the following elevation adjustment function

$$p_{ls} = p_{ref\_int} \left[ \frac{1 + \lambda (z_{ls} - z_{ref})}{1 - \lambda (z_{ls} - z_{ref})} \right] \quad \text{Eq. 4.36}$$

where  $p_{ls}$  is the adjusted precipitation in the spatial resolution of the land surface grid,  $z_{ref}$  is the interpolated RCM elevation and  $\lambda$  is a monthly varying adjustment factor. As this factor is spatially and temporally variable, the precipitation adjustment factors used by LISTON AND ELDER (2006) have been replaced by factors derived for the area of the Upper Danube watershed. The high resolution precipitation data needed for the determination of the precipitation adjustment factors is supplied by the meteorological preprocessor in PROMET (see chapter 3.1.1). The data covering the period 1970-2000 are temporally aggregated to monthly values in a first step and then spatially aggregated to the resolution of the climate model REMO. To guarantee an optimal transferability to the REMO model, the data has been aggregated not only to the grid size but also to the rotated coordinate system used in the RCM by the means of the conservative remapping method described in chapter 4.1.1.3.

Subsequent to the aggregation process, the precipitation data as well as the RCM elevation have been interpolated to the spatial resolution of the LSM. Using Eq. 4.36, the elevation adjustment factor  $\lambda$  could be iteratively determined by finding the value of  $\lambda$  that produces the

lowest MAE between the high resolution precipitation input data and the elevation adjusted interpolations (see Fig. 4.14).

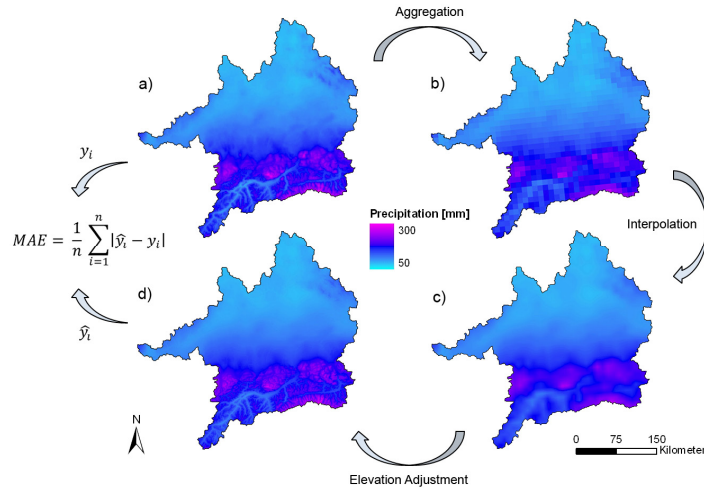


Fig. 4.14: Process chain in the determination of monthly precipitation adjustment factors for the model domain shown for the month of June. a) observation based precipitation (1970-2000) at 1 x 1 km, b) aggregated precipitation at 10 x 10 km, c) bilinear interpolated precipitation at 1 x 1 km, d) adjusted precipitation using the adjustment factor that leads to a smallest MAE compared to the input data set shown in a).

Compared to the factors applied by LISTON AND ELDER (2006), the precipitation-adjustment factors derived for the UD take rather small values. The absolute values together with the total mean absolute error (MAE) and the root mean square error (RMSE) between the elevation adjusted precipitation and the input data are given in Tab. 4.3.

Tab. 4.3: Monthly precipitation adjustment factors presented by LISTON AND ELDER (2006) and those derived for the Upper Danube watershed (1971-2000). The MAE and RMSE (adjusted-input) give an impression to what degree the adjusted monthly precipitation agrees with the distributed observations.

Month	Jan	Feb	Mar	Apr	May	Jun	Jul	Aug	Sep	Oct	Nov	Dec
$\lambda [km^{-1}]$ Liston & Elder (2006)	0.35	0.35	0.35	0.30	0.25	0.20	0.20	0.20	0.20	0.25	0.20	0.35
$\lambda [km^{-1}]$ UD	0.14	0.14	0.14	0.13	0.10	0.10	0.10	0.10	0.10	0.11	0.13	0.13
MAE [mm]	2.0	1.9	2.1	2.0	2.0	2.7	2.7	2.4	1.8	1.7	2.1	2.3
RMSE [mm]	3.4	3.2	3.8	3.7	3.3	4.7	4.8	4.3	3.2	2.9	3.6	3.9

Fig. 4.15 (left) displays the derived precipitation adjustment factors in comparison to those used by LISTON AND ELDER (2006). Both curves unfold considerable seasonal variations. However, variations are less distinct in the case of the factors derived for the UD. On the right, the dependence of the precipitation adjustment function (Eq. 4.36) on elevation difference is illustrated for the month of June using the factors presented by LISTON AND ELDER (2006) and those derived for the UD. As can be seen the correction function under application of both factor variants results in only small deviations from linearity.

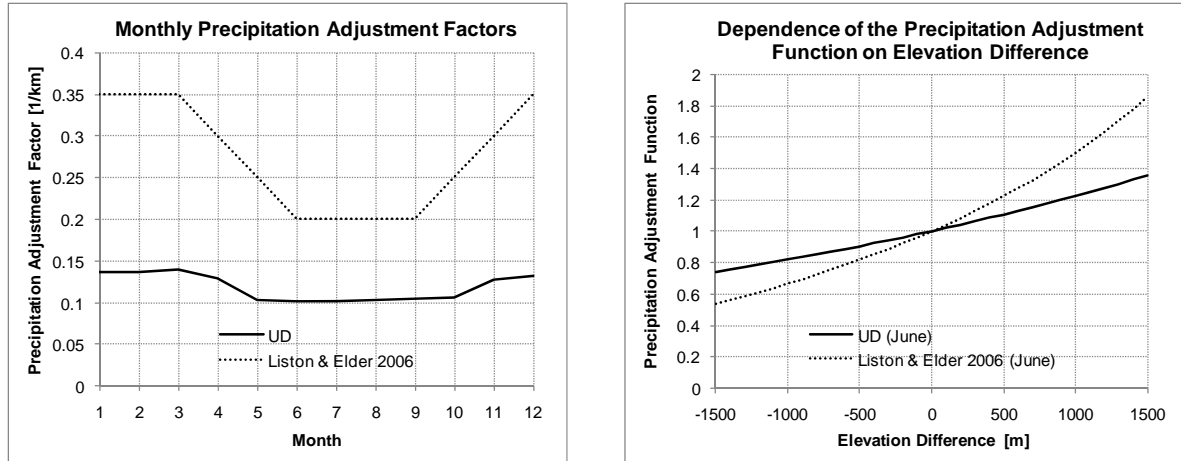


Fig. 4.15: Monthly precipitation adjustment factors derived for the Upper Danube watershed together with those used by LISTON AND ELDER (2006) (left). The diagram on the right shows the dependence of the precipitation adjustment function on elevation difference for a summer month (June).

For a comparison of the performance of the different scaling options available for the remapping of precipitation refer to chapter 5.2.1.2.

#### 4.2.5 INCOMING SHORTWAVE RADIATION

Although solar radiation is expected to increase with elevation due to a reduction of the optical air mass in higher elevations, terrain elevation only poorly predicts the spatial variability in solar radiation fluxes. For the remapping of the incident shortwave radiation a separate solar radiation submodel has been implemented in SCALMET. The included radiation calculations have been shown to satisfactorily predict large proportions of the spatial and temporal variability in radiative fluxes even in complex terrain (LISTON AND ELDER 2006). Direct and diffuse radiation components are computed as a function of the earth-sun geometry, local topographic features (slope and aspect) and cloud cover (LISTON AND ELDER 2006). The incoming shortwave radiation reaching the earth surface ( $R_{sw\_in}$ ) including adjustments for sloping terrain can be expressed as

$$R_{sw\_in} = I_0 (T_{dir} \cos i_s + T_{dif} \cos SZA) \quad \text{Eq. 4.37}$$

where  $SZA$  is the solar zenith angle,  $i_s$  is the angle between the direct solar radiation beam and a sloping surface and  $T_{dir}$  and  $T_{dif}$  are the atmospheric transmissivities for direct and diffuse solar radiation respectively (LISTON AND ELDER 2006). The solar zenith angle  $SZA$  is a function of time and geographic position. Its exact calculation is described in chapter 4.2.1 (Eq. 4.3). The variable  $I_0$  represents the solar irradiance at the top of the atmosphere. Impinging upon a surface normal to the solar beam, the solar constant  $I_0$  can be

approximated as  $1370 \text{ W/m}^2$  (KYLE ET AL. 1985). The angle  $i_s$  between the direct solar radiation beam and a sloping surface is given by

$$\cos i_s = \cos \beta \cos SZA + \sin \beta \sin SZA \cos(\mu - \xi_s) \quad \text{Eq. 4.38}$$

where  $\beta$  is the terrain slope,  $\mu$  is the solar azimuth and  $\xi_s$  is the terrain slope azimuth with both having south as zero azimuth. The solar azimuth  $\mu$  can be computed as

$$\mu = \sin^{-1} \left[ \frac{\cos \theta \sin \tau}{\sin SZA} \right] \quad \text{Eq. 4.39}$$

where  $\theta$  is the solar declination angle (see Eq. 4.29) and  $\tau$  is the hour angle measured from solar noon (see Eq. 4.30). The slope of the terrain is calculated in form of

$$\beta = \tan^{-1} \left[ \left( \frac{\delta z_{ls}}{\delta x_{coord}} \right)^2 + \left( \frac{\delta z_{ls}}{\delta y_{coord}} \right)^2 \right]^{\frac{1}{2}} \quad \text{Eq. 4.40}$$

where  $z_{ls}$  is the terrain elevation and  $x_{coord}$  and  $y_{coord}$  are the horizontal grid coordinates. The three grid dimensions are also used to compute the terrain slope azimuth  $\xi_s$  as:

$$\xi_s = \frac{\pi}{2} - \tan^{-1} \left[ \left( \frac{\delta z_{ls}}{\delta y_{coord}} \right) / \left( \frac{\delta z_{ls}}{\delta x_{coord}} \right) \right] \quad \text{Eq. 4.41}$$

To take into account the absorption, reflection and scattering of shortwave radiation by clouds, the climate model cloud cover  $C_f$  is interpolated to the land surface grid and is used to scale the fraction of solar radiation reaching the earth surface. This is done by modifying the net sky transmissivities following BURRIDGE AND GADD (1974) in form of

$$T_{dir} = (0.6 - 0.2 \cos Z) (1.0 - C_{f\_int}) \quad \text{Eq. 4.42}$$

$$T_{dif} = (0.3 - 0.1 \cos Z) C_{f\_int} \quad \text{Eq. 4.43}$$

where  $C_{f\_int}$  is the interpolated RCM cloud cover. The direct ( $R_{sw\_dir}$ ) and diffuse ( $R_{sw\_dif}$ ) components of the incoming solar radiation can now be calculated as:

$$R_{sw\_dir} = I_0 (T_{dir} \cos i) \quad \text{Eq. 4.44}$$

$$R_{sw\_dif} = I_0 (T_{dif} \cos Z) \quad \text{Eq. 4.45}$$

Successive to the model calculations the results are compared and adjusted to the mean conditions given by the RCM simulations using the approach described in detail in chapter 4.1.3. The parameter used within this modification is the global radiation ( $R_{sw\_in}$ ) representing the sum of direct and diffuse radiation:

$$R_{sw\_in} = R_{sw\_dir} + R_{sw\_dif} \quad \text{Eq. 4.46}$$

Under the assumption that the global radiation has been correctly partitioned into direct and diffuse radiation components (Eq. 4.44 and Eq. 4.45) the fractions given by

$$f_{sw\_dir} = \left[ \frac{(R_{sw\_dir})}{(R_{sw\_in})} \right] \quad \text{Eq. 4.47}$$

$$f_{sw\_dif} = \left[ \frac{(R_{sw\_dif})}{(R_{sw\_in})} \right] \quad \text{Eq. 4.48}$$

are stored for the repartitioning of the global radiation subsequent to the alignment to the RCM simulations. As the global radiation does not belong to the REMO standard deliveries, it is computed using the simulated net shortwave radiation at the land surface  $R_{sw\_net}$  and the shortwave radiation reflected by the land surface  $R_{sw\_out}$  in form of:

$$R_{sw\_in} = R_{sw\_net} + R_{sw\_out} \quad \text{Eq. 4.49}$$

Having adjusted the submodel calculations towards the RCM radiation, the corrected global radiation  $R_{sw\_in\_cor}$  is repartitioned using the weights for direct and diffuse radiation fractions (Eq. 4.47 and Eq. 4.48) in form of

$$R_{sw\_dir\_cor} = f_{sw\_dir} R_{sw\_in\_cor} \quad \text{Eq. 4.50}$$

$$R_{sw\_dif\_cor} = f_{sw\_dif} R_{sw\_in\_cor} \quad \text{Eq. 4.51}$$

where  $R_{sw\_dir\_cor}$  is the corrected direct solar radiation and  $R_{sw\_dif\_cor}$  is the corrected diffuse solar radiation component. Fig. 4.16 shows the calculated direct and diffuse radiation exemplarily for a model time step in the year 1982. As can be seen, the amount of direct and diffuse shortwave radiation striking the land surface is largely dominated by the interpolated climate model cloud cover.

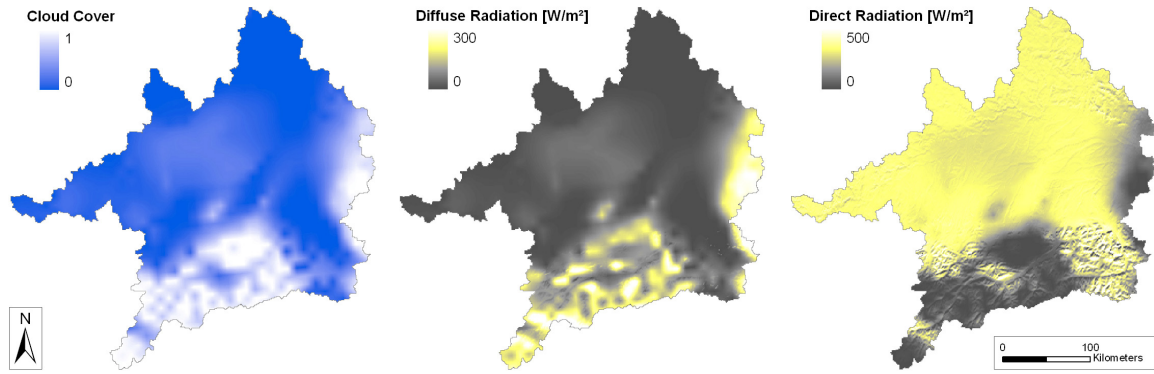


Fig. 4.16: Bilinearly interpolated REMO cloud cover and the amount of diffuse and direct radiation calculated by the shortwave radiation submodel in SCALMET exemplarily for a model time step in the year 1982 (November 5<sup>th</sup>, 11 a.m.).

The RCM global radiation together with the remapping result is pictured in Fig. 4.17. As displayed, the solar radiation submodel clearly brings out small scale topographic features, yet accounting for the actual atmospheric conditions and the energy budget given by the RCM simulations.

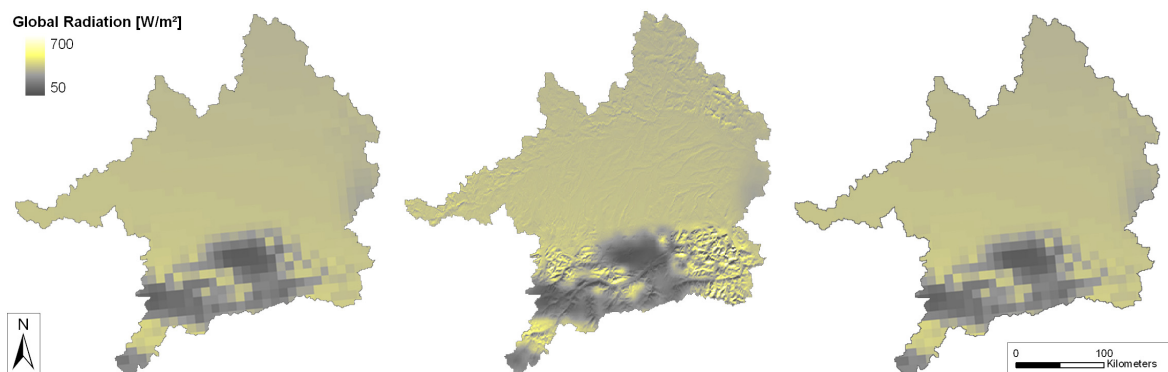


Fig. 4.17: REMO shortwave simulations (calculated out of the net surface shortwave radiation and the outgoing shortwave radiation) (left), remapped shortwave radiation (middle) and conservatively aggregated remapped shortwave radiation (right) for a model time step in the year 1982 (November 5<sup>th</sup>, 11 a.m.).

Although a first glance might suggest that solar energy is not maintained, particularly in the southeast of the model domain (yellow spots), the conservative remapping of the high resolution radiation fields back to the RCM resolution disproves this first impression.

#### 4.2.6 INCOMING LONGWAVE RADIATION

The amount of longwave radiation emitted by the atmosphere is largely dominated by the air temperature and the absolute air moisture content (LISTON AND ELDER 2006). As both typically decrease with increasing elevation, atmospheric downward longwave irradiance can

also be expected to decrease with terrain elevation. An example for the elevation dependence of longwave radiation as reflected in REMO simulations is shown in Fig. 4.18.

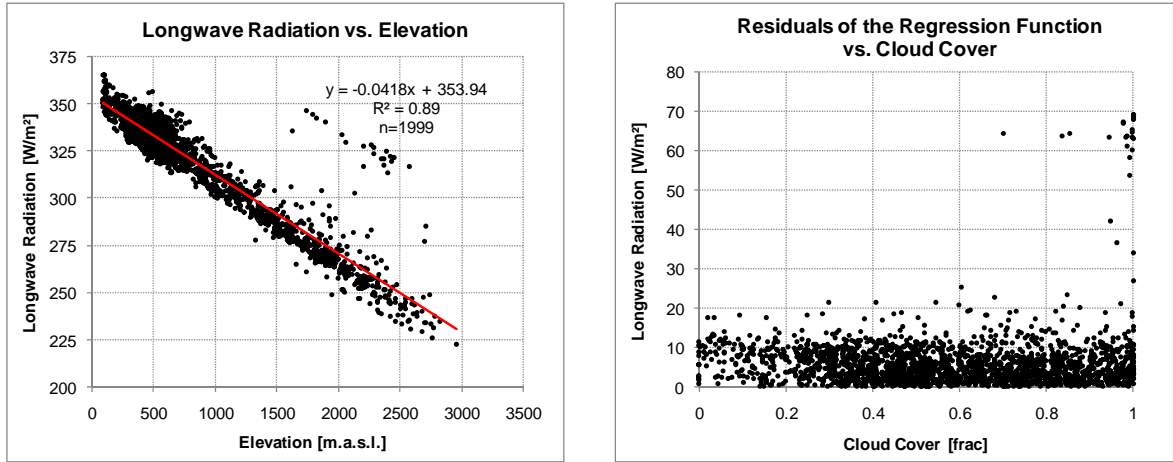


Fig. 4.18: The dependence of incoming longwave radiation on terrain elevation in REMO control run simulations for a model time step in the year 1982 (May 17<sup>th</sup>, 6 p.m.) (left). REMO incoming longwave radiation vs. simulated cloud cover for the same model time step (right).

The frequent presence of clouds in higher elevations and the increased thermal radiation emitted by the water molecules within the clouds often lead to large deviations from the linear elevation dependency. The diagram in Fig. 4.18 (right) clarifies that the largest deviations from the regression function occur together with a densely clouded atmosphere. To account for cloud cover within the downscaling of atmospheric downward irradiance, a longwave radiation submodel has been implemented in SCALMET. The model is based on studies carried out by LISTON AND ELDER (2006) and IZIOMON ET AL. (2003). It calculates the incoming longwave radiation based on the Stefan-Boltzmann law while taking into account cloud cover and elevation-related variations of atmospheric emissivity. The incoming longwave radiation  $R_{lw\_in}$  impinging upon the earth's surface can be written as

$$R_{lw\_in} = \varepsilon_a \sigma (T_k)^4 \quad \text{Eq. 4.52}$$

where  $\sigma$  is the Stefan-Boltzmann constant,  $\varepsilon_a$  is the atmospheric emissivity and  $T_k$  is the air temperature [K]. The atmospheric emissivity  $\varepsilon_a$  is calculated as a function of the spatially interpolated RCM cloud cover  $C_{f\_ls}$ , atmospheric vapor pressure  $e_a$  and air temperature in form of

$$\varepsilon_a = (1 + Z C_{f\_ls}^2) \left[ 1 - X \exp\left(-Y \frac{e_a}{(T_k)}\right) \right] \kappa \quad \text{Eq. 4.53}$$

where  $\kappa$  is an empiric constant defined as 1.083. The equation used for the calculation of the vapor pressure  $e_a$  on the basis of dewpoint temperature is given in the appendix together

with all other equations used for the humidity conversions in SCALMET (see A-1). The coefficients  $X, Y$  and  $Z$  depend on terrain elevation  $z_{ls}$  according to Tab. 4.4.

Tab. 4.4: Coefficients for the calculation of the atmospheric emissivity (LISTON AND ELDER 2006).

Coefficient	$z_{ls} < 200 \text{ m}$	$200 \text{ m} \leq z_{ls} \leq 3000 \text{ m}$	$3000 \text{ m} < z_{ls}$
$X$	0.35	$0.35 + (z_{ls} - 200) \left( \frac{0.51 - 0.35}{3000 - 200} \right)$	0.51
$Y$ [K/Pa]	0.1	$0.1 + (z_{ls} - 200) \left( \frac{0.13 - 0.1}{3000 - 200} \right)$	0.13
$Z$	0.224	$0.224 + (z_{ls} - 200) \left( \frac{1.1 - 0.224}{3000 - 200} \right)$	1.1

As can be seen the values for  $X, Y$  and  $Z$  in elevations between 200 m and 3000 m represent the result of a linear interpolation between the coefficients below 200 m and those above 3000 m, depending on the actual terrain elevation (LISTON AND ELDER 2006). Fig. 4.19 shows an example for the remapping of incoming longwave radiation by means of the longwave radiation submodel in SCALMET.

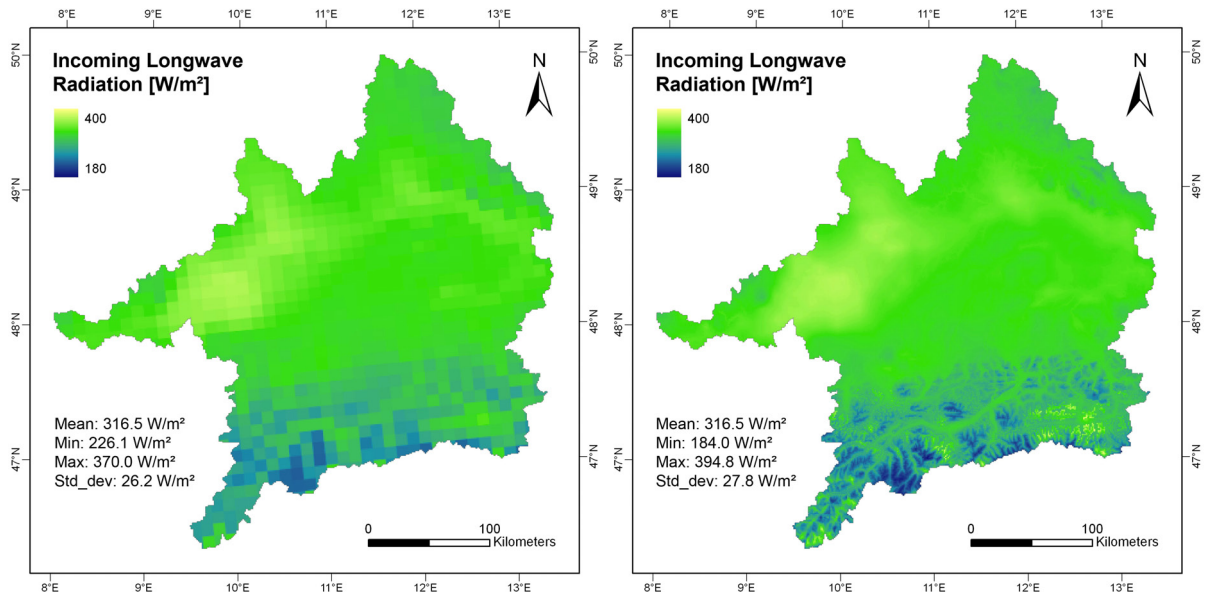


Fig. 4.19: Conservatively remapped incoming longwave radiation together with the results of the submodel calculations for a model time step in the year 1982 (May 17<sup>th</sup>, 6 p.m.).

To give an impression of the REMO inputs, the conservatively remapped REMO simulations are shown on the left. In analogy to the amount of incoming shortwave radiation, incoming longwave radiation is calculated in RCM resolution using the net longwave radiation and the

outgoing longwave radiation simulated by the regional climate model REMO. As shown, the submodel calculations notably pronounce orographic detail. Moreover, the inclusion of humidity and cloud cover influence within the remapping locally increases the amount of incoming radiative energy as a result of an enhanced atmospheric emission.

#### 4.2.7 WIND SPEED

Local wind speed is dominated by a variety of land surface and climate features. Correspondingly manifold are the efforts to determine high resolution local wind conditions on the basis of coarse wind simulations or point observations. While many studies make use of highly complex models (LISTON ET AL. 1993, ROSS ET AL. 1988, SHERMAN 1978), the run-time scaling concept in SCALMET strongly limits model complexity to minimize computational costs.

##### 4.2.7.1 REGRESSION BASED REMAPPING

Taking advantage of the fact that wind velocity, besides its dependence on exposure to the current wind direction, is largely influenced by terrain elevation, WALTER ET AL. (2006) generated a high resolution reference data set of German wind velocity. These authors recommend to rather use the so called 'relative altitude' than the absolute altitude as a predictand for local wind speed. Relative altitude is calculated by centering the available station observations in a 10 x 10 km grid box and by computing the difference between the grid box mean elevation and the station elevation.

For the application in SCALMET, monthly aggregated wind speeds at 221 meteorological stations in Germany and Austria have been analyzed to derive the monthly dependence of wind velocity on relative altitude. While the relative altitude approach yielded results similar to those presented by WALTER ET AL. (2006) using only German stations, the inclusion of the Austrian stations resulted in a very weak relative altitude-wind speed correlation. This behavior can be explained by the fact, that the frequent occurrence of very high elevations in Alpine regions (mountain tops) partly balances the high absolute station altitudes. The results are high wind velocities at moderate relative altitudes. Therefore absolute altitude is preferred to relative altitude for elevation adjustments in SCALMET. The wind velocity-elevation dependence can be determined for every single model time step using the regression based approach (see chapter 4.1.2). An example for the relationship between wind speed and terrain elevation included in REMO simulations is given in Fig. 4.20.

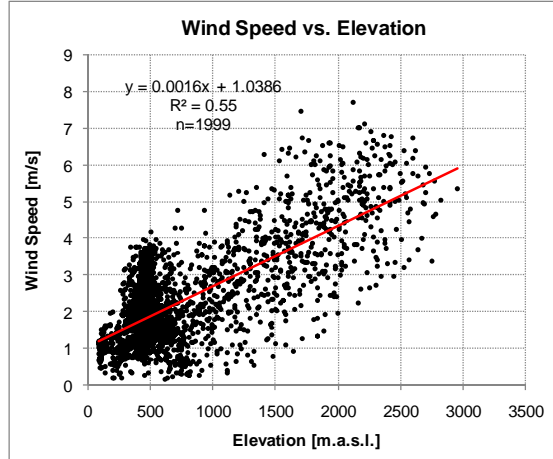


Fig. 4.20: The elevation dependence of simulated wind speed for a model time step in the year 1982 (May 17<sup>th</sup>, 6 p.m.).

Alternative to the regression approach, a wind submodel is provided to quasi physically remap RCM simulations.

#### 4.2.7.2 THE WIND SUBMODEL

The wind submodel is based on RYAN (1977) and LISTON AND STURM (1998) and uses wind-topography relationships to adjust wind speed simulations for subgrid topography. In a first step, the u- and v- wind components simulated by the RCM are directly interpolated to the land surface grid. The interpolated wind components  $ws_{u\_int}$  and  $ws_{v\_int}$  are combined for the calculation of the resulting wind speed  $ws_{ls\_int}$  as:

$$ws_{ls\_int} = \sqrt{ws_{u\_int}^2 + ws_{v\_int}^2} \quad \text{Eq. 4.54}$$

The wind direction  $\vartheta$  is calculated using  $ws_{u\_int}$  and  $ws_{v\_int}$  in form of

$$\vartheta = \frac{3\pi}{2} - \tan^{-1} \left( \frac{ws_{u\_int}}{ws_{v\_int}} \right) \quad \text{Eq. 4.55}$$

where north is defined as zero wind direction (LISTON AND ELDER 2006). To topographically modify the calculated wind speeds and directions, the topographic slope, the slope azimuth and the topographic curvature need to be calculated. The terrain slope  $\beta$  is calculated following Eq. 4.40, the terrain slope azimuth  $\xi_n$  with north given a zero azimuth is calculated as

$$\xi_n = \frac{3\pi}{2} - \tan^{-1} \left[ \frac{\left( \frac{\delta z_{ls}}{\delta y_{coord}} \right)}{\left( \frac{\delta z_{ls}}{\delta x_{coord}} \right)} \right] \quad \text{Eq. 4.56}$$

where  $x_{coord}$  and  $y_{coord}$  are the horizontal grid coordinates and  $z_{ls}$  is the terrain elevation. For the calculation of topographic curvature, a curvature length scale  $\eta$  needs to be specified. The length scale represents the radius used within the curvature calculations and takes values of approximately half the wavelength of the topographic features within the model domain (half the distance between two neighboring mountain ridges) (LISTON AND ELDER 2006). SCALMET calculates the curvature length scale automatically on the basis of the terrain slope in two separate passes for x- and y-direction (see Fig. 4.21).

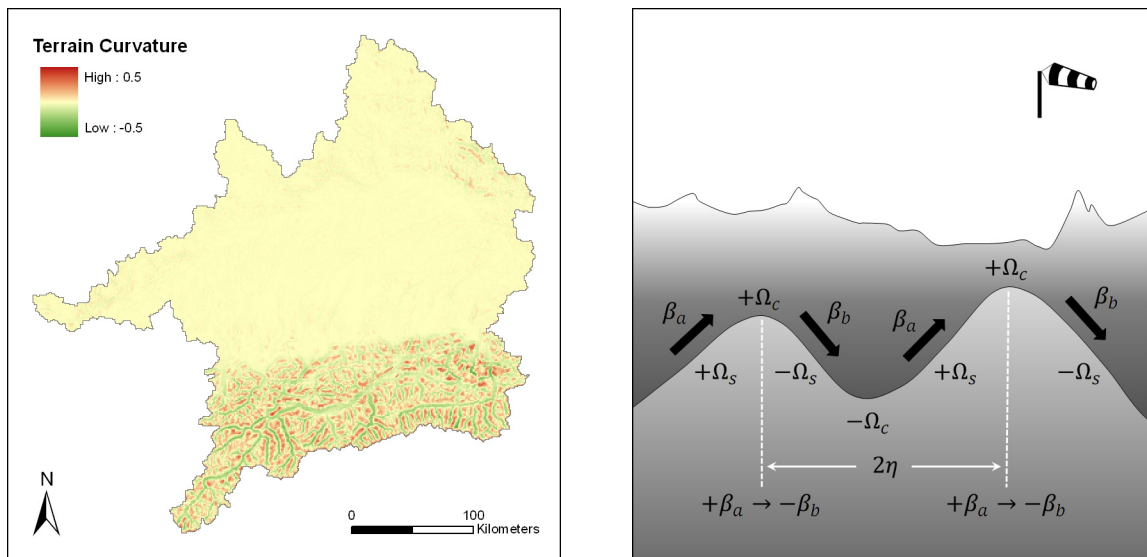


Fig. 4.21: Terrain curvature calculated for the Upper Danube watershed (left) and schematic illustration of the parameters involved in the remapping of wind speed simulations by the wind submodel in SCALMET (right). The curvature length scale  $\eta$  is calculated as half the distance between two slope changes from positive to negative.

Within this process, the user is optionally allowed to specify a threshold for the minimal topographic length scale to be included in the calculation of a mean curvature length scale in x- and y-direction. This offers the choice of focusing on large scale topographic features. If not manually set, the minimum topographic curvature length scale is systematically given by the spatial resolution of the land surface grid. The final value of the curvature length scale is calculated as the mean of the x- and y-length scales. For the model domain of the Upper Danube watershed and the given spatial resolution of 1 x 1 km, SCALMET calculates a mean curvature length scale of 3 grid increments (which at the given spatial resolution of 1 x 1 km corresponds to a distance of 3000 m). The latter is calculated without specifying a minimum for the length scales to be considered. The calculated value shows good accordance with samples taken at selected cross-sections from high resolution remote sensing data. Topographic curvature is calculated for each pixel of the land surface grid by computing the difference between the elevation of the actual grid cell and the average elevation of the two opposite grid cells. Both are located a length scale distance away from the considered grid

cell. This is done for four different directions (S-N, W-E, SW-NE, NW-SE) successively. The final grid cell curvature  $\Omega_c$  is calculated as the mean curvature computed for the different directions in form of

$$\Omega_c = \frac{1}{4} \left[ \frac{z_{ls} - \frac{1}{2}(z_S + z_N)}{2\eta} + \frac{z_{ls} - \frac{1}{2}(z_W + z_E)}{2\eta} + \frac{z_{ls} - \frac{1}{2}(z_{SW} + z_{NE})}{2\eta} + \frac{z_{ls} - \frac{1}{2}(z_{NW} + z_{SE})}{2\eta} \right] \quad \text{Eq. 4.57}$$

where  $z_S, z_N, \dots$  are the grid cell elevations at curvature length scale distance from the considered grid cell and  $z_{ls}$  is the elevation of the considered land surface grid cell. Besides terrain curvature, the slope in wind direction  $\Omega_s$  needs to be calculated using the terrain slope  $\beta$  in form of:

$$\Omega_s = \beta \cos(\vartheta - \xi_n) \quad \text{Eq. 4.58}$$

Following LISTON AND ELDER (2006), both,  $\Omega_c$  and  $\Omega_s$  are scaled to range from -0.5 to +0.5 over the whole model domain to simplify the weight calculation given by

$$\omega_{ws} = 1 + \gamma_c \Omega_c + \gamma_s \Omega_s \quad \text{Eq. 4.59}$$

where  $\omega_{ws}$  is the weight used to modify the interpolated wind speed  $ws_{ls\_int}$  and  $\gamma_c$  as well as  $\gamma_s$  are the curvature weight and slope weight respectively.

According to LISTON AND ELDER (2006), valid values of  $\gamma_c$  and  $\gamma_s$  range from 0 to 1 while the current configuration with values of 0.5 gives equal weight to slope and curvature. In a last step, the topography modified wind speed  $ws_{ls}$  is calculated as:

$$ws_{ls} = ws_{ls\_int} \omega_{ws} \quad \text{Eq. 4.60}$$

Lee and concave slopes yield negative values for  $\Omega_s$  and  $\Omega_c$  and windward and convex slopes yield positive values for  $\Omega_s$  and  $\Omega_c$  respectively. As a result, wind speed is reduced for lee and concave slopes and increased for windward and convex slopes.

Wind direction is terrain modified following RYAN (1977) by introducing a wind direction diverting factor in form of:

$$\vartheta_f = -0.5 \Omega_s \sin[2(\xi_n - \vartheta)] \quad \text{Eq. 4.61}$$

The factor is added to the wind direction resulting in a terrain adjusted wind direction  $\vartheta_{ls}$  given by:

$$\vartheta_{ls} = \vartheta + \vartheta_f \quad \text{Eq. 4.62}$$

Although PROMET does not use the wind direction in the current model version, a terrain modified wind direction is computed to open additional options for future developments in the hydrological model. An example for a remapping based on the presented wind model is shown together with the result of the regression based remapping in Fig. 4.22.

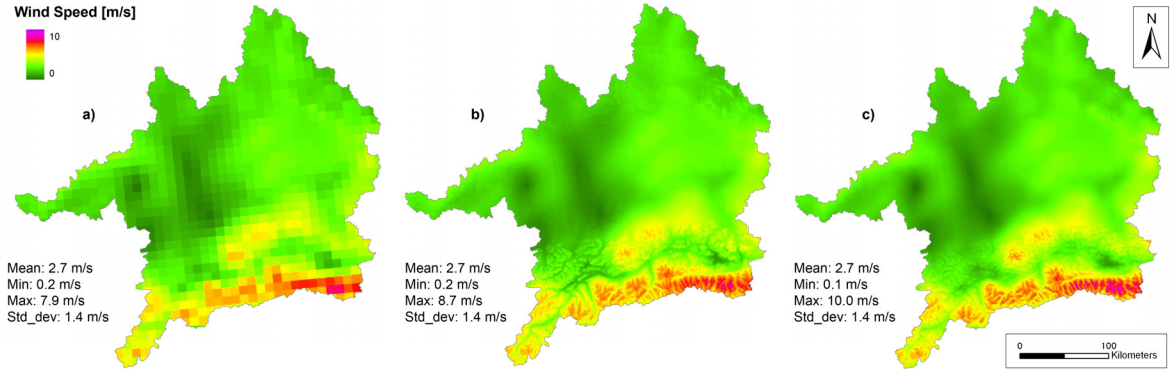


Fig. 4.22: The CI remapped REMO wind speed simulations (a), the regression based wind speed remapping (b) and the results of the wind model calculations (c) by the example of a model time step in the year 1982 (May 17th, 6 p.m.).

As displayed, the regression based remapping and the submodel remapping for the considered model time step produce very similar results with a slight tendency of the wind submodel to produce higher wind speed maxima.

#### 4.2.8 SURFACE PRESSURE

Surface pressure is the one meteorological variable that is most closely connected to terrain elevation giving the option to use terrain elevation as a predictor within the generation of high resolution surface pressure fields. This can be done using a time-independent formulation in form of

$$sp_{ls} = sp_0 \exp\left(-\frac{z_{ls}}{H}\right) \quad \text{Eq. 4.63}$$

where  $sp_{ls}$  is the surface pressure in height  $z_{ls}$ ,  $sp_0$  and is a reference sea level pressure (101300 Pa) and  $H$  is the scale height of the atmosphere ( $\approx 8000$  m) (WALLACE AND HOBBS 1977). In analogy to the regressive approach described in chapter 4.1.2, the residuals representing local deviations from the elevation dependence given by Eq. 4.63, are calculated for each grid cell of the RCM by using the coarse terrain elevation of the RCM and the surface pressure simulations. The correction of the high resolution surface pressure

computations with the interpolated residuals forces the interpolated pressure fields through the simulations, which are spatially referenced to the source grid centers.

Alternatively to the correction of high resolution surface pressure calculations with coarse resolution RCM simulations, a remapping method is implemented that directly adjusts coarse surface pressure simulations using subgrid topography in the spatial resolution of the land surface model. According to COSGROVE ET AL. (2003), a high resolution atmospheric pressure  $p_{ls}$  can be calculated using spatially interpolated pressure simulations  $sp_{clim\_int}$  in form of

$$sp_{ls} = \frac{sp_{clim\_int}}{\exp\left(\frac{g\Delta z}{R_g T_{mean}}\right)} \quad \text{Eq. 4.64}$$

where  $g$  is gravity,  $\Delta z$  is the difference in elevation between the interpolated climate model elevation and the elevation in the spatial resolution of the land surface model,  $R_g$  is the gas constant and  $T_{mean}$  is the mean air temperature [K] assumed to be

$$T_{mean} = [(t_{clim\_int} + t_{ls}) \cdot 0.5] + 273.16 \quad \text{Eq. 4.65}$$

with  $T_{clim\_int}$  representing the directly interpolated climate model temperature and  $T_{ls}$  the air temperature in the spatial resolution of the land surface grid [°C].

#### 4.2.9 METHOD DISCUSSION

The downscaling techniques embedded in SCALMET to adequately remap coarse RCM outputs have been presented in the previous chapters. As has been shown, the majority of the required meteorological variables can be remapped using different approaches. This offers the option to comparatively analyze the different scaling techniques (see chapter Fig. 5.2) and accounts for the fact that different approaches might be most suitable depending on the concrete application. The data available for the regression analysis for example are a function of the spatial resolution of the RCM and the size of LSM domain. While the relatively high spatial resolution of the regional climate model REMO (10 x 10 km) in combination with the spatial extent of the UD provides a large enough sample size for the regression based remapping, the rather low spatial resolutions provided by other RCMs might limit the statistical sample size and therefore constrain the applicability of the regression approach. Besides its limiting effect concerning the available climate model simulations for a given area of interest, a relatively coarse climate model resolution largely levels elevation extremes and thus leads to an increasing degree of extrapolation beyond the elevations used within the regression analysis whenever the regression function is used for the calculation of high

resolution meteorological fields. Moreover, comparatively coarse spatial resolutions raise the risk that horizontal gradients (e.g. gradients in precipitation) are interpreted as vertical gradients within the regression based remapping. Hence, constant lapse rates in some cases might be preferable for the downscaling of rather coarse RCM output (e.g. 50 x 50 km).

Another issue that influences the applicability of some of the presented methods is their need for an adaptation to the prevailing climate conditions in the area of interest. As has been pointed out in the last chapters, lapse rates (temperature, dewpoint temperature) and adjustment factors (precipitation) are subject to large variations over space and time.

Although the adjustment of the required scaling parameters is rather simple, the required meteorological data might not be available in some regions of the earth, due to a too sparse net of meteorological observations. The regression based approach does not need any adjustments as it is completely free of any parameterization. While parameterized elevation corrections are only valid for present climate conditions and can not be assumed to be stable in the future, the regression approach is unrestrictedly applicable on future climate conditions.

### 4.3 UPSCALING OF LAND SURFACE MODEL OUTPUTS

The term ‘upscaling’ as it is used in the following paragraphs denotes the process of remapping fluxes from the finer spatial resolution of the land surface to the comparatively coarse resolution of the atmosphere. Fluxes that can currently be provided as inputs for RCMs in two-way coupled model runs are:

- Latent heat flux [ $\text{W}/\text{m}^2$ ]
- Sensible heat flux [ $\text{W}/\text{m}^2$ ]
- Momentum flux [ $\text{Pa}$ ]
- Reflected shortwave radiation [ $\text{W}/\text{m}^2$ ]
- Outgoing longwave radiation [ $\text{W}/\text{m}^2$ ]

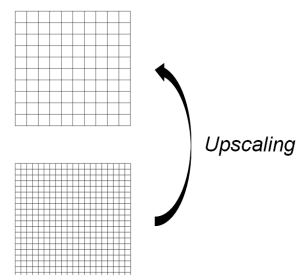


Fig. 4.23: Illustration of the upscaling process.

Heat and radiative fluxes as well as the momentum flux are calculated within the land surface energy and mass balance component in PROMET (see chapter 3.1.2).

Apart from its importance in fully coupled model runs, the remapping from coarse to fine resolutions states an important element within the different downscaling techniques described in the preceding chapters. Whenever fluxes need to be compared between the

scales, the remapped meteorological fields are required to be aggregated to the spatial resolution of the RCM in a conservative manner. Compared to the rather complex remapping algorithms that are needed to adequately bridge the gap from the coarse climate model resolution to the finer land surface grid, the process of upscaling land surface calculations is rather simple. As all fluxes that are provided as inputs for climate models scale linearly, the upscaling merely consists of computing the area weighted mean value of all land surface pixels that are at least partly overlapped by a considered RCM pixel. The technical prerequisites are given by the implementation of the conservative remapping method (JONES 1998b) which allows a conservative treatment of all land surface fluxes within the remapping from the fine spatial resolution of the land surface to the resolution of the RCM. In analogy to the weights needed for remapping from coarse to fine resolutions, the weights for the contrary remapping direction are calculated at the beginning of the coupled model run or can optionally be read from file.

## 5 APPLICATION TO PAST CLIMATE CONDITIONS

The following chapters will attempt to quantify the uncertainties that are included in the different models of the coupled model system (REMO-SCALMET-PROMET). In a first step the performance of the land surface model PROMET will be shown for past climate conditions. In a second step uncertainties related to the downscaling of the meteorological fields with SCALMET will be pointed out. This is done by aggregating meteorological observations provided by the meteorological preprocessor in PROMET to the spatial resolution of REMO. In analogy to the application of re-analysis data as 'perfect boundaries' in regional climate modeling, these aggregated observations serve as 'perfect boundaries' for the downscaling in SCALMET, excluding biases that are possibly included within climate simulations. The downscaling results are later compared to meteorological observations, allowing an evaluation of the performance of the different approaches. Besides the comparison to meteorological observations, the remapped fields are used as meteorological forcings in PROMET. The latter offers the option to quantify the direct impact of the downscaling upon the water cycle. Finally, the analysis of coupled model runs using REMO climate simulations for past climate conditions in the Upper Danube watershed will give an overall impression of the uncertainties arising from the combination of all involved models (REMO, SCALMET and PROMET). Comparing discharge simulations with measurements at the gauge in Achleiten will analyze the coupled model's ability to reproduce past hydrological conditions in the UD.

### 5.1 VALIDATION OF THE LAND SURFACE MODEL PROMET

The following chapter aims at clarifying PROMET's ability to reproduce the determinant hydrological processes in the UD for past climate conditions without applying any area specific calibrations. As the model has been exhaustively validated in a recent study by MAUSER AND BACH (2008) using meteorological observations to drive the hydrological model, only a brief survey of the model performance will be given in the framework of the present work.

In order to show the model's ability to simulate river discharge conditions in the UD, the modeled daily stream flow is compared to discharge measurements at the Gauge of the watershed in Achleiten. The simulated daily stream flow is generated by aggregating hourly simulations to daily values. The data presented in Fig. 5.1 shows the aggregated stream flow over the period 1971-2000 for the proxel representing the gauge in Achleiten together with discharge measurements.

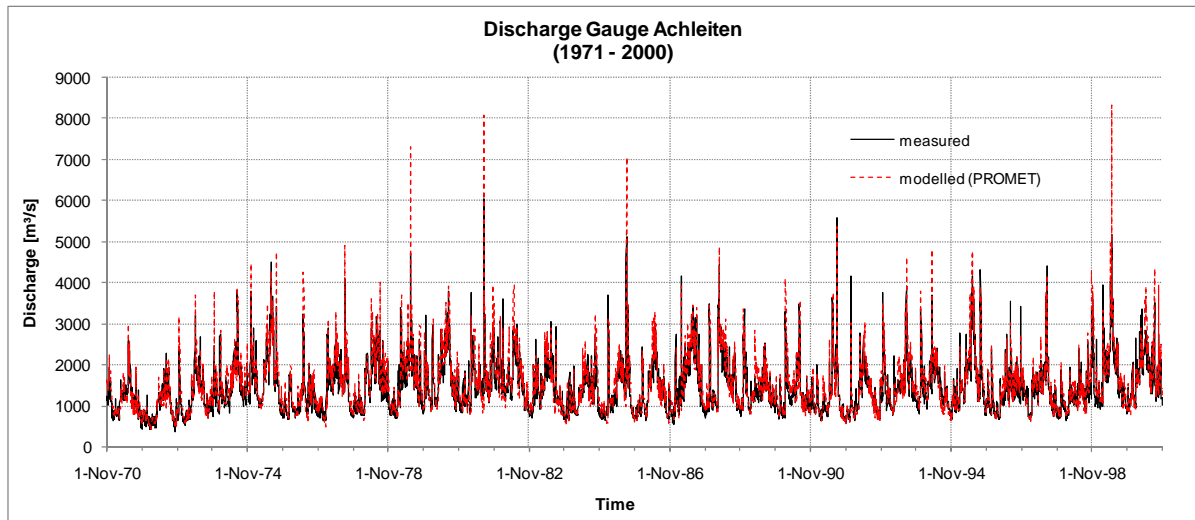


Fig. 5.1: PROMET discharge simulations for the proxel representing the gauge in Achleiten. The displayed daily values have been calculated on the basis of hourly simulations for the hydrological years 1971-2000.

The chronological sequence above is accompanied by a regression based comparison illustrated in Fig. 5.2. Both illustrations show a good reproduction of the stream flow on a daily basis.

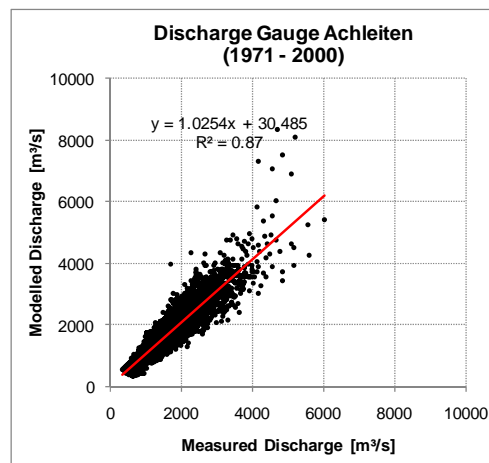


Fig. 5.2: Simulated vs. measured daily discharge at the gauge of the Upper Danube watershed in Achleiten.

The illustrations lead to the conclusion that PROMET is able to model the daily and seasonal variability of water fluxes in the UD with good accuracy. Apart from the validation examples presented above, MAUSER AND BACH (2008) validated the model by:

- comparing the annual modeled water balance with measured annual runoff volumes for the UD and individual subcatchments (1971-2003)

- extending the comparison between daily discharge simulations and daily discharge recordings to several subcatchments
- comparing hourly discharge simulations to hourly discharge recordings
- comparing modeled and measured annual peak discharge volumes
- comparing modeled and measured annual 7-day average low-flow discharge volumes
- comparing modeled and measured flood and low-flow return periods

The validation of the water balance carried out by MAUSER AND BACH (2008) proved that the spatially distributed precipitation amounts together with the simulated evapotranspiration allow to reproduce the long-term runoff volumes as well as their inter-annual variability. The analysis of daily discharge simulations shown for the gauge in Achleiten in Fig. 5.1 and Fig. 5.2 has been extended to several subcatchments of the UD by MAUSER AND BACH (2008). As could be shown, the quality of simulated daily discharge is very good in general with a slight tendency to decrease with decreasing catchment size. As MAUSER AND BACH (2008) could further demonstrate on the example of the flood wave during August 1995, PROMET is able to reproduce hourly discharge with a high level of accuracy. The analysis of extreme events in case of peak discharge volumes showed an overestimation of approximately 16 %. An explanation is given by the fact that the reduction in river discharge due to inundations during flood events is not accounted for in the current version of PROMET. The annual 7-days average low-flow could be reproduced with good accuracy and a small overall bias. Finally, the analysis of modeled flood and low-flow periods carried out by MAUSER AND BACH (2008) show a good agreement with observed return periods with a slight tendency for the simulations to overestimate flood and low-flow discharge volumes for longer return periods. For a more detailed description of the model validation briefly summarized above it is referred to MAUSER AND BACH (2008).

## 5.2 EVALUATION OF THE SCALING METHODS IN SCALMET

In order to show SCALMET's capability to generate high resolution distributions on the basis of a coarse meteorological input grid, the spatially distributed observations provided by the meteorological preprocessor in PROMET are remapped to the grid of the regional climate model REMO. This synthetically derived coarse grid meteorology is redistributed to the finer resolution of the land surface grid in order to examine to what degree SCALMET is able to

reproduce station observations. Further validation is carried out by forcing the hydrological model PROMET with the redistributed meteorology. In combination with hydrological simulations driven by the original meteorological fields this approach gives an impression of the noise related to the scaling of the meteorological fields and its impact on hydrology.

### 5.2.1 METEOROLOGICAL METHOD COMPARISON

The data used for the comparison of the redistributed meteorology with meteorological observations in the framework of this synthetic approach cover the years 1994-1996. Although this time period clearly falls below the standard climate period of 30 years, the general accuracy of the remapping process is expected to be well reflected, even if working with a rather short period of time. The comparison with observations is constrained to those meteorological variables that have been recorded by the meteorological network in the UD (see chapter 3.1.1.2). Hence, the comparison of measured and redistributed values will only be carried out for temperature, precipitation, wind speed and global radiation. Global radiation holds an exceptional position as the incoming radiation that has been redistributed by SCALMET is not based on direct measurements (see chapter 3.1.1.3). A comparison of the redistributed solar radiation therefore includes both, the uncertainties related to the generation of shortwave radiation by PROMET as well as those occurring within the redistribution by SCALMET. Thus an impression is given how well the indirect calculation of solar radiation reproduces the radiative conditions at the climate stations.

Validation for all meteorological variables is carried out on a daily time basis for two reasons. First the meteorological observations are not available on an hourly basis for the majority of the remapped variables. As has been described in chapter 3.1.1, meteorological variables are recorded three times a day with partly varying recording times for the different meteorological parameters and meteorological stations. The second reason for choosing daily values is that the meteorological input distributions themselves do not necessarily represent the observations even if referred to at the exact time and place of the measurement. Precipitation amounts for example are distributed over the time between the measurements, based on several assumptions described in detail in chapter 3.1.1.1. The comparison of daily values minimizes the influence of the temporal interpolation and therefore seems to be an adequate basis for a comparative analysis.

The analysis is carried out on a pixel basis. While a comparison of station (point) recordings with a pixel based (area) remapping, at least in the case of temperature, would require to correct either the observation or the remapping result with respect to the elevation difference between the station altitude and the mean pixel altitude, a methodically consistent and

technically convenient method is given by a direct comparison of pixel values at the locations of the climate stations. For the validation of temperature, precipitation and wind speed remappings, the total number of 377 available climate stations (see chapter 3.1.1) has been reduced to a subset of 73 stations utilizing only

- Stations within the PROMET model domain (Upper Danube watershed)
- Stations that have recorded over the whole period of time (1994-1996)
- Stations that are located in highly complex topographic terrain

The latter seems to be reasonable as all of the described remapping methods are based on topographic corrections. It is obvious that only in complex terrain these techniques unfold their potential and are capable to qualitatively adjust the coarse grid information beyond the possibilities of direct interpolation methods. Including the large number of stations located in the relatively flat terrain of the Alpine Foreland would therefore only weaken the expressiveness of the following analysis as mean errors would notably decrease due to the overrepresentation of stations in flat terrain.

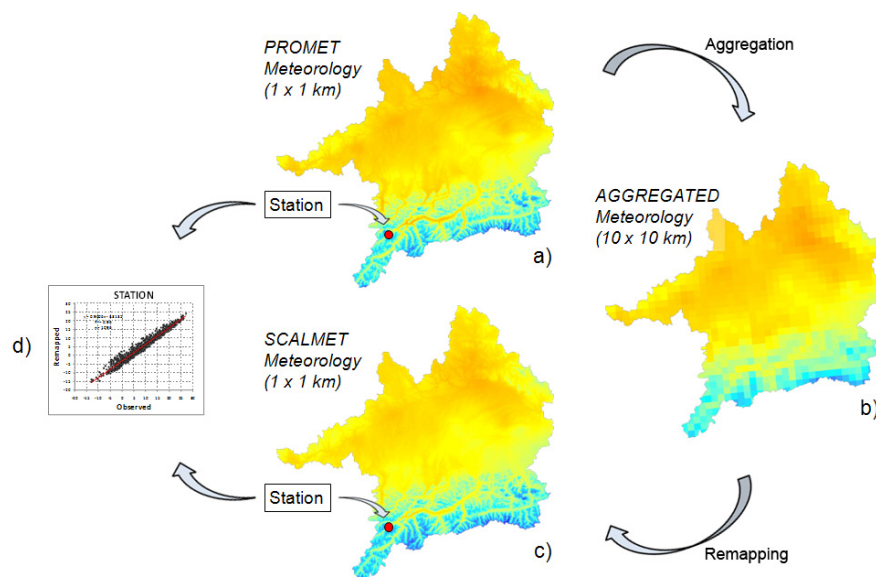


Fig. 5.3: Schematic illustration of the processing of observation based meteorological distributions (PROMET) for the later evaluation of the different remapping approaches (SCALMET). The distributions provided by the meteorological preprocessor in PROMET (a) are aggregated offline from a spatial resolution of 1 x 1 km to 10 x 10 km (b). The aggregated distributions are remapped from 10 x 10 km to a spatial resolution of 1 x 1 km (c). Finally the remapped distributions are compared to the input distributions at the pixels representing the meteorological stations used for the generation of the meteorological fields in PROMET (d).

As Fig. 5.3 shows, the spatially distributed station meteorology is first conservatively transferred to the rotated REMO grid at a spatial resolution of 10 x 10 km. The resulting coarse grid meteorology is then treated the same way as RCM simulations. It is remapped by



remapping results are shown in contrast to those achievable by a direct interpolation using the bilinear and conservative techniques presented in chapter 4.1.1.

Tab. 5.1: Elevation and geographical coordinates of the stations St. Leonhard-Neurur (Austria), Jenbach (Austria), Rauris (Austria) and Weihenstephan (Germany).

Map Number	Station Name	Station Elevation [m.a.s.l.]	DEM 1 x 1 km [m.a.s.l.]	DEM 10 x 10 km [m.a.s.l.]	Latitude [°]	Longitude [°]
1	St. Leonhard-Neurur	1462	1730	2458	47.02	10.86
2	Jenbach	530	527	1341	47.39	11.75
3	Rauris	931	1022	1530	47.22	12.99
4	Weihenstephan	470	485	468	48.40	11.70

#### 5.2.1.1 TEMPERATURE

For the distribution of temperature simulations two remapping approaches, both based on altitudinal corrections, have been presented (see chapter 4.2.2). One is the application of constant monthly temperature lapse rates as proposed by LISTON AND ELDER (2006) or KUNKEL (1989) which will be related to in the following as the constant lapse rate remapping (CLR). The second technique makes use of the temperature-elevation dependence within a run-time statistical data analysis, similar to the approach proposed by MAUSER AND BACH (2008). It will be denoted as the regression based remapping (RBR) in the following. The performance of these two remapping approaches will be shown in comparison to the remapping methods of a bilinear interpolation (BI) and a conservative interpolation (CI).

Fig. 5.5 shows the correlation between the observed daily mean temperatures, represented by the input pixel values at the station locations, and the simulated daily mean temperatures, given by the pixel values of the remapping results at the station locations for three Alpine climate stations over the period 1994-1996. The chosen stations represent three different elevation belts covering altitudes from 530 m.a.s.l. (climate station in Jenbach) to 1463 m.a.s.l. (climate station in St. Leonhard-Neurur). Detailed information about the stations represented in the diagrams is given in Tab. 5.1, information about all 73 stations used in the analysis together with the results of the analysis for all stations can be found in the appendix (see A-7). The coefficient of determination is close to 1 for all remapping approaches, indicating that the correlation between the input data and the remapping result in general is very high at the pixels representing the different station locations.

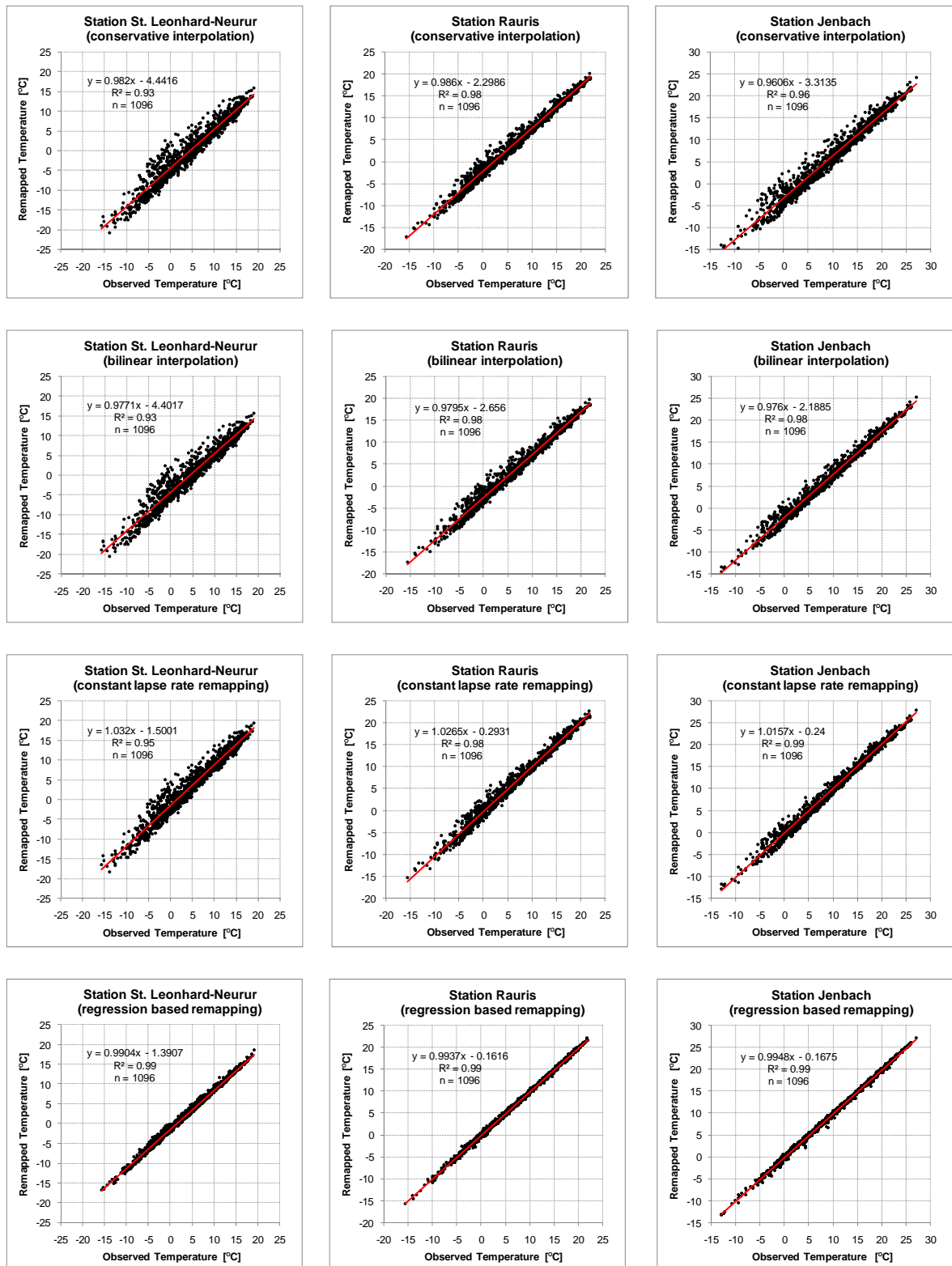


Fig. 5.5: Comparison of remapped and observed daily temperatures at the three climate stations in St. Leonhard-Neurur (left), Rauris (middle) and Jenbach (right) for the period 1994-1996. The graphs show the results of a direct conservative interpolation (CI), a bilinear interpolation (BI), the constant lapse rate remapping (CLR) and the regression based remapping (RBR).

The coefficients of determination further indicate that almost all of the total variance within the observations is explained by the respective remapping results. This is not hard to explain,

considering the fact that the temporal dynamics in local temperature is predetermined by the aggregated station meteorology.

Taking a closer look at the regression line, the intercepts manifest a constant underestimation of temperature for the direct interpolation methods at all stations. An explanation is given by the fact that neither of the direct interpolation methods accounts for the subgrid variability of orography. Temperatures at pixels in higher elevations than the mean elevation of the associated 10 x 10 km pixel are consequently overestimated, whereas temperatures at pixels in elevations lower than the 10 x 10 km mean elevation are underestimated by a direct interpolation in most cases. The altitudinal difference resulting from the spatial resolution of the two grids involved in the remapping process is illustrated in Fig. 5.6.

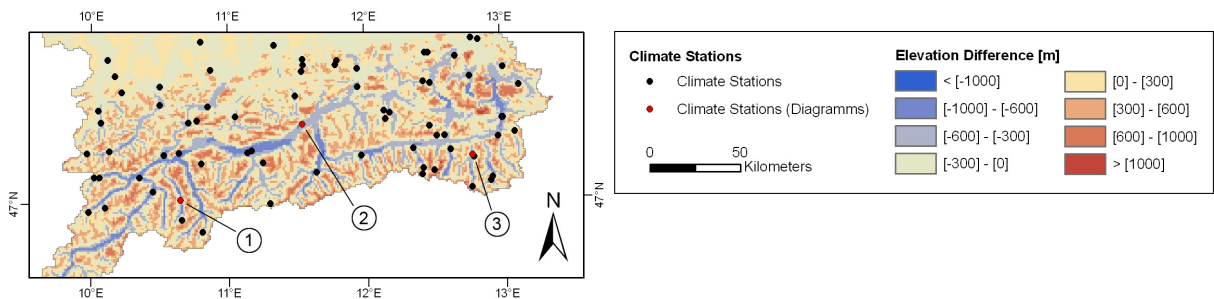


Fig. 5.6: Elevation difference (DEM 1 x 1 km - DEM 10 x 10 km) for the Alpine part of the Upper Danube watershed. The numbers are aligned to the stations St. Leonhard-Neurur (1), Jenbach (2) and Rauris (3).

As shown all three climate stations for a spatial resolution of 1 x 1 km are located in pixels characterized by lower altitudes than the altitude of the associated coarse grid pixel (10 x 10 km). The constant temperature underestimation reflected by the remapping results of the direct interpolation methods (CI and BI) is severely minimized by those remapping methods that apply elevation corrections within the remapping process (CLR and RBR).

The slope of the regression lines is close to 1 for all remapping methods, indicating that the method's ability to reproduce the observations is of similar efficiency over the whole range of daily temperature values. While the coefficients of determination are generally close to 1 for all remapping methods, highest values are found in case of the RBR, followed by the CLR. Similar to the coefficients of determination, the model efficiency described by the Nash-Sutcliffe Coefficient (NASH AND SUTCLIFFE 1970) is very high for all methods. The mean model efficiency considered over the whole period of time (1994-1996) at all 73 stations takes values of 0.93 ( $\text{std\_dev}_{\text{stations}} = 0.09$ ) for both interpolation methods, 0.99 ( $\text{std\_dev}_{\text{stations}} = 0.01$ ) for the CLR and 1.00 ( $\text{std\_dev}_{\text{stations}} = 0.01$ ) for the RBR.

Since the values of the coefficient of determination and the Nash-Sutcliffe model efficiency are close to saturation (1.00), the mean absolute error (MAE) is consulted to serve as an

additional efficiency criterion. While the direct interpolation methods are characterized by mean absolute errors of  $1.59\text{ }^{\circ}\text{C}$  ( $\text{std\_dev}_{\text{stations}} = 1.06\text{ }^{\circ}\text{C}$ ) and  $1.56\text{ }^{\circ}\text{C}$  ( $\text{std\_dev}_{\text{stations}} = 1.06\text{ }^{\circ}\text{C}$ ) for the CI and the BI respectively, the temperature-elevation corrections within the CLR and the RBR notably reduce the mean absolute errors to  $0.52\text{ }^{\circ}\text{C}$  ( $\text{std\_dev}_{\text{stations}} = 0.34\text{ }^{\circ}\text{C}$ ) and  $0.31\text{ }^{\circ}\text{C}$  ( $\text{std\_dev}_{\text{stations}} = 0.28\text{ }^{\circ}\text{C}$ ) respectively. Fig. 5.7 shows the frequency distribution of the MAE, averaged over all 73 stations, related to all considered remapping methods. As can be seen, the methods of the CI and BI lead to a frequent occurrence of comparatively high MAEs.

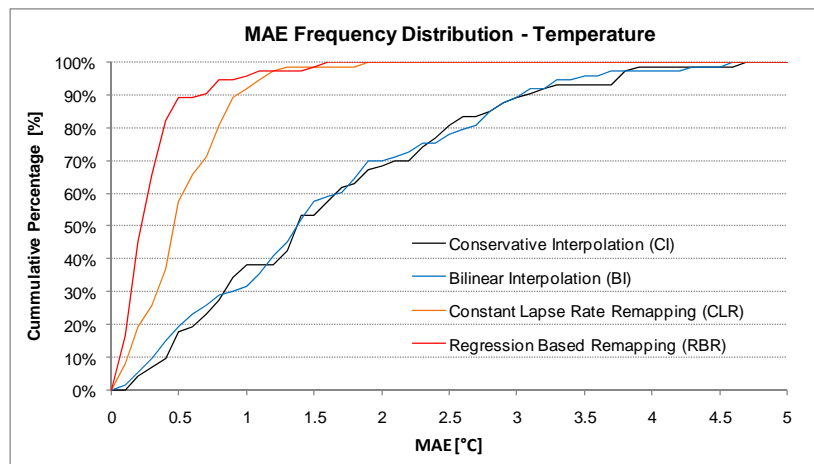


Fig. 5.7: Frequency distribution of the mean absolute error (MAE) in temperature remappings for the conservative interpolation (CI), the bilinear interpolation (BI), the constant lapse rate remapping (CLR) and the regression based remapping (RBR) for the period 1994-1996.

As displayed, the MAE is clearly shifted towards lower values as soon as temperature is corrected for the influence of subgrid elevation. The illustration, in accordance with the analysis of all other statistic criteria used within the evaluation of the different remapping approaches above, manifests that the regression based remapping (RBR) shows the best overall performance in the remapping of coarse grid temperature fields, at least for the current grid constellation ( $10\text{ x }10\text{ km} \rightarrow 1\text{ x }1\text{ km}$ ). A complete survey of the MAE at all 73 stations is given in the appendix (see A-8). The results of all remapping methods included in the analysis are shown in Fig. 5.8. As shown, the inclusion of elevation corrections leads to a more realistic reproduction of the natural climate system. While the mean values is preserved over the model domain, the regression based remapping as well as the constant lapse rate remapping lead to slightly higher temperature extremes in lower elevations and to notably lower temperatures in the higher elevated parts of the Alps. Further the graphic unfolds that both elevation corrections considering the annual mean temperature lead to very similar results. Part of this effect is well explicable considering the fact that the energy to be distributed over each  $10\text{ x }10\text{ km}$  area is predetermined by the RCM meteorology. However,

the regression based method can be expected to better reflect the actual atmospheric conditions on a shorter time basis compared to an application of monthly constant lapse rates, particularly as it allows to account for temperature inversions (see chapter 4.2.2.1).

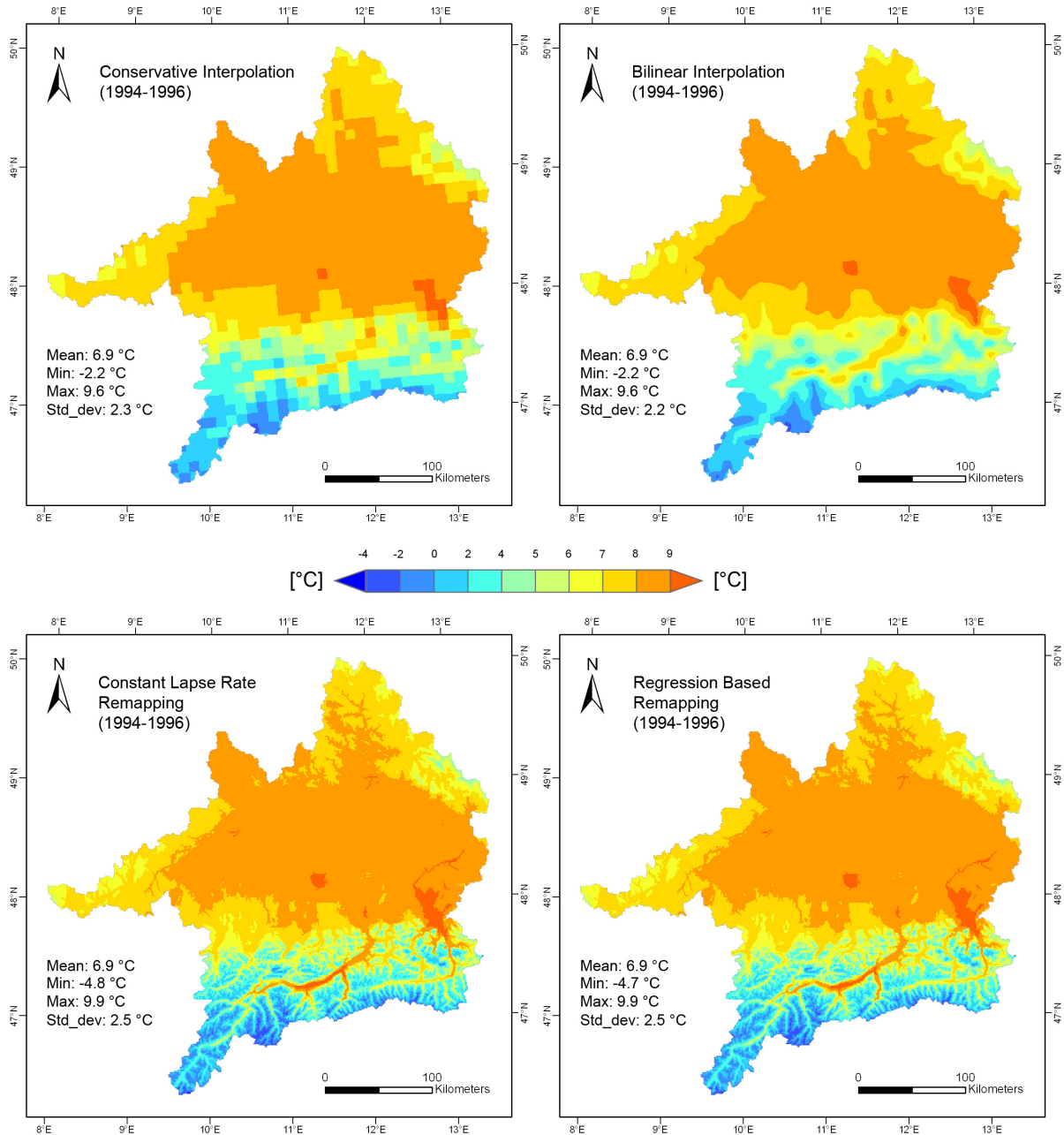


Fig. 5.8: Results of the temperature remappings carried out within the synthetic evaluation approach. The maps represent the annual mean temperature for the period 1994-1996.

### 5.2.1.2 PRECIPITATION

For the remapping of precipitation two methods have been described in the preceding chapters of this work. One is the elevation correction of simulated rainfall by means of a

precipitation factor as proposed by LISTON AND ELDER (2006) and THORNTON ET AL. (1997) which will be referred to in the following as the adjustment factor remapping (AFR). The other method presented is a regression based remapping approach similar to the approach proposed by MAUSER AND BACH (2008), referred to in the following as the regression based remapping (RBR). In analogy to the analysis of temperature remappings, these techniques are confronted with the results of direct interpolation methods (BI and CI). The remapping results of all methods considered are displayed in Fig. 5.9.

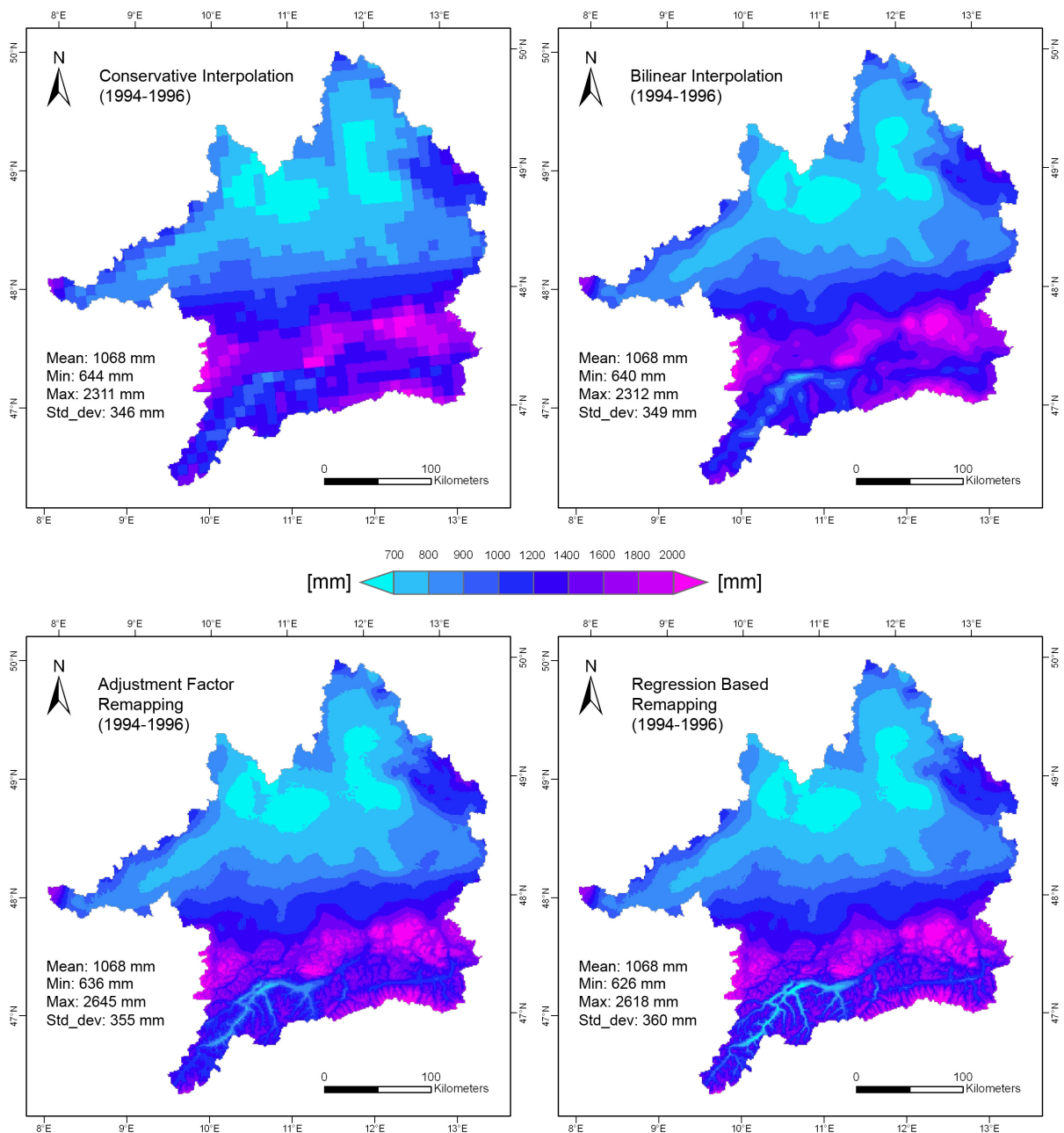
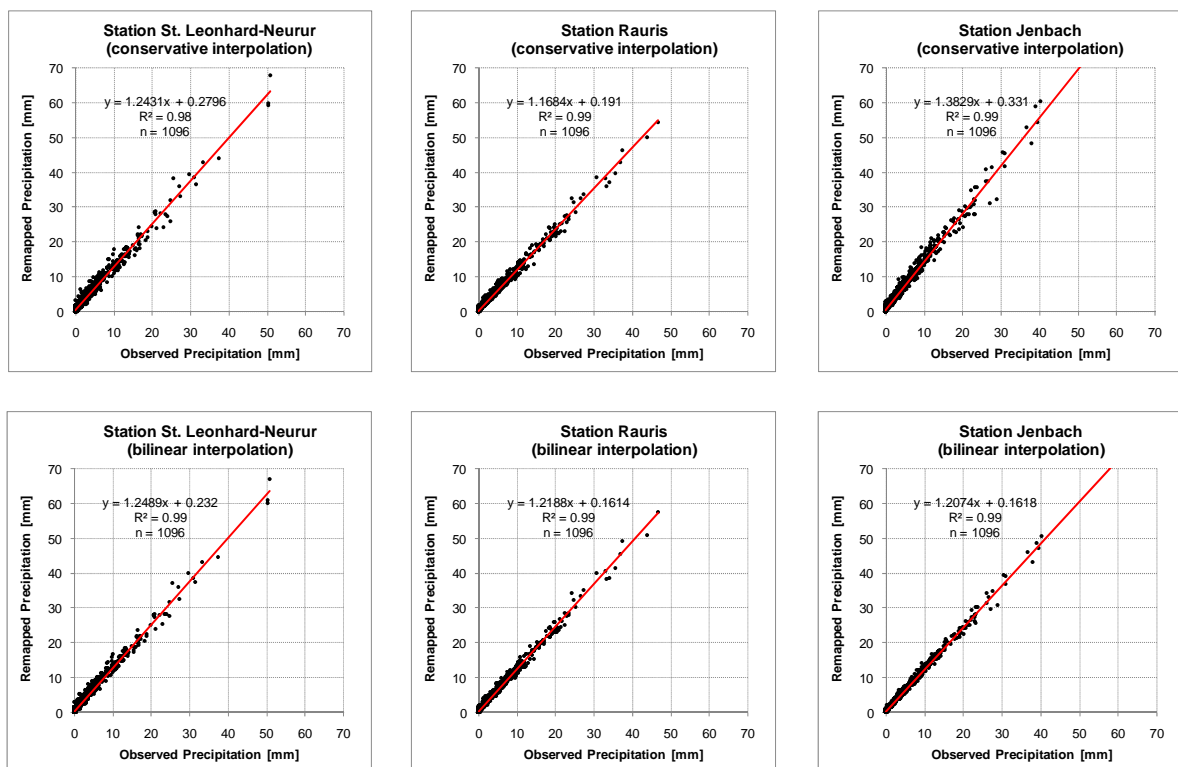


Fig. 5.9: Results of the precipitation remappings carried out within the synthetic evaluation approach. The maps represent the average accumulated precipitation for the period 1994-1996.

As can be seen the conservative interpolation (CI) results in a precipitation distribution that fully follows the grid structure of the coarse grid meteorological inputs (10 x 10 km). While the bilinear interpolation (BI) in large parts of the Alpine Foreland yields results comparable to those of the adjustment factor remapping (AFR) and the regression based remapping (RBR), the small scale orographic variability in Alpine regions is not reflected in the results of the BI. The methods of the AFR and the RBR result in very similar distributions, with a slightly higher elevation sensitivity for the RBR. The latter is also reflected in the standard deviation which increases from the direct interpolation methods over the AFR up to a value of 360 mm for the RBR. The average annual precipitation in the UD for the hydrological years 1994 to 1996 takes a value of 1068 mm for all considered remapping methods.

Continuing the evaluation of the precipitation remappings, the remapped precipitation at those pixels containing the climate stations in St. Leonhard-Neurur, Rauris and Jenbach in a spatial resolution of 1 x 1 km is compared to daily rain gauges at the climate stations (see Fig. 5.10). As has already been experienced in connection with temperature remappings, for the current grid constellation even the direct interpolation techniques are capable of reproducing the general dynamics in daily precipitation, resulting in very high coefficients of determination for all remapping methods. Compared to the coefficients of determination of the RBR, the direct interpolation of rainfall sometimes even leads to higher coefficients of determination at the stations shown in the diagrams.



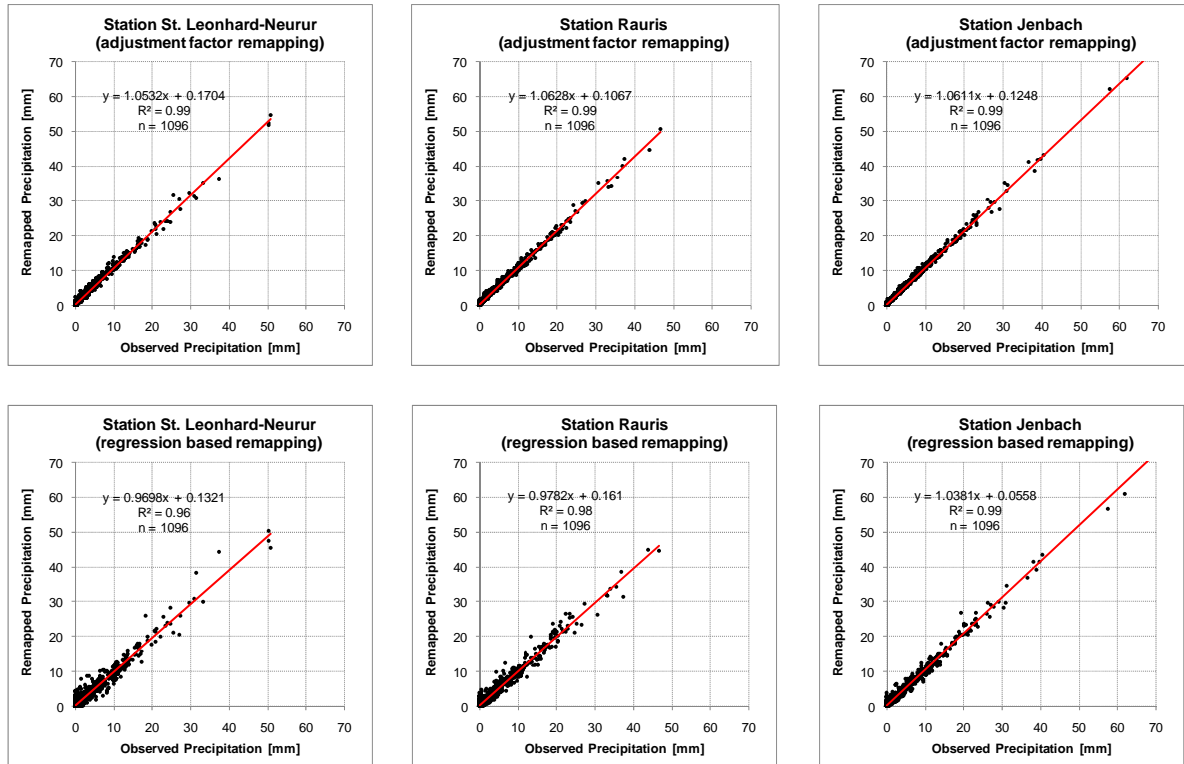


Fig. 5.10: Comparison of remapped and observed daily precipitation at the three climate stations in St. Leonhard-Neurur (left), Rauris (middle) and Jenbach (right) for the period 1994-1996. The graphs show the results of a conservative interpolation (CI), a bilinear interpolation (BI), the adjustment factor remapping (AFR) and the regression based remapping (RBR).

However, the slopes of the regression lines with values significantly greater than 1 show an overestimation of precipitation which is increasing with increasing precipitation amounts for the stations pictured above. With slopes near 1, both remapping methods including elevation corrections within the remapping process (AFR and RBR) clearly reduce this overestimation. The mean Nash-Sutcliffe model efficiency of all 73 stations is close to 1 for all remapping options, ranging from 0.96 ( $\text{std\_dev}_{\text{stations}} = 0.06$ ) and 0.97 ( $\text{std\_dev}_{\text{stations}} = 0.04$ ) for the direct interpolation techniques of the CI and BI respectively to values of 0.98 ( $\text{std\_dev}_{\text{stations}} = 0.03$ ) for the AFR and 0.97 ( $\text{std\_dev}_{\text{stations}} = 0.03$ ) for the RBR. In analogy to the coefficient of determination the high model efficiency can be explained by the fact that dynamics in precipitation amount and occurrence is predetermined by the coarse grid meteorology (10 x 10 km) to a large degree.

Considering the MAE for all 73 stations, highest values occur in combination with the CI (0.56 mm,  $\text{std\_dev}_{\text{stations}} = 0.3$  mm) and the BI (0.48 mm,  $\text{std\_dev}_{\text{stations}} = 0.3$  mm). The elevation corrections performed by the AFR and the RBR slightly decrease the MAE to values of 0.35 mm ( $\text{std\_dev}_{\text{stations}} = 0.25$ ) and 0.45 ( $\text{std\_dev}_{\text{stations}} = 0.27$ ) respectively. Fig. 5.11 shows the frequency distribution of the MAE for all remapping methods. As shown, the CI scheme introduces largest biases within the remapping process. The BI performs slightly better but still shows considerable MAEs in higher ranges, whereas the elevation

adjustments within precipitation remappings noticeably lower the occurrence of MAEs in higher MAE ranges.

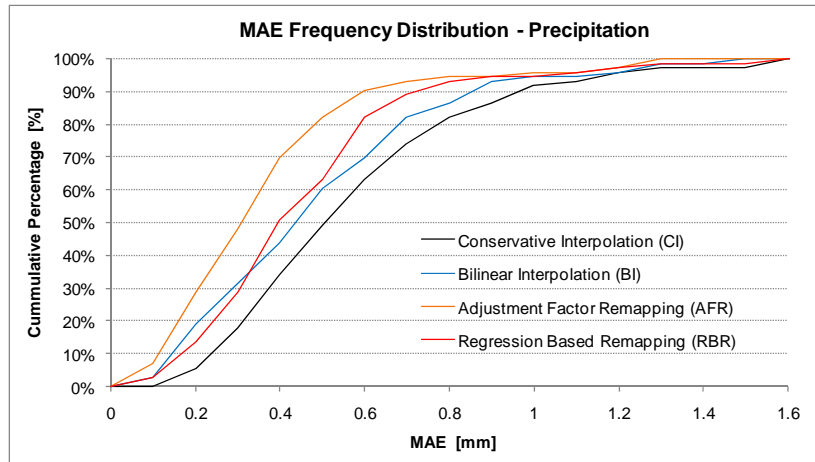


Fig. 5.11: Frequency distribution of the mean absolute error (MAE) in precipitation remappings for the different remapping methods over the period 1994-1996.

Compared to the RBR, the AFR remapping shows a slightly better performance. Obviously, the monthly adjustment factors better reflect the precipitation-elevation dependence than the regression functions that are derived on the basis of hourly precipitation distributions at a spatial resolution of 10 x 10 km. A complete picture of the remapping results for the different years and all 73 stations is given in the appendix (see A-9).

### 5.2.1.3 WIND SPEED

For the distribution of wind speed two approaches have been implemented in SCALMET. Both methods apply subgrid topographic corrections within the remapping process. Since the wind model proposed by LISTON AND STURM (1998) and LISTON AND ELDER (2006) requires information on the wind u- and v-components, which do not belong to the standard recordings at the climate stations, the following meteorological evaluation is constrained to the regression based remapping (RBR). The RBR results together with the results of the direct interpolation techniques are shown for three Alpine stations in Fig. 5.12.

The inclusion of elevation corrections in the remapping process increases the coefficient of determination at all stations considered in the analysis. In analogy to the coefficients of determination the Nash-Sutcliffe efficiency takes lower values for the remapping of wind speed than for the remapping of temperature and precipitation.

The mean model efficiency over all 73 climate stations increases from values of 0.53 ( $\text{std\_dev}_{\text{stations}} = 0.60$ ) and 0.55 ( $\text{std\_dev}_{\text{stations}} = 0.62$ ) for the CI and BI respectively, to a mean model efficiency of 0.73 ( $\text{std\_dev}_{\text{stations}} = 0.35$ ) for the RBR.

While the scattering around the regression line is similar within the direct interpolation methods of the CI and BI, the occurrence of outliers is strongly reduced in the RBR. Considering the MAE over all 73 stations, the CI and the BI show values of 0.49 ( $\text{std\_dev}_{\text{stations}} = 0.35$ ) and 0.46 ( $\text{std\_dev}_{\text{stations}} = 0.36$ ) respectively.

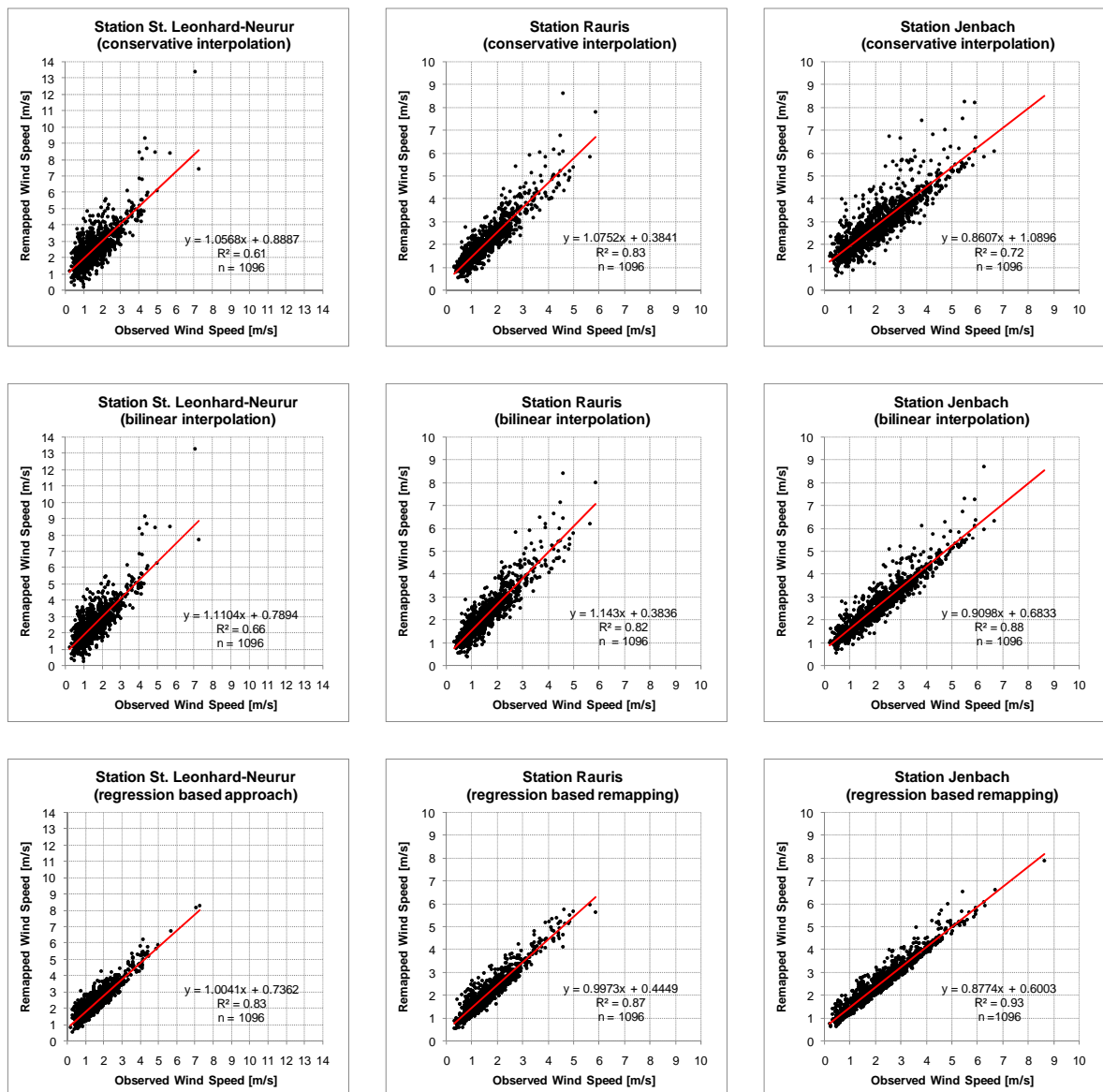


Fig. 5.12: Comparison of remapped and observed daily wind speeds at climate stations in St. Leonhard-Neurur (left), Rauris (middle) and Jenbach (right). The graphs show the results of a conservative interpolation (CI), a bilinear interpolation (BI) and the regression based remapping (RBR).

The application of elevation corrections within the remapping decreases the MAEs to 0.37 ( $\text{std\_dev}_{\text{stations}} = 0.32$ ) for the RBR. Fig. 5.13 shows the MAE frequency distribution for all remapping methods.

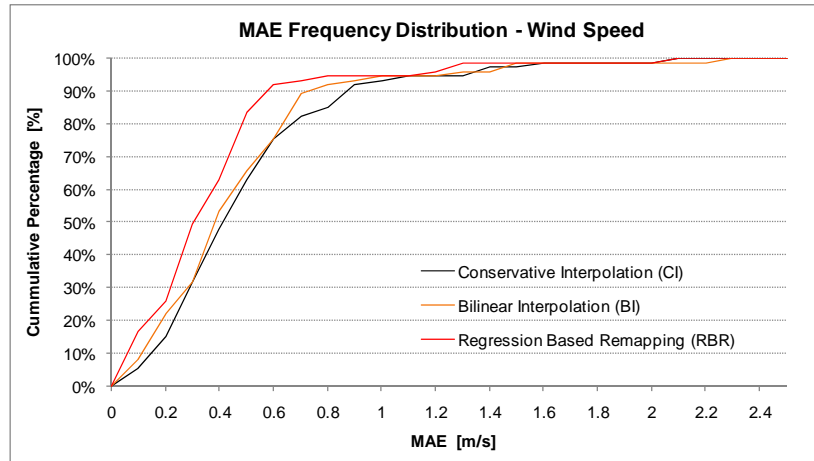


Fig. 5.13: Frequency distribution of the mean absolute error (MAE) in wind speed remappings for the conservative interpolation (CI), the bilinear interpolation (BI) and the regression based remapping (RBR) for the period 1994-1996.

The illustration proves that the inclusion of elevation corrections is able to reduce the occurrence of MAEs in higher error ranges compared to the direct interpolation techniques. For the MAEs at all 73 climate stations refer to the appendix (A-10).

#### 5.2.1.4 SHORTWAVE RADIATION

The quality assessment for shortwave radiation remappings slightly differs from the preceding validation of temperature, precipitation and wind speed remappings. As described PROMET generates the shortwave radiation distributions that are used for the aggregation to 10 x 10 km and the later redistribution to spatial resolution of 1 x 1 km in SCALMET not on the basis of global radiation observations directly. The amount of incoming shortwave radiation is calculated as a function of a pixel's geographic location, time, topographic features and observed cloud cover (see chapter 3.1.1.3). A comparison of pixel values in the input grid with the same pixels in the remapped grid therefore would, even if the exact pixels containing the climate stations are considered, only compare the radiation submodel used in PROMET with the one used in SCALMET.

To give an impression of the accuracy of the remapping result, the remapped pixel radiation is directly compared to observations. This approach of course includes a variety of uncertainties such as

- uncertainties related to the cloud cover observations
- uncertainties occurring from the radiation model in PROMET
- uncertainties occurring from the radiation model/remapping in SCALMET
- uncertainties related to the radiation recordings at the climate stations

that have to be considered when interpreting the results. The comparison of shortwave radiation remappings with radiation measurements is carried out by utilizing recordings taken at three meteorological stations located in Hohenpeissenberg, Weihenstephan and Passau (see red dots in Fig. 5.4). The small number of stations results from the fact that only few of the 377 available climate stations record global radiation. The number is further reduced by the temporal constraint to the years 1994 to 1996. Global radiation recordings at the stations represent mean conditions over the sampling period of 1 hour. These hourly values have been aggregated to a daily mean global radiation in a first step. Days that include erratic measurements have been excluded from the analysis. The observed daily mean global radiation then is compared to the daily mean radiation at those pixels within the remapped grid that include the respective climate station in the spatial resolution of 1 x 1 km. Fig. 5.14 shows the correlation between the observed and the remapped global radiation at the climate station in Weihenstephan for the conservative interpolation (CI), the bilinear interpolation (BI) and the radiation submodel in SCALMET.

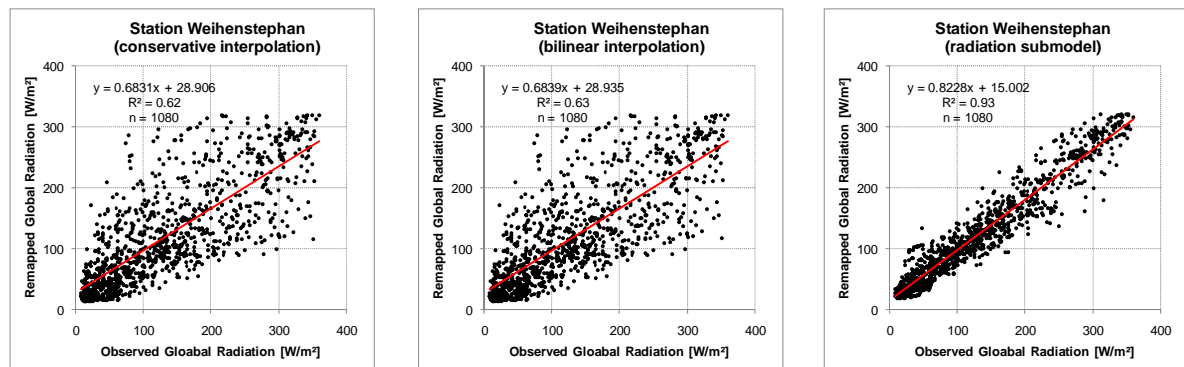


Fig. 5.14: Comparison of remapped and observed daily global radiation at the climate station Weihenstephan (Germany). The graphs show the results of a conservative interpolation (CI), a bilinear interpolation (BI) and the solar radiation submodel for the period 1994-1996.

As displayed the direct interpolation methods produce very similar results which are characterized by a moderate correlation between the observed and the remapped global radiation and large scattering of points around the regression line. The reason for this similarity can be found in the station's relative location to the pixel center. Weihenstephan is located very close to the center of the 10 x 10 km grid box. Here, the result of a bilinear

remapping is very similar to the mean conditions within the grid box, which are conserved for all underlying subpixels when the conservative interpolation method is applied.

The radiation submodel in SCALMET with a coefficient of determination of 0.93 increases the correlation compared to the direct interpolation methods. The scattering around the regression line is visibly reduced, further confirming the enhanced accordance between the observed and the remapped global radiation achieved by applying the submodel remapping approach. Considering the mean Nash-Sutcliffe model efficiency at all three stations for the time from 1994 to 1996, the inclusion of the radiation model within the remapping process enhances the model efficiency to a mean value of 0.90 ( $\text{std\_dev}_{\text{stations}} = 0.02$ ) compared to 0.54 ( $\text{std\_dev}_{\text{stations}} = 0.07$ ) for both direct interpolation methods. While the CI and the BI lead to a relatively high MAE of  $46.8 \text{ W/m}^2$  ( $\text{std\_dev}_{\text{stations}} = 4.3 \text{ W/m}^2$ ) and  $46.8 \text{ W/m}^2$  ( $\text{std\_dev}_{\text{stations}} = 4.4 \text{ W/m}^2$ ) at the stations respectively, for the radiation submodel the MAE is reduced to  $23.4 \text{ W/m}^2$  ( $\text{std\_dev}_{\text{stations}} = 2.4 \text{ W/m}^2$ ). The temporal course of radiation throughout the year 1994 is shown for the station in Weißenstephan in Fig. 5.15.

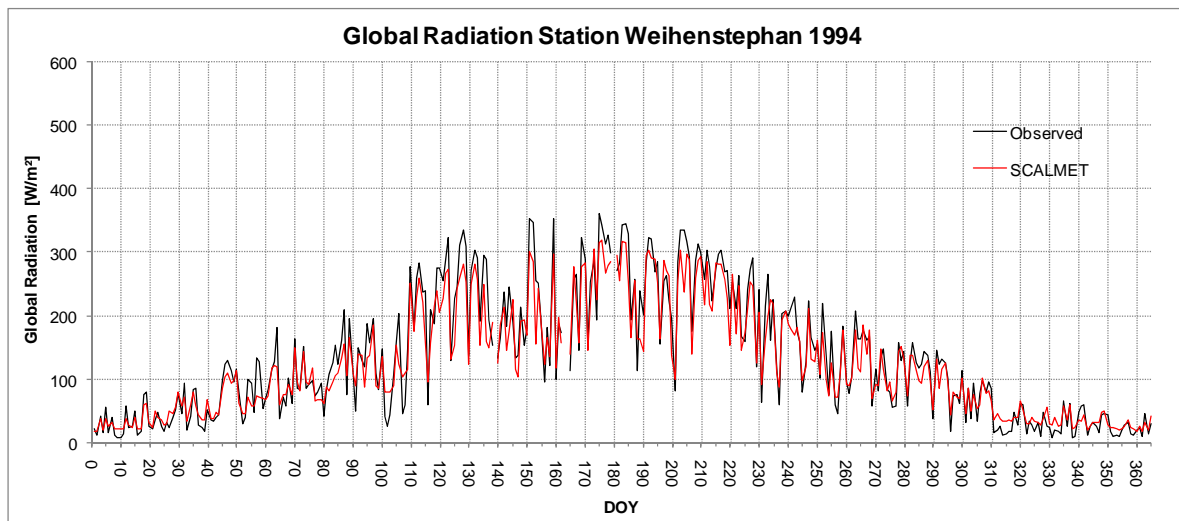


Fig. 5.15: Observed (black) and remapped (red) course of daily global radiation throughout the year 1994 at the climate station Weißenstephan. The remapped radiation represents the value of the pixel containing the climate station. The data used for the remapping in SCALMET is based on meteorological distributions provided by the meteorological preprocessor in PROMET.

The comparison of the observed and the remapped global radiation displays that the temporal changes in radiative fluxes are well reproduced, although the amplitude is slightly smoothed. Since the amplitude is a function of the radiative energy budget predetermined by the coarse grid meteorology, it can be assumed that for a given coarse grid energy budget, the approach performs well in the spatial distribution of the available radiative energy.

The last chapters have shown that the quasi-physically based scaling techniques are capable of enhancing the remapping performance compared to a direct interpolation of the meteorological variables. At the same time the results of the preceding analysis have shown,

that elevation alone, especially for the remapping of wind speed, does not explain all of the spatial variance in wind speed distributions.

## 5.2.2 HYDROLOGICAL METHOD COMPARISON

Following the meteorological evaluation of the different scaling techniques in SCALMET the hydrological impact resulting from an application of the different methods in separate PROMET runs will be examined. Unlike the preceding analysis at the stations, this hydrological comparison will always evaluate a combination of remapping methods, resulting from the remapping methods chosen for the different meteorological parameters. As the variety of methods available for each meteorological parameter principally allows a large number of different remapping combinations, the following analysis will focus on four combinations:

- Quasi-physically based approach (QPB I)
- Quasi-physically based approach (QPB II)
- Conservative interpolation (CI)
- Bilinear interpolation (BI)

Four PROMET model runs have been set up for the hydrological years 1994-1996 using these combinations of remapping methods. Tab. 5.2 presents the remapping methods chosen for the different parameters within the four combinations.

Tab. 5.2: The constellation of remapping methods used within the four PROMET runs over the period 1994-1996.

Parameter	QPB I	QPB II	BI	CI
Solar Zenith	BI	BI	BI	CI
Temperature	Constant lapse rate	Regression based	BI	CI
Air Humidity	Constant lapse rate	Regression based	BI	CI
Precipitation	Adjustment factor	Regression based	BI	CI
Shortwave Radiation (in)	Submodel	Submodel	BI	CI
Longwave Radiation (in)	Submodel	Submodel	BI	CI
Wind Speed	Regression based	Regression based	BI	CI
Surface Pressure	Submodel	Submodel	BI	CI

The remapping combinations denoted as QPB I and QPB II only differ with respect to the remapping of temperature, humidity and precipitation. The two approaches of regression based and constant elevation corrections (lapse rates, precipitation adjustment factors) are compared within the evaluation. As the aggregated meteorological fields do not contain information on the u- and v-component of wind speed, the wind model again could not be included in the evaluation process. In analogy to the meteorological comparison in chapter 5.2.1 the regression based remapping is used for the spatial distribution of wind speed instead. For the remapping of radiative fluxes the submodel approach was chosen for both QPB combinations. The remapping of surface pressure for both QPB combinations is based on an approach by COSGROVE ET AL. (2003), which is described in detail in chapter 4.2.8. As can be seen in case of the CI and the BI combinations, all parameters are consequently remapped using the respective direct interpolation method. In analogy to the meteorological comparison in chapter 5.2.1, these techniques have been included in the analysis to allow a direct comparison to the more sophisticated methods implemented in SCALMET. Similar to the meteorological comparison, the coarse grid meteorology used for the downscaling is derived from observational data that have been spatially distributed by the meteorological preprocessor in PROMET in advance. Fig. 5.16 shows the different stages of the hydrological evaluation process. The meteorological data are aggregated offline from 1 x 1 km to a spatial resolution of 10 x 10 km using the conservative remapping method implemented in SCALMET in a first step.

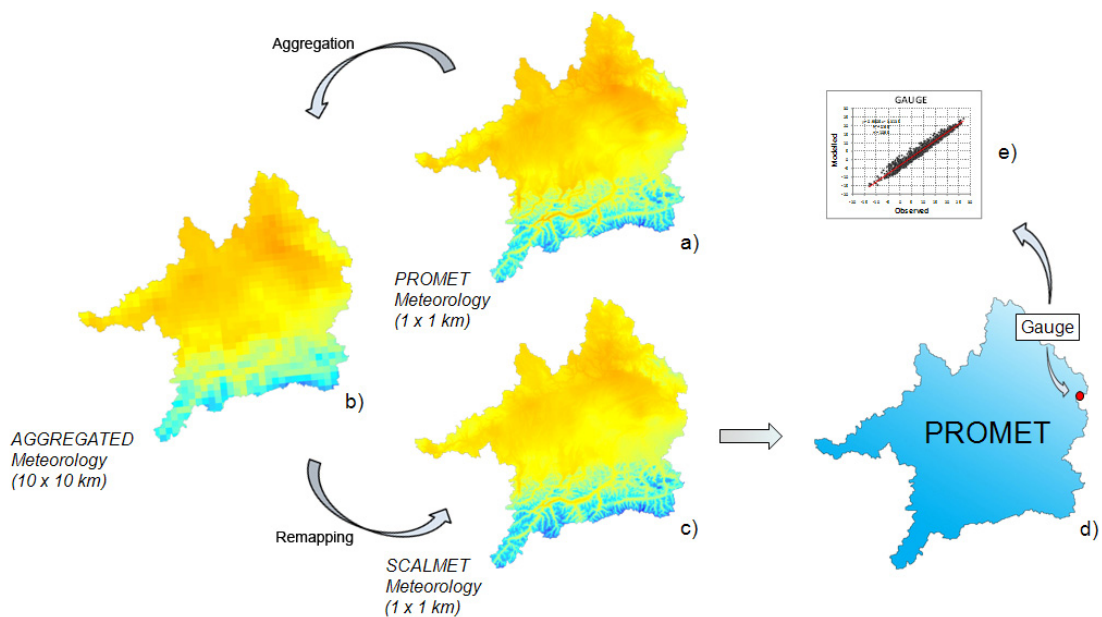


Fig. 5.16: The different steps within the hydrological evaluation of the remapping methods implemented in SCALMET. The spatially distributed observations provided by the meteorological preprocessor in PROMET are aggregated offline from 1 x 1 km to 10 x 10 km in a first step. Various coupled model runs are set up, in which the aggregated meteorology is remapped using the different approaches to be evaluated. The results are compared to discharge measurements at the gauge in Achleiten.

The aggregated hourly values are stored to file and treated similar to RCM simulations. Within four coupled model runs covering the hydrological years 1994-1996, the data are read from file for each model time step and are remapped from the coarse resolution of 10 x 10 km to the finer spatial resolution of 1 x 1 km. The remapping in SCALMET is carried out utilizing the combinations of remapping approaches presented in Tab. 5.2. To get an impression of the performance of the hydrological model forced by the different meteorological boundaries, the hydrological simulations need to be compared to observations. The most accurately measured quantity available is the discharge recorded at the gauge Achleiten. Therefore the simulated discharge at the LSM pixel containing the gauge in Achleiten is compared to the local discharge measurements.

An uncoupled PROMET run has been set up for the same period of time to serve as an additional source of reference. Comparing the model simulations achieved using the different remapping constellations with the results of the PROMET reference run gives an impression of the change in the meteorological forcings and its impact on hydrology.

The correlation between daily discharge observations and the discharge modeled in the uncoupled PROMET run, directly using the distributed observations as provided by the meteorological preprocessor in PROMET as meteorological forcings, is illustrated in Fig. 5.17 (left). The slope of the regression line with a value close to unity together with the coefficient of determination of 0.89 clarify that PROMET is capable of reproducing the measured daily discharge for the period 1994-1996 with good accuracy. This capability is reflected in the temporal course of the modeled discharge at the gauge in Achleiten for the considered period of time as well (see Fig. 5.17, right).

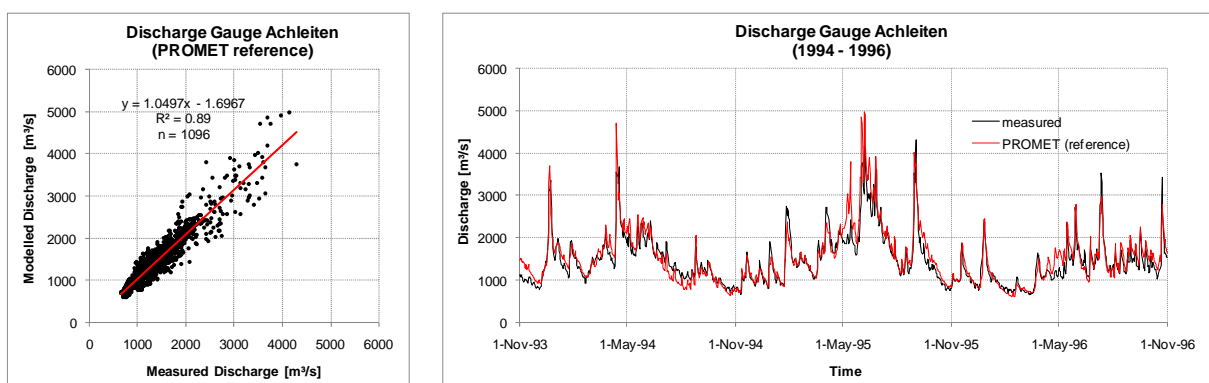


Fig. 5.17: Correlation between modeled and measured discharge at the gauge of the Upper Danube watershed in Achleiten (left) and temporal course of simulated and observed discharge at the gauge for the period 1994-1996 (right). The model results have been generated by directly forcing PROMET with the meteorological distributions provided by the meteorological preprocessor in PROMET.

For the hydrological years 1994-1996, the Nash-Sutcliffe model efficiency (NASH AND SUTCLIFFE 1970) takes a value of 0.84, again confirming the model's ability to reproduce daily discharge volumes with good accuracy.

The first remapping method constellation to be analyzed is the QPB I run. As shown in Tab. 5.2, monthly lapse rates and precipitation adjustment factors are used in this run for elevation corrections within the remapping of temperature/humidity and precipitation respectively. The scatterplot shows a very high correlation between simulated and observed daily discharge volumes for the considered period of time (see Fig. 5.18, left). With a coefficient of determination of 0.89 and a slope very close to that of the reference run, the QPB I run performs as well as the PROMET reference run. The graph in Fig. 5.18 (right) shows the temporal course of the discharge volumes simulated in the reference run and the QPB I run.

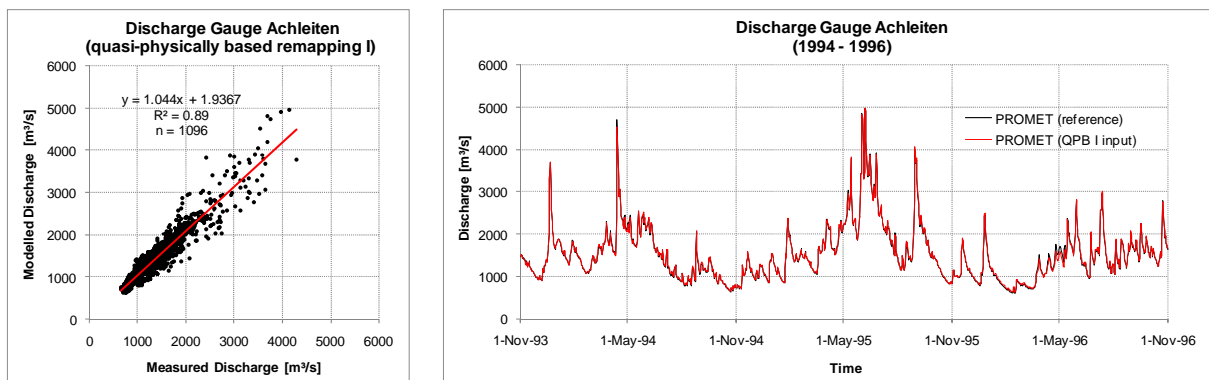


Fig. 5.18: Correlation between modeled (QPB I) and measured discharge at the gauge of the Upper Danube watershed in Achleiten (left) and temporal course of the reference run discharge (black line) and the QPB I run discharge (red line) at the pixel representing the gauge of the Upper Danube watershed in Achleiten for the period 1994-1996 (right).

The line representing the simulated discharge of the QPB I run is almost congruent with that of the reference run. The local discharge maximum in April 1994, which is overestimated in the reference run, is slightly flattened. Discharge at the beginning of May 1996, which is also slightly overestimated in the reference run, is little lower in the QPB I constellation as well. Considering the Nash-Sutcliffe model efficiency (NASH AND SUTCLIFFE 1970), the QPB I run with a value of 0.85 slightly outperforms the reference run. A similar picture is presented by the results of the quasi-physically based remapping constellation II (see Fig. 5.19).

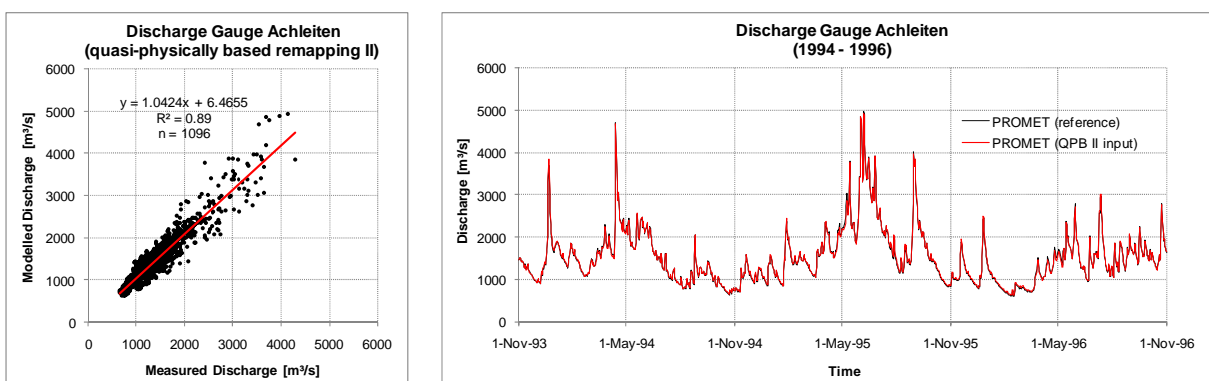


Fig. 5.19: Correlation between modeled (QPB II) and measured discharge at the gauge of the Upper Danube watershed in Achleiten (left) and temporal course of the reference run discharge (black line) and the QPB I run discharge (red line) at the pixel representing the gauge of the Upper Danube watershed in Achleiten for the period 1994-1996 (right).

Differently from the QPB I run, temperature, humidity and precipitation are corrected for subgrid elevation using the run-time regression technique in case of the QPB II run. Showing the same coefficient of determination and a very similar slope, the QPB II run as well performs very similar to the QPB I run and the reference run. While the QPB I run partly lowers the overestimation of discharge peaks in spring, the QPB II meteorology almost fully reproduces the discharge volumes of the reference run. The Nash-Sutcliffe model efficiency with a value of 0.85 for the QPB II run is equal to that of the QPB I run and slightly higher than that of the PROMET reference run.

In a next step the hydrological simulations based on a direct interpolation of all meteorological variables are analyzed. Fig. 5.20 (left) shows the correlation between the observed discharge at Achleiten and the discharge modeled with PROMET using the BI forcings.

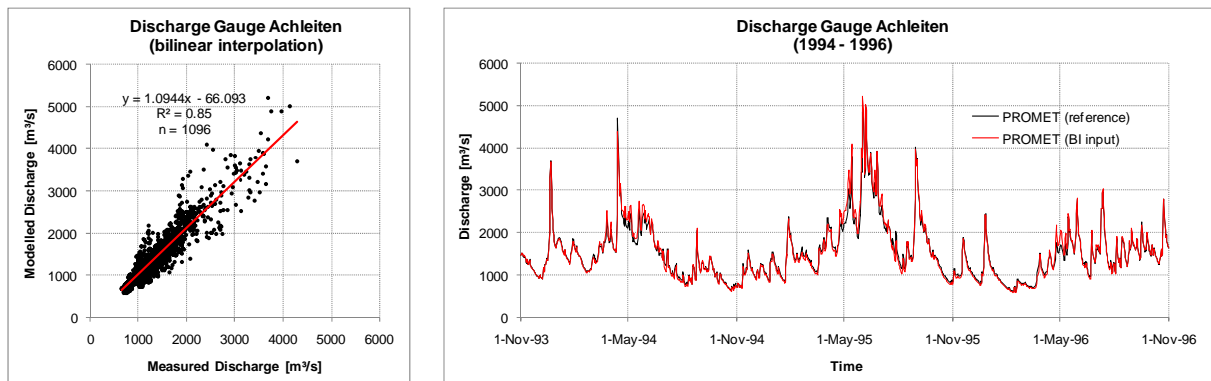


Fig. 5.20: Correlation between modeled (BI) and measured discharge at the gauge of the Upper Danube watershed in Achleiten (left) and temporal course of the reference run discharge (black line) and the BI run discharge (red line) at the pixel representing the gauge of the Upper Danube watershed in Achleiten for the period 1994-1996 (right).

As listed in Tab. 5.2 this constellation is based on a bilinear interpolation of all meteorological parameters. Compared to the reference run the coefficient of determination with a value of 0.85 is slightly lower using the bilinear interpolation method to bridge the scales from the aggregated meteorology (10 x 10 km) to 1 x 1 km.

A very similar picture is given by the analysis of the model results achieved using the conservative interpolation method to transfer all meteorological variables from the coarse to the fine scale. Fig. 5.21 (left) shows the correlation between the observed discharge and the discharge modeled with PROMET using the CI meteorology. While the coefficient of determination is slightly lower than that of the BI run, the temporal course of daily discharge simulations is almost identical. The Nash-Sutcliffe model efficiency for both direct interpolation based meteorologies with values of 0.75 and 0.76 for the CI and BI constellation respectively, is significantly lower than that of the QPB I and QPB II run. Both runs using a direct interpolation for the remapping of all meteorological variables slightly flatten some of

the discharge peaks in the year 1994, which are overestimated by PROMET in the reference run (see Fig. 5.17, right). Taking a closer look at the deviations from the reference run, it becomes evident that a directly interpolated meteorology partly leads to lower discharge values, mainly in winter, and to temporarily higher values, mostly in spring.

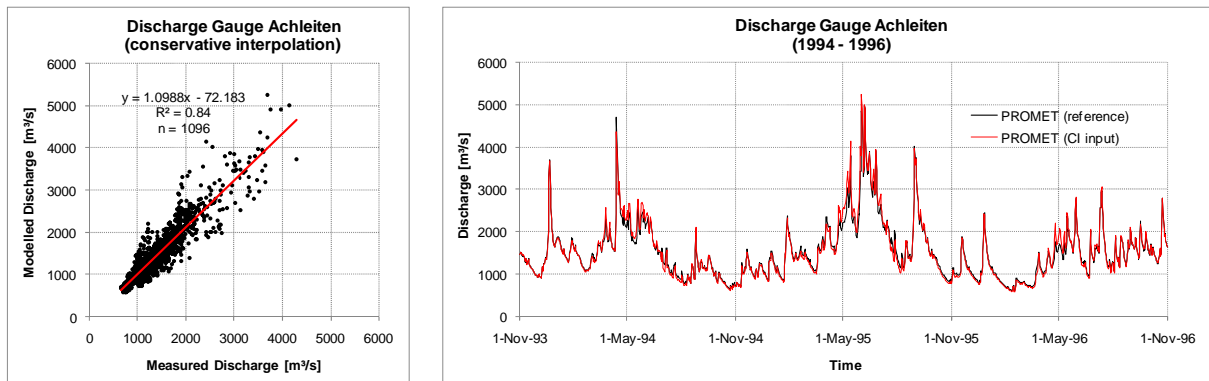


Fig. 5.21: Correlation between modeled (CI) and measured discharge at the gauge of the Upper Danube watershed in Achleiten (left) and temporal course of the reference run discharge (black line) and the CI run discharge (red line) at the pixel representing the gauge of the Upper Danube watershed in Achleiten for the period 1994-1996 (right).

This underestimation of wintery discharge and the subsequent overestimation of discharge in spring both are confirmed by considering the absolute deviation from the discharge measurements as shown for the bilinearly interpolated meteorology in Fig. 5.22.

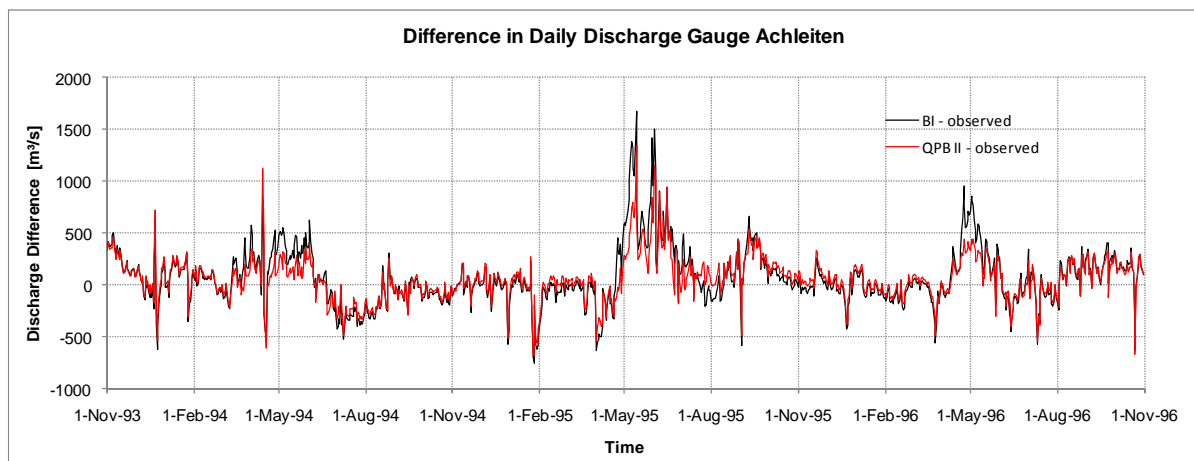


Fig. 5.22: Difference between simulated and observed discharge at the gauge in Achleiten for two SCALMET-PROMET model runs over the period 1994-1996.

Although a more sophisticated remapping, as shown for the QPB II in Fig. 5.22, leads to an overestimation of spring discharge comparable to that found in the reference run as well, the overestimation is significantly lower than that for the BI run. The reason for this behaviour can be found in differences within the seasonal storage of water in the snow pack.

Fig. 5.23 shows the difference in simulated snow water equivalent (SWE) between the BI and the QPB for the 3<sup>rd</sup> of April 1995. As pictured in Fig. 5.23, in case of the BI run much higher

values of SWE occur in the Alpine valleys combined with lower SWE in higher elevations. These conditions can be traced back to the local temperature conditions in the respective altitudinal belts. A bilinear interpolation of the meteorological forcings does not account for subgrid orographic variability. As a result temperatures are overestimated for all subpixels that are characterized by higher elevations than that of the associated 10 x 10 km pixel and underestimated for those subpixels that are located in lower elevations than the 10 x 10 km mean elevation (see chapter 5.2.1.1).

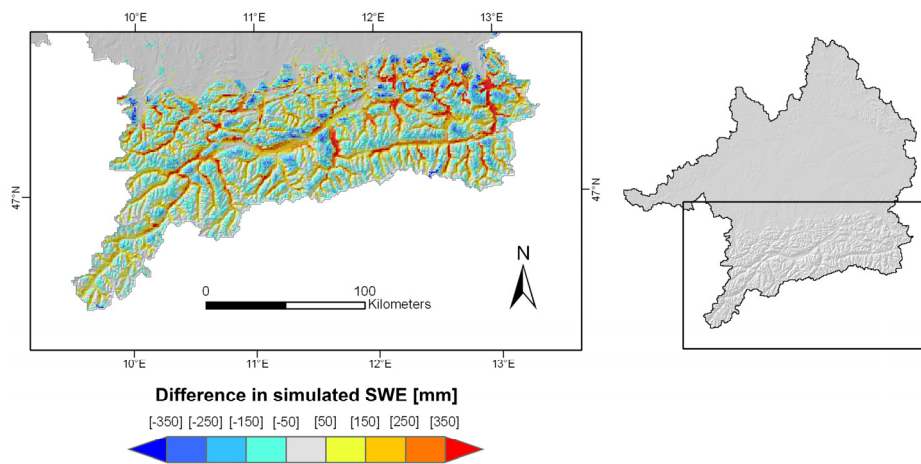


Fig. 5.23: Difference in simulated snow water equivalent (SWE) between two SCALMET-PROMET model runs (April 3<sup>rd</sup>, 1995). The SWE simulations using a quasi-physically based remapping (QPB II) is subtracted from the SWE simulations resulting from a bilinear interpolation (BI) of all meteorological parameters. For the sake of visualization the SWE difference is overlaid by a semitransparent hillshade effect.

This underestimation of temperatures in lower elevations leads to a comparatively high amount of snow in the valleys. Particularly in the small Alpine valleys, where the mean elevation in the spatial resolution of the coarse grid meteorology largely misrepresents the real topographic situation, differences in the SWE of more than 350 mm (corresponding to a snow depth of approximately 70 cm, assuming a snow density of 500 kg/m<sup>3</sup>) occur. The prolonged storage of water in the snow pack leads to comparatively lower discharge volumes in the months of March and April. With temperatures increasing in May, snow water is released leading to higher discharge volumes compared to the QPB II run. The application of elevation corrections, as done in the case of the QPB II run, results in temperature distributions that more realistically represent the temperature conditions in the Alpine valleys. The latter results in an enhanced representation of snow cover dynamics and allows to more accurately reproduce the observed discharge volumes.

### 5.3 COUPLED MODEL RUNS FOR PAST CLIMATE CONDITIONS

The following chapter shows the performance of the coupled model system (REMO-SCALMET-PROMET) for past climate conditions. The simulations will serve as a current state reference for the scenario run in a later chapter of this work. Besides the comparison of discharge volumes simulated for the period 1971-2000 within the coupled reference run to recorded discharge volumes at the gauge in Achleiten, an uncoupled PROMET run forced by spatially distributed meteorological observations will serve as an additional source of reference to evaluate both, the meteorological forcings as well as the hydrological simulations resulting from the coupled reference run. To guarantee a common understanding of the different runs referred to in the following chapters of this work an overview of the main run characteristics is given by Tab. 5.3.

Tab. 5.3: The main characteristics of the different model runs used for the simulation of past and future hydrological conditions in the Upper Danube watershed.

Run Denotation	Atmosphere		Land surface	Time Period	Purpose
	Data	Distribution			
Uncoupled Reference Run (URR)	Station Observations	PROMET	PROMET	1971-2000	Control
Coupled Reference Run (CRR)	REMO Control Run (CNTRL)	SCALMET	PROMET	1971-2000	
		SCALMET	PROMET	1961-2000	Change
Coupled Scenario Run (CSR)	REMO A1B Run	SCALMET	PROMET	2011-2060	

The meteorological drivers for the one-way coupled model run for the period 1961-2000 and 2011-2060 are provided by the REMO control run ('Climate of the 20<sup>th</sup> Century Run') and the REMO A1B scenario run respectively (JACOB AND PODZUN 1997, JACOB ET AL. 2001). Within both runs, the RCM is forced by the global ECHAM5/MPI-OM model at the boundaries of the model domain. The REMO simulations as well as the remapped fields and the hydrological simulations of the reference run, therefore must not be compared directly to measurements related to a certain year (see chapter 3.2). Still, the long-term mean meteorological and hydrological conditions can be compared to observations to get an impression of the performance of the coupled model system. Before the results of the coupled reference run (CRR) are presented and analyzed, the choice of the remapping methods applied within

both, the simulation of past and future hydrological conditions inside the UD will be described.

### 5.3.1 CHOICE OF REMAPPING METHODS

The performance of the different remapping methods implemented in SCALMET has been analyzed in the preceding chapters of this work (see chapter 5.2). The meteorological and hydrological evaluation revealed that for the remapping of all meteorological variables needed for the description of the hydrological relevant processes on the land surface, the quasi-physically based approaches clearly outperform direct interpolation methods.

While a further comparison of the different remapping approaches within long-term simulations (decades to centuries) is undoubtedly worth striving for in the future, for the present work one combination of remapping methods had to be chosen to be consistently used within both, the coupled reference run and the scenario run. Besides the performance within the evaluation process, the degree to what the remapping methods can be expected to be stable under future climate conditions is a central criterion for the selection of the remapping methods applied. The configuration used within the control and scenario runs is given in Tab. 5.4.

*Tab. 5.4: The combination of remapping approaches used for the downscaling of REMO simulations within the reference run (1961-2000) and the scenario run (2011-2100).*

Parameter	Remapping Method
Solar Zenith	Submodel
Temperature	Regression based
Air Humidity	Regression based
Precipitation	Regression based
Shortwave Radiation (in)	Submodel
Longwave Radiation (in)	Submodel
Wind Speed	Submodel
Surface Pressure	Submodel

Temperature, humidity and precipitation are remapped using the regression based approach described in chapter 4.1.2. Although the application of monthly constant elevation corrections in the case of precipitation showed slightly better results, the regression based remapping has been preferred for the coupled model runs, as it is completely unparameterized and therefore unrestrictedly applicable to future conditions. Incoming shortwave and longwave

radiation are scaled using the shortwave and longwave radiation models in SCALMET respectively (see chapter 4.2.5 and 4.2.6). For the remapping of wind speed the wind submodel described in chapter 4.2.7.2 is applied. Although the performance of the wind model could not be evaluated for the UD, the model is expected to improve the results of the remapping process compared to the regression based approach, as wind speed is remapped accounting for wind direction. Since the solar zenith angle does not belong to the available REMO outputs, it is calculated as a function of time and geographical position (see chapter 4.2.1). In analogy to the hydrological evaluation process described in chapter 5.2.2 surface pressure is remapped based on an approach proposed by COSGROVE ET AL. (2003) (see chapter 4.2.8).

### 5.3.2 MODEL RESULTS

The model results of the coupled reference run (REMO-SCALMET-PROMET) cover the years 1961 to 2000. The period is considered to serve as a reasonable reference for a comparison to the scenario run (2011-2060), as it covers a time period of similar length. To provide an adequate spin up time to the hydrological model, the model run has been set up starting with the year 1959. The REMO data providing the meteorological fields for the downscaling in SCALMET, originate from the REMO control run (see Tab. 5.3).

As the discharge measurements needed for the evaluation of runoff simulations are not available for the time before 1970, the period 1971-2000, representing a subset of the coupled reference run data, is chosen to check the plausibility of the model results (see Tab. 5.3). In the following paragraphs, the meteorological input as well as the hydrological output is compared between the coupled and the uncoupled reference run.

#### 5.3.2.1 METEOROLOGY

A comprehensive knowledge of the quality related to the meteorological drivers is of prime importance for the later interpretation of the hydrological model results. The following paragraphs show and discuss the meteorological data used to force the hydrological model PROMET in the coupled reference run. To get an impression of the quality of the remapped REMO simulations the latter are compared to distributed observations. Although the reference distributions are based on observations, they need to be considered as model results as well. KOTLARSKI ET AL. (2005) have shown that the results of a comparison between simulations and observational data largely depend on the reference data set applied. This has to be kept in mind when interpreting the results. However, it is important to

clarify to what degree the meteorological forcings used within the coupled model run differ from those used in the uncoupled reference run, in order to interpret differences in the hydrological model results. The evaluation focuses on temperature and precipitation, as these parameters are most determinant for near surface hydrological processes (KOTLARSKI ET AL. 2005).

### 5.3.2.1.1 Temperature

The spatially distributed average annual mean temperature in the UD (1971-2000) calculated on the basis of remapped REMO simulations is illustrated in Fig. 5.24 (left). As displayed, the regression based remapping leads to a spatial distribution that largely follows topography. To get an impression in how far the remapped REMO simulations differ from the spatially distributed observations (PROMET), the mean observed temperature conditions have been subtracted from the remapped data (see Fig. 5.24, right).

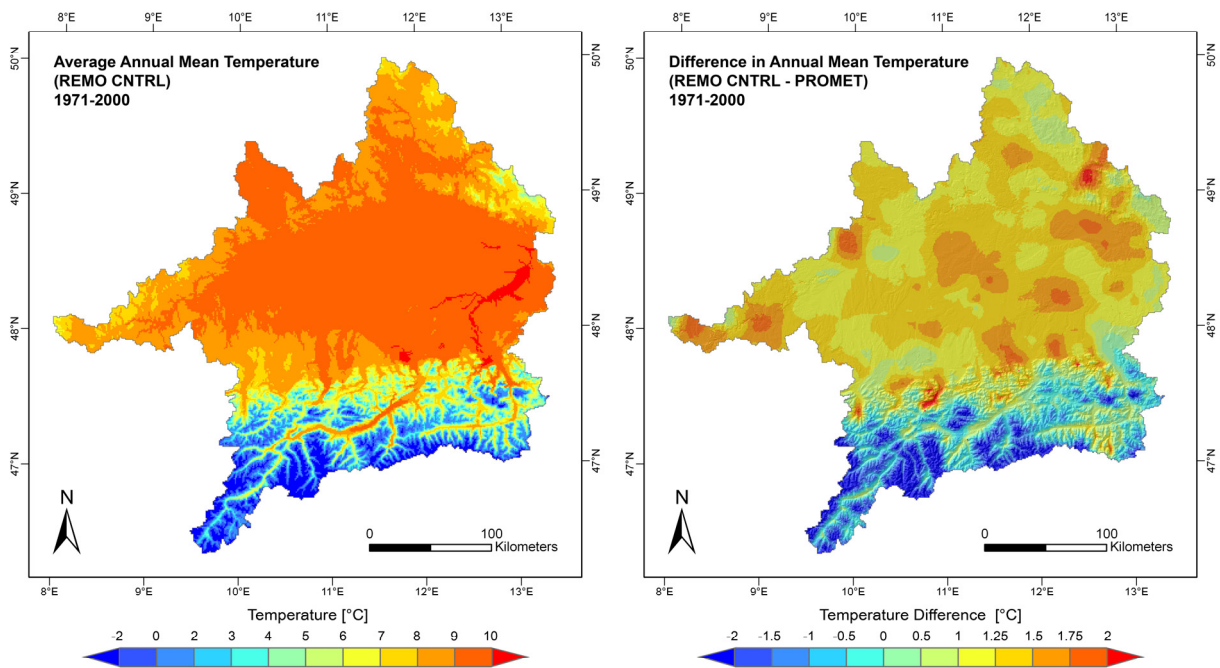


Fig. 5.24: Remapped average annual mean temperature (left) and difference between the remapped distributions and those provided by the meteorological preprocessor in PROMET (right) for the hydrological years 1971-2000. The observation based temperature distributions have been subtracted from the remapped fields for the generation of the map on the right.

The illustration unfolds that the remapped REMO data for the non-alpine part of the catchment considerably overestimates mean annual temperatures by up to 2 °C. This warm bias is well known in the REMO community. It is traced back by KOTLARSKI (2007) to an overestimation of the real temperature conditions in summer, possibly related to inaccuracies within the vertical diffusion in the RCM and a strong reduction of evaporation, due to low soil

moisture conditions in summer. For the UD the largest overestimation of observed temperature conditions for the period 1971-2000 is found in the simulations for April (see Fig. 5.25). A plausible explanation for this overestimation of temperatures could possibly be found in the snow conditions at the land surface of the RCM in the month of April. As the flattened topography leads to an overestimation of temperatures in higher elevations, snow amounts in these regions might be underrepresented. An increased absorption of shortwave radiation together with a not present cooling of near surface air masses by snow at the land surface could result in an overestimation of air temperatures. As REMO snow simulations are not analyzed in the framework of this thesis, this assumption is not further pursued.

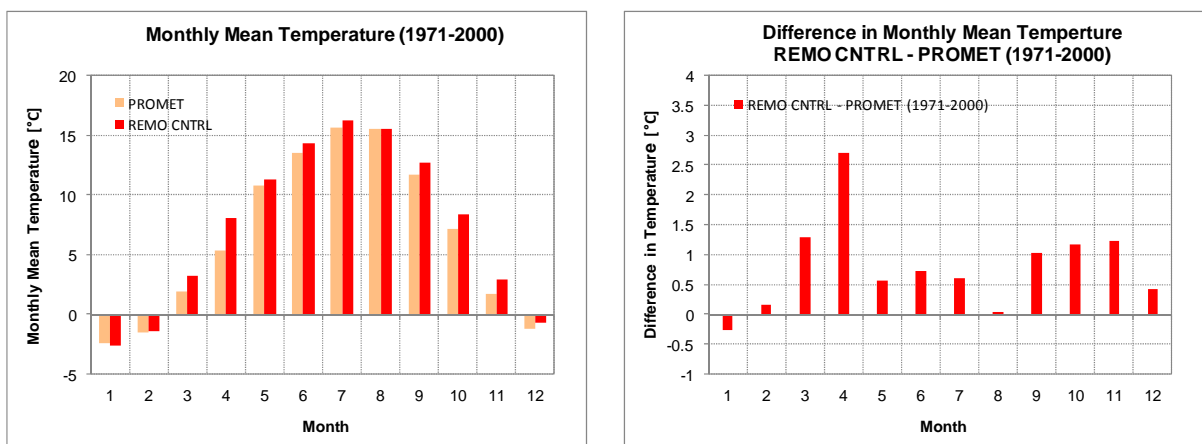


Fig. 5.25: Observation based and remapped monthly mean temperatures in the Upper Danube watershed for the period 1971-2000 (left), difference in monthly mean temperature between remapped REMO control run data and spatially distributed observations (right). The latter have been subtracted from the remapped REMO simulations for the generation of the bar chart above.

The general magnitude of overestimation displayed in Fig. 5.25, as well as that of underestimation of temperatures in January, is comparable to the results of studies by KOTLARSKI ET AL. (2005). Unlike in the plain Alpine Foreland, in some of the higher elevations of the Alps the remapped REMO data show lower annual mean temperatures than those found in the observation based distributions (see Fig. 5.24). While this general tendency is found in the original REMO data as well, it is locally modified due to the temperature-elevation corrections in SCALMET. Considering the area mean temperature, the remapped REMO temperature with  $7.4\text{ °C}$  ( $\text{std\_dev}_{area} = 3.3\text{ °C}$ ) is  $0.8^\circ$  higher than that of the distributed observations ( $6.6\text{ °C}$ ,  $\text{std\_dev}_{area} = 2.4\text{ °C}$ ).

### 5.3.2.1.2 Precipitation

The mean annual precipitation (1971-2000) calculated on the basis of remapped REMO control run data is shown in Fig. 5.26. The map on the left shows that the regression based

remapping in case of precipitation leads to a spatial distribution that is less determined by topography, compared to the remapping of temperature. This can be explained by the fact, that the precipitation-elevation dependence found in REMO simulations is often not significant. In this case, the meteorological simulations are directly interpolated from the model resolution of the RCM to the spatial resolution of the LSM (see chapter 4.1.2).

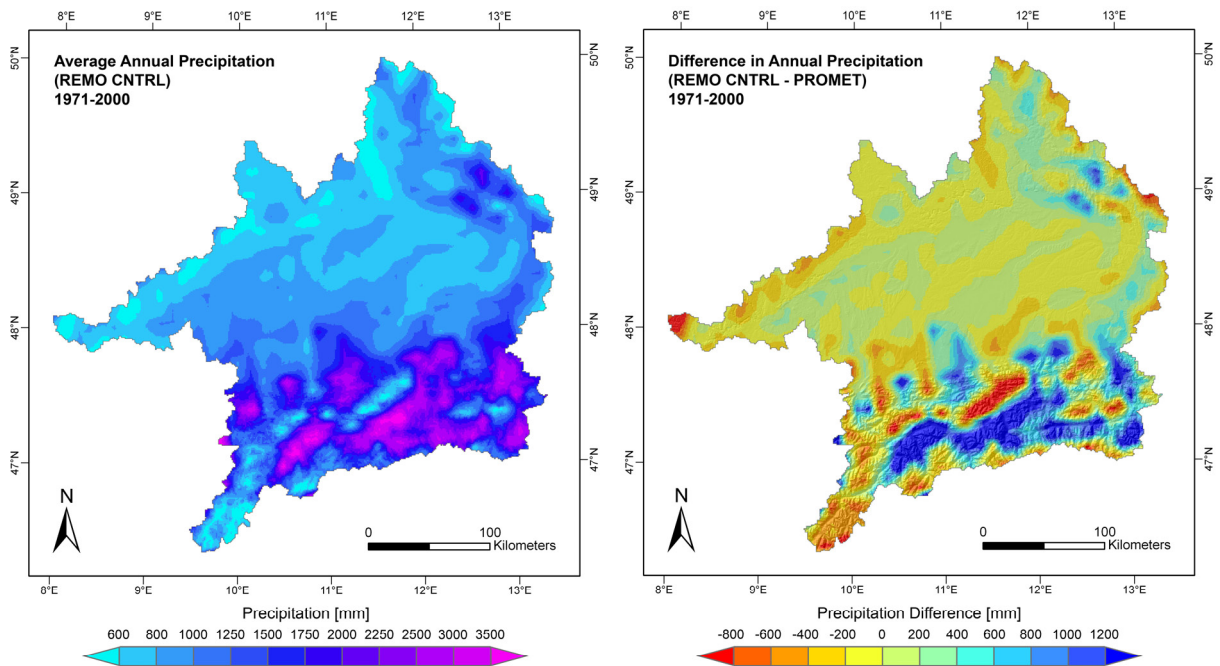


Fig. 5.26: Remapped average annual precipitation (left) and difference between the remapped simulations and the spatially distributed observations (right) for the hydrological years 1971-2000. The observation based precipitation distributions have been subtracted from the remapped REMO fields for the generation for the map on the right.

In order to analyze in how far the remapped REMO precipitation differs from the observation based meteorology, the latter is subtracted from the remapped REMO data. The resulting spatial differences in precipitation are illustrated in Fig. 5.26 (right). The spatially distributed difference in precipitation amounts gives a rather heterogeneous picture. Although some areas are characterized by lower precipitation amounts in the remapped REMO data compared to the distributed observations, the effect is overcompensated by much higher precipitation amounts, in particular in the Alpine areas. With 1157 mm ( $\text{std\_dev}_{\text{area}} = 596$  mm) for the hydrological years 1971-2000 the average annual precipitation in the remapped REMO data is 113 mm higher than that of the PROMET distributions (1044 mm,  $\text{std\_dev}_{\text{area}} = 334$  mm).

To involve another source of reference, the Hydrological Atlas of Austria (HAA) is consulted (KLING ET AL. 2007). The atlas provides digital maps of average annual precipitation amounts in Austria for the years 1961-1990 on a catchment basis. Assuming that discharge and areal evapotranspiration in high Alpine regions can be determined with higher accuracy than areal

precipitation, KLING ET AL. (2007) adjust spatially distributed precipitation recordings with respect to the catchment water balance in form of

$$P_{cor} = \frac{Q + (ET_{pot} - ET_{pot_s}) \cdot y_b + ET_{pot_s} \cdot y_s}{P} \quad \text{Eq. 5.1}$$

- with:
- $P_{cor}$  = Corrected annual precipitation [mm]
  - $Q$  = Annual discharge [mm]
  - $ET_{pot}$  = Potential annual evapotranspiration [mm]
  - $ET_{pot_s}$  = Sum of potential evapotranspiration in months with snow cover [mm]
  - $y_b$  = Ratio of actual and potential evapotranspiration (calculated using the Bargov-Equation (GLUGLA AND TIEMER 1971))
  - $y_s$  = Ratio of actual and potential evapotranspiration for months with snow cover (assumed to be 0.3)
  - $P$  = Annual precipitation [mm]

For more detailed information concerning the calculation of area precipitation within the HAA and the water balance model applied refer to KLING ET AL. (2007a) and KLING ET AL. (2007b). The mean annual precipitation resulting from the calculations above, together with the PROMET distributions and unscaled REMO simulations are shown for the Austrian subcatchments within the UD in Fig. 5.27.

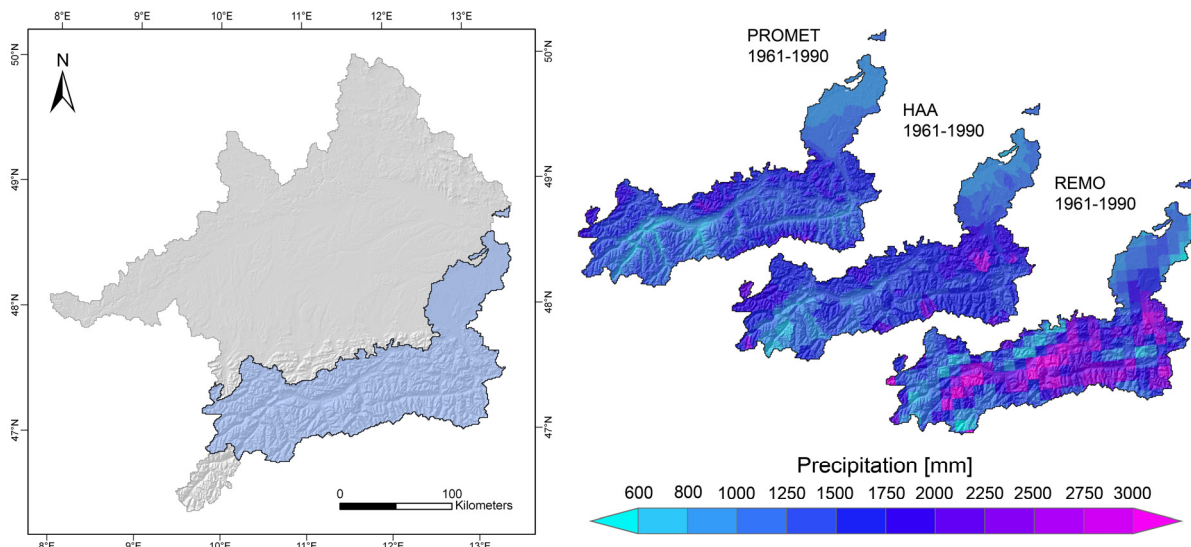


Fig. 5.27: The average annual precipitation for the Austrian subcatchments within the domain of the Upper Danube watershed (1961-1990). The three precipitation maps on the right represent data originating from the meteorological preprocessor in PROMET (top), the Hydrological Atlas of Austria (middle) (KLING ET AL 2007 b) and REMO control run simulations (bottom) (JACOB AND PODZUN. 1997, JACOB ET AL. 2001). For the sake of visualization, all maps are overlaid by a semi transparent hillshade effect.

While there is quite a good agreement in the spatial patterns of precipitation amounts within the observation based distributions (top and middle), the REMO simulations (bottom) locally picture different spatial patterns. In particular in the central part of the displayed area, annual precipitation amounts of more than 2750 mm frequently occur, exceeding the maximum precipitation found in the observation based distributions. A comparison of the average annual precipitation amounts reveals that for the considered area, the REMO simulations deviate from the mean conditions reflected by the HAA and the PROMET distributions by 234 mm and 370 mm respectively (see Tab. 5.5).

*Tab. 5.5: Statistical characteristics for the average annual precipitation in the Austrian subcatchments of the Upper Danube watershed. The data sources PROMET, HAA and REMO represent the PROMET precipitation distributions, the Hydrological Atlas of Austria (KLING ET AL. 2007) and the original REMO control run simulations respectively.*

<b>Data Source</b>	<b>P<sub>mean</sub> [mm]</b>	<b>P<sub>min</sub> [mm]</b>	<b>P<sub>max</sub> [mm]</b>	<b>P<sub>std_dev</sub> [mm]</b>
PROMET	1323	673	2476	301
HAA	1459	651	2683	350
REMO	1693	541	3795	650

Yet, the mean values of the PROMET and REMO precipitation distributions show very similar deviations from the mean of all data sources (1492 mm). The reason for this behavior is that locally higher precipitation amounts in the REMO simulations are partially compensated by areas characterized by lower precipitation amounts than those found in the PROMET and HAA data. Still, the general tendency to higher precipitation values remains. At least in some cases, the locally higher precipitation amounts, as well as the spatial patterns in the REMO simulations illustrated in Fig. 5.27 might rather be the result of a spatial displacement than of a general overestimation. Displacements can be caused due to the coarse spatial resolution and the associated representation of topography, but also due to the fact that REMO belongs to the view climate models that do not use a ‘tuned’ topography. A further explanation for displacements in precipitation amounts consists in the missing advection of falling rain in REMO. To reduce the effects of displacements, the REMO developers suggest to use a 3 x 3 pixel average rather than the originally simulated pixel precipitation. While this advice might be followed in the framework of future one-way coupled model runs, for the current work unfiltered REMO simulations are used to provide the meteorological conditions for the underlying area of 10 x 10 km. This is done deliberately to avoid a manipulation of the original data and to maintain similar conditions to those needed for two-way coupled model runs, where the conservation of mass and energy does not permit a 3 x 3 pixel filter anyhow. To get an impression of the interannual variability found in the observation based

precipitation distributions used within the uncoupled reference run and the remapped REMO data driving PROMET in the coupled reference run, the area mean annual precipitation in the UD is graphically displayed in Fig. 5.28.

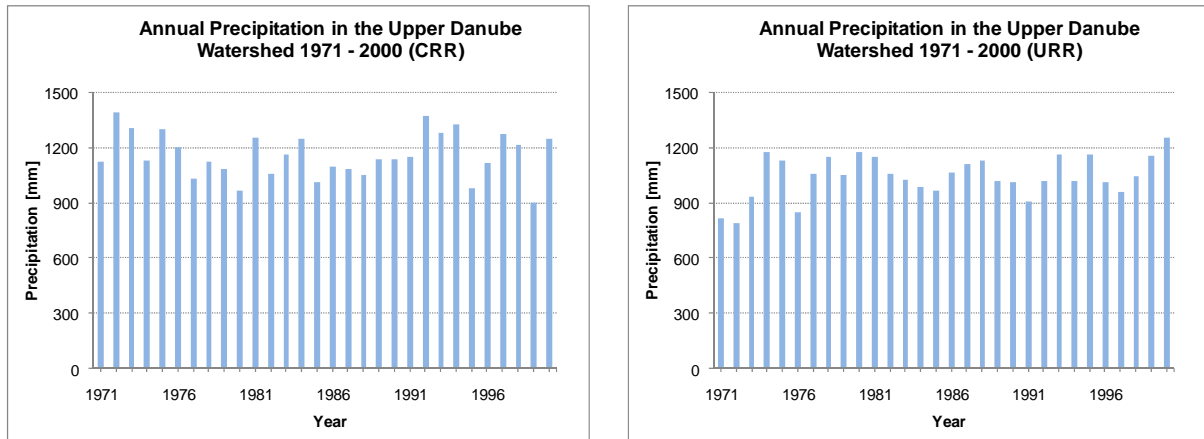


Fig. 5.28: Remapped REMO precipitation as used in the coupled reference run REMO-SCALMET-PROMET (CRR) for the hydrological years 1971-2000 (left) and observation based area mean annual precipitation in the Upper Danube watershed as used within the uncoupled reference run (URR) for the hydrological years 1971-2000 (right). As the REMO model is forced by a simulated ECHAM5/MPI-OM meteorology at the model boundaries, merely the inter-annual variability and general dimensions should be compared between the model runs and not the exact values for a certain year.

Although a direct comparison of yearly values is conceptually prohibitive, the inter-annual variability and the general dimensions can be compared in the two model runs. The statistical characteristics for area mean annual precipitation (1971-2000) are summarized for both model runs in Tab. 5.6. While extreme and mean values, confirm the general tendency of the remapped REMO data to overestimate precipitation, the largest percental deviations from the long-term mean value show similar values to those of the distributed observations.

Tab. 5.6: Statistical characteristics for annual precipitation for the hydrological years 1971-2000 for the uncoupled reference run (URR) and the coupled reference run (CRR).

Statistic Criteria	Precipitation URR	Precipitation CRR
Mean (1971-2000) [mm]	1044	1157
Max (1971-2000) [mm]	1250	1390
Min (1971-2000) [mm]	789	902
Std_Dev [mm]	112	123
Max. Dev. from Mean (↑) [%]	20	20
Max. Dev. from Mean (↓) [%]	24	22

Fig. 5.29 shows the average monthly precipitation in the area of the UD (1971-2000) as displayed in the remapped simulations and the distributed observations. The differences in

average monthly precipitation displayed in Fig. 5.29 (right) are calculated by subtracting the observation based data from the remapped REMO precipitation on a monthly time basis.

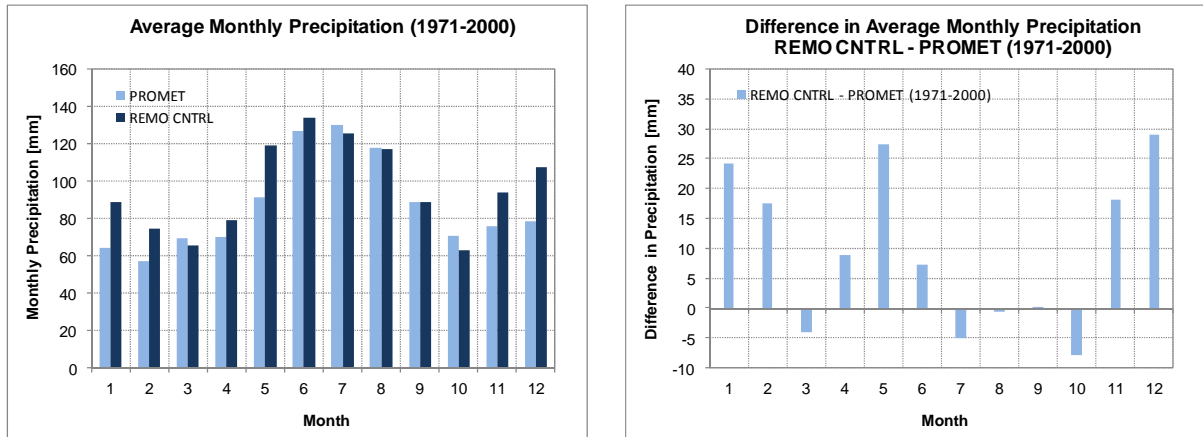


Fig. 5.29: Observation based (PROMET) and remapped average monthly precipitation (REMO CNTRL) in the Upper Danube watershed for the period 1971-2000 (left), difference in monthly precipitation between the remapped REMO data and spatially distributed observations (right).

According to the bar charts, the largest differences in precipitation amounts occur in winter and spring. Similar results have been achieved by KOTLARSKI ET AL. (2005), who compared precipitation simulations of different RCMs including the regional climate model REMO to various observational datasets. According to these authors, an overestimation of precipitation up to 44 % (24 mm/month) is found within the RCM simulations for spring and winter months. As shown in Fig. 5.29 (right), the overestimation of precipitation compared to the PROMET distributions for the months of May and December even exceeds 24 mm/month. The latter can be explained by the fact that KOTLARSKI ET AL. (2005) only considered the German part of the RCM domain excluding large parts of the Alps, which have been shown to be subject to a comparatively high degree of overestimation (see Fig. 5.27). Compared to winter precipitation remapped summer precipitation shows smaller differences to the PROMET distributions. For March, July and October, the remapped simulations even fall below the area mean PROMET precipitation for the UD. In analogy to the overestimation of summer temperatures, KOTLARSKI ET AL. (2005) attribute the low precipitation amounts in summer to an intense evaporation in early summer, resulting in a reduced soil water availability in late summer.

### 5.3.2.2 HYDROLOGY

The following paragraphs analyze the hydrological model results generated within the one-way coupled model run. In a first step the annual water balance is analyzed. The catchment water balance is given by

$$P = ET + Q + \Delta S \quad \text{Eq. 5.2}$$

where  $P$  is the annual precipitation,  $Q$  is the annual runoff,  $ET$  is the annual evapotranspiration and  $\Delta S$  is the change in water storage (BAUMGARTNER AND LIEBSCHER 1995).

#### 5.3.2.2.1 The Water Balance

The annual water balance of the coupled reference run is calculated for each hydrological year in the period 1971-2000 by subtracting the daily evapotranspiration from precipitation. Following MAUSER AND BACH (2008), it is assumed that changes in ground water storage can be neglected from year to year. The resulting water volume under this assumption can be compared to the discharge recorded at the gauge of the watershed in Achleiten. Fig. 5.30 shows the simulated average annual water balance in the UD for the coupled reference run over the years 1971-2000.

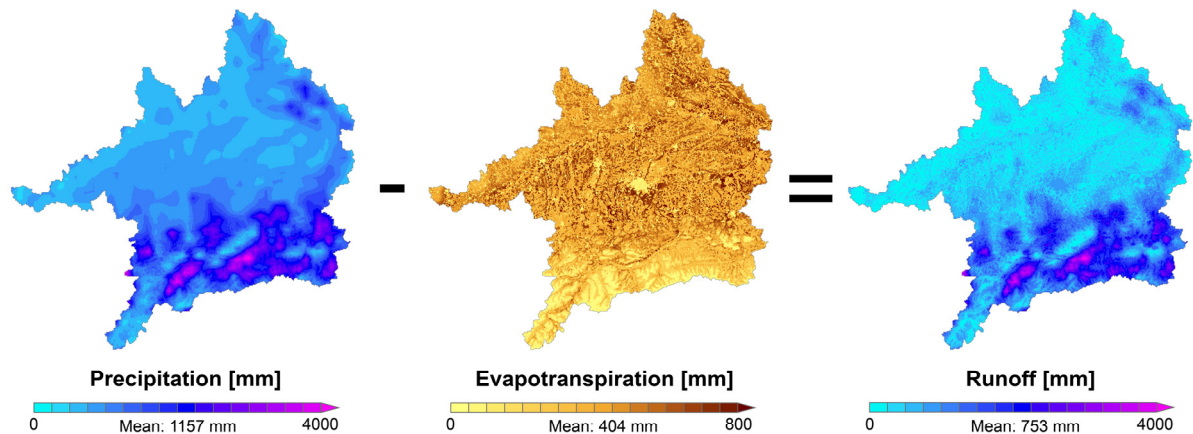


Fig. 5.30: The average modeled water balance in the Upper Danube watershed for the hydrological years 1971-2000. The hydrological model PROMET in the one-way coupled model run was forced by remapped REMO control run simulations.

Forcing PROMET with remapped REMO control run simulations over the standard climate period 1971-2000, the combination of spatially distributed precipitation (1157 mm) and simulated evapotranspiration (404 mm) leads to an area mean runoff of 753 mm. Compared to the recorded discharge of 584 mm at the gauge in Achleiten, the simulated runoff overestimates the real conditions by about 29 % (169 mm).

#### 5.3.2.2.2 Monthly Discharge

To get an impression to what extent the seasonal dynamics in river discharge at the gauge in Achleiten can be reproduced by the coupled model system, the simulated mean monthly

discharge is compared to observed discharge volumes (see Fig. 5.31, left). The diagram on the left shows that mean discharge conditions at the gauge of the watershed in Achleiten are noticeably overestimated in the coupled reference run (CRR). The temporal characteristics of this discharge overestimation are closely linked to the magnitude of overestimation found in the remapped REMO precipitation (see Fig. 5.29, right).

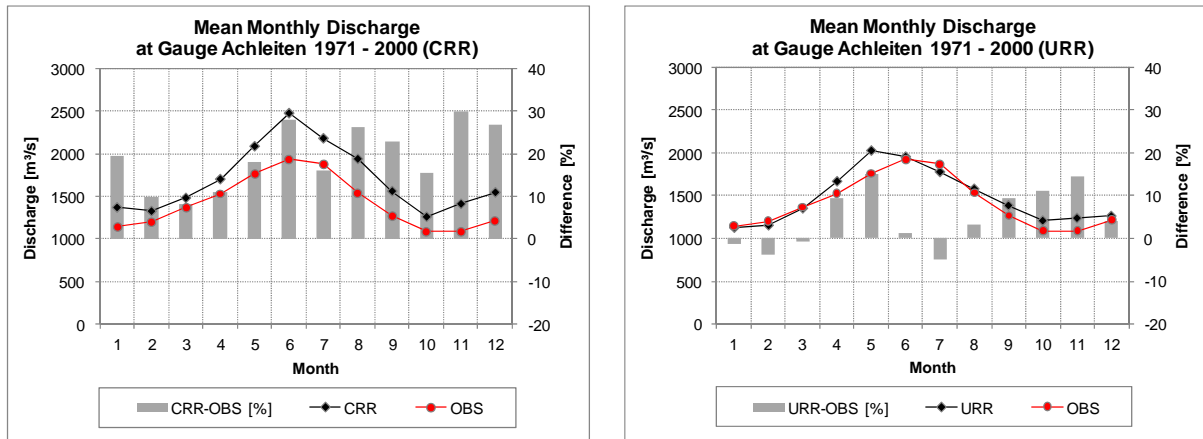


Fig. 5.31: Mean monthly discharge (1971-2000) simulated in the coupled reference run (CRR) together with discharge observations (left) and mean monthly discharge simulated in the uncoupled reference run (URR) together with discharge observations at the gauge in Achleiten (right).

However, the comparatively strong overestimation of precipitation in the winter months of January and February does not fully result in a congruent overestimation of discharge volumes. The reason for this behavior can be found in the low temperatures in winter, which in the remapped REMO data are even lower than in reality due to a general underestimation of temperatures in January (see Fig. 5.25). Combined with a certain underestimation of temperatures in higher elevations (see Fig. 5.24, right), the latter result in an increase in water storage in a solid state reducing runoff and in consequence the degree of discharge overestimation in January and February. With rising temperatures in spring and summer the water temporarily stored in the snow pack is released due to snowmelt and contributes to the comparatively high discharge overestimation in spring and summer. As shown in Fig. 5.31 (right) the uncoupled model run, which is based on distributed meteorological observations, much better reproduces the annual course of discharge volumes at the catchment outlet.

In a next step, the simulated peak-flow and low-flow discharge volumes are compared to observed discharge volumes at the gauge in Achleiten for both reference runs. To calculate the analyzed quantities, the years 1971-2000 have been analyzed separately for the highest/lowest daily discharge value found in the different months of the year. The peak-flow/low-flow discharge volumes shown in Fig. 5.32 and Fig. 5.33 represent the average value of the monthly peak-flow/low-flow discharge volumes found in the years 1971-2000.

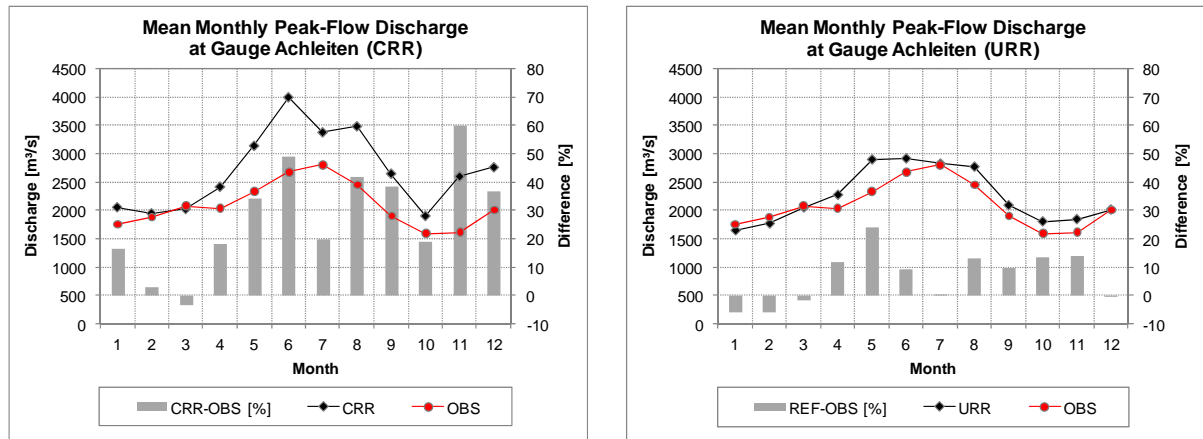


Fig. 5.32: Monthly peak-flow discharge (1971-2000) simulated in the coupled reference run (CRR) together with discharge observations (left) and monthly peak-flow discharge simulated in the uncoupled reference run (URR) together with discharge observations at the gauge in Achleiten (right).

Analogously to mean monthly discharge, the coupled reference run for the considered period overestimates mean peak-flow discharge volumes with a highest degree of overestimation in November (60 %) (see Fig. 5.32, left). In contrast to all other months of the year, the simulated peak-flow discharge for March is characterized by a slight underestimation compared to the observed discharge volumes.

The observation based meteorology of the uncoupled reference run allows a much better reproduction of the observed peak-flow conditions (see Fig. 5.32, right). The highest overestimation here can be observed in May with a percentage of 24 %. The months from January to March are characterized by a certain underestimation of observed peak-flow discharge in the uncoupled reference run.

Considering the mean monthly low-flow discharge volumes simulated in the coupled reference run, the low-flow discharge volumes recorded at the gauge at Achleiten are almost continuously overestimated by around 20 % (see Fig. 5.33, left).

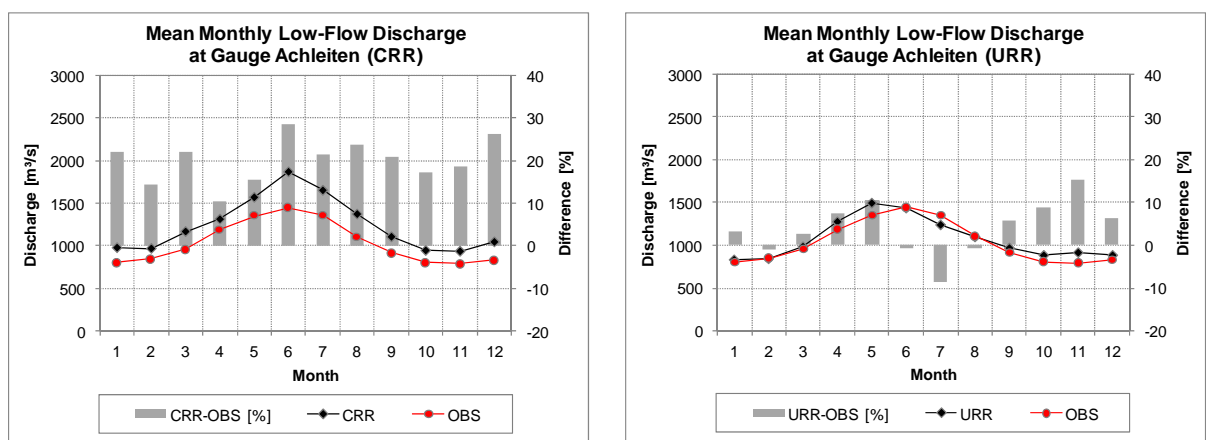


Fig. 5.33: Monthly low-flow discharge (1971-2000) simulated in the coupled reference run (CRR) together with discharge observations (left) and monthly low-flow discharge simulated in the uncoupled reference run (URR) together with discharge observations at the gauge in Achleiten (right).

The month of June is characterized by the highest overestimation of mean monthly low-flow discharge (28.5 %), whereas April shows the lowest degree of overestimation of measured discharge volumes with about 10 %.

As displayed in Fig. 5.33 (right), the uncoupled reference run, which is based on distributed meteorological observations, reproduces the low-flow conditions at the outlet of the UD with good accuracy. The highest overestimation can be found in November. With +15 % it is small compared to the general tendency to overestimate discharge volumes in the coupled reference run.

### 5.3.2.2.3 Return Periods of Extreme Events

The last paragraphs have shown the performance of the coupled model system concerning the reproduction of discharge characteristics on a monthly time basis. In the following, the capability to reproduce flood and low-flow return periods is investigated. The determination of return periods for extreme events is connected to a probabilistic extrapolation beyond the available data base. A distribution function that is often recommended to analyze the frequency of extreme discharge events is the lognormal distribution (PLATE 1993). It is particularly suitable for the analysis of flood return periods as the function asymptotically converges to 0 for extremely high discharge values. The latter corresponds to the conceptual understanding of flood discharge, which is expected to occur with decreasing frequency with increasingly extreme values.

By fitting the parameters  $\mu_{d_e}$  and  $\sigma_{d_e}$  to the observed/simulated extreme flow discharge volumes  $d_e$ , the probability density function  $f(d_e)$  in form of

$$f(d_e) = \frac{1}{\sigma_{d_e} \sqrt{2\pi}} \frac{1}{d_e} e^{-\frac{(\ln d_e - \mu_{d_e})^2}{2\sigma_{d_e}^2}} \quad \text{Eq. 5.3}$$

can be used to describe the frequency related to the occurrence of a certain discharge event (EVANS ET AL. 1993). The parameter  $\mu_{d_e}$  and  $\sigma_{d_e}$  represent the mean value and the standard deviation of the logarithmized observed/simulated extreme discharge volumes, which according to the definition of the lognormal distribution are normally distributed if  $d_e$  follows a lognormal distribution. To calculate the probability  $P_e$  that a discharge value  $D_e$  occurs which is less or equal  $d_e$ , the probability distribution function  $F(d_e)$  is calculated as the integral of the probability density function in form of (EVANS ET AL. 1993):

$$P_e(D_e \leq d_e) = F(d_e) = \frac{1}{\sigma_{d_e} \sqrt{2\pi}} \int_0^{d_e} \frac{1}{t} e^{-\frac{(\ln t - \mu_{d_e})^2}{2\sigma_{d_e}^2}} dt \quad \text{Eq. 5.4}$$

While the probability of  $D_e \leq d_e$  is needed for the investigation of low-flow return periods, the investigation of flood return periods requires the return probability of a discharge that equals or is greater than  $d_e$ . This probability is given by:

$$P_e(D_e \geq d_e) = 1 - P_e(D_e \leq d_e) \quad \text{Eq. 5.5}$$

The probability connected to the occurrence of an extreme event is related to the return period  $RP$  as:

$$P_e = 1/RP \quad \text{Eq. 5.6}$$

Eq. 5.1 to Eq. 5.6 permit to establish a relation between a certain discharge volume and its return period. Applying the lognormal distribution to extrapolate extreme flow discharge on the basis of 25 yearly low-flow and peak-flow discharge values, the return periods displayed in Fig. 5.34 (left) can be calculated. The peak-flow discharge represents the highest daily mean discharge, whereas the low-flow discharge represents the lowest 7-day average discharge in the course of the hydrological year. As displayed the flood return periods calculated on the basis of the coupled reference run simulations severely differ from reality. The observed peak-flow discharge with a return period of 25 years occurs every 2.5 years according to the model results of the coupled reference run. The discharge volume corresponding to a return period of 25 years in the coupled reference run (11380 m<sup>3</sup>/s) is almost twice as high as that for the same return period calculated on the basis of discharge recordings (5890 m<sup>3</sup>/s). As can be seen the gap between the observed and modeled discharge widens towards longer return periods.

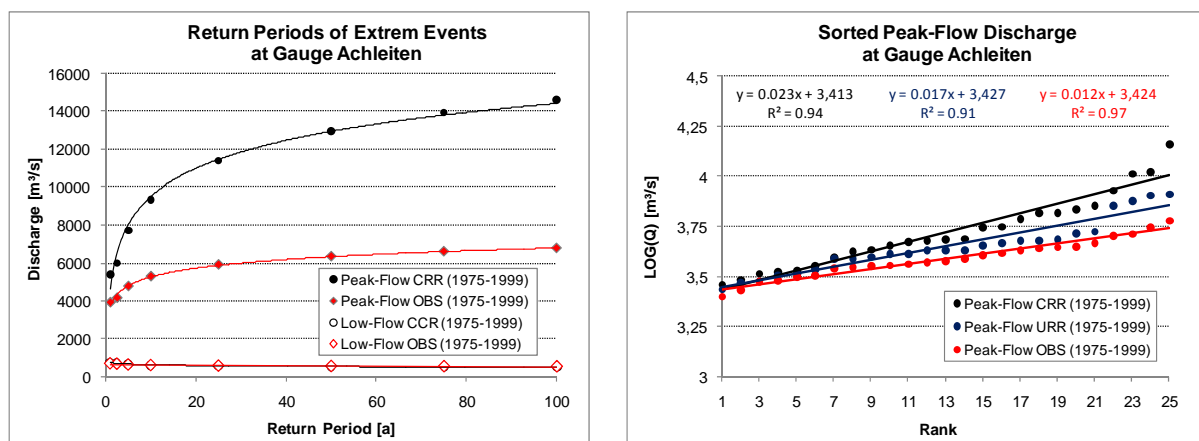


Fig. 5.34: Low-flow and flood return periods based on PROMET simulations for the coupled reference run (CRR) and observations (OBS) (left). Sorted peak-flow simulations (CRR and URR) together with sorted peak-flow observations (OBS) for the gauge at Achleiten (right).

Although PROMET tends to slightly overestimate peak-flow discharge by approximately 16 % (MAUSER AND BACH 2008), the high degree of overestimation in the coupled model run as it is displayed in Fig. 5.34 (left) cannot be attributed to this rather small percentage of overestimation. The explanation can rather be found in the mean monthly peak-flow discharge displayed in Fig. 5.32 (left). The illustration unfolds that the highest absolute overestimation of peak-flow discharge in June (1320 m<sup>3</sup>/s) temporally coincides with naturally high peak-flow discharge volumes, resulting in a severe overestimation of yearly peak-flow discharge in the coupled reference run.

Fig. 5.34 (right) shows the logarithm of the yearly peak-flow discharge used within the analysis together with the logarithm of the yearly peak-flow discharge resulting from the uncoupled reference run. As shown the degree of overestimation rises with increasingly extreme peak flow discharge. While the coefficients of determination are high in case of both, the observation based and the simulation based peak-flow discharge, the simulated peak-flow discharge volumes show comparatively high deviations from the regression line in higher ranks. This particularly applies to the results of the coupled reference run indicating that the lognormal distribution does not satisfactorily reflect the actual data distribution. As the lognormal distribution well describes the distribution of observed peak-flow discharge, it could be argued that the peak-flow discharge simulated by the coupled model system on the basis of remapped REMO simulations does not correctly reflect the natural discharge conditions in the UD. Considering the reproduction of low-flow return periods biases appear to be comparatively small.

#### *5.3.2.2.4 Evapotranspiration*

To complete the analysis of the water balance, the simulated evapotranspiration is analyzed in the following. Again, the statistical characteristics of the coupled reference run are compared to those of the uncoupled reference run for the time period 1971-2000. The average annual evapotranspiration with a value of 404 mm is very close to that simulated by PROMET on the basis of spatially distributed meteorological observations (398 mm). Considering the combination of the comparatively high precipitation amounts found in the REMO data and the warm bias in REMO temperatures, much higher evapotranspiration rates could be expected for the coupled model run. The fact that only a small part of the additionally available precipitation is returned to the atmosphere via evapotranspirative processes, can be explained by the limiting effect of the available energy budget. With a fraction of 81 % the largest part of the overall difference in precipitation amounts is found in the winter half year, where the available energy strongly limits evapotranspiration. However

the comparatively high temperatures in spring lead to notably higher evapotranspiration rates in spring for the coupled reference run.

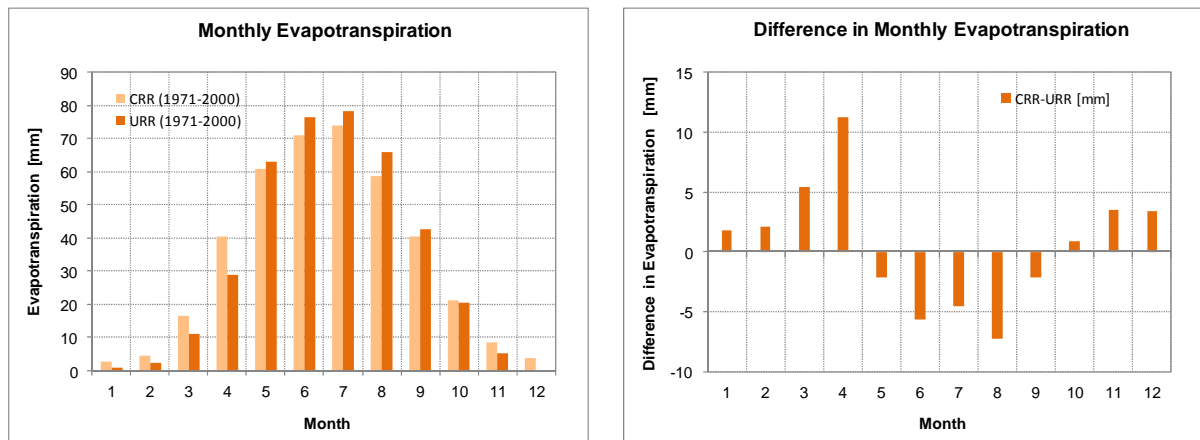


Fig. 5.35: Average monthly evapotranspiration (1971-2000) as reflected by the results of the coupled reference run (CRR) and the uncoupled reference run (URR) (left) and difference in monthly evapotranspiration (CRR-URR) (right).

In particular in April, the month characterized by the highest overestimation of temperatures in the remapped REMO data (see Fig. 5.25), evapotranspiration is much higher in the coupled reference run than in the uncoupled reference run.

To get an impression of the inter-annual variability, the mean annual evapotranspiration for the years 1971-2000 together with the area standard deviation from the area mean value are shown in Fig. 5.36. As can be seen the mean annual evapotranspiration as well as the spatial statistics, represented by the areal standard deviation, are very similar in both model runs.

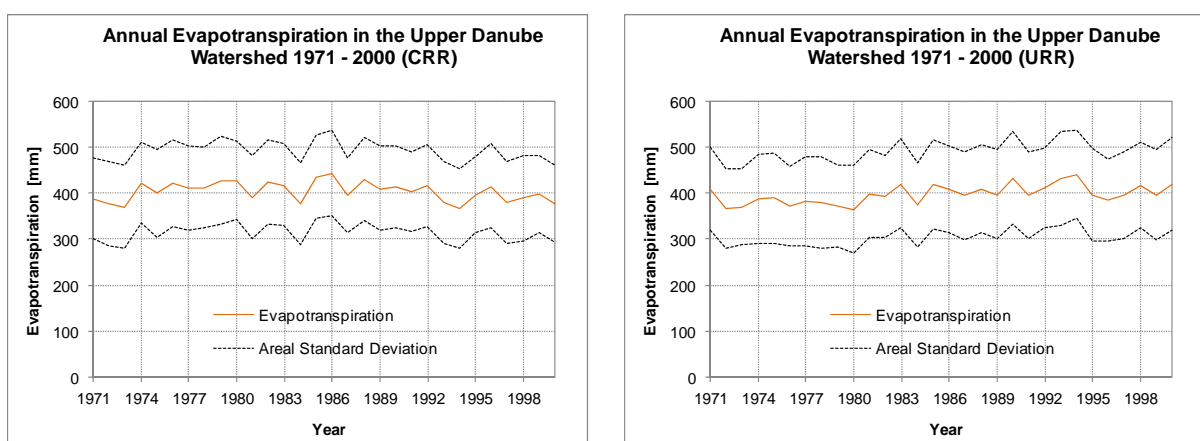


Fig. 5.36: Annual mean evapotranspiration in the Upper Danube watershed and areal standard deviation for the coupled reference run (left) and the uncoupled reference run (right). As the REMO model is forced by a simulated ECHAM5/MPI-OM meteorology at the model boundaries, merely the inter-annual variability and general dimensions should be compared between the model runs.

### 5.3.2.3 DISCUSSION

The last paragraphs have discussed both, the meteorological forcings as well as the hydrological results of the coupled reference run (REMO-SCALMET-PROMET). Summarizing the analysis of remapped REMO temperature and precipitation simulations for the years 1971-2000, the comparison of remapped simulations to spatially distributed observations show a noticeable overestimation of mean temperatures and annual precipitation for the area of the UD. However it has to be noted, that all reference datasets used within the comparison are based on model results and therefore include considerable uncertainties. This is partly reflected by the rather large differences between the two observation based precipitation datasets of the HAA and the PROMET distributions (see chapter 5.3.2.1.2). Besides the inaccuracies related to the spatial distribution of precipitation, the input precipitation gauges are subject to large measurement errors as a consequence of evaporative losses and wind drift. As RCMs are not affected by such errors, this might partly explain the higher precipitation amounts in regional climate simulations. Despite all explanations, there is evidence that the real rainfall conditions within the UD are overestimated to a certain degree. As most of the overrepresentation of rainfall occurs in the winter half year, where evapotranspiration rates are naturally low, runoff volumes simulated in the coupled model run are higher than those recorded at the catchment outlet in Achleiten. This applies to annual and monthly mean conditions as well as to low- and peak-flow discharge volumes. The overestimation in peak-flow discharge volumes further leads to considerable biases in the return periods of peak-flow discharge.

Within the scenario run, the coupled model system will be utilized in the same configuration as in the coupled reference run. As all uncertainties related to the different components of the coupled model system can be expected to be in a similar dimension within both runs, it is possible to analyze the climate change signal in the model runs. This so-called 'delta change approach' is particularly recommended when using meteorological simulations to force physically based hydrological models, as the latter are very sensitive to biases in the meteorological input (ANDRÉASSON ET AL. 2004, GERLINGER 2004).

## 6 APPLICATION TO CLIMATE PROJECTIONS

### 6.1 THE IPCC SCENARIOS

Climate models are utilized to model and to quantify the climatic response to present and future human activities. To gain confidence in the climate model simulations, the models have to prove their ability to reproduce past and current climate conditions without changes in external climate forcing. Given a satisfactory model performance, these simulations serve as a baseline for a comparison to the results obtained for possible future atmospheric conditions.

For the generation of a possible future climate, the climate models are forced by different greenhouse gas and aerosol scenarios. The scenarios provide time-dependent profiles of atmospheric aerosol and greenhouse gas concentrations for the future and are based on different assumptions concerning future emissions of climate relevant gases into the atmosphere. Of course the estimation of future developments comes with a large number of uncertainties including both, the range of emissions and future gas concentrations in the atmosphere as well as the climate reaction upon these altered boundary conditions. To coordinate the worldwide efforts in the field of climate change research, but also to allow an intercomparison of climate model simulations, international standards for possible future greenhouse gas concentrations are required. In the year 2000 the Intergovernmental Panel on Climate Change (IPCC), representing the world's leading scientists in the field of climate change, presented a set of emission scenarios in the Special Report on Emission Scenarios (SRES) (IPCC 2000).

The scenarios are based on different storylines of socioeconomic and demographic developments covering a wide range of plausible and consistent possible future developments. Depending on several assumptions related to economic growth, energy intensity and efficiency as well as the growth of the world population, four scenario families have been worked out providing the radiative forcings for a large number of climate model runs (A1, A2, B1, B2).

The A-families are characterized by a domination of economic drivers, whereas the B-families assume environmental concerns to be the driving force. A further differentiation is given by the number associated with the scenario families. While the A1 and B1 scenario families are rather globally orientated, the A2 and B2 scenario families pursue a rather regional policy.

The following gives a brief survey of the scenario families and their main characteristics as presented by the IPCC (2000):

- A1: The A1 storyline and the associated scenario are based on an expanding economic prosperity together with a rapid introduction of new and efficient technologies. The global population reaches its maximum in the mid-century followed by a later decline in population up to the year 2100. Following its rather global orientation, an increase of cultural and social interactions as well as a substantial reduction in regional differences in per capita income is assumed. The scenario family distinguishes between three directions of technical change in the energy system represented by three different scenario groups. While for the A1T scenario group technological emphasis is put on non-fossil energy sources, the A1FI scenario group assumes an intensive use of fossil energy sources. Not relying on one particular energy source, the A1B scenario group assumes a balanced employment and further development of all available energy sources.
- A2: The A2 storyline and scenario pictures a very heterogeneous world characterized by a society willing to preserve local identities. Population is continuously growing due to a retarding convergence of fertility patterns across the regions. Economic development takes place on a regional level with per capita economic growth and changes in technology taking much more time compared to other scenarios.
- B1: The B1 scenario and storyline displays a convergent world with similar population growth as in the A1 scenario storyline. Economic structures develop toward a service and information economy going together with an introduction of clean and resource efficient technologies. Solutions to social, economic and environmental sustainability are pursued on a global level, thus not creating additional climate initiatives.
- B2: The B2 scenario and storyline pictures a world in which the goals of economic, social and environmental sustainability are pursued on a local and regional level. The world population is continuously growing, however not as rapidly as in the A2 storyline. Economic development is less distinct and technical change takes more time and is more diverse compared to the storylines of B1 and A1B.

The course of CO<sub>2</sub>-emissions from 1990-2100 together with the related increase of air temperatures are displayed for all scenarios described above in Fig. 6.1. For further information concerning the scenario families and storylines refer to IPCC (2000).

The scenarios describe possible future evolutions of the driving forces for future greenhouse gas emissions. All scenarios assume that no additional climate initiatives will be brought up

and that none of the currently pursued targets (e.g. those of the Kyoto Protocol) will be reached. The IPCC puts strong emphasis on the fact, that all scenarios are equally probable.

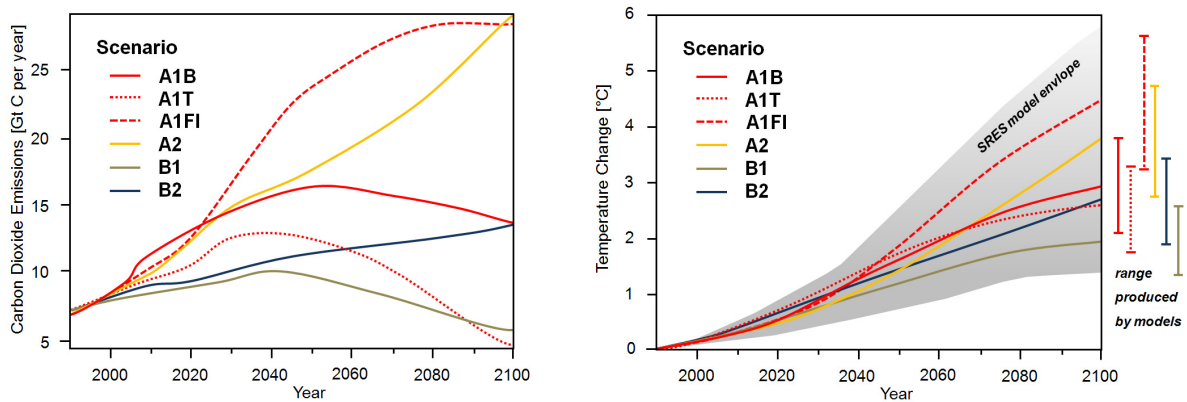


Fig. 6.1: The CO<sub>2</sub>-emissions and changes in temperature for the different IPCC scenarios (based on IPCC 2000).

## 6.2 THE A1B SCENARIO – METEOROLOGICAL CONDITIONS IN THE UPPER DANUBE WATERSHED

The last chapter has given an introduction to the different IPCC scenarios and their main characteristics. For this thesis the A1B scenario was chosen to provide the radiative forcings for the regional climate model REMO. The scenario belongs to the family of the A1 scenarios and represents the scenario group, for which a balanced utilization of energy sources (fossil and non-fossil) is assumed (see chapter 6.1). The following paragraphs will show the regional impact of globally altered radiative forcings as predetermined by the A1B emission scenario. Only temperature and precipitation will be considered, as these variables are known to be very sensitive to changes in atmospheric greenhouse gas concentrations. Moreover, temperature and precipitation represent the most important atmospheric quantities in hydrological applications (KOTLARSKI ET AL. 2005). All comparisons that are shown in the following represent remapped REMO simulations. The data used within the one-way coupled reference run originates from the REMO control run, whereas the data used within the scenario run originates from the REMO A1B run (see Tab. 5.3). The time span to be considered in the scenario run has been defined within the GLOWA-Danube Project to cover the years 2011 to 2060 to deliberately exclude present day climate conditions.

Within the analysis both, changes relative to the reference run as well as trends within the scenario period will be identified. Trends within the scenario period are tested for significance

---

using a nonparametric Mann-Kendall test (MANN 1945). Depending on the significance level  $\alpha$  the trends are regarded as significant ( $\alpha \leq 10\%$ ) or not significant ( $\alpha > 10\%$ ).

### 6.2.1 TEMPERATURE

Temperature is the one meteorological parameter that is most commonly analyzed and referred to in the context of climate change. The increasing amount of greenhouse gases in the atmosphere – the most important ones are water vapor (H<sub>2</sub>O), carbon dioxide (CO<sub>2</sub>), ozone (O<sub>3</sub>), nitrous oxide (N<sub>2</sub>O) and methane (CH<sub>4</sub>) – alters the radiation budget of the earth-atmosphere-system. The result is an increase in thermal radiation emitted by the atmosphere, an effect that is also known as the greenhouse-effect. Surface temperature and as a direct consequence the temperature of the surrounding air masses increase. Besides the general rise in temperatures as a result of altered greenhouse gas concentrations, important changes in the large scale circulation are simulated by RCMs that also affect regional temperature conditions. The increased frequency of westerlies in winter enhances the warming in central Europe, whereas more frequent easterly flows lead to an increased frequency of very warm months in summer (VAN ULDEN ET AL. 2007). The changes in circulation as well as a diversity of local factors lead to locally different change signals, although the radiative forcings are globally predetermined in the framework of the A1B scenario (see Fig. 6.1). Fig. 6.2 shows the change in mean annual temperatures as reflected by the remapped REMO simulations used within the coupled reference run (1961-2000) and the scenario run (2011-2060) for the domain of the UD. The area mean temperature rise between the coupled reference run and the scenario run for the UD takes a value of 1.17 °C ( $\text{std\_dev}_{area} = 0.11\text{ °C}$ ). Lowest temperature increases of about 1 °C are primarily found for the area of the Danube Valley near Passau, while values of around 1.9 °C occur in the higher elevated parts of the Alps. Besides the general tendency to higher values in the Alpine areas that is predetermined by the REMO simulations, the change signal in the remapped annual mean temperature shows a certain elevation dependency. An explanation is given by the fact that the temperature-elevation dependence reflected by the REMO scenario simulations is different from that reflected by the meteorology of the reference run. With a mean annual lapse rate of 5.5 °C/km the temperature decrease with elevation in the coupled reference run for all REMO pixels inside the UD is slightly larger than that of the scenario run (5.3 °C/km). As a consequence temperatures for subgrid pixels in higher elevations than the mean 10 x 10 km elevation are less corrected towards lower values within regression based remapping for the scenario run than for the reference run. The temperature increase for these pixels therefore is higher than that of the associated 10 x 10 km REMO pixel. This emphasizes the

importance of applying remapping methods that are able to adapt to changing meteorological conditions.

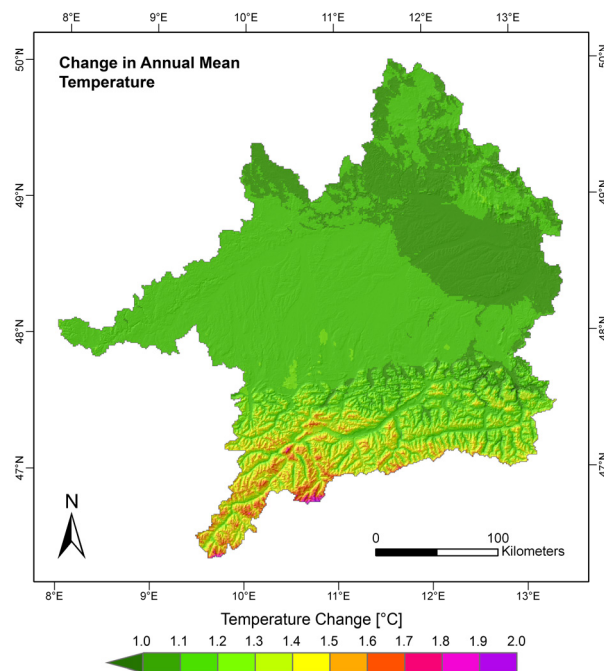


Fig. 6.2: Change in annual mean temperature in the Upper Danube watershed (A1B (2011-2060) - Reference (1961-2000)). For the sake of visualization the map is overlaid by a semitransparent hillshade effect.

The temperature rise shown in Fig. 6.2 is the result of a highly significant ( $\alpha = 0.1\%$ ) continuous increase in near surface air temperatures in the domain of the UD (see Fig. 6.3). Although only the years 2011 to 2060 have been regarded in the coupled scenario run (REMO-SCALMET-PROMET), the years 2061 to 2100 have been included in Fig. 6.3 to show the development of temperature conditions for the subsequent years.

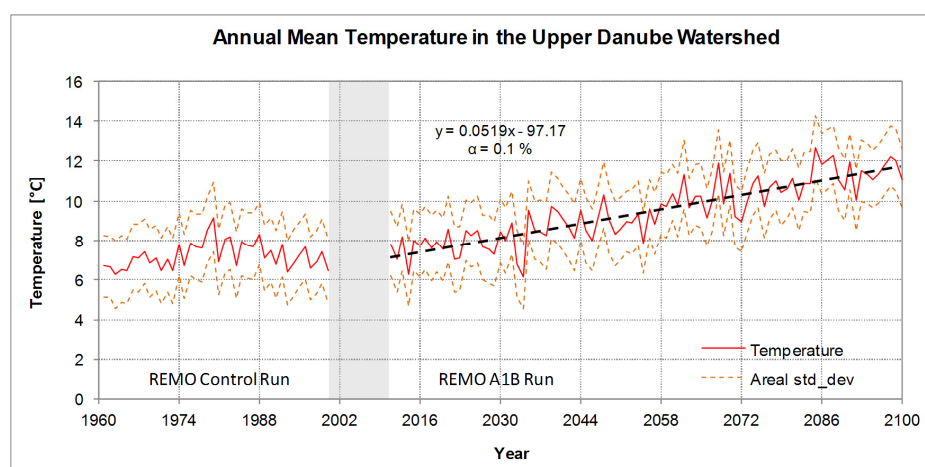


Fig. 6.3: Annual area mean temperature in the Upper Danube watershed as reflected in remapped REMO control run and A1B scenario run data.

The average increase rate found in area mean annual temperatures simulated for the UD takes a value of about 5.2 °C/100 years. Comparing this increase rate to the global trend of approximately 2.9 °C/100 years as it is characteristic for the A1B scenario family (IPCC 2007) unfolds, that the regional trend in the UD is 1.8 times larger than the global mean. Besides the inter-annual variability displayed in Fig. 6.3, a certain seasonal variability can be found in the temperature trends (see Fig. 6.4).

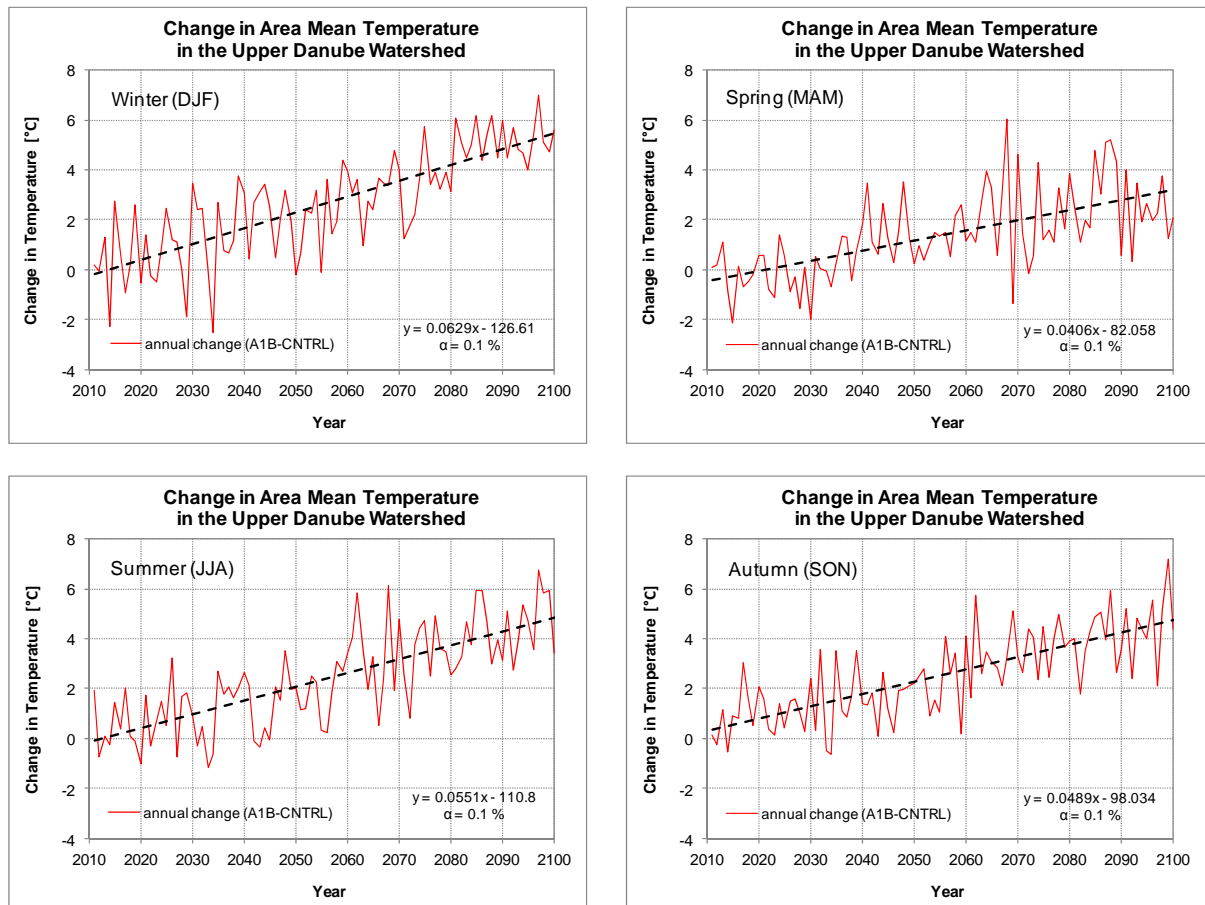


Fig. 6.4: Seasonal change in area mean temperature in the Upper Danube watershed. The seasonal area mean temperature of the reference period (1961-2000) is subtracted from the seasonal area mean temperature of a considered year in the scenario period).

Highest increases of mean air temperatures are simulated for the winter months ( $\approx 0.06$  °C/year). While for the years 2011 to 2060 an increase in mean monthly temperatures of approximately 1.7 °C can be observed for February, the subsequent months of March and April are characterized by a significantly lower increase in monthly temperatures of 0.6 and 0.3 °C respectively (see Fig. 6.5). As shown in Fig. 5.25 (chapter 5.3.2.1.1) within the direct comparison between remapped REMO control run data and spatially distributed meteorological observations, these two months are characterized by the highest degree of overestimation of monthly mean temperatures in the control run simulations (1971-2000).

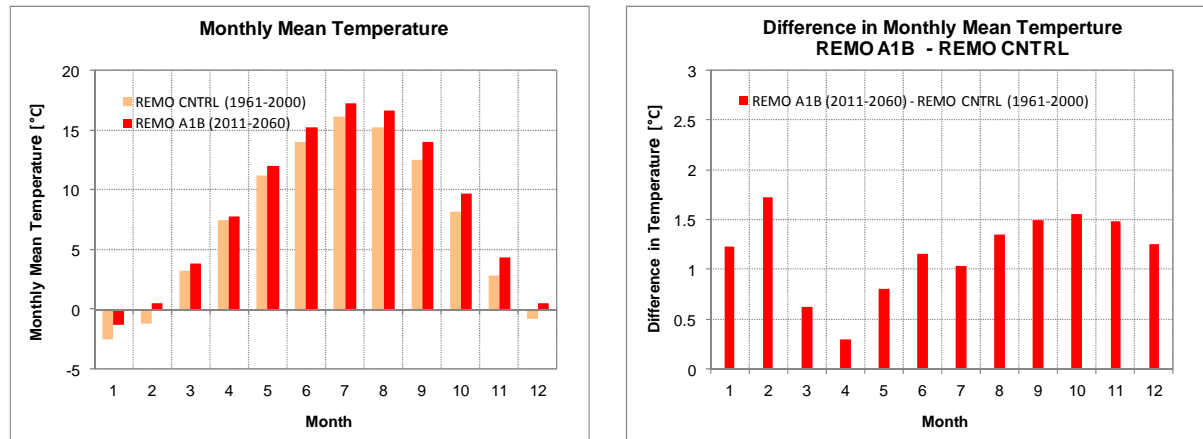


Fig. 6.5: Monthly mean temperatures of the coupled reference run and the scenario run (left) and absolute change in monthly mean temperatures for the Upper Danube watershed (right) (A1B (2011-2060) - Reference (1961-2000)).

While summer and autumn are characterized by similar trends of approximately 0.05 °C/year, the spring months of March, April and May are characterized by slightly lower temperature increase rates of approximately 0.04 °C/year.

The increase in air temperatures has several hydrological consequences. Higher temperatures can be expected to result in higher evapotranspiration rates. The temperature increase in winter is of particular hydrological relevance as precipitation to an increasing degree falls in the liquid phase in winter. Further the water quantities stored in the solid state of snow generally decrease with increasing temperatures. As a direct consequence discharge regimes might change in the future.

## 6.2.2 PRECIPITATION

The amount of water in the atmosphere is largely determined by the air temperature. Higher temperatures lead to an increased evapotranspiration of water from the land surface and water bodies into the surrounding air. Warmer air shows an increased ability to hold and transport water. As a consequence Atlantic air masses will be able to transport increasing amounts of water into the Central European areas. The changes in the circulation for Central Europe further lead to an increase in precipitation in winter due to the increased frequency of westerly flows. Many RCMs further simulate a decrease in summer precipitation as a result of an increased frequency of easterly flows in combination with a more pronounced summer drying (VAN ULDEN ET AL. 2007). The change signal in annual precipitation in the area of the UD is illustrated in Fig. 6.6. The changes are calculated relative to the remapped meteorology of the coupled reference run. Thereby, the average annual precipitation of the reference run (1961-2000) is subtracted from the average annual precipitation of the scenario run (2011-2060). The resulting difference in precipitation is then divided by the

reference run conditions and multiplied by 100 to get the percental change in precipitation amounts. As can be seen there is an increase in annual precipitation in the UD for the period 2011 to 2060 relative to the reference run.

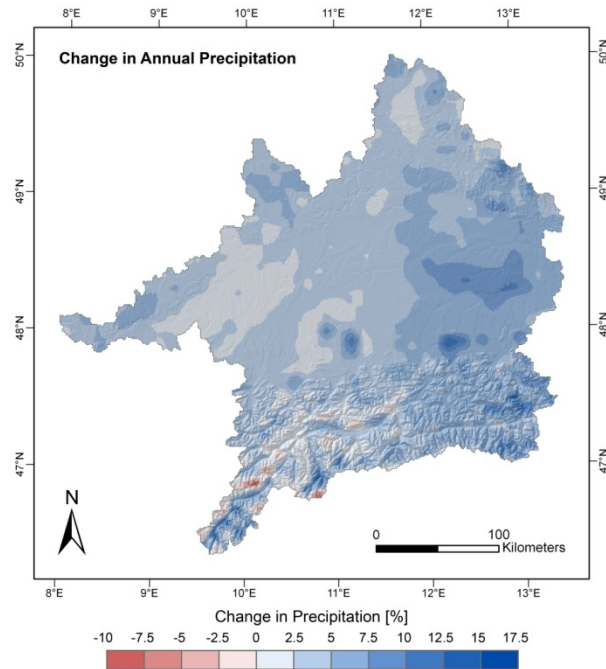


Fig. 6.6: Relative change in average annual precipitation in the Upper Danube watershed (A1B (2011-2060) - Reference (1961-2000)). For the sake of visualization the map is overlaid by a semitransparent hillshade effect.

While the increase relative to 1961-2000 considering the years 2011-2060 with approximately 5 % is comparatively high, the inclusion of the years 2061-2100 reduces the increase relative to 1961-2000 to less than 1 %. This can be explained by the fact that there is a decrease in annual precipitation for the years from approximately 2060 to 2100 (see Fig. 6.7).

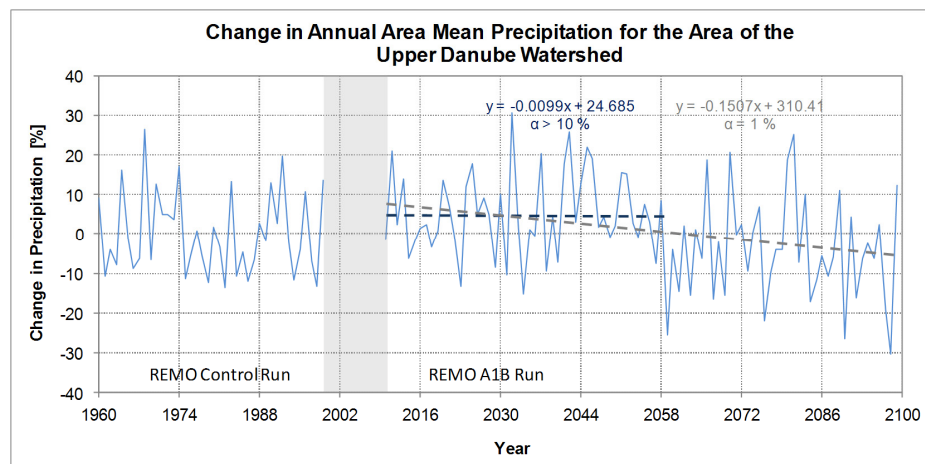


Fig. 6.7: Change in annual area mean precipitation for the area of the Upper Danube watershed. The change signal represents the deviation from the mean conditions in the reference period (1961-2000).

Considering the trend within the scenario period, a significant decrease in annual precipitation can only be observed including the years 2061-2100 into the analysis (see Fig. 6.7). This emphasizes that simulated changes in meteorological variables largely depend on the time period considered.

Changes in precipitation amounts are expected to vary seasonally. For the area of Germany an increase in winter rainfall combined with decreasing precipitation amounts in summer is simulated by the majority of climate models (MAHRENHOLZ 2007). Again changes are displayed including the years 2061-2100. As linear trends in case of precipitation have shown to be very sensitive to the time period considered (see Fig. 6.7), a five year running average is introduced as an additional criterion to give a smoothed impression of the long term trend in precipitation. The changes in remapped REMO precipitation for the area of the UD are shown over the period 2011-2100 in Fig. 6.8.

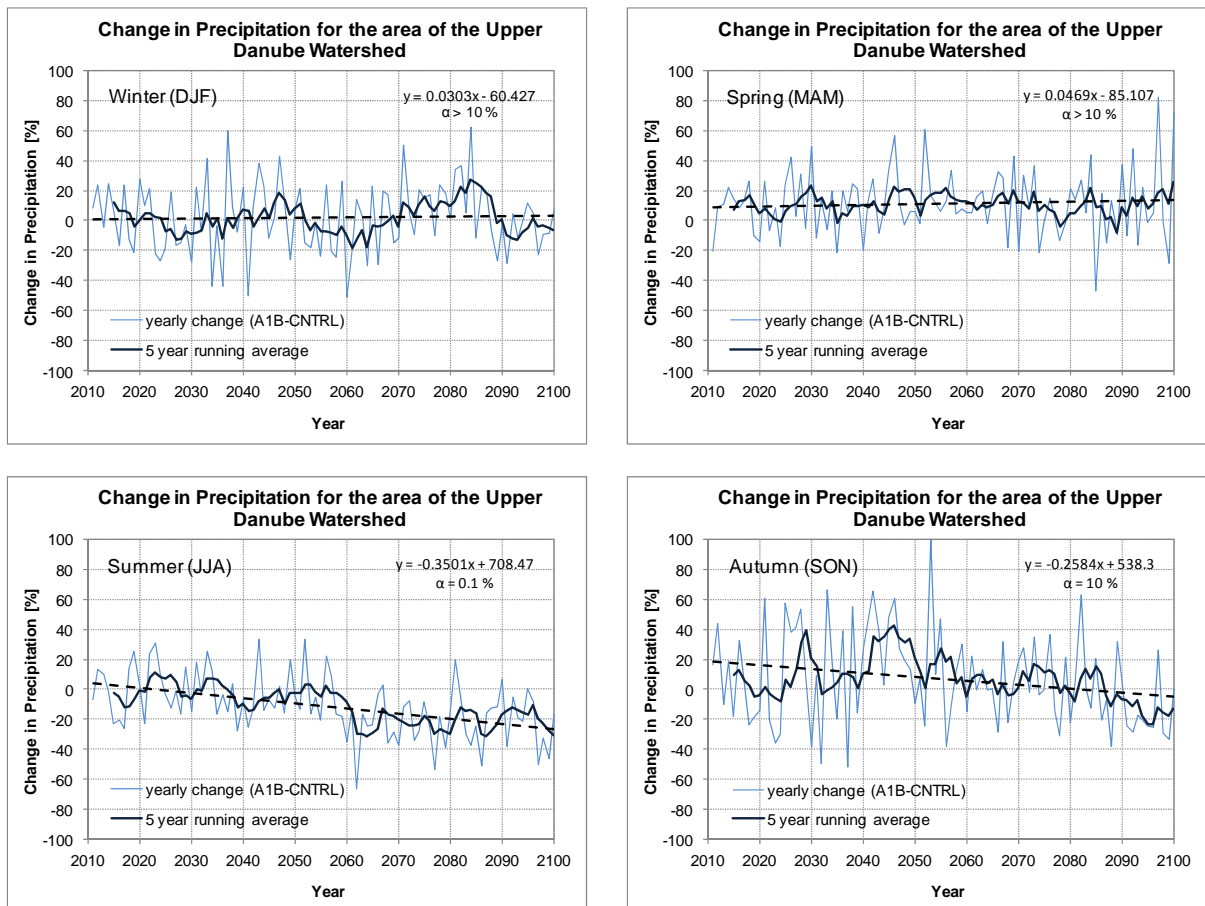


Fig. 6.8: Seasonal change in area mean precipitation for the area of the Upper Danube watershed. The change signal represents the deviation from the mean conditions in the reference period (1961-2000).

As displayed, the inter-annual variability of simulated precipitation is very high for all seasons. The increase in winter precipitation is rather moderate for the area of the UD largely depending on the time period considered. While comparatively strong increases in

precipitation amounts can be found for the years 2070-2090, the years 2011-2060 only show very little increases in winter precipitation. In spring, remapped precipitation of the scenario period is almost continuously above the mean reference run precipitation. This is due to the increased rainfall in March, which shows the highest increase compared to the reference period (see Fig. 6.9). While the decrease in summer rainfall is rather little for the period 2011-2060, there is a distinct falloff in the subsequent years 2061-2100 (see Fig. 6.8).

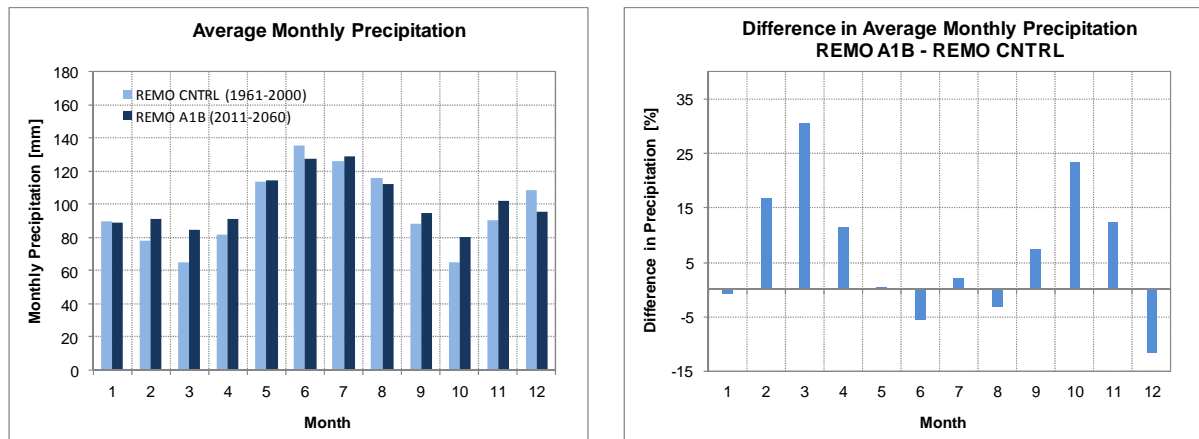


Fig. 6.9: Average monthly precipitation for the reference run and scenario run meteorology (left) and change in average monthly precipitation in the Upper Danube watershed (right) (A1B (2011-2060) - Reference (1961-2000)).

Simulations for autumn within the period 2011-2060 show increased rainfall amounts, followed by a decline for the subsequent years (2060-2090). The change in precipitation amounts is not only subject to seasonal variations, it further shows distinct spatial patterns. The spatial distribution of the change signal in remapped rainfall simulations is shown in Fig. 6.10 for all four seasons. While spring and autumn precipitation show a distinct increase over the whole domain, changes in seasonal precipitation for winter and summer produce a rather heterogeneous picture. However, in summer the few areas with increased precipitation amounts cannot compensate the dominant decrease of rainfall amounts in the major part of the domain. The increase in winter for the period 2011-2060 is rather moderate as the highest increases in winter precipitation are found in the subsequent years 2070 to 2100.

As a result of the seasonal changes in precipitation that have been analyzed above, the average annual precipitation in the domain of the UD increases from 1160 mm in the reference run (1961-2000) to 1217 mm in the scenario period (2011-2060). This absolute increase of 57 mm corresponds to a relative gain of approximately 5 %.

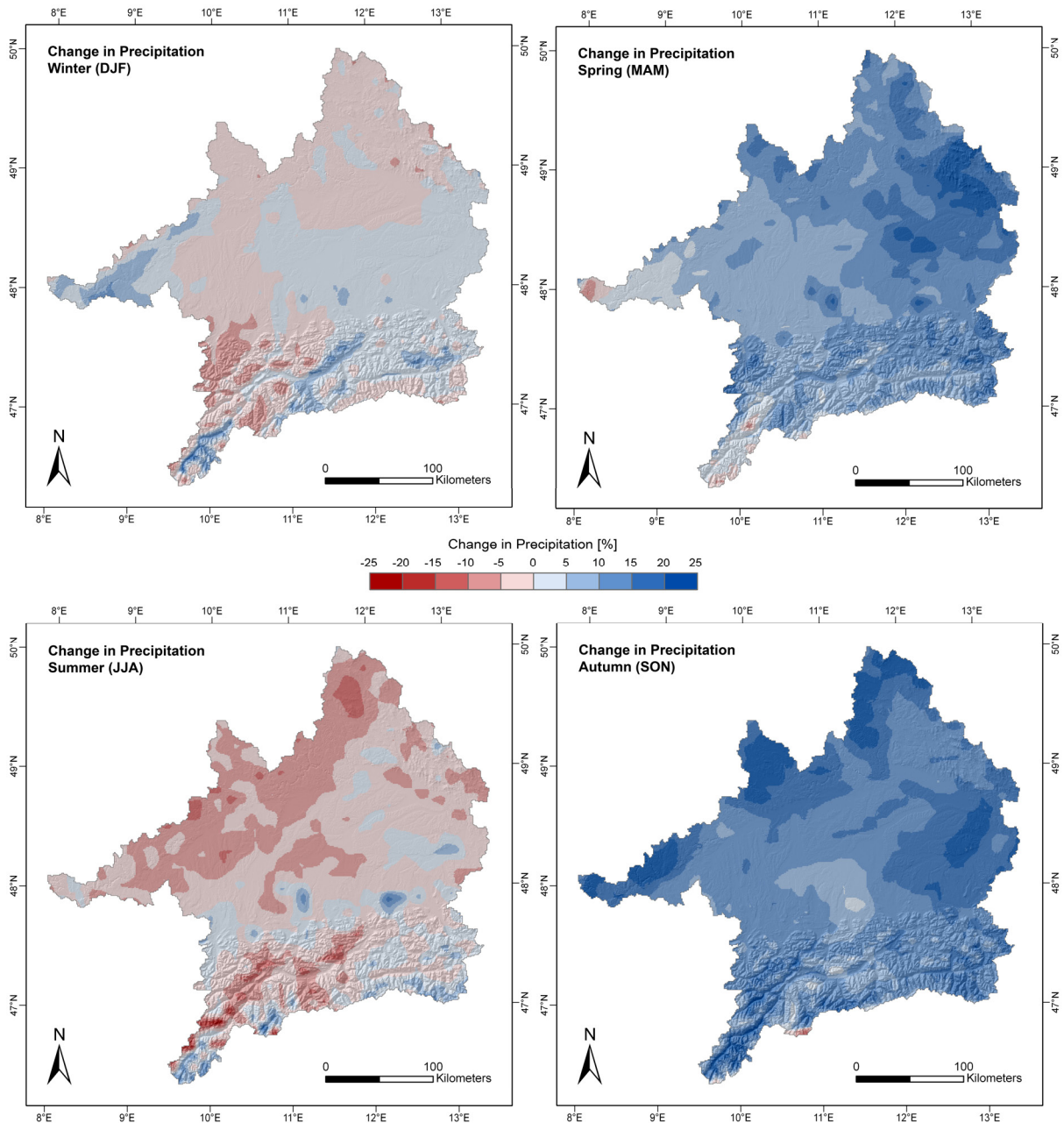


Fig. 6.10: Relative change in average seasonal precipitation for the Upper Danube watershed (A1B (2011-2060) - Reference (1961-2000)). For the sake of visualization all maps are overlaid by a semitransparent hillshade effect.

### 6.3 THE A1B SCENARIO – HYDROLOGICAL IMPACT IN THE UPPER DANUBE WATERSHED

The previous chapters of this work have shown the climate change signal given by the differences in temperature and precipitation between the coupled reference run (1961-2000) and the coupled A1B scenario run (2011-2060). In the following, the hydrological impact of these altered meteorological boundary conditions will be analyzed. Thereby, the results of the

coupled scenario run are compared to those of the coupled reference run. In a first step the mean annual water balance for the scenario run is analyzed. In analogy to the reference run, this is done by subtracting the daily evapotranspiration from rainfall. The result is displayed in Fig. 6.11.

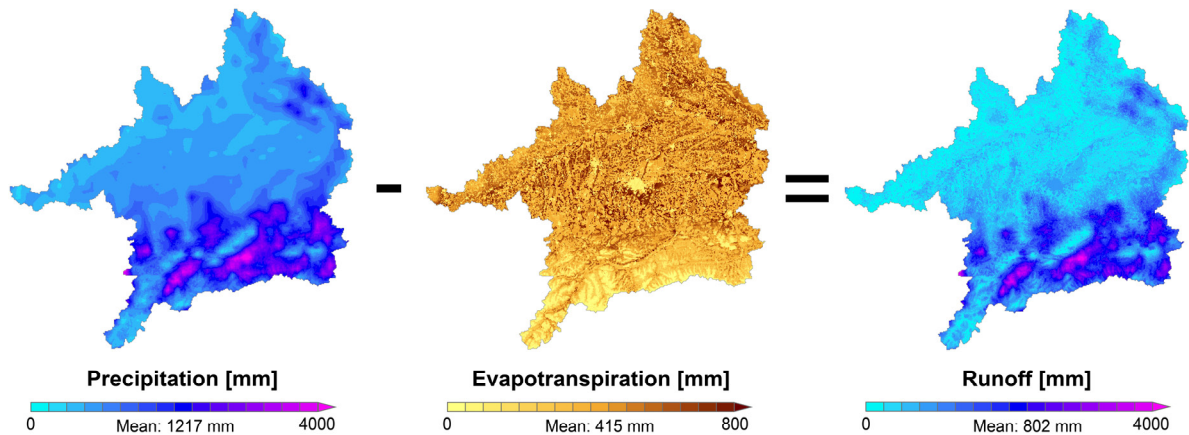


Fig. 6.11: The average modeled water balance in the Upper Danube watershed for the hydrological years 2011-2060. The hydrological model PROMET in the one-way coupled model run was forced by a remapped REMO (A1B) meteorology.

### 6.3.1 EVAPOTRANSPIRATION

The amount of water returned to the atmosphere within the process of evapotranspiration largely depends on the water and energy budget. Further plant transpiration which contributes to the total evapotranspiration is highly sensitive to the duration of the vegetation period. Due to the increase in temperature and precipitation and the prolonged vegetation period, evapotranspiration with a mean value of 415 mm is 14 mm (3.5 %) higher in the scenario run than in the reference run (401 mm).

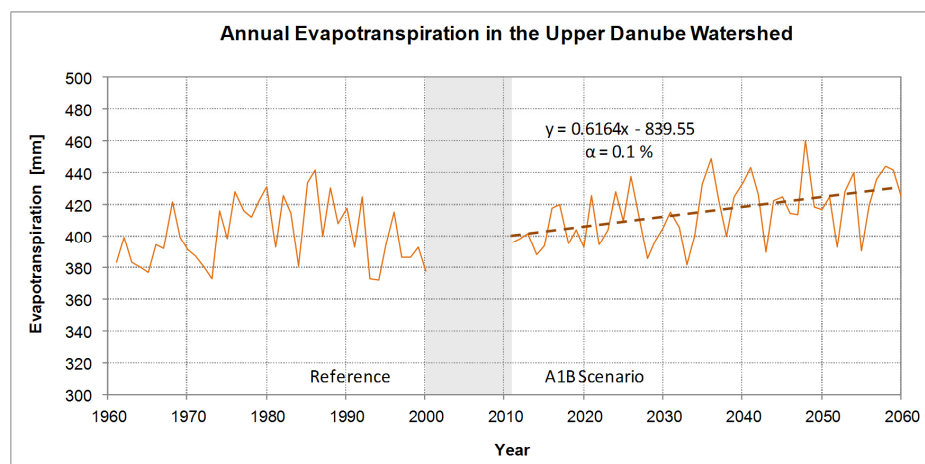


Fig. 6.12: Modeled annual evapotranspiration for the coupled reference run and the scenario run

Parallel to the increase in temperature, evapotranspiration continuously increases up to the end of the time period considered (see Fig. 6.12). Analyzing the trend by means of a Mann-Kendall test (MANN 1945) reveals that the trend in evapotranspiration is highly significant ( $\alpha = 0.1\%$ ). In analogy to temperature and precipitation, the changes in evapotranspiration show a high seasonal variability (see Fig. 6.13).

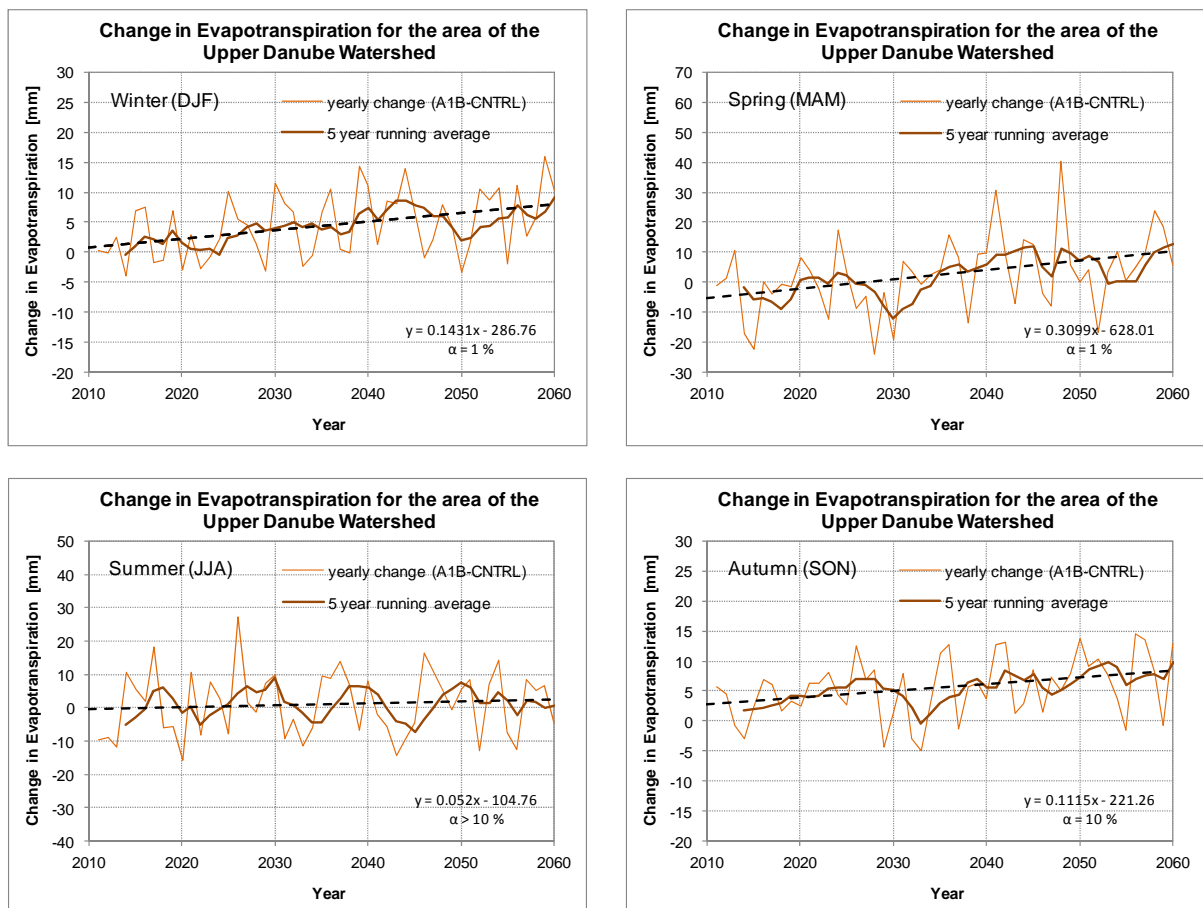


Fig. 6.13: Change in area mean evapotranspiration for the area of the Upper Danube watershed (A1B (2011-2060) - Reference (1961-2000)).

As displayed, the most notable and significant trends are found in winter and spring. Considering the absolute increase a considerable rise in monthly evapotranspiration can be observed for spring, autumn and winter (see Fig. 6.14). These seasons are characterized by little evapotranspiration in the reference run. The increase in monthly mean temperatures in the months of January, February and December together with the increase in precipitation amounts (in a liquid state) lead to a monthly evapotranspiration occasionally exceeding 10 mm/month. Similar tendencies can be observed in the case of spring and autumn. Summer evapotranspiration does not show a significant increase. As shown in Fig. 6.14, for the month of July even a decline in evapotranspiration can be observed comparing the evapotranspirated water quantities of the scenario run to those of the reference run. It is

necessary to point out that evapotranspiration in July is generally very high. In the reference run the month of July is characterized by the highest monthly rates of approximately 74 mm.

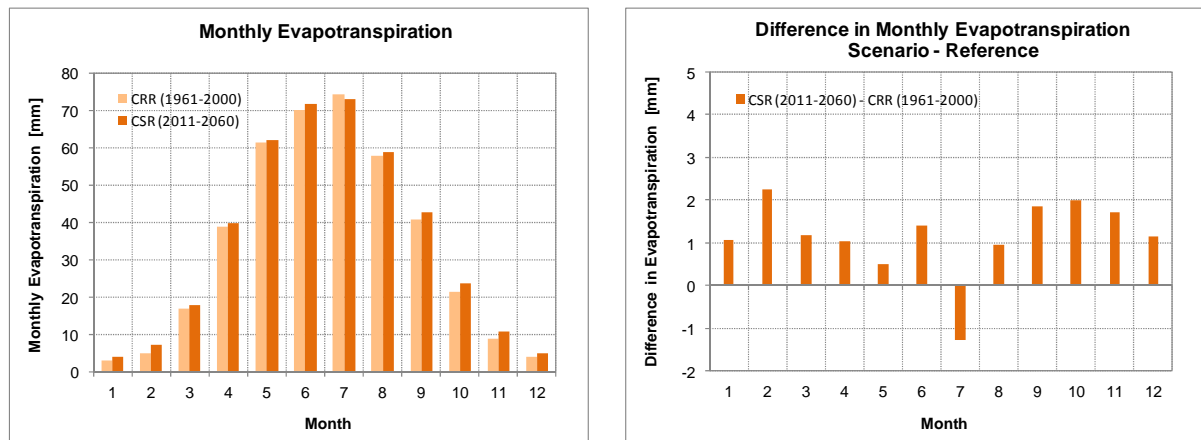


Fig. 6.14: Simulated mean monthly evapotranspiration for the coupled reference run (CRR) and the coupled scenario run (CSR) (left) and difference in evapotranspiration between both runs (right) (A1B (2011-2060) - Reference (1961-2000)).

The cause for the fact that evapotranspiration in July is not subject to further increases in the scenario run is found in the limiting effect of water availability. Fig. 6.15 shows the change in the average plant available soil water content in the top soil layer, which represents the upper 20 cm of the total soil column for the month of July.

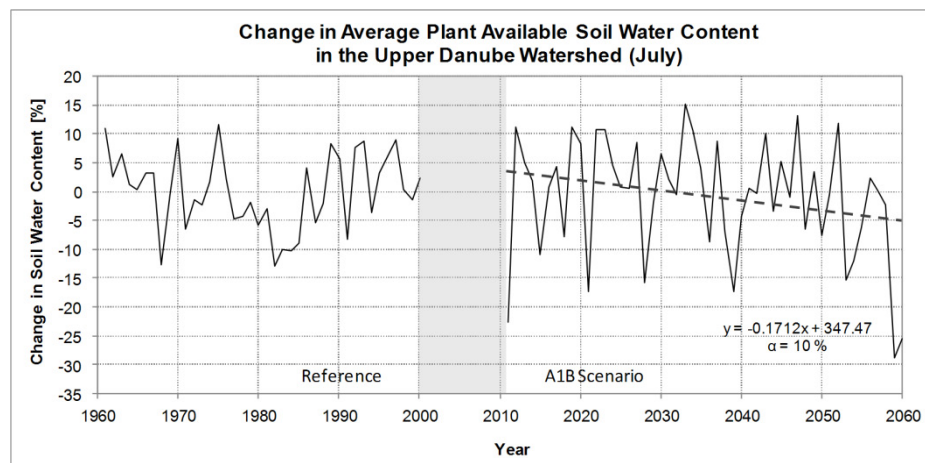


Fig. 6.15: Change in average plant available soil water (upper 20 cm of the soil) in July for the area of the Upper Danube watershed. The change signal represents the deviation from the mean conditions in the reference run (1961-2000).

The diagram shows an increase in soil water variability for the month of July in the scenario period (2011-2060). Further a severe decrease in the average plant available soil water up to the end of the considered period can be observed that has been proven to be significant at a significance level of  $\alpha = 10\%$ . The decrease in soil water in July is the result of a strongly increased evapotranspiration in June in combination with a decrease in precipitation in this month.

### 6.3.2 SNOW HYDROLOGY

Water fluxes in the UD are largely determined by the seasonal storage of water in the snow pack. Moreover, snow plays an important role for winter tourism in the research area of the UD. This huge importance together with the manifold reactions of snow dynamics to different climate change signals (e.g. changes in temperature, precipitation and radiation) call for a detailed examination of changes in snow cover and snow fall between the reference period (1961-2000) and the scenario period (2011-2060).

As a consequence of the rise in temperatures, the duration of the seasonal snow cover as well as the time and duration of snowmelt can be expected to change in the scenario period. Further the amount of solid precipitation is expected to decrease parallel to the rise in temperatures. All these circumstances are of particular hydrological relevance, as they largely dominate the amount of hydrologically available precipitation and in consequence the river discharge regimes in the catchment. To investigate the snow hydrological impact of the scenario meteorology, the number of days characterized by snow cover (snow water equivalent > 1 mm) together with the annual amount of solid precipitation has been compared between the reference run (1961-2000) and the scenario run (2011-2060). Fig. 6.16 shows the change in annual snowfall relative to the mean conditions of the reference period.

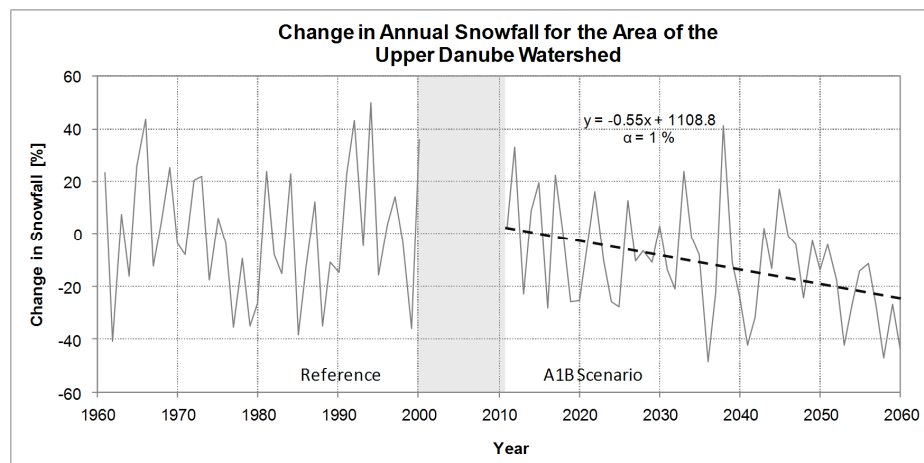


Fig. 6.16: Change in annual snowfall for the area of the Upper Danube watershed. The change signal represents the deviation from the mean conditions in the reference run (1961-2000).

It has to be pointed out that the visualized snowfall quantities are not based on REMO simulations directly. Snowfall amounts have been computed by the hydrological model PROMET on the basis of remapped precipitation simulations. Thereby, the wet bulb temperature is used to decide whether the precipitation is liquid or solid. To minimize all uncertainties that are connected to the combination of the individual components of the coupled model system, only relative changes are considered.

As Fig. 6.16 shows, there is a strong decrease in annual snowfall that could be proven to be highly significant ( $\alpha = 1\%$ ). The spatial distribution of simulated changes in annual snowfall is shown together with the change in the number of days characterized by the presence of a snow cover in Fig. 6.17. The illustrations unfold a decrease in both, snowfall and snow cover days for the whole domain. As displayed the change signal in yearly snowfall and that in the number of days with snow cover give a very similar picture. Temperatures in higher elevated parts of the Alps and the Bavarian Forest still allow a comparatively high number of snow cover days and large snowfall amounts in the scenario run.

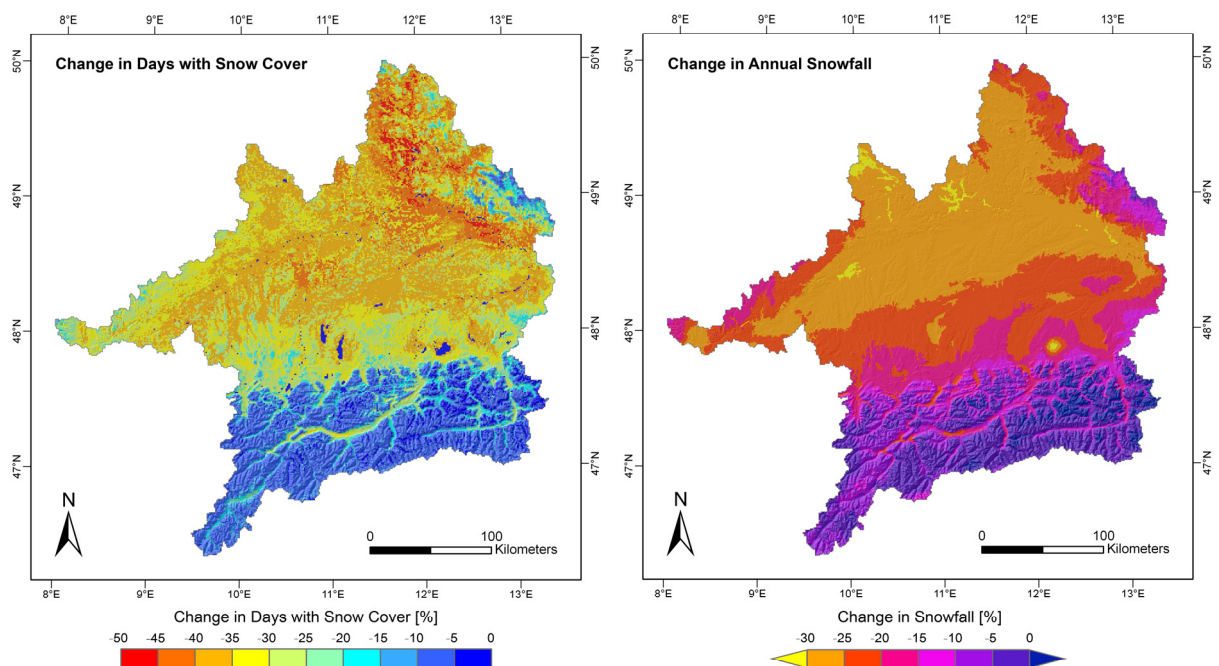


Fig. 6.17: Change in the number of days characterized by the presence of a snow cover (SWE > 1 mm) and change in annual snowfall in the Upper Danube watershed (A1B (2011-2060) - Reference (1961-2000)).

In those higher elevated regions which are characterized by an increase in precipitation (see Fig. 6.6 and Fig. 6.10) snowfall is even increased and snow cover duration at least not shortened. A different picture unfolds considering the lower elevations of the Alpine valleys. Here, the number of snow cover days decreases by sometimes over 30 % combined with a decrease in annual snowfall of up to 25 %. Even higher decrease rates can be found in the Alpine foreland with a general tendency from lower decrease rates in the south to higher decrease rates in the north. Fig. 6.18 shows the decadal change in days with snow cover for the Alpine part of the catchment. The different stages represent the change calculated by comparing the mean conditions of the considered decade to the mean conditions of the reference run (1961-2000). Again, a day with snow cover is defined as a day with a SWE larger than 1 mm. As shown the decrease in snow cover days traces the continuous rise in temperatures up to the end of the scenario period in the year 2060. Again, highest decrease

rates are observed in the lower elevations of the Alpine foreland and the Alpine Valleys. Some of the higher elevated places in the Alps are characterized by a comparatively small decrease in snow cover days due to an increase in precipitation in combination with very low temperatures in these regions.

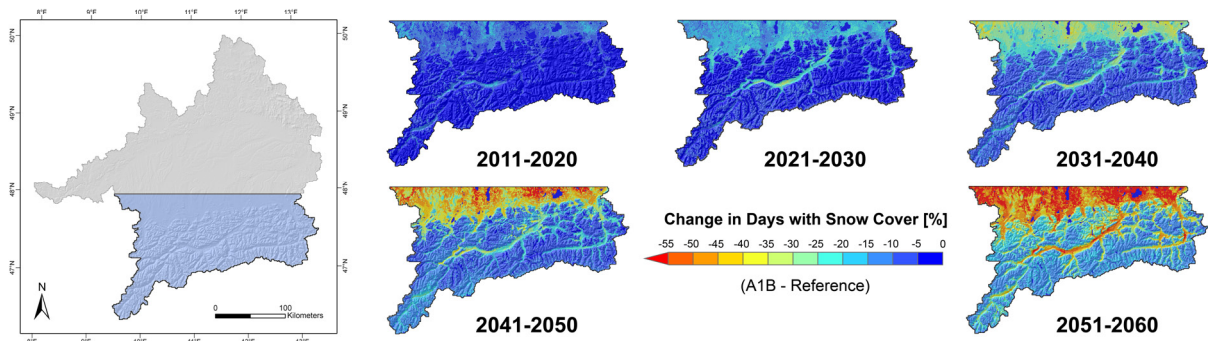


Fig. 6.18: Decadal change in the number of days characterized by the presence of a snow cover (SWE > 1 mm) relative to the reference period (1961-2000).

The simulated changes in snow cover severely modify the water quantities seasonally stored in form of snow. Changes in discharge conditions, in particular in summer can be expected to be the direct consequence. Winter tourism, which represents an important economic branch in the catchment, would be severely affected by the simulated development of snow cover in the Alps.

### 6.3.3 AREA RUNOFF AND RIVER DISCHARGE

The last paragraphs have analyzed various aspects of climatic and hydrological change in the UD. All of these altered climatological and hydrological boundaries directly or indirectly affect the runoff characteristics in the UD. Changes in the spatial and temporal distribution of precipitation dominate the water budget of the catchment. Temperature conditions, on the other hand, determine whether rainfall is solid or liquid and, as a consequence, whether the precipitating water is hydrologically available or stored in the snowpack. Further, a rise in temperature increases evaporative losses and therefore reduces the water quantities available for runoff formation at the land surface. A more frequent occurrence of extreme low-flow conditions in the future could be the direct consequence. The latter would have manifold consequences on the natural and socio-economic system in the UD. Hydropower stations as well as thermal power stations and river navigation particularly depend on river discharge. The increase in precipitation on the other hand could lead to an increase in peak-flow discharge and to severe floods in the future.

The following analyzes the climate change impact on the runoff conditions in the UD. As has been shown in Fig. 6.11, the subtraction of annual evapotranspiration from rainfall leads to an area mean runoff of 802 mm for the years 2011 to 2060 within the model domain of the UD. Compared to the area mean runoff of the reference run (759 mm) this corresponds to an increase of 43 mm ( $\approx 5.7\%$ ). The incline can be explained by the enhanced water availability due to an increase in precipitation of 57 mm compared to the reference run (see chapter 6.2.2). As reflected by the increase in evapotranspiration of 14 mm, the increased water availability is only partly compensated by an intensification of evapotranspirative processes. Apart from the average change in runoff compared to the reference run, the annual mean routed discharge at the gauge in Achleiten can be examined for the presence of a trend within the scenario period. Fig. 6.19 shows the annual mean river discharge simulated for the gauge of the watershed in Achleiten.

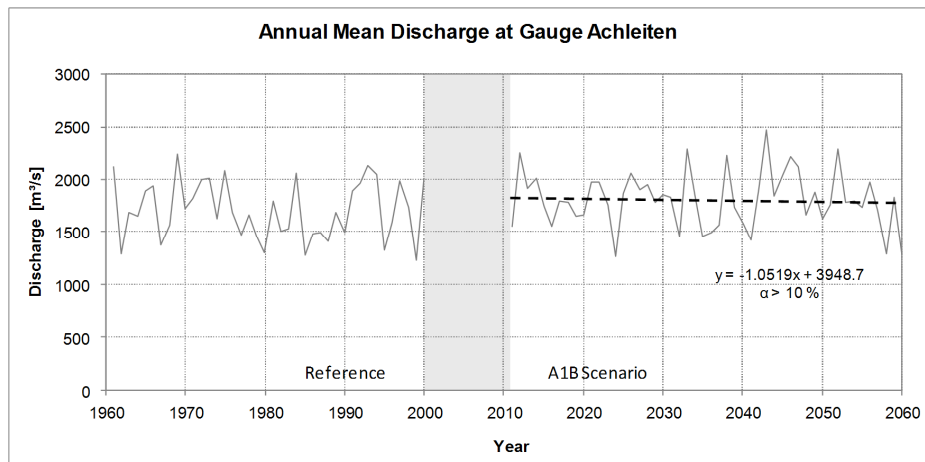


Fig. 6.19: Modeled annual mean discharge at the gauge in Achleiten for the reference period (1961-2000) and the scenario period (2011-2060).

As can be seen the regression line indicates a slight decrease in simulated discharge volumes from 2011 to 2060. However, testing the trend on the basis of a nonparametric Mann-Kendall test (MANN 1945) leads to the result that the decrease in simulated discharge volumes is not statistically significant ( $\alpha > 10\%$ ). In other words, the probability that a negative trend would be falsely assumed is greater than 10%. Beyond the analysis of yearly discharge volumes changes in monthly discharge need to be analyzed.

The simulated mean monthly discharge at the gauge in Achleiten is illustrated in Fig. 6.20 for the control run and the scenario run. As displayed, monthly mean discharge volumes are characterized by a considerable increase relative to the reference run, in particular in the hydrological winter half year from November to April (20% in February). An explanation is given by the strong increase in runoff available water due to higher precipitation amounts in most of these months, parallel to an increase in temperatures. The latter rises the percentage

of liquid precipitation in winter and reduces the water quantities stored in form of snow. Spring melt in the Alpine part of the catchment is most probably slightly shifted towards the beginning of the year further increasing runoff available water in late winter and early spring.

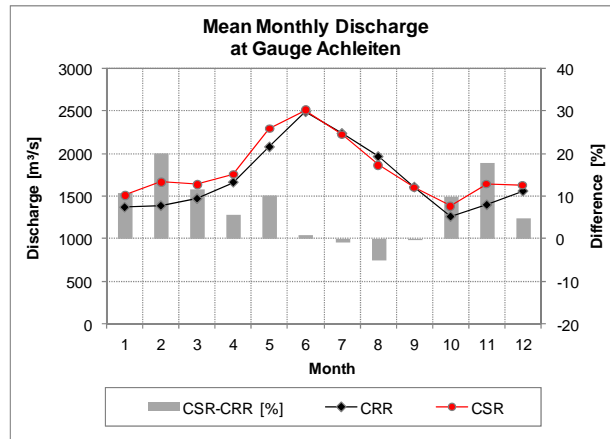


Fig. 6.20: Mean monthly discharge volumes at the gauge in Achleiten modeled within the reference run (1961-2000) and the scenario run (2001-2060). The grey bars indicate the difference between both model runs (A1B - Reference).

The hydrological summer half year (May-October) shows rather little increases in mean monthly discharge. The period from July to September is even characterized by lower monthly discharge volumes in the scenario run as a result of the decrease in summer precipitation in combination with lower melt water contributions to summer discharge.

Fig. 6.21 shows the mean monthly peak-flow discharge together with the mean monthly low-flow discharge for the coupled reference run and the scenario run. For both runs, the peak- and low-flow discharge quantities have been calculated on the basis of daily discharge simulations.

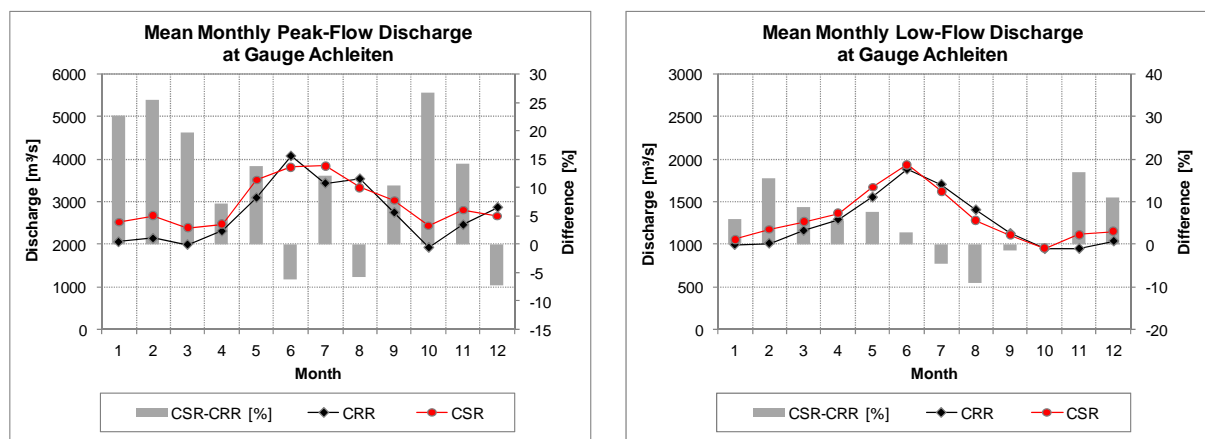


Fig. 6.21: Mean monthly peak-flow discharge and low-flow discharge volumes at the gauge in Achleiten modeled for the reference run (1961-2000) and the scenario run (2011-2060). The grey bars indicate the difference between both model runs (A1B - Reference).

The graphs provide a picture quite similar to that of average monthly discharge characterized by a tendency to higher discharge values in the scenario run. In particular in the winter half year the increased water availability notably increases mean monthly flood and low-flow discharge volumes. Analogously to the mean monthly discharge conditions, the decrease in precipitation in summer together with a decrease in melt water discharge for some summer months lowers monthly peak- and low-flow discharge. In contrast, the month of July in the case of peak-flow discharge and the month of June in the case of low-flow discharge show higher discharge volumes in the coupled scenario run than in the reference run.

Although the mean monthly low-flow discharge for most months of the year shows an increase in discharge volumes in the scenario run, the increase in temperatures together with the decrease in rainfall amounts in summer might lead to extreme low-flows events that are not captured by comparing the mean conditions of the reference run to those of the scenario run. To research into this presumption, the 7-days average low-flow discharge (NM7Q) is considered as a sensitive measure of drought. It represents the lowest mean discharge over the period of seven subsequent days in the course of one year. Fig. 6.22 (left) shows the NM7Q for the reference run and the scenario run. The black line in the diagram on the left represents the 7-days average low-flow discharge with a return period of 50 years (NM7Q<sub>50</sub>). It is calculated for a considered year by fitting a lognormal distribution to the NM7Q values of the precedent 25 years. As described in detail in chapter 5.3.2.2.3, the latter allows the computation of the low-flow discharge related to a certain return period.

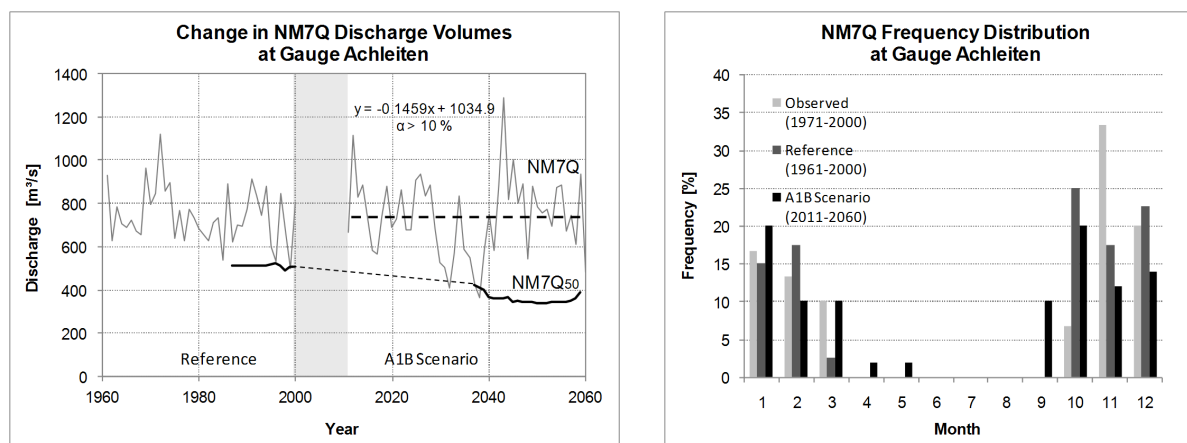


Fig. 6.22: NM7Q and NM7Q<sub>50</sub> discharge volumes at the gauge in Achleiten for the reference run and the scenario run (left) and frequency distribution of the NM7Q occurrence according to discharge simulations (reference run and scenario run) and discharge recordings (right).

The figure (left) shows that there is no significant trend in NM7Q discharge volumes within the scenario run ( $\alpha > 10\%$ ). An explanation for the fact that the NM7Q volumes do not significantly decrease within the period 2011 to 2060 can be found in the frequency distribution of the NM7Q (see Fig. 6.22, right). For both, measured and simulated discharge

volumes for past conditions, the NM7Q values at gauge Achleiten entirely occur in the months from October to March. As almost all of the months that show a frequent occurrence of NM7Q discharge volumes in the past, are characterized by increases in precipitation and temperature in the scenario run, water availability in these months is rather enhanced than reduced. However, the change in the meteorological boundary conditions leads to a 14 % occurrence of NM7Q discharge in the months from April to September indicating a slight shift of NM7Q occurrence towards the hydrological summer half year for the scenario run. Compared to the reference period, the  $NM7Q_{50}$  is characterized by lower values at the end of the scenario run period, which is mostly due to the low NM7Q values in the middle of the scenario period that largely affect the  $NM7Q_{50}$  for the years 2040 to 2060. The two lowest NM7Q discharge volumes found in the scenario run with 405 m<sup>3</sup>/s (2032) and 362 m<sup>3</sup>/s (2038) considerably fall below the lowest NM7Q volumes found in the reference run indicating that there is an increased potential for the occurrence of extreme low-flow events in the future.

In order to analyze changes in extreme peak-flow discharge between the reference and the scenario run, the HQ representing the highest daily discharge for a given year, is graphically displayed in Fig. 6.23.

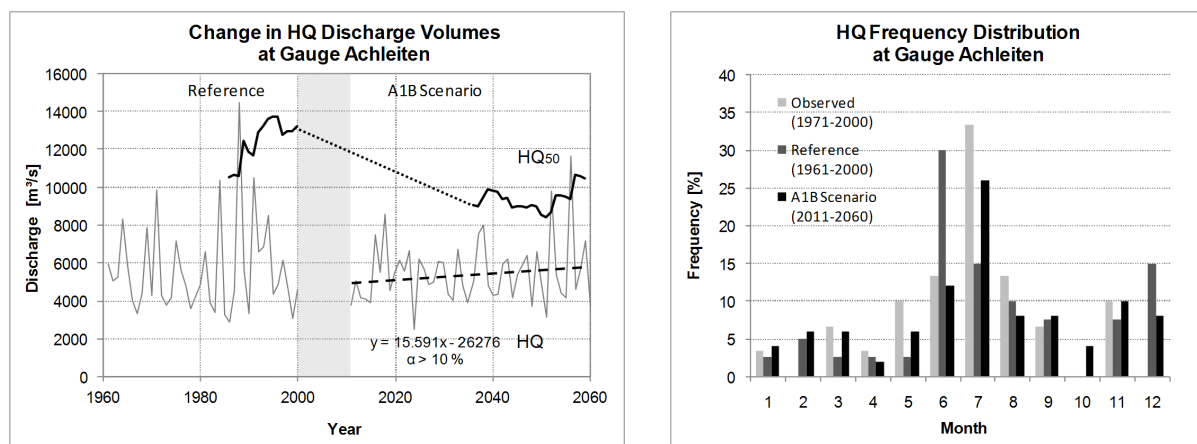


Fig. 6.23: HQ and  $HQ_{50}$  discharge volumes at the gauge in Achleiten for the reference run and the scenario run (left) and frequency distribution of the HQ occurrence according to discharge simulations (reference run and scenario run) and discharge recordings (right).

The illustration displays a noticeably reduced variability in HQ volumes within the scenario run. While a slight but not significant trend towards higher HQ volumes can be observed for the scenario period, the HQ discharge with a return period of 50 years ( $HQ_{50}$ ) takes lower values in the scenario run compared to the  $HQ_{50}$  discharge at the end of the reference period. Again, the frequency distribution of the HQ occurrence is consulted to explain the comparatively low HQ volumes in the scenario run. As displayed in Fig. 6.23 (right), highest daily discharge volumes in the course of one year are most frequently found in summer

within both, the coupled reference run and the scenario run. A similar picture has already been given by Fig. 6.21 (left) showing the mean monthly peak-flow discharge, which is characterized by highest peak-flow discharge volumes in summer. The decreases in precipitation and melt water in summer reduce runoff available water in summer and in consequence the HQ discharge volumes in the scenario run.

The reduction in extreme peak-flow discharge is confirmed considering the flood return periods of the reference and the scenario run. As Fig. 6.24 shows the peak-flow discharge associated to a certain return period is notably reduced in the scenario run compared to the return periods calculated for the reference run.

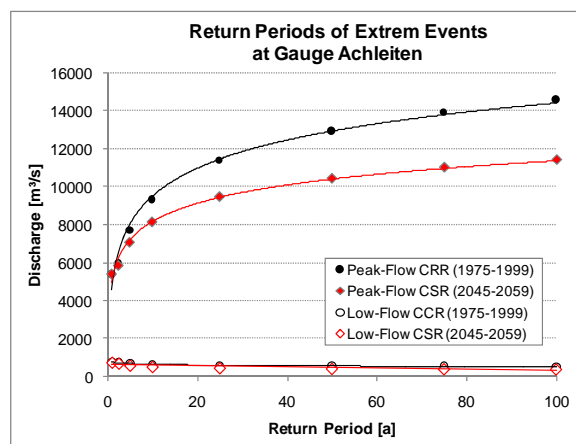


Fig. 6.24: Low-flow and flood return periods based on PROMET simulations for the coupled reference run (CRR) and the scenario run (CSR). A lognormal distribution is applied to calculate the displayed return periods.

The discharge related to a return period of 25 years in the reference run corresponds to a discharge with a return period of 100 years in the scenario run. Compared to the change in flood discharge, the low-flow return periods seem to be rather unaffected. However, care has to be taken when interpreting the results of an extrapolation of extreme events. Since the statistical distribution of the discharge data and its parameters assume stationary conditions, the expressiveness of the extrapolations might be weakened under climate change conditions.

## 7 CONCLUSION AND OUTLOOK

The preceding chapters of this work have analyzed the potential of RCM simulations as input for land surface models. As the spatial resolution at which atmospheric processes can be resolved is still computationally limited to at best 10 x 10 km the land surface representation in RCMs strongly differs from natural realities. Particularly in complex terrain, the limited spatial resolution of RCMs does not fully capture the small scale variability in the natural climate system. To overcome these drawbacks, adequate scaling techniques need to be applied in advance of utilizing the RCM data as meteorological drivers for high resolution land surface models (1 x 1 km).

The coupling tool SCALMET has been presented as a model interface developed to bridge the gap between the model scales. Different interpolation techniques have been described, including a remapping scheme that allows a conservative treatment of fluxes within the remapping process. However, these interpolation techniques do not compensate the loss of subscale climate variability in climate model simulations. To overcome these drawbacks, the direct interpolation methods are combined with more sophisticated methods.

A regression based remapping method was presented that allows the analysis of the elevation dependence of a considered meteorological variable for every model time step separately. For the case that a significant linear relationship between a considered variable (e.g. temperature) and elevation is detected, the determined regression function is used to topographically adjust the RCM outputs. While the approach produces good results for a remapping from 10 x 10 km to 1 x 1 km, it is not quite clear in how far a much coarser spatial resolution of the RCM might limit its applicability ( $\geq 50 \times 50$  km). Therefore alternative techniques have been implemented that apply monthly lapse rates (temperature and dewpoint temperature) or a precipitation adjustment factor to adjust simulated fields for the influence of subgrid topography. Naturally, not all of the meteorological variables required to describe processes at the land surface are characterized by a significant elevation dependence. Hence, several submodels have been implemented in SCALMET that use additional topographic information (e.g. slope, aspect or exposure) to adequately span the gap between the model scales.

Irrespective of the applied remapping approach, the adjusted high resolution meteorology is realigned to the mass/energy budget predetermined by the RCM simulations. This conservative treatment of fluxes represents a crucial prerequisite for coupling regional climate models with land surface models, in particular in a two-way coupled model setup. However conservatively remapping climate model simulations implies fully taking over all biases that might be included in the RCM output.

The biases that are known to exist in climate model simulations hamper the verification of the remapping methods. Therefore a synthetic experiment is carried out to analyze the performance of the different remapping approaches. Spatially distributed observations are aggregated to the RCM resolution of 10 x 10 km using the conservative remapping method implemented in SCALMET. The coarse grid meteorology is later used for the downscaling in SCALMET. The comparison of the remapped fields with station observations showed that the remapping approaches accounting for subgrid variability considerably enhance the remapping results compared to conventional interpolation techniques. Further, using the remapped fields as meteorological drivers for the hydrological model PROMET clarified that the more sophisticated downscaling techniques lead to a more realistic simulation of water fluxes and in consequence enhance the accuracy of discharge simulations.

A one-way coupled model run is set up to investigate the overall performance of the coupled model system for past climate conditions (1961-2000). The meteorological drivers are supplied by the regional climate model REMO and are remapped by SCALMET using the regression based approach in combination with different submodels for a quasi-physically based remapping of all required meteorological variables. These remapping techniques have been chosen as they do not include calibrations carried out under present-day climate conditions and can therefore be expected to be valid under future climate conditions. Additionally an uncoupled model run is setup covering the years 1971 to 2000. Both, the spatially distributed observations used to drive the hydrological model PROMET in this uncoupled model run as well as the hydrological model results provide a basis of comparison to the remapped climate model simulations and the model results of the one-way coupled reference run. A comparison of the remapped REMO data with spatially distributed observations provided by the meteorological preprocessor in PROMET reveals a mean overestimation of annual mean temperatures of 0.8 °C for the Upper Danube watershed (1971-2000). Highest deviations from the observation based meteorology occur in April with an overestimation of monthly mean temperature exceeding 2.5 °C. In case of precipitation for both, the remapped as well as the original REMO simulations, an overestimation of area mean annual precipitation of approximately 11 % is observed. The largest deviations from the observation based meteorology occur in the months of May and December. A further comparison additionally consulting precipitation data originating from the Hydrological Atlas of Austria (KLING ET AL. 2007b) showed that the highest overestimation of annual precipitation considering the period 1961 to 1990 can be found in the Alpine part of the catchment. Please note that although much care has been taken to only compare data covering exactly the same years, all precipitation distributions involved in the comparison somehow represent model results and therefore include considerable uncertainties.

The examination of the hydrological simulations carried out within the coupled model run (REMO-SCALMET-PROMET) showed that the biases included in the meteorological simulations largely affect the results of the hydrological model PROMET. The warm bias in REMO near surface temperature simulations, together with the increased water availability caused by a certain overestimation of precipitation amounts, lead to a slightly enhanced evapotranspiration relative to the results of the uncoupled model run considering the period 1971-2000. Comparing the modeled annual area mean runoff for the Upper Danube watershed to discharge measurements at the gauge in Achleiten further revealed an overestimation of discharge recordings of 29 %. Similar overestimations unfold considering the mean monthly discharge as well as the mean monthly low-flow and peak-flow discharge. The general tendency to overestimate discharge volumes could be shown to strongly limit the capability of the coupled model system to reproduce the return periods of low-flow and flood return periods.

A second one-way coupled model run is setup for the period 2011 to 2060. The biases quantified for the coupled reference run (1961-2000) are assumed to affect the hydrological model results to a similar extent for both runs. This assumption allows a relative comparison of the meteorological and hydrological simulations yielded within the reference and the scenario run. Within the change analysis, both, changes relative to the reference run as well as trends within the scenario period have been identified. Considering the climate change signal in the remapped REMO simulations, a notable increase in the annual mean temperature (2011-2060) in the Upper Danube watershed is observed ( $\approx 1.2$  °C) compared to the temperatures of the reference period (1961-2000). It was found that the average temperature increase rate in the Upper Danube watershed with approximately 5.2 °C/100 years is elevated by a factor of 1.8 compared to the global average temperature rise resulting from the atmospheric greenhouse gas concentrations defined for the A1B scenario family.

The increase is stronger in the higher elevations of the Alps than in the Alpine foreland. Beyond this trend that is predetermined by the 10 x 10 km simulations, a slight subgrid elevation dependence is found in the change signal. This is due to the fact that the mean temperature lapse rate determined within the regression based remapping on the basis of the REMO control run simulations (5.5 °C/km) differs from that reflected in the REMO scenario simulations (5.3 °C/km). This shows the importance of applying downscaling techniques that are not parameterized and are therefore capable to react to altered meteorological conditions.

The analysis of seasonal trends in precipitation simulated for the scenario period revealed a significant decrease in precipitation in summer (JJA) and autumn (SON) and a slight but not significant increase in precipitation in spring (MAM) and winter (DJF). However, it became

evident that the change signal in simulated precipitation strongly depends on the time period considered within the REMO scenario run from 2000 to 2100. This in particular applies to changes in summer and autumn precipitation which are characterized by much stronger decreases for the end of the century (2070-2100). It further applies to winter precipitation showing comparatively high increases for the years 2070 to 2100. Considering the years 2011 to 2060, the general increase in annual precipitation compared to the reference period amounts to approximately 5 %.

The hydrological consequences of these altered meteorological conditions are quantified by comparing the hydrological simulations of the coupled reference run (1961-2000) to those of the scenario run (2011-2060). Thereby a significant increase in annual evapotranspiration can be observed that largely follows the linear trend in the temperature increase up to the end of the considered period in the year 2060. Highest increase rates are found for the seasons of winter (DJF), spring (MAM) and autumn (SON). This is well explicable when considering the increase in the water and energy budget in these seasons. In summer much lower increases in evapotranspiration are simulated. For the month of July even a decline in monthly evapotranspiration can be observed. The analysis of changes in plant available soil water has shown that this decline is most probably due to limitations in water availability as a result of the decrease in summer precipitation and the enhanced evapotranspirative water consumption in the preceding months. The total increase in evapotranspiration relative to the reference run takes a value of 3.5 %.

As the catchment hydrology is largely affected by the amount of water temporarily stored in the snow pack, the annual days of snow coverage as well as the annual amount of solid precipitation have been analyzed in order to detect snow hydrological changes between the reference and the scenario run. Both analyzed criteria show a very similar picture characterized by the largest decreases in the northern part of the watershed. While the lower elevations of the Alps also show high decreases in annual snowfall and snow cover days, the low temperatures in the higher elevated Alpine regions as well as in parts of the Bavarian Forest still allow comparatively high snowfall amounts and a large number of snow cover days.

The impact of the scenario meteorology upon the runoff conditions in the Upper Danube watershed is analyzed by comparing the simulated annual area mean runoff of the scenario run to that of the reference run. The comparison reveals an increase in mean annual runoff of 5.7 % (43 mm). This is well explicable when considering the fact that only a small fraction of the additionally available precipitation (57 mm) is returned to the atmosphere by an intensification of evapotranspiration at the land surface (14 mm). Considering the mean annual discharge simulated for the gauge in Achleiten no significant trend can be found

within the scenario period. Yet, the increase in precipitation and temperature is shown to affect the mean monthly discharge, the mean monthly low-flow discharge and the mean monthly peak-flow discharge at the gauge of the watershed in Achleiten. For all discharge criteria a considerable increase is observed, in particular for the hydrological winter half year (November-April). However, the decrease in summer precipitation in combination with a decrease in melt water discharge in the case of some summer months leads to a reduction in discharge for all considered discharge criteria. To analyze changes in the occurrence of extreme low-flow events, the lowest 7-days average discharge (NM7Q) is analyzed for both coupled model runs. No significant trend towards lower values is found within the scenario run. An explanation is given by the fact that the lowest NM7Q values mainly occur in the winter half year. The increase in runoff available water due to an increase in (liquid) precipitation and near surface temperatures tends to raise the NM7Q in the winter half year. However, the lowest NM7Q discharge volumes found in the scenario run are significantly lower than those of the reference run. Moreover, the NM7Q occurrence is slightly shifted towards the hydrological summer half year in the scenario run indicating an increased potential for the occurrence of extreme low-flow events in summer in the future.

The highest daily discharge in the course of one year (HQ) does not show a significant trend within the scenario period as well. However, the comparison of the flood and low-flow return periods calculated for the scenario run to the return periods determined for the coupled reference run unfolds much lower discharge volumes for a considered return period (e.g. 50 years) in the case of flood flow. As most flood events in the Upper Danube watershed occur in the summer half year, the lower discharge volumes for a given return period are most probably due to the decrease in precipitation in summer combined with lower melt water contributions to summer discharge. Low-flow return periods do not differ notably between both runs.

The present work has given proof of the general applicability of the one-way coupled model system in climate change investigations. The introduced scaling techniques could be shown to more realistically reproduce the natural climate system and to enhance the results of one-way coupled model runs within a synthetic model approach. Forcing PROMET with remapped REMO simulations showed that PROMET is able to fully utilize the large potential of RCM simulations. The hydrological model has successfully shown its unrestricted ability to translate the climate change signal included in the remapped REMO meteorology into a land surface reaction.

In the framework of the present study only some aspects of climatic change and its impacts on the hydrological conditions within the Upper Danube watershed could be presented. The inclusion of recently developed PROMET components within one-way coupled model runs

opens further opportunities for climate change research in the near future. The biophysical, fully dynamic vegetation model recently implemented by HANK (2008) allows the simulation of a biophysically based plant reaction upon the increasing mediterraneanization of climate conditions. Including the dynamic vegetation model within two-way coupled model runs further allows the atmosphere to react upon a vegetation response to climate change conditions. The integration of the dynamic glacier model that is currently implemented into the hydrological model by PRASCH ET AL. (2008b) in coupled model runs allows to simulate the retreat of glaciers in the Upper Danube watershed as a response to climate change. The medium-term goal is to transfer the knowledge and technology established within the current model setup (PROMET-SCALMET-REMO) into the interdisciplinary DANUBIA model. Particularly with respect to the fact that hydrology on a regional scale is to an increasing degree affected by human decisions, the human dimensions simulated within the interdisciplinary DANUBIA model open further possibilities for the land surface to influence climate conditions.

However, comparatively large biases still persist in the coupled model system (REMO-SCALMET-PROMET) that limit its ability to reproduce present-day conditions to a certain degree. Biases in simulated near surface temperature and precipitation have been shown to cause biases in the runoff simulated by means of the physically based hydrological model PROMET. The uncertainties in RCM simulations can be attributed to both, uncertainties related to the process formulation in the RCM as well as uncertainties resulting from the driving climate model. In order to reflect a wider range of uncertainties, future one-way coupled model runs carried out in the framework of GLOWA-Danube will involve additional RCMs including the mesoscale climate model MM5 (GRELL ET AL. 1995) and the climate version of the 'Lokal Model' CLM (BÖHM ET AL. 2006). The latter will not only be utilized to simulate meteorological conditions within the Upper Danube watershed. In the framework of the BRAHMATWINN (BRAHMATWINN 2008) project, the coupled model system (CLM-SCALMET-PROMET) will be utilized to analyze climate change impacts on the water resources in the river basin of the Brahmaputra.

Apart from the uncertainties related to the reproduction of present-time meteorological and hydrological conditions in the Upper Danube watershed, additional uncertainties are introduced when projecting climate into the future. The climate projection used within the current work only states one of many realizations that have been carried out on the basis of the radiative forcings defined within the A1B scenario family (IPCC 2000). To provide a more comprehensive picture of potential climate change and its impacts, different scenarios and realizations need to be utilized within one-way coupled model runs in the future.

Besides the biases found in the simulated climate, downscaling techniques are known to introduce additional uncertainties. For the scaling methods in SCALMET, these uncertainties inter alia arise from the fact that most approaches strongly simplify the natural system. While slope and aspect are accounted for in the remapping of solar radiation, temperature distributions are not affected by the different solar radiation levels found at north- and south-facing slopes. Further, the spatially distributed temperatures are not modified according to the sensible and latent heat flux at the land surface. Theoretically, both limitations described above could be overcome by including energy balance calculations as they are performed by the hydrological model PROMET into the remapping process. However, this would drastically increase complexity while at the same time there is an increasing potential concerning the introduction of additional biases. The elevation adjustments carried out within the remapping of precipitation in SCALMET further do not include the orographically induced spatial variability of precipitation. To overcome these deficiencies an orographic precipitation submodel would need to be implemented (PANDEY ET AL. 2000, SMITH AND BARSTAD 2004). Apart from the fact that accurate high resolution precipitation models accounting for the whole range of precipitation mechanisms and structures are not available at present, it is not clear in how far a more complex approach can help to improve the quality of the remapping results. As SCHULZ AND BEVEN (2003) successfully demonstrated, increasingly complex models do not necessarily lead to better model results. Besides the questionable benefit, such efforts would notably increase computational costs. As can be seen many simplifications in SCALMET are due to a strong limitation of complexity for the sake of computational efficiency. The latter represents a top priority in SCALMET as all meteorological variables need to be remapped during the run-time of the coupled model system. However possibilities exist to enhance the quality of the remapping products in a computationally efficient manner. (FRÜH ET AL. 2006) propose a statistical method based on a local scaling factor for each day of the year. Within the approach local subgrid variability is accounted for by making use of a high resolution observed climatology. In a second step a bias correction is carried out which in case of precipitation reduces displacements in simulated precipitation by shifting modeled precipitation from inner Alpine regions towards the edges of the Alps. Although the approach can be expected to enhance the results of the coupled model system it requires a large degree of area- and model-specific adjustments. It is further not clear in how far such approaches are applicable in two-way coupled model setups, which represent a top priority for near future applications of SCALMET.

In a medium-term view climate model simulations can be expected to show further improvements in both, the quality of the simulations as well as the spatial resolution at which atmospheric processes can be resolved. A rather pragmatic approach to reduce the effect of

present-time biases in precipitation simulations that is recommended by the developers of the regional climate model REMO is to rather use the mean value of a 3 x 3 pixel window than the exact precipitation simulated for a considered climate model pixel. Although similar filtering techniques have shown little effect on the catchment hydrology in other climate change studies (GERLINGER 2004), the approach might be followed in future one-way coupled model runs to study the effect on the precipitation amounts and patterns in the Upper Danube watershed.

Although the land surface model components add further inaccuracies, in case of the hydrological model PROMET systematic biases could be shown to be rather small. Further there is evidence that inaccuracies in the model partly compensate with increasing size of the model domain as a result of a larger sample size (MAUSER AND BACH 2008). This, together with its physically based model concept sets the ideal prerequisites for fully coupling PROMET with RCMs on a regional level.

Two-way coupled model runs will be realized by coupling PROMET with the regional climate model REMO as well as with the mesoscale climate model MM5. Simulating water, energy and momentum fluxes at a high resolution within two-way coupled model runs, PROMET is expected to make a valuable contribution towards an improved understanding of land-atmosphere interactions. Although practical difficulties can be expected to arise when coupling a high resolution land surface model with medium resolution atmospheric models, the technical preparations for two-way coupled model runs have been successfully completed with the development of SCALMET in the framework of this work.

---

## 8 REFERENCES

- ANDRÉASSON, J., BERGSTRÖM, S., CARLSSON, B. GRAHAM, L. P. AND LINDSTRÖM, G. (2004). Hydrological Change – Climate Change Impact Simulations for Sweden. *Ambio*, 33 (4-5), 228-234.
- ASSELIN, R. (1972). Frequency filter for time integrations. *Monthly Weather Review*, 100, 487-490.
- BAHRENBERG, G., GIESE, E. AND NIPPER, J. (1999). *Statistische Methoden in der Geographie* 1. Teubner Verlag, Stuttgart.
- BALDOCCHI, D. D., HICKS, B. B. AND CAMARA, P. (1987). A Canopy Stomatal Resistance Model for Gaseous Deposition to Vegetated Surfaces. *Atmospheric Environment*, 21, 91-101.
- BARRY, R. G. AND CHORLEY, R. J. (1987). *Atmosphere, weather and climate*. Routledge, London.
- BARTH, M., HENNICKER, R., KRAUS, A. AND LUDWIG, M. (2004). DANUBIA: An Integrative Simulation System for Global Change Research in the Upper Danube Basin. *Cybernetics and Systems*, 35 (7-8), 639-666.
- BARTHEL, R., ROJANSCHI, V., WOLF, J. AND BRAUN, J. (2005). Large-scale water resources management within the framework of GLOWA-Danube. Part A: The groundwater model. *Physics and Chemistry of the Earth*, 30 (7-8), 372-382.
- BARTHEL, R., MAUSER, W. AND BRAUN, J. (2007). Integrated modelling of global change effects on the water cycle in the upper Danube catchment (Germany). The groundwater management perspective. *IAH Selected Papers on Hydrogeology*, 12, 47-72.
- BASIST, A., BELL, G. D. AND MEENTEMEYER, V. (1994). Statistical Relationships between Topography and Precipitation Patterns. *Journal of Climate*, 7, 1305-1315.
- BAUMGARTNER, A. AND LIEBSCHER, H.-J. (1995). *Allgemeine Hydrologie – Quantitative Hydrologie* (2nd Edition). Gebrüder Bornträger, Berlin.
- BECKMANN, B. R. AND BUIHAND, T. A. (2002). Statistical Downscaling Relationships for Precipitation in the Netherlands and North Germany. *International Journal of Climatology*, 22, 15-32.
- BETTS, A. K., CHEN, F., MITCHELL, K. AND JANJIC, Z. I. (1997). Assessment of the land surface and boundary layer models in two operational versions of the NCEP Eta model using FIFE data. *Monthly Weather Review*, 125, 2896-2916.
- BIJL, W. (1997). Impact of a wind climate change on the surge in the southern North Sea. *Climate Research*, 8, 45-59.
- BLFW (BAYERISCHES LANDESAMT FÜR WASSERWIRTSCHAFT) (1999). *Gewässerkundliches Jahrbuch – Donauegebiet 1995*, München.

- 
- BMU (BUNDESMINISTERIUM FÜR UMWELT, NATURSCHUTZ UND REAKTORSICHERHEIT) (2000). Digitaler Hydrologischer Atlas von Deutschland.
- BÖHM, U., KÜCKEN, M., AHRENS, W., BLOCK, A., HAUFFE, D., KELUER, K., ROCKEL, B. AND WILL, A. (2006). CLM – the climate version of LM: Brief description and long-term applications. *COSMO Newsletter*, 6.
- BOLZ, H. M. (1949). Die Abhängigkeit der infraroten Gegenstrahlung von der Bewölkung. *Zeitschrift für Meteorologie*, 3 and 4.
- BOOCH, G., RUMBAUGH, J. AND JACOBSON, I. (2005). The Unified Modelling Language User Guide (2nd Edition). Reading.
- BRAHMATWINN (2008). <http://www.brahmatwinn.uni-jena.de>, accessed January 2008.
- BRUDSAERT, W. (1982). Evaporation into the Atmosphere – Theory, History and Application. D. Reidel Publishing Company, Dordrecht-Boston-London.
- BUCK, A. L. (1981). New equations for computing vapor pressure and enhancement factor. *Journal of Applied Meteorology*, 20, 1527-1532.
- BURRIDGE, D. M. AND GADD, A. J. (1974). The Meteorological Office operational 10 level numerical weather prediction model. U.K. Meteorological Office Technical Notes, 12 and 48.
- BURROUGH, P. A. AND R., A. MCDONNELL. (2000). Principles of Geographic Information Systems. Oxford University Press.
- CAMPBELL, G. S. AND NORMAN, J. M. (1998). An Introduction to Environmental Biophysics (2nd Edition). Springer, New York.
- CAVAZOS, T. (1999). Large scale circulation anomalies conducive to extreme precipitation events and derivation of daily rainfall in northeastern Mexico and southeastern Texas. *Journal of Climate*, 12, 1506-1523.
- COHN, T. A., DELONG, L. L., GILROY, E. J., HIRSCH, R. M. AND WELLS, D. K. (1989). Estimating constituent loads. *Water Resources Research*, 25, 937-942.
- COSGROVE, B. A., LOHMANN, D., MITCHELL, K. E., HOUSER, P. R., WOOD, E. F., SCHAAKE, J. C., ROBOCK, A., MARSHALL, C., SHEFFIELD, J., DUAN, Q., LUO, L., HIGGINS, R. W., PINKER, R. T., TARPLEY, J. D. AND MENG, J. (2003). Real-time and retrospective forcing in the North American Land Data Assimilation System (NLDAS) project. *Journal of Geophysical Research*, 108, DOI:10.1029/2002JD003118.
- CUBASCH, U. (2001). Simulations of Regional Climate Change. In: LOZAN, J. L., GRAßL, H. AND HUPFER, P. (EDS.). Climate of the 21st century: Changes and Risks, Hamburg.
- CUNGE, J. A. (1969). On the subject of a flood propagation computing method (Muskingum Method). *Journal of Hydraulic Research*, 7 (2), 205-230.
-

- 
- DALY, C. AND NEILSON, R. P. (1992). A digital topographic approach to modeling the distribution of precipitation in mountainous terrain. In: JONES, M. E. AND LAENEN, A. (EDS.). *Interdisciplinary approaches in hydrology and hydrogeology*. American Institute of Hydrology, 437-454, Minneapolis.
- DALY, C. (2002). Variable influence of terrain on precipitation patterns: Delineation and Use of Effective Terrain Height in PRISM. Oregon State University.
- DALY, C., GIBSON, W. P., TAYLOR, G. H., JOHNSON, G. L. AND PASTERIS, P. (2002). A knowledge-based approach to the statistical mapping of climate. *Climate Research*, 22, 99-113.
- DALY, C., TAYLOR, G. H., GIBSON, W. P., PARZYBOK, T. W., JOHNSON, G. L. AND PASTERIS, P. (2001). High-quality spatial climate data sets for the United States and beyond. *Transactions of the American Society of Agricultural Engineers*, 43, 1957-1962.
- DALY, C., NEILSON, R. P. AND PHILLIPS, D. L. (1994). A statistical-topographic model for mapping climatological precipitation over mountainous terrain. *Journal of Applied Meteorology*, 33, 140-158.
- DAVIES, H. C. (1976). A lateral boundary formulation for multi-level prediction models. *Quarterly Journal of the Royal Meteorological Society*, 102, 405-418.
- DE ROOY, W. C. AND KOK, K. (2004). A Combined Physical-Statistical Approach for the Downscaling of Model Wind Speed. *Weather and Forecasting*, 19, 485-495.
- DIETZ, E. J. (1987). A comparison of robust estimators in simple linear regression. *Communication in Statistics-Simulation*, 16, 1209-1227.
- DODSON, R. AND MARKS, D. (1997). Daily air temperature interpolation at high spatial resolution over a large mountainous region. *Climate Research*, 8, 1-20.
- DOMOKOS, M. AND SASS, J. (1990). Long-term Water Balances for Subcatchments and Partial National Areas in the Danube Basin. *Journal of Hydrology*, 112, 267-292.
- EAGLESON, P. S. (1978). Climate, Soil and Vegetation – 1. Introduction to Water Balance Dynamics. *Water Resources Research*, 14, 705-712.
- EAGLESON, P. S. (1978). Climate, Soil and Vegetation – 2. The Distribution of Annual Precipitation Derived from Observed Storm Sequences. *Water Resources Research*, 14, 713-721.
- EAGLESON, P. S. (1978). Climate, Soil and Vegetation – 3. A Simplified Model of Soil Movement in the Liquid Phase. *Water Resources Research*, 14, 722-730.
- EAGLESON, P. S. (1978). Climate, Soil and Vegetation – 4. The Expected Value of Annual Evapotranspiration. *Water Resources Research*, 14, 731-739.
- EAGLESON, P. S. (1978). Climate, Soil and Vegetation – 5. A Derived Distribution of Storm Surface Runoff. *Water Resources Research*, 14, 741-748.
-

- 
- EAGLESON, P. S. (1978). Climate, Soil and Vegetation – 6. Dynamics of the Annual Water Balance. *Water Resources Research*, 14, 749-764.
- EAGLESON, P. S. (1978). Climate, Soil and Vegetation – 7. A Derived Distribution of Annual Water Yield. *Water Resources Research*, 14, 765-776.
- ELLENBERG, H. (1996). Vegetation Mitteleuropas mit den Alpen in ökologischer, dynamischer und historischer Sicht. Ulmer Verlag, Stuttgart.
- ESBN (EUROPEAN SOIL BUREAU NETWORK AND THE EUROPEAN COMMISSION) (2004). European Soil Database (v 2.0). <http://eusoils.jrc.it>, accessed December 2007.
- ESRI (2008). <http://www.esri.com/data>, accessed January 2008.
- EVANS, M., HASTINGS, N. AND PEACOCK, B. (1993). Statistical Distributions, 2nd Edition, John Wiley and Sons, New York.
- FRÜH, B., SCHIPPER, J. W., PFEIFFER, A. AND WIRTH, V. (2006). A pragmatic approach for downscaling precipitation in alpine-scale complex terrain. *Meteorologische Zeitschrift*, 15 (6), 631-646.
- FLOHN, H. (1971). Arbeiten zur allgemeinen Klimatologie. Wissenschaftliche Buchgesellschaft, Darmstadt.
- GACHON, P. AND DIBIKE, Y. (2007). Temperature change signals in northern Canada: convergence of statistical downscaling results using two driving GCMs. *International Journal of Climatology*, 27, 1623-1641.
- GATES, W. L. (2003). Ein kurzer Überblick über die Geschichte der Klimamodellierung. *Promet Jahrgang 29*, 1- 4, 140. Deutscher Wetterdienst, Offenbach am Main.
- GERLINGER, K. (2004). Simulation des Wasserhaushaltes im Neckareinzugsgebiet unter verwendung regionaler Klimaszenarien. Klimaveränderung und Konsequenzen für die Wasserwirtschaft. *KLIWA-Berichte*, 4, 87-102.
- GERSTENGARBE, F.-W. (2001). Conditions and Potentials for Climate Projections. In: LOZAN, J.L., GRAßL, H. AND HUPFER, P. (EDS.). *Climate of the 21st Century: Changes and Risks*, Hamburg.
- GIBSON, J. K., KÄLLBERG, P., UPPLALA, S., HERNANDEZ, A., NOMURA, A. AND SERRANO, E. (1999). ERA-15 Description. ECMWF Re-Analysis Project Report Series 1, European Centre for Medium-Range Weather Forecasts, Reading.
- GLOWA-DANUBE (2008). <http://www.glowa-danube.de>, accessed December 2007
- GLUGLA, G. AND TIEMER, K. (1971). Ein verbessertes Verfahren zur Berechnung der Grundwasserneubildung. *Wasserwirtschaft – Wassertechnik*, 21(10), 349-351.
- GOOVAERTS, P. (2000). Geostatistical approaches for incorporating elevation into the spatial interpolation of rainfall. *Journal of Hydrology*, 228, 113-129.
-

- 
- GRELL, G.A., DUDHIA, J. AND STAUFFER, D. R. (1995). A description of the fifth-generation PennState/NCAR Mesoscale Model (MM5). NCAR Technical Note NCAR/TN-398 + STR.
- HÄCKEL, H. (1999). Meteorologie. Ulmer Verlag, Stuttgart.
- HANK, T. (2008). A Biophysically Based Coupled Model Approach for the Assessment of Canopy Processes Under Climate Change Conditions. PHD Department of Geography. Ludwig-Maximilians-Universität München.
- HANSON, C. L. (1982). Distribution and stochastic generation of annual and monthly precipitation on a mountainous watershed in southwest Idaho. *Water Resources Bulletin*, 18, 875-883.
- HARBAUGH, A. W., BANTA, E. R., HILL, M. C. AND McDONALD, M. G. (2000). MODFLOW-2000 The U.S. Geological Survey Modular Ground-Water Model – User Guide to Modularization Concepts and the Ground-Water Flow Process. U.S. Geological Survey, Open-File Report 00-92.
- HECHTEL, C. M., MOENG, C. H. AND STULL, R. B. (1990). The effects of non-homogeneous surface fluxes on the convective boundary layer. A case study using large eddy simulation. *Journal of Atmospheric Sciences*, 47, 1721-1741.
- HELSEL, D. R. AND HIRSCH, R. M. (1992). Statistical methods in water resources. Elsevier Science Publishing, New York.
- HENDERSON-SELLERS, A. AND MCGUFFIE, K. (1994). Land-Surface Characterization in Greenhouse Climate Simulations. *International Journal of Climatology*, 14, 1065-1094.
- HEWITSON, B. C. AND CRANE, R. G. (1996). Climate downscaling: techniques and application. *Climate Research*, 7, 85-95.
- HIBBERT, A. R. (1977). Distribution of precipitation on rugged terrain in central Arizona. *Hydrology and Water Resources in Arizona and the Southwest*, 7, 163-173.
- HIJMANS, R. J., CAMERON, S. E., PARRA, J. L., JONES, P. G. AND JARVIS, A. (2005). Very High Resolution Interpolated Climate Surfaces for Global Land Areas. *International Journal of Climatology*, 25, 1965-1978.
- HINTERMAIER-ERHARD, G. AND ZECH, W. (1997). Wörterbuch der Bodenkunde – Systematik, Genese, Eigenschaften, Ökologie und Verbreitung von Böden, Stuttgart.
- HOTTEL, H. C. (1976). A simple method for estimating the transmittance of direct solar radiation through clear atmospheres. *Solar Energy*, 18, 129-134.
- HUSSIAN, S. S. AND SPRENT, P. (1983). Nonparametric regression. *Journal of the Royal Statistical Society*, 146 (A), 182-191.
-

- 
- HUTCHINSON, M. F. (2004). Anusplin Version 4.3. Centre for Resource and Environmental Studies. The Australian National University, Canberra.
- HUTCHINSON, M. F. (1998). Interpolation of Rainfall Data with Thin Plate Smoothing Splines – Part I: Two Dimensional Smoothing of Data with Short Range Correlation. *Journal of Geographic Information and Decision Analysis*, 2, 139-151.
- HUTCHINSON, M. F. (1991). The application of thin plate splines to continent-wide data assimilation. In: JASPER, J. D. (EDS.). Data Assimilation Systems. Bureau of Meteorology, BMRC Research Report 27, 104-113, Melbourne.
- ICPD (INTERNATIONAL COMMISSION FOR THE PROTECTION OF THE DANUBE RIVER) (2005). The Danube River Basin District. ICPDR Document IC/084, Vienna.
- IPCC (2000). NAKIC-ENOVIC, N., ALCAMO, J., DAVIS, G., DE VRIES, B., FENHANN, J., GAFFIN, S., GREGORY, K., GRÜBLER, A., YONG JUNG, T., KRAM, T., LA ROVERE, E. L., MICHAELIS, L., MORI, S., MORITA, T., PEPPER, W., PITCHER, H., PRICE, L., RIAHI, K., ROEHL, A., ROGNER, H.-H., SANKOVSKI, A., SCHLESINGER, M., SHUKLA, P., SMITH, S., SWART, R., VAN ROOIJEN, S., VICTOR, N. AND DADI, Z. (EDS.). Special Report on Emissions Scenarios. A Special Report of Working Group III of the Intergovernmental Panel on Climate Change. Cambridge University Press, Cambridge.
- IPCC (2001). HOUGHTON, J. T., DING, Y., GRIGGS, D. J., NOGUER, M., VAN DER LINDEN, P. J., DAI, X., MASKELL, K. AND JOHNSON, C. A. (EDS.). Climate Change 2001: The Scientific Basis. Contribution of Working Group I to the Third Assessment Report of the Intergovernmental Panel on Climate Change. Cambridge University Press, Cambridge.
- IPCC (2007), SOLOMON, S., QIN, D. AND MANNING, M. (EDS.). Climate Change 2007: The Physical Science Basis. Contribution of Working Group I to the Fourth Assessment Report of the Intergovernmental Panel on Climate Change. Cambridge University Press, Cambridge.
- IZIOMON, M. G., MAYER, H. AND MATZARAKIS, A. (2003). Downward atmospheric longwave irradiance under clear and cloudy skies: Measurement and parameterization. *Journal of Atmospheric and Solar-Terrestrial Physics*, 65, 1107-1116.
- JACOB, D. (2001). A note to the simulation of the Annual and Interannual Variability of the Water Budget over the Baltic Sea Drainage Basin. *Meteorology and Atmospheric Physics*, 77 (1-4), 61-74.
- JACOB, D. AND PODZUN, R. (1997). Sensitivity studies with the regional climate model REMO. *Meteorology and Atmospheric Physics*, 63, 119-129.
-

- JACOB, D., VAN DEN HURK, B. J. J. M., ANDRAE, U., ELGERED, G., FORTELIUS, C., GRAHAM, L. P., JACKSON, S. D., KARSTENS, U., KÖPKEN, C., LINDAU, R., PODZUN, R., ROCKEL, B., RUBEL, F., SASS, B. H., SMITH, R. N. B. AND YANG, X. (2001). A comprehensive model inter-comparison study investigating the water budget during the BALTEX-PIDCAP period. *Meteorology and Atmospheric Physics*, 77, 19-43.
- JOHNSON, G. L., DALY, C., HANSON, C. L., LU, Y. Y., AND TAYLOR, G. H. (2000). Spatial variability and interpolation of stochastic weather simulation model parameters. *Journal of Applied Meteorology*, 39, 778-796.
- JONES, P. W. (1998a). A User's Guide for SCRIP: A Spherical Coordinate Remapping and Interpolation Package, Version 1.4. Los Alamos National Laboratory, University of California.
- JONES, P. W. (1998b). First- and Second-Order Conservative Remapping Schemes for Grids in Spherical Coordinates. *Monthly Weather Review*, 127, 2204-2210.
- JUNGCLAUS, J. H., KEENLYSIDE, N., BOTZET, M., HAAK, H., LUO, J. J., LATIF, M., MAROTZKE, J., MIKOLAJEVICZ, U. AND ROECKNER, E. (2003). Ocean Circulation and Tropical Variability in the Coupled Model ECHAM5/MPI-OM. *Journal of Climate*, 19.
- KATO, H., RODELL, M., BEYRICH, F., CLEUGH, H., VAN GORSEL, E., LIU, H. AND MEYERS, T. P. (2007). Sensivity of Land Surface Simulations to Model Physics, Land Characteristics and Forcings at Four CEOP Sites. *Journal of the Meteorological Society of Japan*, 85 (A), 187-204.
- KIDSON, J. W. AND THOMPSON, C. S. (1998). A comparison of statistical and model-based downscaling techniques for estimating local climate variations. *Journal of Climate*, 11, 735-753.
- KILSBY, C. G., COWPERTWAIT, P. S. P., O'CONNELL, P. E. AND JONES, P. D. (1998). Predicting rainfall statistics in England and Wales using atmospheric circulation variables. *International Journal of Climatology*, 18, 523-539.
- KIM, J. W., CHANG, J. T., BAKER, N. L., WILKS, D. S. AND GATES, W. L. (1984). The statistical problem of climate inversion: determination of the relationship between local and largescale climate. *Monthly Weather Review*, 112, 2069-2077.
- KING, L. J. (1969). *Statistical Analysis in Geography*, New Jersey.
- KLING, H., NACHTNEBEL, H. P. AND FÜRST, J. (2007a). Mean annual areal actual evapotranspiration using water balance data. Hydrologischer Atlas Österreichs, Wien.
- KLING, H., NACHTNEBEL, H. P. AND FÜRST, J. (2007b). Mean annual areal precipitation using water balance data. Hydrologischer Atlas Österreichs, Wien.
- KLINK, K. (1995). Surface Aggregation and Subgrid-scale Climate, *International Journal of Climatology*, 15, 1219-1240.

- 
- KÖPPEN, W. (1936). Das geographische System der Klimate. In: KÖPPEN, W. AND GEIGER, R. (EDS.). *Handbuch der Klimatologie*, Gebrüder Borntraeger, Berlin.
- KOLMOGOROV, A. N. (1933). Sulla determinazione empirica di una legge di distribuzione. *Giornale dell' Istituto Italiano degli Attuari*, 4, 83-91.
- KOSTER, R. D. AND SUAREZ, M. J. (1992). Modelling the land surface boundary in climate models as a composite of independent vegetation stands. *Journal of Geophysical Research*, 97, 2697-2716.
- KOTLARSKI, S. (2007). A Subgrid Glacier Parameterization for Use in Regional Climate Modelling. Reports on Earth System Science 42, Max-Planck-Institute for Meteorology, Hamburg.
- KOTLARSKI, S., BLOCK, A., BÖHM, U., JACOB, D., KEULER, K., KNOCHE, R., RECHID, D. AND WALTER, A. (2005). Regional climate model simulations as input for hydrological applications: evaluation of uncertainties. *Advances in Geosciences*, 5, 119-125.
- KOTTEK, M., GRIESER, J., BECK, C., RUDOLF, B. AND RUBEL, F. (2006). World Map of the Köppen-Geiger climate classification updated. *Meteorologische Zeitschrift*, 15, 259-263.
- KUNKEL, A. E. (1989). Simple Procedures for Extrapolation of Humidity Variables in the Mountainous Western United States. *Journal of Climate*, 2, 656-669.
- KUNTZE, H., ROESCHMANN, G. AND SCHWERDTFEGER, G. (1994). *Bodenkunde*, Stuttgart.
- KYLE, H. L., ARDANUY, P. E. AND HURLEY, E. J. (1985). The status of the Nimbus-7 Earth-Radiation-Budget data set. *Bulletin of the American Meteorological Society*, 66, 1378-1388.
- LETTENMAIER, P. D. (1995). Stochastic modeling of precipitation with applications to climate model downscaling. In: VON STORCH, H. AND NAVARRA, A. (EDS.). *Analysis of Climate Variability: Applications of Statistical Techniques*. Springer Verlag.
- LI, Z. AND MÖLDERS, N. (2008). Interaction of impacts of doubling CO<sub>2</sub> and changing regional land-cover on evapotranspiration, precipitation, and runoff at global and regional scales. *International Journal of Climatology*, DOI: 10.1002/joc.1666.
- LISTON, G. E. (2004). Representing Subgrid Snow Cover Heterogeneities in Regional and Global Models. *Journal of Climate*, 17, 1381-1397.
- LISTON, G. E. AND ELDER, K. (2006). A Meteorological Distribution System for High-Resolution Terrestrial Modeling (MicroMet). *Journal of Hydrometeorology*, 7.
- LISTON, G. E. AND STURM, M. (1998). A snow-transport model for complex terrain. *Journal of Glaciology*, 44(148), 498-516.

- 
- LISTON, G. E., BROWN, R. L. AND DENT, J. D. (1993). A two-dimensional computational model of turbulent atmospheric surface flows with drifting snow. *Annals of Glaciology*, 18, 281-286.
- LIU, B. Y. H. AND JORDAN, R. C. (1960). The interrelationship and characteristic distribution of direct, diffuse and total solar radiation. *Solar Engineering*, 4, 1-19.
- LORENZ, P. AND JACOB, D. (2005). Influence of regional scale information on the global circulation: A two-way nesting climate simulation. *Geophysical Research Letters*, 32, doi:10.1029/2005GL023351.
- LOZAN, J. L., GRAßL, H. AND HUPFER, P. (EDS.) (2001). *Climate of the 21st century: Changes and Risks*, Hamburg.
- LUDWIG, R. (2000). Die flächenverteilte Modellierung von Wasserhaushalt und Abflußbildung im Einzugsgebiet der Ammer. *Münchener Geographische Abhandlungen*, 32, 173.
- LUDWIG, R., MAUSER, W., NIEMEYER, S., COLGAN, A., STOLZ, R., ESCHER-VETTER, H., KUHN, M., REICHSTEIN, M., TENHUNEN, J., KRAUS, A., LUDWIG, M., BARTH, M. AND HENNICKER, R. (2003). Web-based modelling of energy, water and matter fluxes to support decision making in mesoscale catchments – the integrative perspective of GLOWA-Danube. *Physics and Chemistry of the Earth*, 28, 621-634.
- LUDWIG, R., PROBECK, M. AND MAUSER, W. (2003). Mesoscale water balance modelling in the Upper Danube watershed using sub-scale land cover information derived from NOAA-AVHRR imagery and GIS-techniques. *Physics and Chemistry of the Earth*, 1351-1364.
- MACHENHAUER, B., WINDELBRAND, M., BOZET, M., DEQUE, M. (1996). Validation of present-day regional climate simulations over Europe: Nested LAM and variable resolution global model simulations with observed or mixed ocean boundary conditions. Report 191, Max-Planck-Institute for Meteorology, Hamburg.
- MAHRENHOLZ, P. (2007). Künftige Klimaänderungen in Deutschland – ein Anlass zur Sorge? Klimaveränderungen und Konsequenzen für die Wasserwirtschaft. *KLIWA-Berichte*, 10, 33-44.
- MAJEWSKI, D. (1991). The Europa-Modell of the Deutscher Wetterdienst. ECMWF Seminar on Numerical Methods in Atmospheric Models, 2, 147-191.
- MANABE, S. AND WETHERALD, R. T. (1967). Thermal Equilibrium of the Atmosphere with a Given Distribution of Relative Humidity, *Journal of the Atmospheric Sciences*, 24 (3), 241-259.
- MANN, H. B. (1945). Non-parametric tests against trend. *Econometrica*, 13, 245-259.

- 
- MARKE, T. AND MAUSER, W. (2008). SCALMET – A tool for bidirectional coupling of climate models with physically-based simulations of land surface processes. *Abstracts of the International Congress 'Managing Alpine Future – strategies for sustainability in times of change'*. Proceedings (in press).
- MARQUÍNEZ, J., LASTRA, J. AND GARCÍA, P. (2003). Estimation models for precipitation in mountainous regions: the use of GIS and multivariate analysis. *Journal of Hydrology*, 270, 1-11.
- MARSLAND, S., HAAK, H., JUNGCLAUS, J., LATIF, M. AND RÖSKE, F. (2003). The Max-Planck-Institute global ocean/sea ice model with orthogonal curvilinear coordinates. *Ocean Modelling*, 5, 91-127.
- MARTÍNEZ-COB, A. (1996). Multivariate geostatistical analysis of evapotranspiration and precipitation in mountainous terrain. *Journal of Hydrology*, 174, 19-35.
- MAUSER, W. AND BACH, H. (2008). PROMET – a Physical Hydrological Model to Study the Impact of Climate Change on the Water Flows of Medium Sized, Complex Watersheds, *Journal of Hydrology (submitted)*.
- MAUSER, W. AND LUDWIG, R. (2002). GLOWA-DANUBE – A research concept to develop integrative techniques, scenarios and strategies regarding the global change of the water cycle. In: BENISTON, M. (ED.). *Climatic Change: Implications for the hydrological cycle and for water management. Advances in Global Change Research*, 10, 171-188. Kluwer Academic Publishers, Boston.
- MAUSER, W. AND SCHÄDLICH (1998). Modelling the spatial distribution of evapotranspiration different scales using remote sensing data. *Journal of Hydrology*, 213, 250-267.
- MCCLATCHY, R.A., FENN, R.W., SELLEY, E.A., VOLZ, F.E. AND GARING, J.S. (1972). *Optical Properties of the Atmosphere (3rd Edition)*, Air-Force Cambridge Research Laboratories, AFCRL-72-0497, *Environmental Research Paper*, 411.
- MILLY, P.C. D. AND SHMAKIN, A. B. (2002). Global Modeling of Land Water and Energy Balances. Part I: The Land Dynamics (LaD) Model. *Journal of Hydrometeorology*, 3, 283-299.
- MONIN, A.S. AND OBUKHOV, A.M. (1954). Basic laws of turbulent mixing in the ground layer of the atmosphere. In: GOERING, H. (ED.). *Sammelband zur Statistischen Theorie der Turbulenz (German translation)*. Akademie Verlag, Berlin.
- MONTEITH, J. L. (1965). Evaporation and the environment. *Symposium of the Society for Experimental Biology*, 19, 205-234.
- MONTEITH, J. L. (1978). *Grundzüge der Umweltphysik*. Dr. Friedrich Steinkopf Verlag, Darmstadt.
- MONTEITH, J. L. (1973). *Principles of Environmental Physics*. Elsevier, New York.
-

- 
- MÖSER, W. AND RASCHKE, E. (1983). Mapping of Global Radiation and of Cloudiness from METEOSAT Image Data. *Meteorologische Rundschau*, 36 (2), 33-41.
- MURPHY, J. (1999). An Evaluation of Statistical and Dynamical Techniques for Downscaling Local Climate. *Journal of Climate*, 12, 2256-2284.
- MURPHY, J. (2000). Predictions of climate change over Europe using statistical and dynamical downscaling techniques. *International Journal of Climatology*, 20, 489-501.
- NASH, J. E. AND SUTCLIFFE, J. V. (1970). River flow forecasting through conceptual models, Part I – A discussion of principles. *Journal of Hydrology*, 10, 282-290.
- NGDC (NATIONAL GEOPHYSICAL DATA CENTER) (1998). <http://www.ngdc.noaa.gov>, accessed February 2008.
- NINYEROLA, M., PONS, X. AND ROURE, J. M. (2000). A methodological approach of climatological modelling of air temperature and precipitation through GIS techniques. *International Journal of Climatology*, 20 (14), 1823-1841.
- OKE, T. R. (1987). Boundary layer climates. Routledge, London.
- OSBORN, H. B. (1984). Estimating precipitation in mountainous regions. *Journal of Hydraulic Engineering*, 110, 1859-1863.
- OSBORN, T. J., CONWAY, D., HULME, M., GREGORY, J. M. AND JONES, P. D. (1999). Air flow influences on local climate: Observed and simulated mean relationships for the United Kingdom. *Climate Research*, 13, 173-191.
- PANDEY, G. R., CAYAN, D. R., DETTINGER, M. D. AND GEORTAKAKOS, K. P. (2000): A hybrid orographic plus statistical model for downscaling daily precipitation in northern California. *Journal of Hydrometeorology*, 1, 491-506.
- PAWELLEK, F., FRAUENSTEIN, F. AND VEIZER, J. (2001). Hydrochemistry and isotope geochemistry of the upper Danube River. *Geochimica et Cosmochimica Acta*, 66, 21.
- PEGORARO, A. (1991). Revision of the Theil fitting method. *Astronomy and Astrophysics*, 259, 386-393.
- PENMAN, H. L. (1956). Estimating Evaporation. *Transactions of the American Geophysical Union*, 37, 43-46.
- PFEIFER, S. (2006). Modeling cold cloud processes with the regional climate model REMO. Reports on Earth System Science 23, Max-Planck-Institute for Meteorology, Hamburg.
- PITMAN, A. J. (2003). Review – The Evolution of, and Revolution in, Land Surface Schemes designed for Climate Models, *International Journal of Climatology*, 23, 479-510.
- PLATE, E. J. (1993). Statistik und angewandte Wahrscheinlichkeitslehre für Bauingenieure. Ernst & Sohn Verlag, Berlin.

- 
- PRASCH, M., STRASSER, U. AND MAUSER, W. (2008a). Validation of a physically based snow model for the simulation of the accumulation and ablation of snow (ESCIMO). *Berchtesgaden National Park research report*, 53 (in print).
- PRASCH, M., WEBER, M. AND STRASSER, U. (2008b). Embedded grid-modelling of 500 glaciers in the upper Danube basin, *Abstracts of the Alpine Glaciological Meeting*, Chamonix.
- PRUDHOMME, C. AND DUNCAN, W. R. (1999). Mapping extreme rainfall in a mountainous region using geostatistical techniques: a case study in Scotland. *International Journal of Climatology*, 19 (12), 1337-1356.
- RANDALL, D. A., WOOD, R. A., BONY, S., COLMAN, R., FICHEFET, T., FYFE, J., KATTSOW, V., PITMAN, A., SHUKLA, J., SRINIVASAN, J., STOUFFER, R. J., SUMI, A., TAYLOR AND TAYLOR, K. E. (2007). Climate Models and Their Evaluation. In: SOLOMAON, S. ET AL. (EDS.). *Climate Change 2007: The Physical Science Basis. Contribution of Working Group I to the Fourth Assessment Report of the Intergovernmental Panel on Climate Change*. Cambridge University Press, Cambridge, United Kingdom and New York.
- RANDALL, D., KHAIROUTDINOV, M., ARAKAWA, A. AND GRABOWSKI, W. (2004). Breaking the cloud parameterization deadlock. *Bulletin of the American Meteorological Society*, 84, 1547-1564.
- RANK, D., PAPESCH, W. AND TESCH, R. (2005). Runoff characteristics of the upper Danube basin: conclusions from long-term environmental isotope records. *Geophysical Research Abstracts*, 7.
- ROECKNER, E., ARPE, K., BENTSSON, L., CHRISTOPH, M., CLAUSSEN, M., DÜMENIL, L., ESCH, M., GIORGETTA, M., SCHLESE, U. AND SCHULZWEIDA, U. (1996). The atmospheric general circulation model ECHAM-4: Model Description and simulation of present day climate. MPI Report 218, Max-Planck-Institute for Meteorology, Hamburg.
- ROECKNER, E., BÄUML, G., BONAVENTURA, L., BROKOPF, R., ESCH, M., GIORGETTA, M., HAGEMANN, S., KIRCHNER, I., KORNBLUEH, L., MANZINI, E., RHODIN, A., SCHLESE, U., SCHULWEIDA, U., SCHULZWEIDA, U. AND TOMKINS, A. (2003). The Atmospheric General Circulation Model ECHAM5. Part I: Model Description. MPI Report 349, Max-Planck-Institute for Meteorology, Hamburg.
- ROSS, D. G., SMITH, I. N., MANINS, P. C. AND FOX, G. D. (1988). Diagnostic wind fields modelling for complex terrain: model development and testing. *Journal of Applied Meteorology*, 27 (7), 785-796.
- RYAN, B. C. (1977). A mathematical model for diagnosis and prediction of surface winds in mountainous terrain. *Journal of Applied Meteorology*, 16 (6), 571-584.
- RZD (REGIONALE ZUSAMMENARBEIT DER DONAULÄNDER) (1986). Die Donau und ihr Einzugsgebiet – Eine Hydrologische Monographie, Teil 1: Texte.
-

- SCHÄR, C., VIDALE, P. L., LÜTHI, D., FREI, C., HÄBERLI, C., LINIGER, M. A. AND APPENZELLER, C. (2004). The role of increasing temperature variability for European summer heat waves. *Nature*, 427, 332-336.
- SCHÄR, C., LÜTHI, D., BEYERLE, U. AND HEISE, E. (1999). The soil-precipitation feedback: A process study with a regional climate model. *Journal of Climate*, 12, 722-741.
- SCHMIDLI, J., GOODESS, C. M., FREI, C., HAYLOCK, M. R., HUNDECHA, Y., RIBALAYGUA, J. AND SCHMITH, T. (2007). Statistical and dynamical downscaling of precipitation: An evaluation and comparison of scenarios for the European Alps. *Journal of Geophysical Research*, 112, doi:10.1029/2005JD007026.
- SCHÖNWIESE, C. D. (2000). *Praktische Statistik für Meteorologen und Geowissenschaftler*. Gebrüder Borntraeger, Stuttgart.
- SCHULZ, K. AND BEVEN, K. (2003). Data-supported robust parameterizations in land surface-atmosphere flux predictions: towards a top-down approach. *Hydrological Processes*, 17, 2259-2277.
- SCHWARB, M., DALY, C., FREI, C. AND SCHAR, C. (2001). Mean annual precipitation throughout the European Alps, 1971-1990. Hydrological Atlas of Switzerland. National Hydrological Service, Bern.
- SCHWARB, M., DALY, C., FREI, C. AND SCHAR, C. (2001). Mean seasonal precipitation throughout the European Alps, 1971-1990. Hydrological Atlas of Switzerland. National Hydrological Service, Bern.
- SEMENOV, M. A., BROOKS, R. J., BARROW, E. M. AND RICHARDSON, C. W. (1998). Comparison of the WGEN and LARS-WG stochastic weather generators for diverse climates. *Climate Research*, 10, 95-07.
- SEN, P. K. (1968). Estimates of the regression coefficient based on Kendall's tau. *Journal of the American Statistical Association*, 63, 1379-1389.
- SHEFFIELD, J., GOTETI, G. AND WOOD, E. F. (2006). Development of a 50-Year High-Resolution Global Dataset of Meteorological Forcings for Land Surface Modeling. *Journal of Climate*, 19, 3088-3111.
- SHERMAN, C. A. (1978). A mass consistent model for wind fields over complex terrain. *Journal of Applied Meteorology*, 17 (3), 312-319.
- SMIRNOV, N. (1933). Estimate of deviation between empirical distribution functions in two independent samples. *Bulletin Moscow University*, 2 (2), 3-16.
- SMITH, R. B. (1979). The influence of mountains on the atmosphere. *Advances in Geophysics*, 21, 27-230.
- SMITH, R. B. AND BARSTAD, I. (2004): A linear theory of orographic precipitation. *Journal of the Atmospheric Sciences*, 61, 1377-1391.

- 
- SPREEN, W. C. (1947). A determination of the effect of topography upon precipitation. *Transactions of the American Geophysical Union*, 28, 285-290.
- STRASSER, U. (1998). Regionalisierung des Wasserhaushaltes mit einem SVAT-Modell am Beispiel des Weser-Einzugsgebietes. *Münchener Geographische Abhandlungen*, 28 (B).
- STRASSER, U., FRANZ, H. AND MAUSER, W. (2008). Distributed modelling of snow processes in the Berchtesgaden National Park (Germany). Berchtesgaden National Park research report, 53 (in print).
- THEIL, H. (1950). A rank-invariant method of linear and polynomial regression analysis. *Indagationes Mathematicae*, 12, 85-91.
- THOMASON, A. M., BROWN, R. A., ROOSENBURG, N. J., SRINIVASAN, R. AND IZAURRALDE, R. C. (2005). Climate Change Impacts for the Conterminous USA: An integrated Assessment. Part 4: Water Resources. *Climatic Change*, 69 (1), 67-88.
- THOMPSON, R.D. AND PERRY, A. (1997). Applied Climatology. Routledge, London, New York.
- THORNTON, P. W., RUNNING, S. W. AND WHITE, M. A. (1997). Generating surfaces of daily meteorological variables over large regions of complex terrain. *Journal of Hydrology*, 190, 214-251.
- TODINI, E. (2007). A mass conservative and water storage consistent variable parameter Muskingum-Cunge approach. *Hydrology and Earth System Sciences Discussions*, 4, 1549-1592.
- USDOC. (1968). Climatic atlas of the United States. Environmental Science Services Administration and US Department of Commerce, Washington, DC.
- VALCKE, S., REDLER, R. (2006). OASIS4 User Guide (OASIS4\_0\_2). PRISM Report No 3, 2nd Edition.
- VAN ULDEN, A., LENDERINK, G., VAN DEN HURK, B. AND VAN MEIJGAARD, E. (2007). Circulation statistics and climate change in Central Europe: PRUDENCE simulations and observations. *Climatic Change*, 81, 179-192, DOI 10.1007/s10584-006-9212-5.
- VON STORCH, H. AND ZWIERS, F. W. (1995). Statistical Analysis in Climate Research. Cambridge University Press, Cambridge.
- VON STORCH, H., ZORITA, E. AND CUBASCH, U. (1993). Downscaling of climate change estimates to regional scales: application to winter rainfall in the Iberian Peninsula. *Journal of Climate*, 6, 1161-1171.
- VUGLINSKI, V. S. (1972). Methods for the study of laws for the distribution (illustrated by the Vitim River Basin). Distribution of precipitation in mountainous areas. WMO Publications, 326(2), 212-221.
-

- 
- WALLACE, J. M. AND HOBBS, P. V. (1977). *Atmospheric Science: An Introductory Survey*. Academic Press.
- WALTER, A., KEULER, K., JACOB, D., KNOCHE, R., BLOCK, A., KOTLARSKI, S., MÜLLER-WESTERMEIER, G., RECHID, D. AND AHRENS, W. (2006). A high resolution reference data set of German wind velocity 1951-2001 and comparison with regional climate model results. *Meteorologische Zeitschrift*, 15 (6), 585-596.
- WEBER, D. D. AND ENGLUND, E. J. (1994). Evaluation and Comparison of Spatial Interpolators II. *Mathematical Geology*, 26 (5), 589-603.
- WEISSE, A. K. AND BOIS, P. (2001). Topographic effects on statistical characteristics of heavy rainfall and mapping in the French Alps. *Journal of Applied Meteorology*, 40, 720-740.
- WIDMANN, M., BRETHERTON, C. S. AND SALATHÉ, E. P. (2003). Statistical Precipitation Downscaling over the Northwestern United States Using Numerically Simulated Precipitation as a Predictor. *Journal of Climate*, 16, 799-815.
- WILBY, R. L., CHARLES, S. P., ZORITA, E., TIMBAL, B., WHETTON, P. AND MEARN, L. O. (2004). Guidelines for Use of Climate Scenarios Developed from Statistical Downscaling Methods. Data Distribution Centre of the IPCC. Technical report.
- WILBY, R. L., HAY, L. E., GUTOWSKI, W. J., ARRITT, R. W., TAKLE, E. S., PAN, Z., LEAVESLEY, G. H. AND CLARK, M. P. (2000). Hydrological responses to dynamically and statistically downscaled climate model output. *Geophysical Research Letters*, 27(8), 1199-1202.
- WILBY, R. L., WIGLEY, T. M. L., CONWAY, D., JONES, P. H., HEWITSON, B. C., MAIN, J. AND WILKS, D. S. (1998). Statistical Downscaling of general circulation model output: A comparison of methods. *Water Resources Research*, 34, 2995-3008.
- WOOD, A. W., LEUNG, L. R., SRIDHAR, V. AND LETTENMAIER, D. P. (2004). Hydrological impacts of dynamical and statistical approaches to downscaling climate model outputs. *Climatic Change*, 62 (1-3), 189-216.
- WOTLING, G., BOUVIER, C., DANLOUX, J. AND FRITSCH, J.-M. (2000). Regionalization of extreme precipitation distribution using the principal components of the topographical environment. *Journal of Hydrology*, 233, 86-101.
- ZORITA, E. AND VON STORCH, H. (1999). The Analog Method as a Simple Statistical Downscaling Technique: Comparison with More Complicated Methods. *Journal of Climate*, 12, 2474-2489.

## 9 APPENDIX

A-1: Equations used to convert between different forms of air humidity (BUCK 1981, CAMPBELL AND NORMAN 1998, COSGROVE ET AL. 2003)

Saturation vapor pressure  $e_s$  [Pa]:

$$e_s = a_h \exp\left(\frac{b_h T_c}{c_h + T_c}\right) \quad \text{Eq. 9.1}$$

with:

- $a_h$  = 611.21 (over water) and 611.15 (over ice)
- $b_h$  = 17.502 (over water) and 22.452 (over ice)
- $c_h$  = 240.97 (over water) and 272.55 (over ice)
- $T_c$  = Air temperature [°C]

Actual vapor pressure  $e_a$  [Pa]:

$$e_a = a_h \exp\left(\frac{b_h T_d}{c_h + T_d}\right) \quad \text{Eq. 9.2}$$

with:

- $a_h$  = 611.21 (over water) and 611.15 (over ice)
- $b_h$  = 17.502 (over water) and 22.452 (over ice)
- $c_h$  = 240.97 (over water) and 272.55 (over ice)
- $T_d$  = Dewpoint temperature [°C]

Relative air humidity  $RH$  [%]:

$$RH = 100 \frac{e_a}{e_s} = 100 \frac{q}{q_s} \quad \text{Eq. 9.3}$$

with:

- $e_s$  = Saturation vapor pressure [Pa]
- $e_a$  = Actual vapor pressure [Pa]
- $q_s$  = Specific humidity at saturation [kg/kg]
- $q$  = Specific humidity [kg/kg]

---

Specific humidity  $q$  [kg/kg]:

$$q = \frac{RH q_s}{100} \quad \text{Eq. 9.4}$$

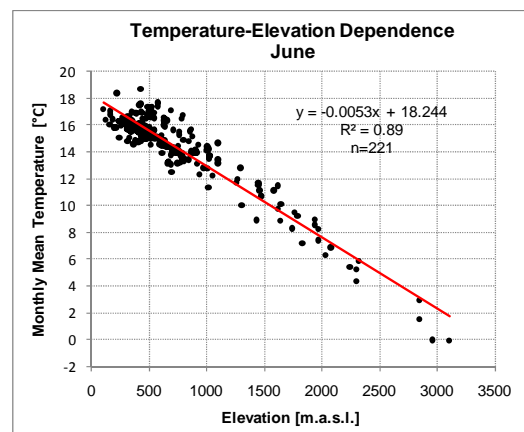
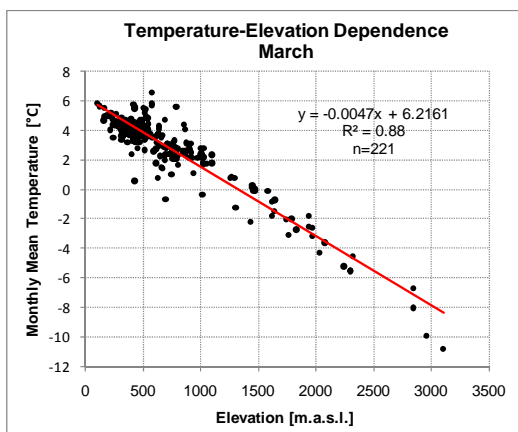
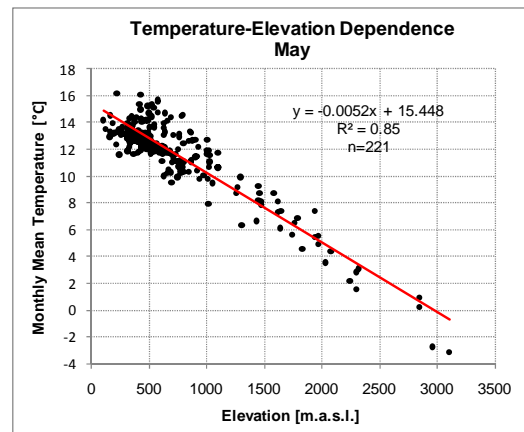
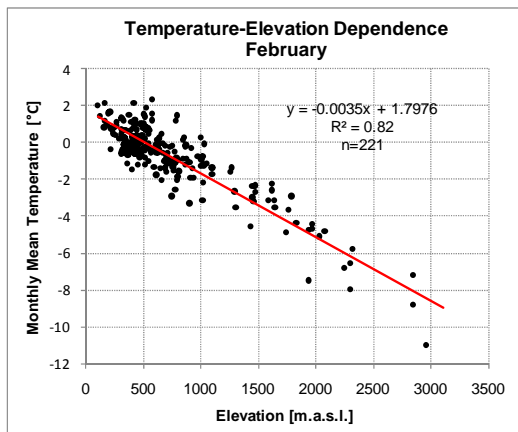
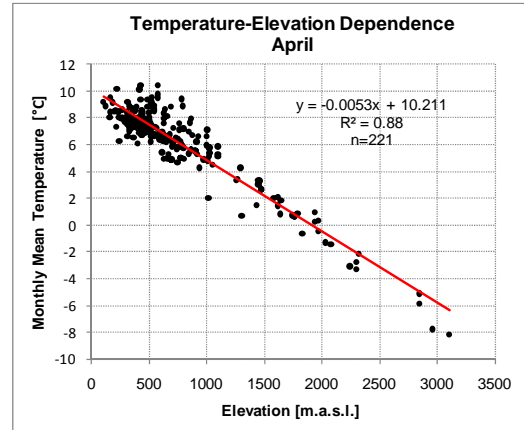
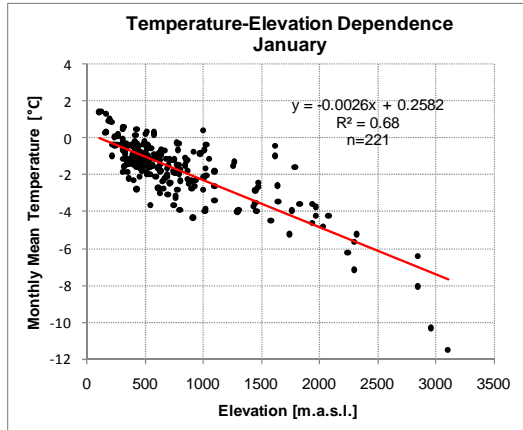
with:  $q_s$  = Specific humidity at saturation [kg/kg]  
 $RH$  = Relative humidity [%]

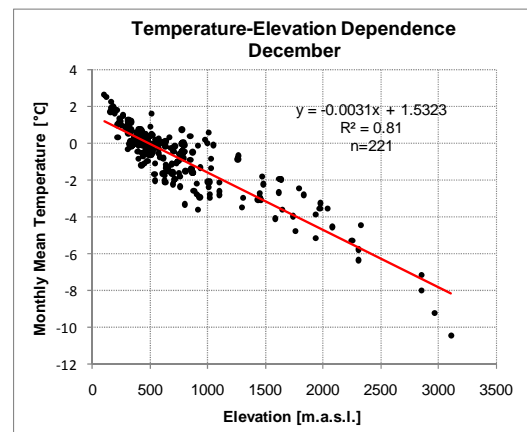
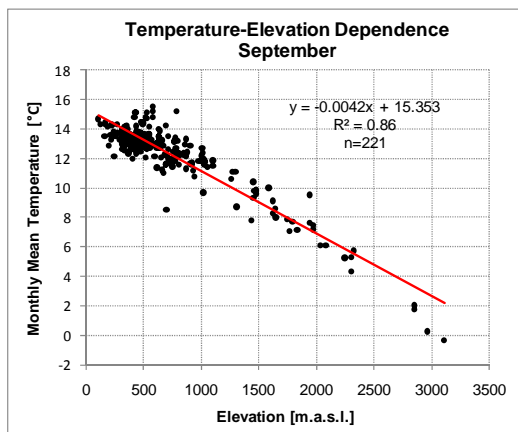
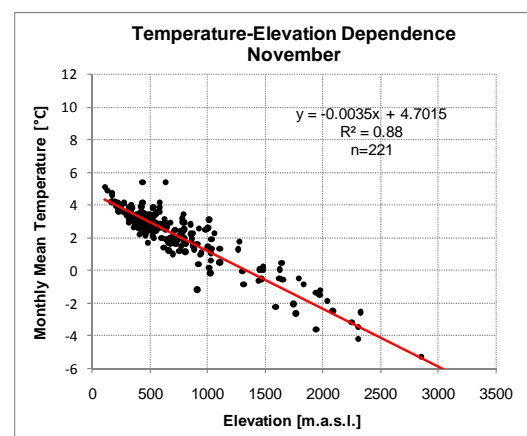
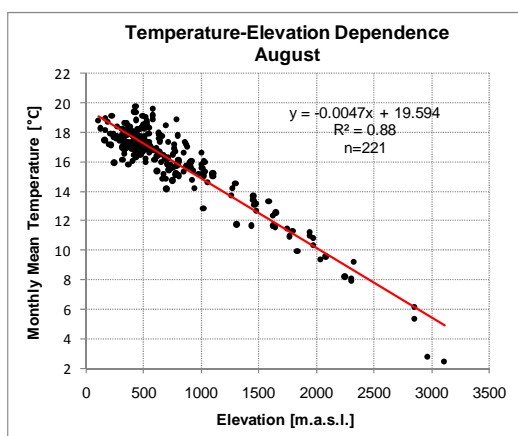
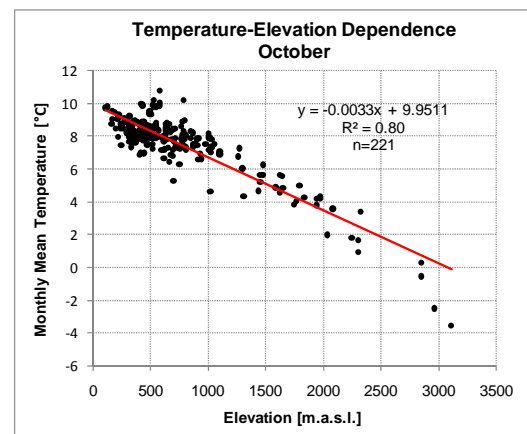
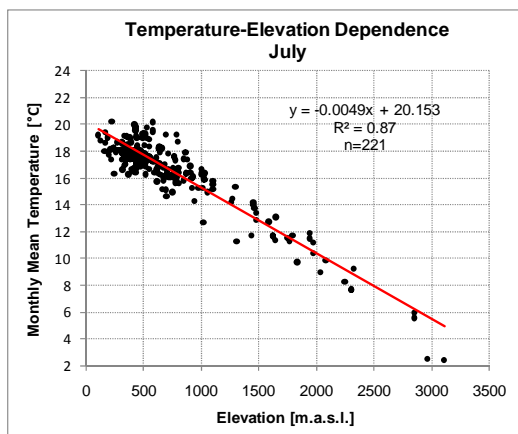
Dewpoint Temperature  $T_d$  [°C]:

$$T_d = \frac{c_h \ln \left( \frac{e_a}{a_h} \right)}{b_h - \ln \left( \frac{e_a}{a_h} \right)} \quad \text{Eq. 9.5}$$

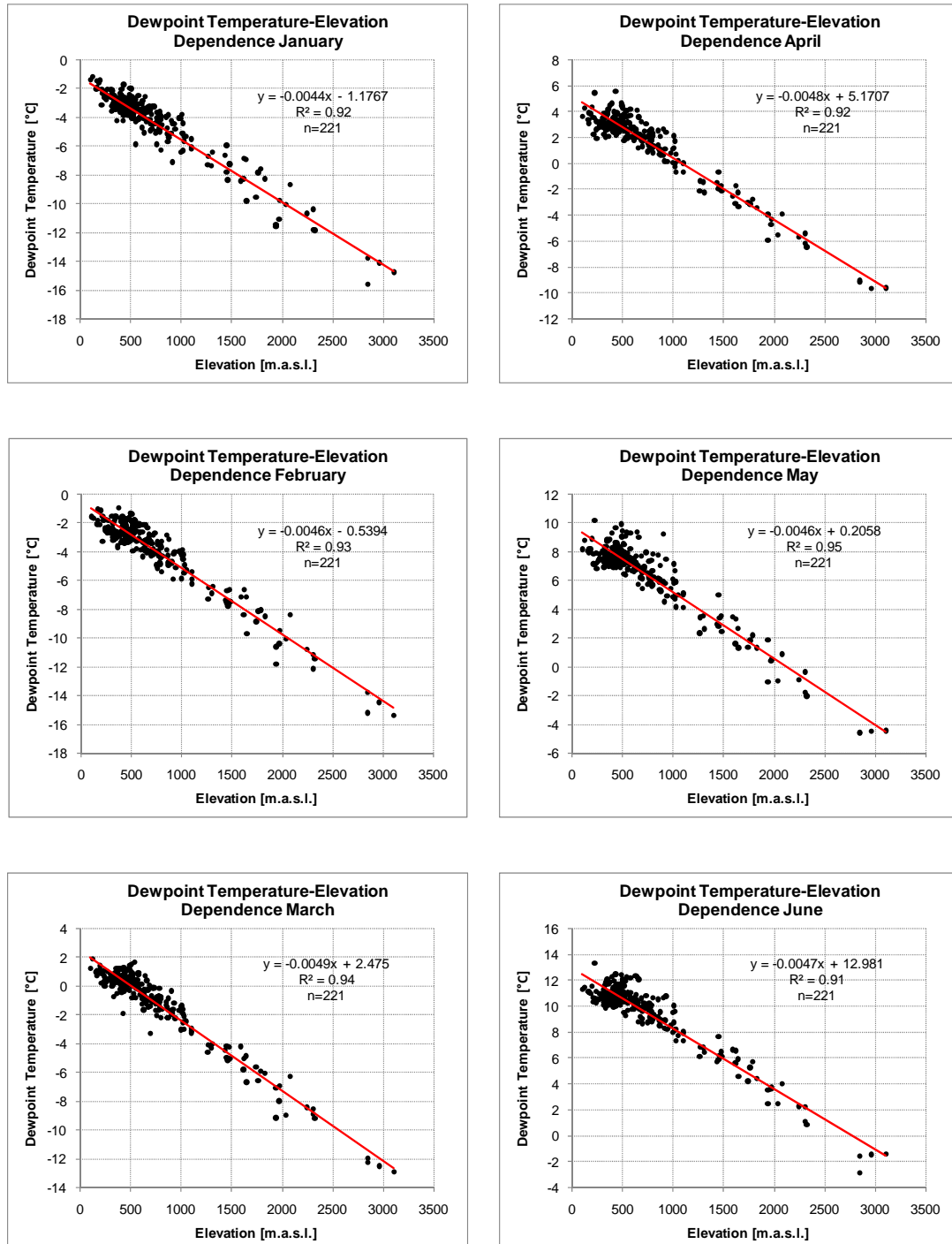
with:  $a_h$  = 611.21 (over water) and 611.15 (over ice)  
 $b_h$  = 17.502 (over water) and 22.452 (over ice)  
 $c_h$  = 240.97 (over water) and 272.55 (over ice)  
 $e_a$  = Actual vapor pressure [Pa]

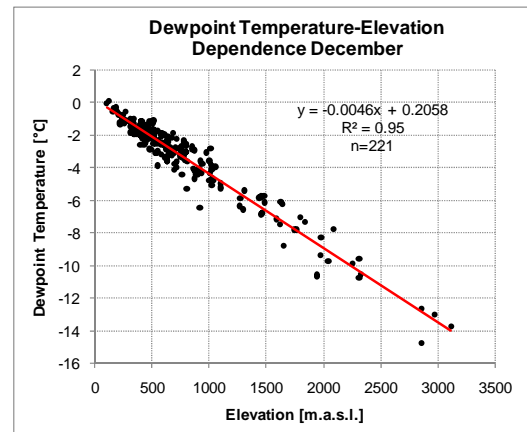
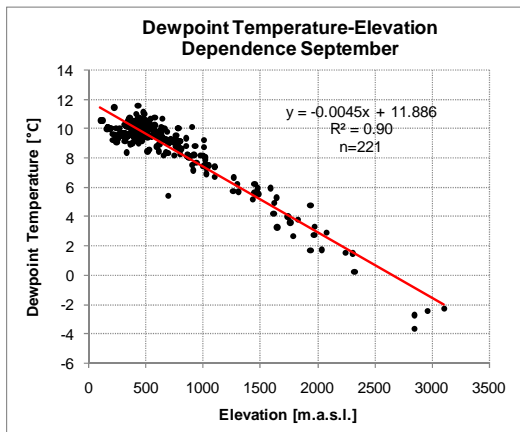
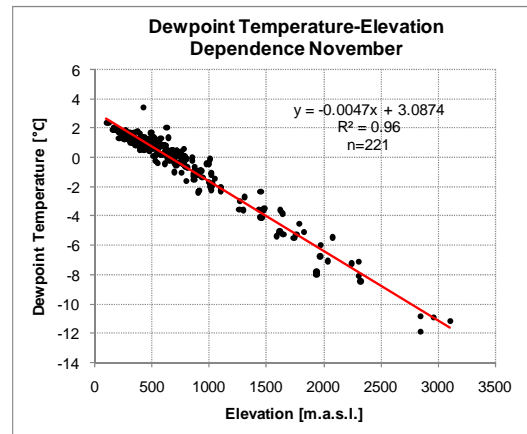
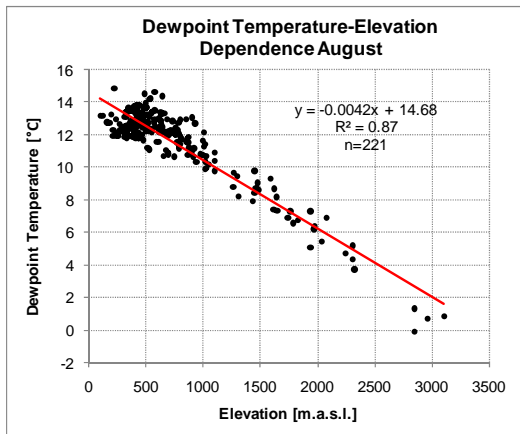
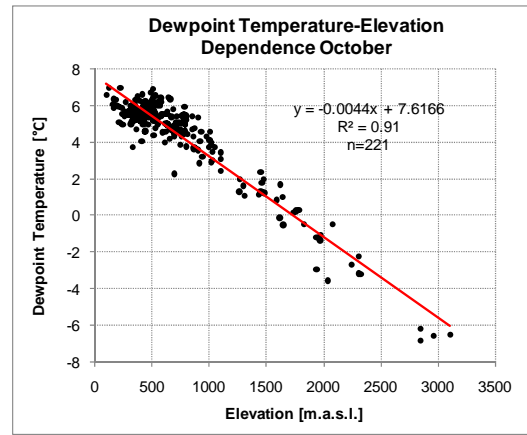
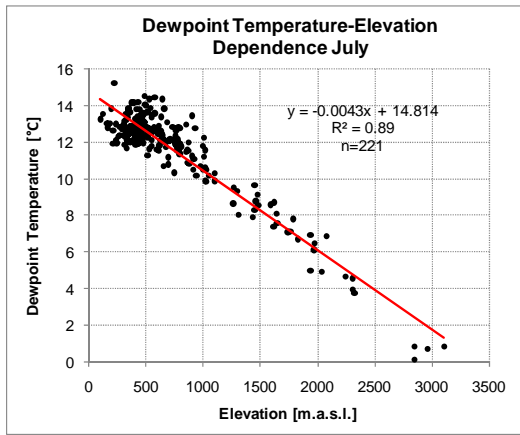
A-2: Temperature-elevation dependence as reflected in the station observations used for the determination of monthly lapse rates for the UD (chapter 4.2.2.2)





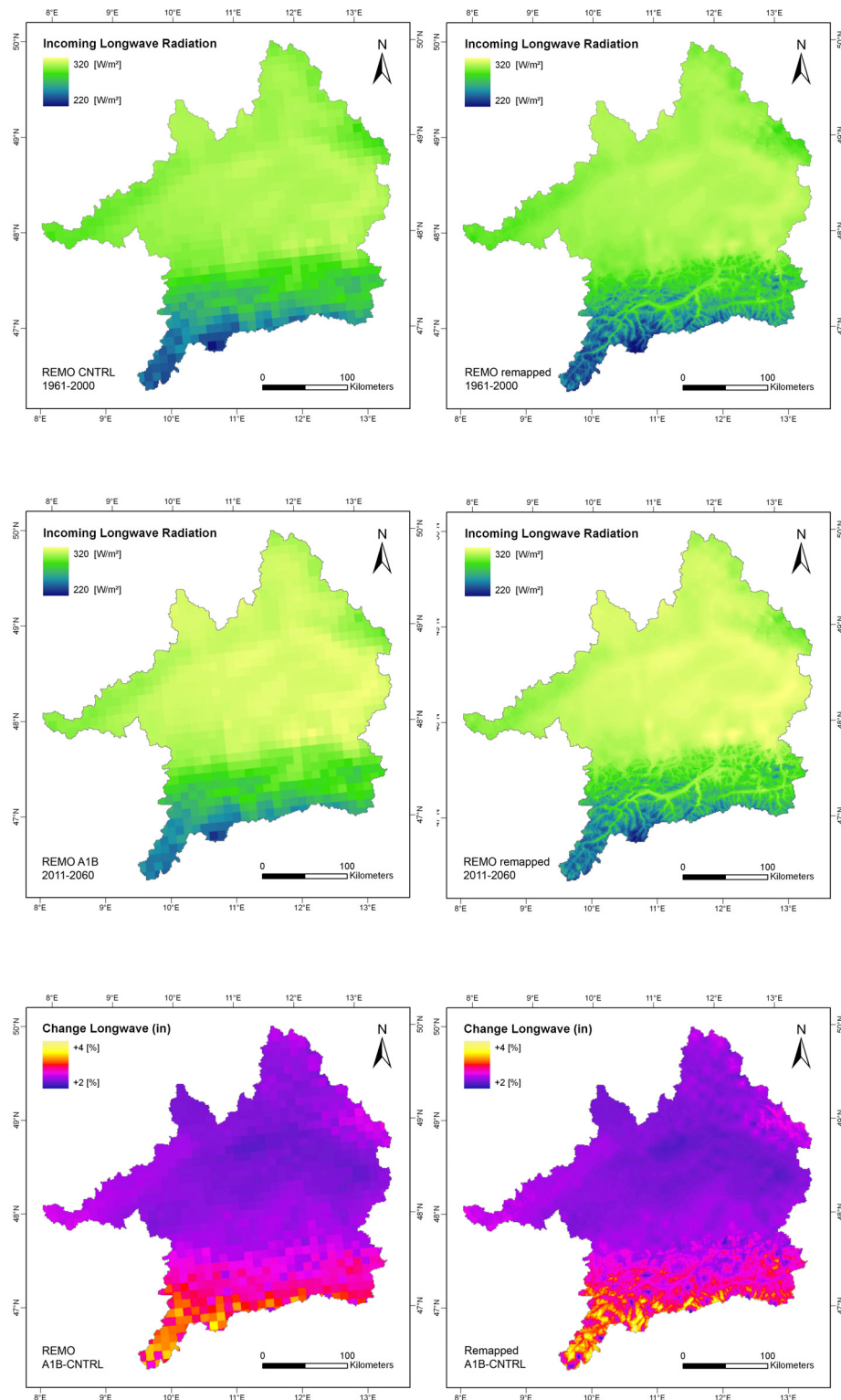
A-3: Dewpoint temperature-elevation dependence as reflected in the station observations used for the determination of monthly lapse rates for the UD (chapter 4.2.3.2)



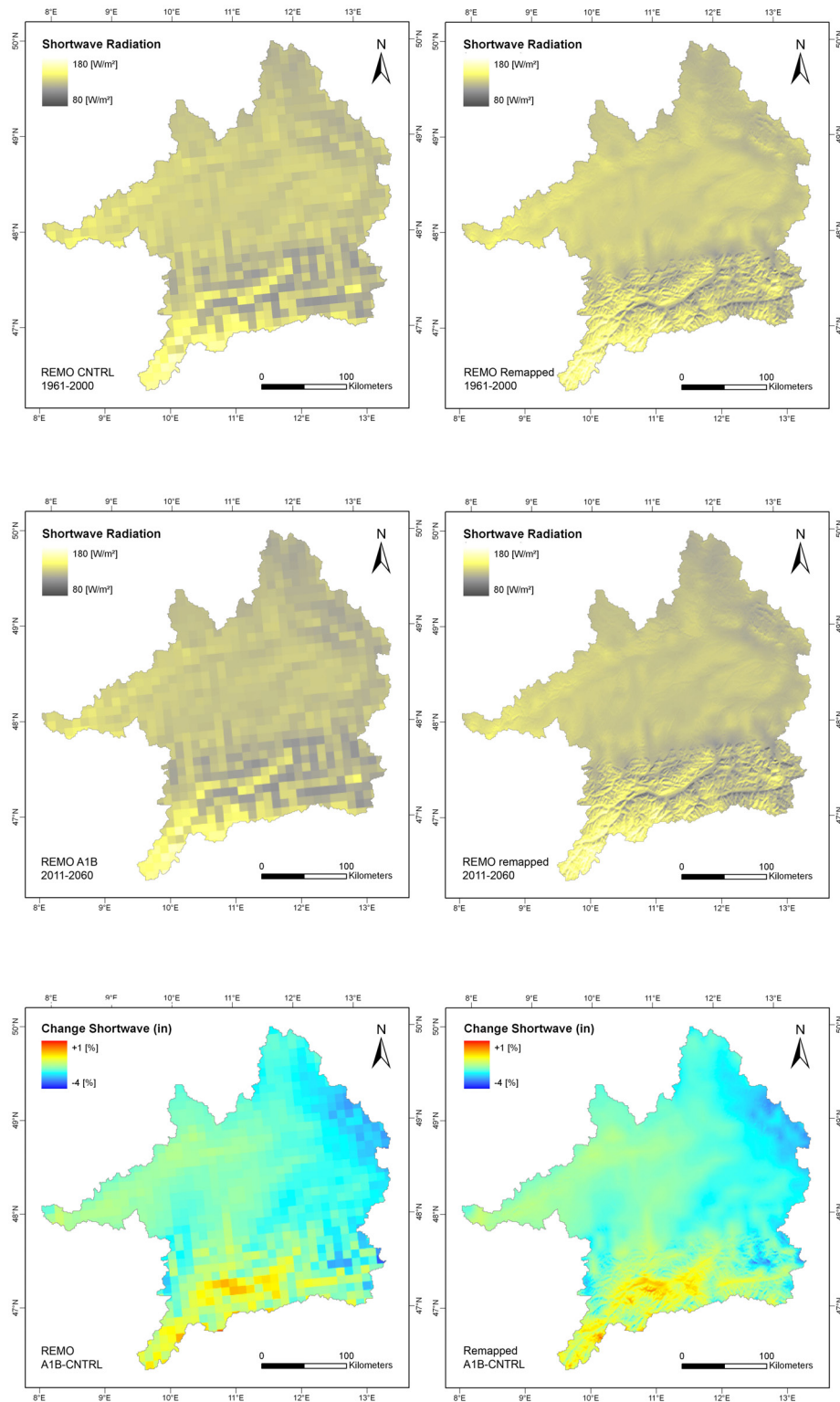




A-5: Incoming Longwave Radiation for the reference run (1961-2000) and the scenario run (2011-2060). REMO simulations (left), SCALMET longwave radiation model (right).



A-6: Incoming Shortwave Radiation for the reference run (1961-2000) and the scenario run (2011-2060). REMO simulations (left), SCALMET shortwave radiation model (right).



## A-7: The meteorological stations used for the evaluation of the remapping techniques in SCALMET

STATION NR	STATION NAME	COUNTRY	ALTITUDE [m]	LATITUDE [°]	LONGITUDE [°]
4137	KEMPTEN (WST)	GERMANY	705	47.71	10.33
4142	HINDELANG-UNTERJ. (AKKST)	GERMANY	1053	47.55	10.43
4144	OBERSTDORF (WST)	GERMANY	810	47.40	10.28
4146	FISCHEN, KR.OBERALLGAEU	GERMANY	757	47.46	10.26
4151	SCHWANGAU-HORN	GERMANY	792	47.58	10.71
4152	OY-MITTELBERG-PETERSTHAL	GERMANY	872	47.63	10.38
4155	ZUGSPITZE (WST)	GERMANY	2960	47.41	10.98
4156	GARMISCH-PARTENK. (WST)	GERMANY	719	47.48	11.06
4157	MITTENWALD	GERMANY	920	47.43	11.26
4161	HOHENPEISSENBERG (OBS)	GERMANY	977	47.80	11.01
4168	KOHLGRUB,BAD (ROSSHOF)	GERMANY	734	47.66	11.08
4169	BAD TOELZ	GERMANY	640	47.78	11.55
4175	TEGERNSEE	GERMANY	838	47.71	11.76
4176	ROTTACH-EGERN	GERMANY	747	47.68	11.76
4179	KREUTH (KKST)	GERMANY	776	47.65	11.75
4535	REICHENHALL.BAD	GERMANY	470	47.71	12.88
4536	SCHOENAU A.KOE.SEE AKKST	GERMANY	616	47.61	12.98
4541	RAUSCHBERG B.RUHPOLDING	GERMANY	1640	47.73	12.68
4543	RUHPOLDING	GERMANY	692	47.73	12.66
4546	BAYRISCHZELL	GERMANY	789	47.68	12.00
4548	WENDELSTEIN (WST)	GERMANY	1832	47.70	12.01
4549	OBERAUDORF	GERMANY	480	47.66	12.16
6300	SALZBURG-FLUGHAFEN	AUSTRIA	430	47.80	13.00
6305	SALZBURG-FREISAAL	AUSTRIA	420	47.79	13.05
8800	ACHENKIRCH	AUSTRIA	905	47.53	11.70
9016	KUFSTEIN	AUSTRIA	493	47.57	12.16
9210	LOFER	AUSTRIA	629	47.58	12.69
9215	LOFERER ALM	AUSTRIA	1623	47.59	12.64
9450	ST.KOLOMAN	AUSTRIA	1000	47.65	13.23
9500	ABTENAU	AUSTRIA	714	47.56	13.34
11305	WARTH	AUSTRIA	1475	47.25	10.18
11400	HOLZGAU	AUSTRIA	1100	47.26	10.34
11505	REUTTE	AUSTRIA	850	47.49	10.71
11602	EHRWALD	AUSTRIA	960	47.40	10.92
11803	INNSBRUCK-UNIV.	AUSTRIA	578	47.26	11.38
11804	INNSBRUCK-FLUGPLATZ	AUSTRIA	579	47.25	11.35
11901	JENBACH	AUSTRIA	530	47.39	11.75
12200	KITZBUEHEL	AUSTRIA	763	47.44	12.39
12201	KITZBUEHEL	AUSTRIA	763	47.45	12.35
12215	HAHNENKAMM-EHRENBACHHOEHE	AUSTRIA	1790	47.41	12.36
12220	UTTENDORF	AUSTRIA	803	47.26	12.56
12301	SAALBACH	AUSTRIA	1022	47.37	12.68
12311	SCHMITTENHOEHE	AUSTRIA	1973	47.32	12.73
12322	ZELL AM SEE	AUSTRIA	766	47.32	12.79
12504	BISCHOFSHOFEN	AUSTRIA	543	47.40	13.22
12505	ST.JOHANN IM PONGAU	AUSTRIA	634	47.31	13.18
12506	BISCHOFSHOFEN-BUCHBERG	AUSTRIA	733	47.40	13.21
12620	WAGRAIN	AUSTRIA	880	47.33	13.30
14300	ST.ANTON AM ARLBERG	AUSTRIA	1298	47.13	10.27
14305	GALZIG	AUSTRIA	2081	47.13	10.23
14403	LANDECK	AUSTRIA	798	47.13	10.56
14512	IMST	AUSTRIA	860	47.24	10.74
14520	PRUTZ	AUSTRIA	870	47.06	10.66
14600	HAIMING	AUSTRIA	695	47.25	10.85
14610	KUEHTAI	AUSTRIA	1970	47.20	11.01
14621	ST.LEONHARD-NEURUR	AUSTRIA	1462	47.02	10.86
14801	BRENNER	AUSTRIA	1450	47.00	11.51
14812	PATSCHERKOFEL	AUSTRIA	2247	47.20	11.46
15001	MAYRHOFEN	AUSTRIA	643	47.15	11.85
15101	KRIMML	AUSTRIA	1000	47.23	12.18
15300	ENZINGERBODEN	AUSTRIA	1480	47.16	12.63
15310	MOOSERBODEN	AUSTRIA	2036	47.15	12.71
15321	RUDOLFSHUETTE	AUSTRIA	2304	47.13	12.62
15400	RAURIS	AUSTRIA	945	47.21	13.00
15401	RAURIS	AUSTRIA	916	47.25	12.83
15402	RAURIS	AUSTRIA	931	47.22	12.99
15430	KOLM SAIGURN	AUSTRIA	1618	47.06	12.98
15500	BADGASTEIN	AUSTRIA	1100	47.11	13.13
15515	BADGASTEIN/BOECKSTEIN	AUSTRIA	1100	47.09	13.12
17001	GALTUER	AUSTRIA	1648	46.96	10.19
17005	ISCHGL-IDALPE	AUSTRIA	2323	46.98	10.31
17301	OBERGURGL	AUSTRIA	1938	46.86	11.02
17315	PITZTALER GLETSCHER	AUSTRIA	2850	46.92	10.87

### A-8: MAE statistic for all stations used within the evaluation of temperature remappings (chapter 5.2.1.1)

TEMPERATURE	1994-1996	CONSERVATIVE INTERPOLATION			BILINEAR INTERPOLATION		
STATION NR.	MEAN obs [°C]	MEAN mod [°C]	MAE [°C]	Std_dev MAE [°C]	MEAN mod [°C]	MAE [°C]	Std_dev MAE [°C]
6300	9.80	9.59	0.24	0.17	9.37	0.46	0.32
6305	9.56	9.08	0.50	0.21	9.29	0.31	0.21
4161	7.24	7.95	0.77	0.30	7.97	0.78	0.48
4169	8.01	7.62	0.41	0.16	7.67	0.34	0.20
4543	6.55	5.96	0.61	0.31	5.21	1.36	0.83
4541	4.48	5.96	1.51	0.49	5.49	1.02	0.61
4535	5.75	7.03	1.32	0.51	6.94	1.21	0.72
4137	7.48	7.24	0.26	0.11	7.54	0.06	0.04
4175	7.62	6.33	1.34	0.49	6.51	1.12	0.67
4548	3.91	6.11	2.33	0.98	5.63	1.76	1.06
4176	7.54	6.33	1.25	0.45	6.16	1.41	0.84
4546	6.50	6.11	0.43	0.30	5.52	1.01	0.67
9450	7.04	6.62	0.43	0.19	6.55	0.50	0.30
4549	8.10	8.15	0.35	0.28	7.85	0.40	0.30
4168	6.10	6.80	0.72	0.30	6.66	0.57	0.35
4179	7.23	6.33	0.93	0.36	5.90	1.35	0.81
4536	8.25	5.81	2.49	0.90	6.87	1.40	0.85
4152	6.66	6.06	0.63	0.25	6.40	0.27	0.17
9215	7.00	4.81	2.25	0.87	4.84	2.20	1.33
9210	7.29	5.73	1.60	0.63	5.85	1.47	0.89
9500	8.12	7.16	0.97	0.35	6.78	1.35	0.81
4151	7.41	6.15	1.33	0.57	6.47	1.00	0.66
9016	9.01	7.16	1.88	0.66	7.71	1.33	0.78
4142	5.98	5.18	0.82	0.32	5.42	0.57	0.34
8800	6.91	5.28	1.67	0.65	5.31	1.64	0.99
11505	7.26	5.25	2.04	0.71	5.51	1.76	1.02
4156	6.98	4.25	2.77	0.98	4.82	2.19	1.23
4146	6.75	5.99	0.78	0.30	6.40	0.35	0.24
12201	6.34	6.23	0.16	0.10	6.49	0.16	0.11
12200	6.26	6.23	0.20	0.16	5.66	0.62	0.37
4157	6.87	4.60	2.34	0.88	5.03	1.86	1.05
12506	7.99	6.65	1.37	0.51	6.18	1.84	1.09
12504	8.34	6.65	1.73	0.64	6.56	1.81	1.08
12215	3.26	4.57	1.35	0.56	4.99	1.76	1.07
4155	-1.80	2.04	3.85	1.11	2.41	4.22	2.17
4144	6.32	5.55	0.82	0.35	5.32	1.04	0.64
11602	6.99	3.72	3.26	0.71	3.76	3.23	1.58
11901	9.29	5.61	3.75	1.36	6.87	2.46	1.47
12301	5.62	4.38	1.26	0.50	4.36	1.28	0.80
12620	5.59	5.48	0.13	0.07	5.44	0.15	0.09
12311	4.00	5.83	1.86	0.69	6.04	2.08	1.24
12322	7.41	5.83	1.64	0.61	6.21	1.25	0.75
12505	6.36	5.89	0.50	0.20	6.10	0.27	0.16
12220	4.95	4.65	0.39	0.22	4.23	0.86	0.57
15401	7.08	3.41	3.75	1.35	4.06	3.08	1.83
11803	9.68	7.11	2.60	0.91	6.82	2.90	1.71
11400	6.21	3.23	3.11	1.26	3.53	2.76	1.69
11804	9.48	7.11	2.43	0.89	7.01	2.53	1.52
11305	4.73	3.16	1.65	0.74	3.26	1.52	0.98
14600	8.89	6.09	2.87	1.14	6.17	2.76	1.67
15101	6.13	3.94	2.21	0.79	2.78	3.40	2.02
15402	6.19	3.81	2.43	0.88	3.41	2.83	1.68
14512	8.07	5.06	3.06	1.14	5.09	3.03	1.85
15400	4.74	3.81	0.95	0.35	3.36	1.41	0.83
14610	1.26	2.14	0.88	0.25	1.12	0.24	0.20
14812	5.56	6.87	1.32	0.45	6.73	1.19	0.71
15300	2.92	1.06	1.87	0.67	0.22	2.71	1.51
15310	1.12	-0.06	1.21	0.52	-0.07	1.19	0.71
15001	5.94	5.43	0.51	0.18	5.82	0.13	0.09
15321	-0.98	-1.31	0.62	0.45	-1.55	0.75	0.54
15500	5.19	3.87	1.34	0.50	3.00	2.22	1.33
14305	3.01	2.50	1.30	0.83	2.13	1.19	0.78
14300	4.99	2.49	2.59	1.16	2.19	2.91	1.88
14403	5.88	3.69	2.24	0.82	3.32	2.61	1.55
15515	5.40	1.69	3.76	1.37	2.20	3.25	1.95
15430	-0.05	0.76	0.82	0.30	0.48	0.53	0.32
14520	7.21	4.35	2.93	1.08	3.60	3.67	2.18
14621	4.40	-0.12	4.61	1.69	-0.10	4.58	2.73
14801	4.61	3.13	1.51	0.58	3.34	1.31	0.79
17005	1.38	0.91	0.48	0.20	0.97	0.41	0.25
17001	3.10	1.23	1.91	0.73	1.32	1.81	1.06
17315	-2.31	-1.50	0.83	0.33	-1.63	0.70	0.43
17301	1.97	-0.86	2.87	1.03	-0.44	2.45	1.47

TEMPERATURE	1994-1996	CONSTANT LAPSE RATE REMAPPING			REGRESSION BASED REMAPPING		
STATION NR.	MEAN obs [°C]	MEAN mod [°C]	MAE [°C]	Std_dev MAE [°C]	MEAN mod [°C]	MAE [°C]	Std_dev MAE [°C]
6300	9.80	9.56	0.31	0.20	9.55	0.30	0.20
6305	9.56	9.56	0.18	0.15	9.54	0.20	0.15
4161	7.24	7.20	0.29	0.25	7.25	0.18	0.18
4169	8.01	8.01	0.10	0.08	7.98	0.06	0.06
4543	6.55	6.53	0.44	0.34	6.47	0.16	0.16
4541	4.48	4.56	0.30	0.23	4.60	0.16	0.13
4535	5.75	5.90	0.38	0.27	5.97	0.26	0.22
4137	7.48	7.49	0.03	0.02	7.49	0.02	0.03
4175	7.62	7.55	0.33	0.25	7.50	0.17	0.15
4548	3.91	3.94	0.53	0.44	3.99	0.37	0.29
4176	7.54	7.47	0.43	0.34	7.41	0.20	0.18
4546	6.50	6.43	0.43	0.34	6.40	0.19	0.19
9450	7.04	7.02	0.15	0.12	7.01	0.05	0.04
4549	8.10	8.34	0.35	0.31	8.31	0.33	0.29
4168	6.10	6.17	0.21	0.16	6.20	0.15	0.15
4179	7.23	7.16	0.42	0.33	7.11	0.18	0.16
4536	8.25	8.23	0.43	0.34	8.16	0.18	0.17
4152	6.66	6.65	0.09	0.07	6.64	0.05	0.08
9215	7.00	6.93	0.71	0.55	6.84	0.26	0.24
9210	7.29	7.27	0.47	0.37	7.21	0.18	0.16
9500	8.12	8.02	0.42	0.32	7.96	0.20	0.17
4151	7.41	7.35	0.43	0.39	7.31	0.25	0.25
9016	9.01	8.79	0.41	0.27	8.73	0.37	0.26
4142	5.98	5.95	0.18	0.14	5.94	0.07	0.05
8800	6.91	6.88	0.51	0.40	6.84	0.18	0.14
11505	7.26	7.11	0.49	0.37	7.05	0.38	0.31
4156	6.98	6.51	0.72	0.47	6.44	0.91	0.69
4146	6.75	6.59	0.19	0.15	6.58	0.19	0.16
12201	6.34	6.34	0.08	0.07	6.35	0.06	0.06
12200	6.26	6.23	0.17	0.15	6.22	0.13	0.10
4157	6.87	6.69	0.52	0.42	6.64	0.31	0.30
12506	7.99	7.87	0.57	0.44	7.80	0.24	0.19
12504	8.34	8.23	0.56	0.43	8.13	0.26	0.23
12215	3.26	3.37	0.61	0.48	3.42	0.19	0.16
4155	-1.80	-0.71	1.26	0.72	-0.64	1.58	1.17
4144	6.32	6.41	0.37	0.30	6.36	0.16	0.15
11602	6.99	6.22	0.85	0.51	6.15	1.01	0.73
11901	9.29	9.19	0.75	0.59	9.07	0.32	0.28
12301	5.62	5.52	0.47	0.36	5.49	0.26	0.25
12620	5.59	5.58	0.05	0.04	5.59	0.03	0.03
12311	4.00	4.12	0.63	0.50	4.18	0.26	0.18
12322	7.41	7.36	0.37	0.32	7.30	0.33	0.26
12505	6.36	6.35	0.08	0.07	6.36	0.05	0.05
12220	4.95	5.03	0.40	0.37	5.02	0.41	0.36
15401	7.08	6.92	0.94	0.73	6.82	0.38	0.28
11803	9.68	9.47	0.85	0.65	9.35	0.43	0.36
11400	6.21	6.01	0.89	0.69	5.96	0.50	0.35
11804	9.48	9.49	0.78	0.64	9.39	0.32	0.27
11305	4.73	4.73	0.61	0.50	4.69	0.24	0.22
14600	8.89	8.46	0.86	0.59	8.36	0.74	0.49
15101	6.13	5.92	1.02	0.79	5.84	0.42	0.29
15402	6.19	6.06	0.85	0.66	5.99	0.32	0.23
14512	8.07	8.03	1.01	0.76	7.93	0.36	0.34
15400	4.74	4.69	0.42	0.33	4.66	0.15	0.12
14610	1.26	1.41	0.25	0.19	1.40	0.18	0.12
14812	5.56	5.66	0.37	0.28	5.70	0.17	0.12
15300	2.92	2.37	0.81	0.58	2.32	0.79	0.70
15310	1.12	0.99	0.37	0.28	0.96	0.18	0.16
15001	5.94	5.93	0.06	0.06	5.94	0.05	0.07
15321	-0.98	-0.79	0.47	0.46	-0.81	0.29	0.30
15500	5.19	5.04	0.67	0.51	5.00	0.26	0.20
14305	3.01	2.91	0.75	0.59	2.89	0.65	0.49
14300	4.99	4.63	1.17	0.88	4.57	0.71	0.48
14403	5.88	5.74	0.79	0.62	5.68	0.29	0.20
15515	5.40	5.20	0.99	0.76	5.13	0.37	0.27
15430	-0.05	0.01	0.17	0.13	0.02	0.07	0.05
14520	7.21	6.98	1.11	0.86	6.88	0.43	0.29
14621	4.40	3.04	1.89	1.15	2.97	1.44	0.53
14801	4.61	4.58	0.43	0.34	4.55	0.13	0.09
17005	1.38	1.33	0.13	0.10	1.32	0.09	0.06
17001	3.10	3.00	0.51	0.39	2.96	0.23	0.17
17315	-2.31	-2.29	0.24	0.19	-2.27	0.07	0.05
17301	1.97	1.84	0.76	0.59	1.79	0.24	0.18

A-9: MAE statistic for all stations used within the evaluation of precipitation remappings (chapter 5.2.1.2)

PRECIPITATION STATION NR.	1994-1996	CONSERVATIVE INTERPOLATION			BILINEAR INTERPOLATION		
	MEAN obs [°C]	SUM mod [mm]	MAE [mm]	Std_dev MAE [mm]	SUM mod [mm]	MAE [mm]	Std_dev MAE [mm]
6300	1339.17	1346.76	0.38	0.86	1448.77	0.54	1.21
6305	1445.63	1605.35	0.53	1.00	1523.02	0.43	0.96
4161	1068.66	1037.10	0.14	0.30	1047.04	0.14	0.29
4169	1367.34	1426.99	0.23	0.43	1435.43	0.22	0.36
4543	2125.08	2133.62	0.35	0.65	2243.62	0.35	0.59
4541	2276.11	2133.62	0.48	0.93	2217.75	0.18	0.30
4535	1959.04	1892.79	0.51	0.89	1859.76	0.53	0.93
4137	1252.09	1334.56	0.28	0.53	1259.66	0.07	0.14
4175	1557.05	1772.88	0.64	1.06	1760.70	0.57	0.92
4548	1762.82	1642.23	0.84	1.51	1726.30	0.36	0.68
4176	1709.02	1772.88	0.25	0.44	1829.34	0.36	0.57
4546	1626.19	1642.23	0.35	0.68	1732.54	0.44	0.84
9450	1710.71	1774.78	0.32	0.57	1756.58	0.15	0.23
4549	1474.85	1438.97	0.79	1.45	1485.59	0.55	1.03
4168	1548.46	1389.30	0.57	1.15	1428.13	0.37	0.74
4179	1818.61	1772.88	0.34	0.72	1856.94	0.23	0.40
4536	1677.07	1799.00	0.49	0.83	1777.60	0.31	0.50
4152	1528.98	1628.56	0.50	0.86	1518.09	0.13	0.24
9215	1761.08	1756.67	0.51	0.85	1865.15	0.36	0.62
9210	1682.82	1756.55	0.31	0.49	1774.06	0.30	0.49
9500	1562.88	1639.66	0.23	0.41	1593.00	0.23	0.40
4151	1345.91	1444.92	0.94	1.75	1446.56	0.77	1.49
9016	1265.95	1420.68	0.46	0.75	1391.83	0.46	0.80
4142	1750.54	1763.33	0.53	0.91	1736.51	0.16	0.27
8800	1616.59	1825.48	0.66	1.27	1836.24	0.62	1.11
11505	1437.97	1518.15	0.73	1.42	1531.28	0.64	1.25
4156	1395.83	1508.48	0.89	1.51	1492.56	0.69	1.18
4146	1575.48	1727.78	0.54	0.93	1674.56	0.44	0.84
12201	1400.27	1375.10	0.21	0.35	1330.56	0.21	0.37
12200	1377.21	1375.10	0.40	0.70	1404.62	0.14	0.23
4157	1448.95	1555.56	0.75	1.37	1515.46	0.45	0.77
12506	1051.67	1270.14	0.62	1.03	1295.32	0.68	1.14
12504	1103.12	1270.14	0.49	0.79	1265.64	0.48	0.80
12215	1593.41	1434.19	0.51	0.95	1420.85	0.50	0.84
4155	1850.32	1583.41	1.18	1.87	1616.98	1.20	1.90
4144	1769.74	1789.09	0.40	0.75	1779.44	0.33	0.57
11602	1327.95	1489.11	0.76	1.30	1546.04	0.77	1.26
11901	1136.00	1691.61	1.52	2.75	1430.60	0.81	1.49
12301	1332.89	1427.52	0.69	1.38	1393.32	0.61	1.25
12620	1432.93	1418.15	0.14	0.26	1477.33	0.13	0.25
12311	1396.59	1188.33	0.58	0.98	1155.03	0.67	1.08
12322	1097.70	1188.33	0.44	0.77	1139.37	0.30	0.57
12505	1308.27	1215.48	0.38	0.68	1241.06	0.19	0.31
12220	1405.53	1369.77	0.31	0.63	1440.15	0.43	0.77
15401	1102.19	1450.30	1.07	1.87	1403.21	0.84	1.43
11803	853.28	959.93	0.31	0.56	1020.50	0.46	0.83
11400	1354.08	1614.77	0.96	1.56	1552.96	0.67	1.09
11804	844.93	959.93	0.41	0.75	991.35	0.46	0.83
11305	1837.64	1933.65	0.79	1.35	1918.03	0.58	1.06
14600	681.49	937.45	0.79	1.54	856.23	0.54	1.04
15101	1094.55	1282.12	0.62	1.06	1383.21	0.80	1.34
15402	1076.78	1327.81	0.69	1.15	1371.32	0.81	1.38
14512	702.60	1095.51	1.12	2.22	1031.75	0.94	1.91
15400	1263.74	1327.81	0.21	0.34	1384.17	0.34	0.57
14610	1368.17	1228.43	0.40	0.70	1319.68	0.19	0.35
14812	1073.21	994.17	0.23	0.36	972.62	0.28	0.46
15300	1703.31	1960.14	1.00	1.80	2166.29	1.40	2.49
15310	2041.10	1883.13	0.59	1.01	2042.20	0.24	0.39
15001	1216.83	1244.93	0.11	0.21	1231.17	0.09	0.18
15321	2426.67	2332.81	0.64	1.06	2451.80	0.49	0.81
15500	1249.78	1337.85	0.36	0.63	1493.90	0.67	1.15
14305	1488.60	1716.74	1.54	2.62	1572.00	1.28	2.08
14300	1348.19	1440.53	1.25	2.09	1457.13	1.29	2.10
14403	932.21	1098.40	0.47	0.82	1078.70	0.41	0.70
15515	1386.22	1696.23	0.86	1.46	1633.67	0.70	1.18
15430	2055.87	1900.04	0.46	0.78	1920.92	0.37	0.59
14520	722.95	933.33	0.61	1.13	987.11	0.75	1.27
14621	936.91	1266.77	0.91	1.57	1254.78	0.88	1.51
14801	1070.14	1102.29	0.27	0.48	1104.89	0.19	0.34
17005	1214.03	1226.20	0.14	0.22	1229.27	0.10	0.17
17001	1026.43	1133.48	0.34	0.62	1082.49	0.17	0.35
17315	1503.29	1400.92	0.29	0.48	1410.12	0.26	0.42
17301	1081.26	1289.27	0.57	0.93	1275.79	0.53	0.89

PRECIPITATION	ADJUSTMENT FACTOR REMAPPING				REGRESSION BASED REMAPPING		
	1994-1996	SUM mod [mm]	MAE [mm]	Std_dev MAE [mm]	SUM mod [mm]	MAE [mm]	Std_dev MAE [mm]
6300	1339.17	1432.02	0.52	1.18	1430.01	0.52	1.18
6305	1445.63	1499.72	0.41	0.93	1495.48	0.40	0.92
4161	1068.66	1092.75	0.14	0.29	1111.62	0.25	0.48
4169	1367.34	1409.64	0.16	0.26	1407.55	0.19	0.31
4543	2125.08	2091.21	0.22	0.46	2118.92	0.30	0.54
4541	2276.11	2327.31	0.19	0.35	2315.67	0.24	0.44
4535	1959.04	1962.62	0.46	0.85	1968.19	0.54	0.96
4137	1252.09	1265.64	0.08	0.15	1263.60	0.07	0.14
4175	1557.05	1660.80	0.31	0.53	1662.60	0.41	0.68
4548	1762.82	1893.90	0.42	0.93	1888.85	0.65	1.15
4176	1709.02	1700.36	0.15	0.26	1706.59	0.30	0.50
4546	1626.19	1645.84	0.36	0.64	1652.52	0.29	0.60
9450	1710.71	1708.56	0.07	0.11	1703.81	0.11	0.19
4549	1474.85	1443.22	0.55	1.08	1436.66	0.53	1.02
4168	1548.46	1464.37	0.30	0.60	1473.64	0.33	0.64
4179	1818.61	1730.76	0.31	0.58	1737.19	0.39	0.65
4536	1677.07	1645.19	0.15	0.28	1635.16	0.33	0.56
4152	1528.98	1494.89	0.14	0.27	1496.19	0.13	0.25
9215	1761.08	1658.46	0.34	0.59	1650.62	0.56	0.97
9210	1682.82	1638.45	0.19	0.32	1624.52	0.36	0.63
9500	1562.88	1487.91	0.29	0.58	1468.27	0.34	0.65
4151	1345.91	1375.37	0.73	1.44	1363.23	0.67	1.37
9016	1265.95	1308.35	0.37	0.63	1280.02	0.46	0.81
4142	1750.54	1685.51	0.22	0.39	1683.78	0.21	0.36
8800	1616.59	1681.98	0.26	0.44	1673.16	0.36	0.65
11505	1437.97	1397.75	0.61	1.27	1379.12	0.74	1.39
4156	1395.83	1353.75	0.67	1.19	1355.40	0.79	1.38
4146	1575.48	1655.52	0.42	0.80	1658.66	0.42	0.81
12201	1400.27	1343.86	0.18	0.32	1347.22	0.17	0.30
12200	1377.21	1360.25	0.11	0.20	1339.60	0.16	0.28
4157	1448.95	1378.58	0.45	0.85	1352.10	0.53	0.92
12506	1051.67	1174.33	0.36	0.61	1121.05	0.34	0.58
12504	1103.12	1150.90	0.20	0.35	1096.79	0.28	0.50
12215	1593.41	1552.21	0.25	0.42	1613.74	0.39	0.69
4155	1850.32	1913.56	1.12	1.90	1962.63	1.52	2.51
4144	1769.74	1675.67	0.40	0.75	1681.42	0.39	0.73
11602	1327.95	1357.91	0.55	0.98	1317.99	0.88	1.45
11901	1136.00	1250.91	0.33	0.61	1199.70	0.37	0.74
12301	1332.89	1304.15	0.58	1.29	1259.18	0.57	1.21
12620	1432.93	1463.48	0.10	0.20	1460.71	0.10	0.21
12311	1396.59	1289.59	0.34	0.53	1382.56	0.33	0.56
12322	1097.70	1067.87	0.31	0.61	1013.45	0.40	0.79
12505	1308.27	1219.92	0.25	0.40	1209.86	0.27	0.44
12220	1405.53	1369.43	0.43	0.83	1344.40	0.45	0.89
15401	1102.19	1189.71	0.33	0.53	1124.85	0.53	0.84
11803	853.28	866.13	0.21	0.42	764.18	0.54	0.99
11400	1354.08	1342.77	0.49	0.86	1313.20	0.68	1.16
11804	844.93	852.32	0.28	0.58	749.72	0.55	1.03
11305	1837.64	1769.73	0.59	1.11	1773.77	0.61	1.13
14600	681.49	743.04	0.35	0.71	644.29	0.56	1.08
15101	1094.55	1152.79	0.32	0.56	1066.23	0.57	0.96
15402	1076.78	1183.30	0.32	0.55	1112.08	0.46	0.78
14512	702.60	861.97	0.53	1.11	774.06	0.55	1.02
15400	1263.74	1285.57	0.11	0.19	1231.42	0.23	0.43
14610	1368.17	1297.60	0.23	0.42	1277.32	0.27	0.45
14812	1073.21	1029.46	0.17	0.26	1092.84	0.20	0.36
15300	1703.31	1930.26	0.93	1.69	1935.49	1.03	1.73
15310	2041.10	1919.36	0.38	0.68	1915.25	0.41	0.75
15001	1216.83	1215.30	0.08	0.14	1213.54	0.10	0.17
15321	2426.67	2362.43	0.50	0.85	2361.16	0.49	0.83
15500	1249.78	1326.41	0.29	0.50	1274.23	0.36	0.58
14305	1488.60	1498.84	1.26	2.11	1481.40	1.19	2.02
14300	1348.19	1262.81	1.29	2.23	1197.90	1.24	2.20
14403	932.21	927.37	0.13	0.23	812.46	0.59	0.99
15515	1386.22	1385.45	0.31	0.54	1341.13	0.62	0.99
15430	2055.87	1963.21	0.26	0.42	1973.58	0.24	0.39
14520	722.95	807.39	0.30	0.48	664.54	0.70	1.13
14621	936.91	1048.96	0.35	0.60	956.85	0.55	0.92
14801	1070.14	1029.60	0.22	0.46	969.50	0.34	0.64
17005	1214.03	1203.84	0.09	0.13	1183.26	0.13	0.21
17001	1026.43	981.73	0.13	0.25	983.17	0.25	0.43
17315	1503.29	1456.28	0.14	0.23	1487.39	0.14	0.24
17301	1081.26	1119.52	0.16	0.28	1023.96	0.49	0.79

A-10: MAE statistic for all stations used within the evaluation of wind speed remappings (chapter 5.2.1.3)

WIND SPEED	1994-1996	CONSERVATIVE INTERPOLATION			BILINEAR INTERPOLATION		
STATION NR.	MEAN obs [m/s]	MEAN mod [m/s]	MAE [m/s]	Std_dev MAE [m/s]	MEAN mod [m/s]	MAE [m/s]	Std_dev MAE [m/s]
6300	2.60	2.23	0.38	0.25	2.17	0.47	0.34
6305	1.66	1.89	0.27	0.20	1.99	0.37	0.27
4161	4.69	4.26	0.44	0.21	4.28	0.41	0.20
4169	3.26	3.29	0.08	0.07	3.38	0.12	0.07
4543	1.67	1.83	0.18	0.15	2.00	0.34	0.21
4541	2.11	1.83	0.30	0.19	1.95	0.17	0.13
4535	1.96	1.75	0.27	0.24	1.84	0.20	0.18
4137	1.87	1.91	0.09	0.08	1.84	0.04	0.03
4175	3.91	4.37	0.47	0.28	4.14	0.24	0.16
4548	6.94	5.63	1.38	1.08	6.30	0.67	0.51
4176	3.92	4.37	0.45	0.27	4.25	0.33	0.21
4546	5.85	5.63	0.38	0.36	5.73	0.33	0.29
9450	1.97	2.12	0.16	0.10	2.08	0.11	0.07
4549	3.33	2.88	0.63	0.51	3.38	0.46	0.39
4168	1.38	1.59	0.27	0.18	1.53	0.18	0.13
4179	3.89	4.37	0.48	0.34	4.17	0.29	0.21
4536	1.71	2.18	0.49	0.32	2.03	0.32	0.21
4152	2.05	2.24	0.22	0.16	2.14	0.09	0.05
9215	1.32	1.89	0.58	0.34	1.90	0.59	0.33
9210	1.27	1.70	0.44	0.25	1.67	0.41	0.23
9500	1.56	1.77	0.22	0.14	1.83	0.28	0.18
4151	1.89	2.16	0.46	0.39	2.07	0.35	0.31
9016	2.16	2.69	0.54	0.35	2.76	0.61	0.35
4142	2.29	2.56	0.30	0.22	2.41	0.13	0.09
8800	3.13	3.33	0.27	0.24	3.50	0.39	0.24
11505	1.88	2.29	0.54	0.47	2.25	0.48	0.42
4156	1.24	2.82	1.59	0.92	2.54	1.30	0.75
4146	2.59	2.47	0.33	0.32	2.41	0.32	0.33
12201	1.93	2.16	0.24	0.14	2.00	0.09	0.09
12200	1.78	2.16	0.39	0.18	1.92	0.15	0.13
4157	1.80	2.56	0.82	0.45	2.30	0.56	0.30
12506	1.10	1.39	0.30	0.19	1.46	0.37	0.24
12504	1.01	1.39	0.38	0.25	1.37	0.37	0.24
12215	2.38	2.01	0.39	0.21	1.99	0.40	0.22
4155	5.81	3.77	2.04	1.04	3.55	2.26	1.15
4144	1.79	2.17	0.42	0.37	2.10	0.34	0.27
11602	1.30	2.63	1.33	0.67	2.71	1.42	0.68
11901	2.20	2.98	0.81	0.61	2.69	0.50	0.39
12301	1.23	1.65	0.49	0.35	1.66	0.48	0.34
12620	1.46	1.51	0.06	0.06	1.49	0.03	0.03
12311	2.04	1.69	0.36	0.24	1.58	0.47	0.31
12322	1.47	1.69	0.31	0.32	1.63	0.24	0.25
12505	1.40	1.54	0.15	0.12	1.45	0.06	0.04
12220	1.44	1.60	0.18	0.19	1.70	0.29	0.30
15401	1.45	2.26	0.83	0.60	2.12	0.68	0.45
11803	2.10	2.62	0.53	0.35	2.69	0.60	0.40
11400	1.49	2.12	0.74	0.51	2.06	0.62	0.42
11804	2.12	2.62	0.58	0.38	2.67	0.61	0.40
11305	1.52	2.25	0.75	0.52	2.10	0.60	0.44
14600	0.69	1.29	0.60	0.39	1.33	0.64	0.38
15101	1.40	1.94	0.68	0.67	2.16	0.83	0.57
15402	1.63	2.14	0.52	0.38	2.25	0.63	0.43
14512	0.64	1.46	0.83	0.52	1.37	0.75	0.48
15400	1.96	2.14	0.19	0.15	2.26	0.31	0.22
14610	2.81	2.71	0.12	0.09	2.91	0.12	0.10
14812	2.88	2.63	0.26	0.17	2.61	0.27	0.19
15300	1.89	2.94	1.05	0.60	3.31	1.42	0.95
15310	2.97	3.25	0.31	0.19	3.35	0.37	0.19
15001	1.90	2.02	0.12	0.11	1.91	0.04	0.06
15321	4.69	4.16	0.59	0.55	4.34	0.42	0.38
15500	1.85	2.12	0.32	0.20	2.33	0.48	0.30
14305	2.49	2.85	0.68	0.56	2.71	0.54	0.42
14300	2.01	2.25	0.62	0.50	2.43	0.69	0.54
14403	1.35	1.82	0.47	0.32	1.90	0.55	0.36
15515	1.81	2.62	0.82	0.52	2.50	0.70	0.43
15430	3.05	2.86	0.23	0.18	2.94	0.12	0.07
14520	1.02	1.60	0.60	0.43	1.80	0.79	0.51
14621	1.55	2.52	1.00	0.67	2.51	0.98	0.64
14801	2.03	2.39	0.36	0.27	2.35	0.32	0.21
17005	2.82	2.90	0.10	0.10	2.92	0.10	0.07
17001	2.60	2.98	0.40	0.28	2.99	0.39	0.27
17315	3.06	2.87	0.20	0.16	2.91	0.16	0.12
17301	2.38	2.97	0.60	0.40	2.91	0.53	0.36

WIND SPEED	1994-1996		REGRESSION BASED REMAPPING	
	STATION NR.	MEAN obs [m/s]	MEAN mod [m/s]	MAE [m/s]
6300	2.60	2.16	0.47	0.34
6305	1.66	1.97	0.36	0.28
4161	4.69	4.33	0.37	0.22
4169	3.26	3.35	0.10	0.08
4543	1.67	1.91	0.24	0.15
4541	2.11	2.01	0.11	0.10
4535	1.96	1.91	0.15	0.13
4137	1.87	1.85	0.03	0.02
4175	3.91	4.08	0.17	0.14
4548	6.94	6.41	0.59	0.55
4176	3.92	4.17	0.24	0.16
4546	5.85	5.67	0.29	0.25
9450	1.97	2.05	0.08	0.05
4549	3.33	3.35	0.47	0.41
4168	1.38	1.56	0.20	0.12
4179	3.89	4.09	0.20	0.15
4536	1.71	1.94	0.23	0.16
4152	2.05	2.12	0.07	0.04
9215	1.32	1.77	0.44	0.23
9210	1.27	1.58	0.31	0.17
9500	1.56	1.74	0.20	0.14
4151	1.89	2.01	0.31	0.28
9016	2.16	2.69	0.54	0.34
4142	2.29	2.38	0.09	0.07
8800	3.13	3.40	0.28	0.21
11505	1.88	2.15	0.43	0.38
4156	1.24	2.43	1.20	0.79
4146	2.59	2.40	0.32	0.33
12201	1.93	2.01	0.09	0.09
12200	1.78	1.89	0.12	0.11
4157	1.80	2.19	0.49	0.33
12506	1.10	1.35	0.26	0.18
12504	1.01	1.26	0.25	0.18
12215	2.38	2.10	0.29	0.17
4155	5.81	3.75	2.06	1.30
4144	1.79	2.03	0.28	0.28
11602	1.30	2.55	1.27	0.79
11901	2.20	2.53	0.35	0.28
12301	1.23	1.58	0.41	0.28
12620	1.46	1.48	0.03	0.02
12311	2.04	1.71	0.33	0.20
12322	1.47	1.55	0.20	0.20
12505	1.40	1.43	0.04	0.03
12220	1.44	1.64	0.25	0.24
15401	1.45	1.93	0.47	0.32
11803	2.10	2.51	0.42	0.30
11400	1.49	1.89	0.45	0.31
11804	2.12	2.50	0.45	0.31
11305	1.52	2.01	0.50	0.32
14600	0.69	1.17	0.49	0.33
15101	1.40	1.95	0.63	0.48
15402	1.63	2.07	0.44	0.30
14512	0.64	1.17	0.53	0.33
15400	1.96	2.17	0.22	0.15
14610	2.81	2.89	0.09	0.07
14812	2.88	2.68	0.20	0.13
15300	1.89	3.16	1.28	0.84
15310	2.97	3.27	0.30	0.14
15001	1.90	1.90	0.04	0.08
15321	4.69	4.28	0.46	0.43
15500	1.85	2.19	0.36	0.24
14305	2.49	2.66	0.49	0.39
14300	2.01	2.27	0.51	0.37
14403	1.35	1.73	0.38	0.27
15515	1.81	2.30	0.50	0.33
15430	3.05	2.97	0.09	0.08
14520	1.02	1.57	0.55	0.36
14621	1.55	2.29	0.74	0.37
14801	2.03	2.26	0.23	0.15
17005	2.82	2.90	0.08	0.08
17001	2.60	2.88	0.28	0.21
17315	3.06	2.95	0.12	0.09
17301	2.38	2.75	0.37	0.25

## 10 CURRICULUM VITAE

**Name:** Thomas Marke  
**Date of Birth:** 27.06.1977  
**Place of Birth:** Munich (Germany)  
**Nationality:** German  
**Degree:** Dipl. Geogr. (phys.)  
**Marital Status:** Unmarried  
**Postal Address:** Lierstrasse 24  
 80639 Munich  
**Email:** t.marke@iggf.geo.uni-muenchen.de

### Education:

2005-2008: PHD-studies,  
 Ludwig-Maximilians-Universität (LMU) Munich (Germany)  
 2004: Degree in physical geography,  
 Ludwig-Maximilians-Universität (LMU) Munich (Germany)  
 2004: Diploma Thesis:  
 Parameterization of a SVAT-Type Evapotranspiration Model for Oilseed  
 Rape using Eddy-Flux Data  
 2000-2004: Advanced studies of physical geography,  
 Ludwig-Maximilians-Universität (LMU) Munich (Germany)  
 2000: Intermediate diploma in physical geography,  
 Ludwig-Maximilians-Universität (LMU) Munich (Germany)  
 1998-2000: Basic studies of physical geography,  
 Ludwig-Maximilians-Universität (LMU) Munich (Germany)  
 1988-1997: High school, Gymnasium Puchheim (Germany)  
 1987-1988: Secondary school (Germany)  
 1983-1987: Elementary School (Germany)

### Experience:

2007: Assistant lecturer at the Department of Geography,  
 Ludwig-Maximilians-Universität (LMU) Munich (Germany)  
 2005: Scientific researcher at the chair of geography and geographical  
 remote sensing, Ludwig-Maximilians-Universität (LMU) Munich  
 (Germany)  
 2001-2003: Student worker at the Ground Truth Center Oberbayern (Gtco),  
 Germering (Germany)  
 2002: Internship at Thomas Reid Associates (TRA) – Environmental  
 Consultans, Palo Alto, California (USA)  
 2002: Internship at the German Aerospace Center (DLR),  
 Oberpfaffenhofen (Germany)  
 2001: Internship at Vista – remote sensing applications GmbH,  
 Luisenstraße 45, Munich (Germany)  
 1999-2001: Student assistant at the Ludwig-Maximilians-Universität (LMU)  
 Munich in different fields of operation

### General Conscription:

1997-1998: Civilian Service at the Johanniter Unfallhilfe, Puchheim (Germany)